

Modelling of material interfaces at different length scales

von der Fakultät Maschinenbau
der Technischen Universität Dortmund
zur Erlangung des akademischen Grades

Doktor-Ingenieur (Dr.-Ing.)

genehmigte Dissertation

von

Tim Steffen Heitbreder

aus Gladbeck

Referent:	Prof. Dr.-Ing. J. Mosler
Korreferenten:	Prof. N.S. Ottosen, Ph.D. Prof. Dr.-Ing. Dr.-Ing. E.h. A. E. Tekkaya
Tag der Einreichung:	01.08.2019
Tag der mündlichen Prüfung:	15.11.2019

Bibliografische Information Der Deutschen Bibliothek

Die Deutsche Bibliothek verzeichnet diese Publikation in der Deutschen Nationalbibliografie; detaillierte bibliografische Daten sind im Internet über <http://dnb.ddb.de> abrufbar.

Bibliographic information published by Die Deutsche Bibliothek

Die Deutsche Bibliothek lists this publication in the Deutsche Nationalbibliografie; detailed bibliographic data is available in the Internet at <http://dnb.ddb.de>.

Schriftenreihe des Instituts für Mechanik

Herausgeber: Institut für Mechanik
Fakultät Maschinenbau
Technische Universität Dortmund
Leonhard-Euler-Str. 5
D-44227 Dortmund

Druck: Koffler DruckManagement GmbH

© Tim Steffen Heitbreder 2019

This work is subject to copyright. All rights are reserved, whether the whole or part of the material is concerned, specifically the rights of translation, reprinting, reuse of illustrations, recitation, broadcasting, reproduction on microfilm or in any other way, and storage in data banks. Duplication of this publication or parts thereof is permitted in connection with reviews or scholarly analysis. Permission for use must always be obtained from the author.

Alle Rechte vorbehalten, auch das des auszugsweisen Nachdrucks, der auszugsweisen oder vollständigen Wiedergabe (Photographie, Mikroskopie), der Speicherung in Datenverarbeitungsanlagen und das der Übersetzung.

Als Manuskript gedruckt. Printed in Germany.

ISSN 2191-0022

ISBN 978-3-947323-18-0

“Give me a place to stand and I shall move the world”

Archimedes (c. 287 – c. 212 BC)

Acknowledgements

This thesis was developed during my work as a PhD student at the Institute of Mechanics at TU Dortmund University. This has been a great time for my personal and scientific development. Over the past years I have met so many people who supported me and thereby enabled me to write this thesis. I should like to take this opportunity to mention and thank some of the persons who encouraged me in various ways.

First of all, I want to thank Professor Jörn Mosler for his continuous support and the many interesting and instructive discussions during my time at the institute. He welcomed me in his team in March 2014 and gave me the possibility to deepen and expand my knowledge in continuum mechanics and inspired me with many helpful ideas and interesting topics. I also thank Professor Niels Saabye Ottosen for agreeing to be the co-referee of my thesis. His contributions in the field of interface modelling that have been carried out in collaboration with Professor Matti Ristinmaa build an important cornerstone and motivation for my thesis.

I would also like to take this opportunity to thank Professor Erman Tekkaya for acting as third referee of my thesis and Professor Andreas Brümmer for being the chairman of the examination committee.

Special thanks go to the whole team of the Institute of Mechanics. During my time I really enjoyed the collegial and friendly relationship between all team members. In this context I would like to thank Professor Andreas Menzel for his enormous contribution to the nice working atmosphere. I thank Kerstin Walter and Christina McDonagh for helping with all the organisational, formal and administrative stuff but beyond this for managing all the social events during the last years that I always enjoyed. Even though our taste concerning football differs from blue and white to black and yellow, we always had a lot of fun discussing the current ongoing in the Bundesliga.

Next, I want to express my thanks to all my colleagues that I have met during the last years. During my time at the institute some real friendships have been created. I thank Dr. Thorsten Bartel for the inspiring discussions far beyond the field of continuum mechanics. Besides that, of course, especially his interest and expertise in all mechanical topics is very helpful for all doctoral candidates at the institute. Furthermore, I was really happy when Dr. Patrick Kurzeja joined our team since I already admired his knowledge and inventiveness during my time as a student assistant in Bochum where he promoted my interest in continuum mechanics. Particularly, I want to thank my room mates Ph.D. Guillermo Diaz and Volker Fohrmeister who were the first ones who shared my happiness when I received quadratic convergence and who helped me out when things did not go well. As I already mentioned, I was always impressed by the

nice atmosphere at the institute. The high willingness of helping out with problems is carried out by every group member. Therefore, I would like to thank Serhat Aygün, Tim Furlan, Dr. Raphael Holtermann, Dr. Tobias Kaiser, Professor Sandra Klinge, Manuel Kröger, Henning Lammen, Kai Langenfeld, Isabelle Noll, Dr. Richard Ostwald, Lars Rose, Markus Schewe, Robin Schulte, Christian Sievers, Leon Sprave, Tillmann Wiegold and Hendrik Wilbuer for their helpful and engaged teamwork. I also want to thank Matthias Weiss who professionally serviced the hardware and software at the institute.

Moreover, I want to thank my former colleagues Dr. Rolf Berthelsen, Dr. Alexander Bartels, Dr. Karsten Buckmann, Dr. Dinesh Dusthakar, Professor Björn Kiefer, Ph.D. Cesar Polindara, Professor Ralf Denzer, Dr. Tobias Waffenschmidt and Dr. Till Clausmeyer. Especially their help and cooperation during my beginnings at the institute enabled me a quick entry into the team.

Furthermore, I want to thank Professor Ali Javili for his support of my work during his time at TU Dortmund University and the many inspiring contributions in the field of interface modelling.

Last but not least, I would like to thank my family and friends for their support. The cornerstone for writing this thesis has been built by my parents Margret and Jürgen by giving me the best help I could imagine during my whole educational process. My brother Jörn and all my friends from Buer gave me the possibility for deflection and having fun together at all phases where I needed to see something different other than equations. Finally, I would like to thank my wife Janina for her support over the last years and for making my life something special.

Dortmund, November 2019

Tim Heitbreder

Zusammenfassung

Die vorliegende Arbeit befasst sich mit der Entwicklung und Implementierung von neuen Materialmodellen zur Beschreibung von Grenzflächen unter großen Verformungen in einem geometrisch exakten Rahmen. Klassische Kohesivzonenmodelle sind eine weit verbreitete Methode um das Materialverhalten von Grenzflächen zu beschreiben und zu simulieren. In vielen solcher Modelle werden allerdings fundamentale physikalische Bedingungen, wie z.B. thermodynamische Konsistenz, Bilanzgleichungen oder das Prinzip der Objektivität, vernachlässigt. Im Gegensatz dazu wird in dieser Arbeit ein erweiterter Ansatz für ein Kohesivzonenmodell vorgestellt. Das Modell ermöglicht die Untersuchung von lokalisierten plastischen Deformationen, welche nur vom Verschiebungssprung entlang der Grenzfläche abhängen. Darüberhinaus, wird ein generalisierter Ansatz herausgearbeitet, der im Gegensatz zu früheren konstitutiven Kohesivzonenmodellen eine Beschreibung von beliebigen Anisotropien im Bereich der Grenzflächen ermöglicht. Dabei werden fundamentale physikalische Bedingungen, wie z.B. die Bilanzgleichungen oder das Prinzip der materiellen Objektivität, erfüllt.

Grenzflächen beeinflussen die Materialantwort eines Werkstoffes sowohl auf der technologisch wichtigen Makroskala als auch auf der aus materialwissenschaftlicher Sicht wichtigen Mikroskala. Unabhängig von der betrachteten Skala wird in dieser Arbeit im Rahmen von numerischen Beispielen gezeigt, dass die Zusammenführung von Volumen- und Grenzflächenenergien zu einem Größeneffekt führt. Abhängig von der Wahl des konstitutiven Modells für die Grenzfläche werden verschiedene Effekte gezeigt und diskutiert.

Abschließend wird die Berücksichtigung von höheren Gradiententermen im konstitutiven Modell untersucht.

Abstract

This thesis deals with the derivation and implementation of novel material models suitable for material interfaces undergoing large deformations in a geometrically exact setting. The classic cohesive zone framework is a widespread tool to describe and simulate the behaviour of material interfaces. However, the constraints imposed by fundamental physical principles such as thermodynamical consistency, balance equations and material frame indifference are often ignored in classic formulations. By way of contrast, a consistent cohesive zone framework suitable for the analysis of localised elastic and inelastic deformations which only depends on the displacement jump is elaborated in this thesis. Furthermore, a general interface framework is presented that, in contrast to previous works, permits the description of arbitrary material anisotropies by fulfilling all fundamental balance laws in physics as well as the principle of material objectivity.

Interfaces highly influence the material behaviour at the technologically relevant macroscale as well as at the microscale which is important, e.g., in materials science. Independent of the considered scale, it is shown by numerical examples that the interaction of bulk energies and interface energies leads, in a very natural manner, to a complex size effect. Depending on the chosen interface framework different effects are presented and discussed.

The incorporation of higher gradients into the constitutive interface framework is also investigated.

Publications

Key parts of this thesis are based on peer-reviewed journal articles, which were either published, submitted or prepared during the progress of this thesis.

1. T. Heitbreder, N.S. Ottosen, M. Ristinmaa, J. Mosler: *Consistent elastoplastic cohesive zone model at finite deformations – Variational formulation*, International Journal of Solids and Structures, 106–107:284–293, 2017 [40].
2. T. Heitbreder, N.S. Ottosen, M. Ristinmaa, J. Mosler: *On damage modeling of material interfaces: Numerical implementation and computational homogenization*, Computer Methods in Applied Mechanics and Engineering, 337:1–27, 2018 [41].
3. T. Heitbreder, P. Kurzeja, J. Mosler: *On higher-order interface models*, under preparation.

Some parts of the contents of the listed articles as well as some figures have been partly modified in order to avoid unnecessary repetitions and to connect the essential parts of this thesis. All authors that were included in the publishing process of the articles are listed above. The author of this thesis contributed essential parts of the underlying theories. Furthermore, he prepared the algorithmic formulations, derivatives and carried out all the numerical simulations and examples.

Contents

Notation	xi
1 Introduction	1
1.1 Motivation	1
1.2 State of the art	2
1.3 Structure of the thesis	7
2 Introduction to continuum mechanics – bulk materials	11
2.1 Kinematics	11
2.2 Balance laws	15
2.2.1 Balance of linear momentum	15
2.2.2 Balance of angular momentum	16
2.2.3 Balance of energy - first law of thermodynamics	17
2.2.4 Entropy inequality - second law of thermodynamics	18
2.3 Variational principles in continuum mechanics	19
2.3.1 Introduction to hyperelasticity	20
2.3.2 Introduction to plasticity	24
3 Review of classic cohesive zone models	31
3.1 Kinematics of non-coherent interfaces	32
3.2 Thermodynamical consistency	34
3.3 Balance of linear and angular momentum	35
3.3.1 Variational formulation of balance of linear momentum	37
3.4 Extension to isotropic damage	38
3.4.1 Variational formulation for isotropic interface damage models	39
3.5 Extension to elastoplasticity	41
3.5.1 Eulerian framework	41
3.5.2 Lagrangian framework	43
4 Consistent cohesive zone framework I – sliding of the fiber’s corner points	47
4.1 Kinematics of the generalised fiber model	48
4.2 Balance laws of the generalised cohesive zone sliding framework	50
4.2.1 Balance of linear momentum	51
4.2.2 Balance of angular momentum	51
4.2.3 Second law of thermodynamics	52

4.3	Constitutive modelling	53
4.3.1	Elasticity	53
4.3.2	Elastoplasticity	54
4.4	Consistent elastoplastic fiber model – prototype model of the generalised cohesive zone framework	58
4.4.1	Elastoplastic prototype model	61
4.4.2	Prototype model including damage	62
4.5	Novel unloading approach	63
4.5.1	Preliminaries	63
4.5.2	Novel unloading behaviour - wrinkling of fibers	64
4.6	Variational structure of the cohesive zone framework	66
4.7	Numerical examples	68
5	Consistent cohesive zone framework II – coupling with surface elasticity	77
5.1	Kinematics of coherent interfaces - introduction to surface elasticity . . .	77
5.2	Balance laws of the generalised interface framework	80
5.2.1	Preliminaries	80
5.2.2	Work conjugacy and second law of thermodynamics	81
5.2.3	Balance of linear momentum	82
5.2.4	Balance of angular momentum	85
5.3	Prototype model – a quasi-brittle mixed-mode damage model	86
5.3.1	Numerical implementation	91
5.4	Numerical investigation of balance of angular momentum	96
6	Size effects due to material interfaces	101
6.1	Preliminaries	101
6.2	Average theorems for interface homogenisation	102
6.3	Numerical implementation	105
6.3.1	Computation of macroscopic stresses based on volume integrals . .	106
6.3.2	Computation of macroscopic stresses based on surface integrals . .	106
6.3.3	Computation of macroscopic stresses based on the vector of internal forces	107
6.4	Numerical Examples	108
6.4.1	Analysis of the anisotropy induced by the general interface model	109
6.4.2	Analysis of the size effect induced by interface models	111
7	Higher-order interfaces	117
7.1	Enhancement with the gradient of the displacement jump	119
7.1.1	Preliminaries – Objectivity requirements	119
7.1.2	Balance of linear momentum	120
7.2	Interface models in homogenisation theory	122
7.2.1	Preliminaries for the local interface model	124

7.2.2	Preliminaries of the effective interface model	125
7.2.3	Comparison of the different approaches	127
7.2.4	Possibilities to expand the equivalence	131
7.2.5	Physical interpretation of the interface contributions	133
7.3	Gradient of surface deformation gradient	136
7.3.1	Motivation	136
7.3.2	Kinematics	139
7.3.3	Objectivity requirements	140
7.3.4	Symmetry properties of $\overline{\text{GRAD}}(\overline{\mathbf{F}})$	141
7.3.5	On the relation between the mean curvature and $\overline{\text{GRAD}}(\overline{\mathbf{F}})$. . .	142
8	Conclusion and Outlook	147
8.1	Concluding remarks	147
8.1.1	Inconsistencies in classic cohesive zone models	147
8.1.2	Generalised interface framework	147
8.1.3	Size effect due to material interfaces	148
8.1.4	Higher-order interfaces	149
8.2	Outlook	150
A	Differential geometry for fiber sliding	151
A.1	Derivation of quantity j according to the relation between the upper and lower tractions (Eq. (4.13))	151
B	Implementation of generalised interfaces	153
B.1	Vector of internal forces and stiffness matrix of the prototype model according to Table 5.1	153
C	Derivation of contributions concerning the gradient of $[[\mathbf{u}]]$	161
C.1	Representation of local energy including higher order displacement jump contributions	161
D	Derivation of curvature contributions	165
D.1	Symmetry properties of $\overline{\text{GRAD}}(\overline{\mathbf{F}})$	165
D.2	Laplace-Beltrami operator	166
D.3	Re-derivation of the gradient of the inverse deformation gradient	166
D.4	Symmetry properties of $\overline{\text{GRAD}}(\overline{\mathbf{F}}^{-1})$	167
D.5	Coefficient comparison for the covariant representation of mean curvature h	167
	Bibliography	171

Notation

The notation used in this thesis becomes obvious from its context. However, the following essential relations are collectively provided for the sake of the reader's convenience. They are used in the entire thesis. In some places the descriptions are presented in index notation which implies the Einstein summation rule. Throughout the thesis Latin indices take the values 1, 2 and 3 and describe quantities belonging to bulk materials. In contrast to that Greek indices take the values 1 and 2 and quantities using such notation belong to surfaces respectively interfaces.

Tensors In a three-dimensional Euclidean space spanned by the Cartesian basis vectors $\{\mathbf{e}_i\}, i = 1, 2, 3$, tensors of first, second, third and fourth order are expressed in terms of their coefficients $(\bullet)_i$ following Einstein's summation convention, namely

$$\begin{aligned} \mathbf{a} &= a_i \mathbf{e}_i \quad , & (\text{first-order tensor, i.e. vector}) \\ \mathbf{B} &= B_{ij} \mathbf{e}_i \otimes \mathbf{e}_j \quad , & (\text{second-order tensor}) \\ \mathbf{C} &= C_{ijk} \mathbf{e}_i \otimes \mathbf{e}_j \otimes \mathbf{e}_k \quad . & (\text{third-order tensor}) \\ \mathbb{D} &= D_{ijkl} \mathbf{e}_i \otimes \mathbf{e}_j \otimes \mathbf{e}_k \otimes \mathbf{e}_l \quad . & (\text{fourth-order tensor}) \end{aligned}$$

Standard and non-standard inner tensor products Inner tensor products are denoted by dots where the number of dots characterises the number of contractions, i.e.

$$\begin{aligned} \mathbf{a} \cdot \mathbf{b} &= a_i b_i \quad , \\ \mathbf{A} \cdot \mathbf{b} &= A_{ij} b_j \mathbf{e}_i \quad , \\ \mathbf{A} \cdot \mathbf{B} &= A_{ij} B_{jk} \mathbf{e}_i \otimes \mathbf{e}_k \quad , \\ \mathbf{A} : \mathbf{B} &= S_{ij} T_{ij} \quad , \\ \mathbf{A} \cdot \mathbf{b} &= A_{ijk} b_k \mathbf{e}_i \otimes \mathbf{e}_j \\ \mathbf{A} : \mathbf{B} &= A_{ijk} B_{jk} \mathbf{e}_i \\ \mathbf{A} \dot{\cdot} \mathbf{B} &= A_{ijk} B_{ijk} \quad , \\ \mathbf{A} \bar{\cdot} \mathbf{B} &= A_{ijl} B_{jlm} \mathbf{e}_i \otimes \mathbf{e}_l \otimes \mathbf{e}_m \quad . \end{aligned}$$

In this regard only the definition of the operation $(\bar{\cdot})$ is non-standard since it represents inner tensor product with the second index. An n -fold contraction of two n th-order tensors always results in a scalar. A generalised scalar product of two n -th order tensors \mathcal{A} and \mathcal{B} is denoted by the (\circ) symbol, i.e., $\mathcal{A} \circ \mathcal{B}$.

Outer tensor products Outer tensor products—also referred to as dyadic products—are represented by the classical symbol \otimes using the definitions

$$\begin{aligned}\mathbf{u} \otimes \mathbf{v} &= u_i v_j \mathbf{e}_i \otimes \mathbf{e}_j \quad , \\ \mathbf{S} \otimes \mathbf{T} &= S_{ij} T_{kl} \mathbf{e}_i \otimes \mathbf{e}_j \otimes \mathbf{e}_k \otimes \mathbf{e}_l \quad .\end{aligned}$$

The dyadic product of two first-order tensors, i.e. vectors, results in second-order tensors, whereas the dyadic products of two second-order tensors result in fourth-order tensors.

Identity tensors The second-order bulk identity tensor is denoted \mathbf{i} or \mathbf{I} in the spatial and material configurations, respectively. Both notations are identical as

$$\mathbf{I} = \delta_{ij} \mathbf{e}_i \otimes \mathbf{e}_j = \mathbf{i}$$

with the Kronecker delta symbol $\delta_{ij} = \mathbf{e}_i \cdot \mathbf{e}_j$.

The second-order surface identity tensor is denoted $\bar{\mathbf{i}}$ or $\bar{\mathbf{I}}$ in the spatial and material configurations, respectively and reads

$$\begin{aligned}\bar{\mathbf{I}} &= \mathbf{I} - \bar{\mathbf{N}} \otimes \bar{\mathbf{N}} \quad \text{and} \\ \bar{\mathbf{i}} &= \mathbf{i} - \bar{\mathbf{n}} \otimes \bar{\mathbf{n}},\end{aligned}$$

with $\bar{\mathbf{N}}$ and $\bar{\mathbf{n}}$ being the normal vector of surface corresponding to the material respectively spatial configuration. In general $\bar{\mathbf{i}}$ and $\bar{\mathbf{I}}$ are not identical.

Gradient and divergence operators With \mathbf{G}^i and \mathbf{g}^i denoting the contravariant bulk base vectors and their surface counter parts \mathbf{G}^α and \mathbf{g}^α , the following gradient and divergence operators are used throughout the thesis:

$$\begin{aligned}\text{GRAD}(\bullet) &= \frac{\partial(\bullet)}{\partial\theta^i} \otimes \mathbf{G}^i & \text{grad}(\bullet) &= \frac{\partial(\bullet)}{\partial\theta^i} \otimes \mathbf{g}^i \\ \overline{\text{GRAD}}(\bullet) &= \frac{\partial(\bullet)}{\partial\theta^\alpha} \otimes \mathbf{G}^\alpha & \overline{\text{grad}}(\bullet) &= \frac{\partial(\bullet)}{\partial\theta^\alpha} \otimes \mathbf{g}^\alpha \\ \text{DIV}(\bullet) &= \frac{\partial(\bullet)}{\partial\theta^i} \cdot \mathbf{G}^i & \text{div}(\bullet) &= \frac{\partial(\bullet)}{\partial\theta^i} \cdot \mathbf{g}^i \\ \overline{\text{DIV}}(\bullet) &= \frac{\partial(\bullet)}{\partial\theta^\alpha} \cdot \mathbf{G}^\alpha & \overline{\text{div}}(\bullet) &= \frac{\partial(\bullet)}{\partial\theta^\alpha} \cdot \mathbf{g}^\alpha\end{aligned}$$

1 Introduction

1.1 Motivation

Material interfaces have been a subject of interest for a long time since they can be observed at all spatial scales and they often strongly affect the overall behaviour of the considered material (system). Illustrative examples of material interfaces at the macroscopic scale include, for instance, cracks in quasi-brittle materials. While the relevance of such macroscopic material interfaces for the structural response is obvious, material interfaces observed at smaller length scales also frequently have a significant impact on the macroscopic structural response. This is, for instance, confirmed by nanocrystalline materials. Typical further examples for such microscopic interfaces are shear bands in ductile materials, phase boundaries in solids or grain boundaries in polycrystals. Furthermore, many materials are interspersed with inclusions, where different material properties interact and thereby influence the overall mechanical response. Interfaces in a material may be classified as coherent or non-coherent. In coherent interfaces the displacement is continuous across the interface, whereas in non-coherent interfaces a displacement jump exists across the interface. In addition to a possible jump of the traction vector acting on the upper and lower side of the interface, coherent interfaces also show in-plane membrane forces in the interface.

A modelling framework which falls into the range of non-coherent material interfaces is the cohesive zone modelling approach. Cohesive zone models provide a powerful and widespread tool for fracture simulation at the macroscopic scale as well as for the evolution of material interfaces on microscopic scales. However, in most of the existing cohesive zone models fundamental physical requirements are neglected. This is particularly true in the case of finite deformations. For instance, it can be shown that only isotropic classic cohesive models can be derived in a thermodynamically consistent way. Furthermore, only isotropic models fulfill balance of angular momentum. This limits the possibility of modelling shear and anisotropic effects. However, due to experimental observations, it is known that many materials behave differently in the case of normal or shear loading. Thus, classic cohesive models cannot depict the realistic material

behaviour. Further problems occur if elastoplastic effects are to be considered in the constitutive framework.

As mentioned above, material interfaces at the microscale highly influence the overall mechanical response. Since nearly all materials can be described as heterogeneous at a certain length scale, it is important to evaluate effective macroscopic properties of such materials. They can be estimated from the response of its underlying micro-structure using homogenisation procedures. The combination of bulk and interface energies naturally includes a size-effect due to the increasing area to volume ratio. Such size effects are not described within classic first-order computational homogenisation schemes.

The main goal of this thesis is to avoid the aforementioned limitations and to investigate the influence of material interfaces at different scales. Therefore, an extension of the classic cohesive interface framework is introduced. This framework enables the consistent modelling of elastoplastic effects within the interface. Furthermore, a general type of interface formulation is presented. The novel framework combines the classic cohesive zone theory and the theory of surface elasticity. The main features of the elaborated generalised interface framework are:

- geometrically exact description based on finite deformations
- thermodynamical consistency
- fulfillment of all fundamental balance laws
- fulfillment of the principle of material frame indifference
- modelling of shear and anisotropic effects
- consideration of different fracture properties in normal and shear direction

Besides the extension of the interface framework, the classic homogenisation scheme also has to be extended in order to capture the interface size effect. A possible solution will be shown in this thesis and several size effects are investigated. Furthermore, this thesis offers an insight into the incorporation of higher gradients into the interface description. To the best knowledge of the author, no further investigations concerning higher gradients in cohesive zone models exist up to now. The incorporation of higher-order gradients opens up the possibility of capturing new effects such as a bending resistance which is becoming increasingly important at smaller length scales.

1.2 State of the art

Non-coherent interfaces embody the cohesive zone modelling concept which dates back to the pioneering works by Barenblatt [4, 5] on quasi-brittle materials and by Dugdale [25] on ductile materials. Probably inspired by the aforementioned works, the so-called fictitious crack model has been proposed by Hillerborg et al. [42]. These works can be

considered as cornerstones in classic cohesive zone modelling. Here, the stress vector acting at the surface of an opened crack, frequently denoted as cohesive traction vector, is usually given in terms of the crack opening width, indicated by a displacement discontinuity. The cohesive tractions resist the opening of the bulk material along the cohesive zone. Accordingly, they are based on traction-separation laws – instead of a classic stress-strain-relationship in bulk materials. Already now it should be outlined that classic cohesive models do not consider in-plane or out-of-plane membrane forces and that the traction vector is continuous across the interface.

The elaboration of suitable traction-separation laws is one of the main challenges in cohesive zone modelling. Many different forms of functions and parameters have been elaborated within the last decades. The applicability of the most common functions to different material interfaces and crack behaviour was investigated, e.g., in Alfano [1], Chandra et al. [16], Park and H. Paulino [78] amongst others.

In line with Mosler and Scheider [68], Park et al. [79], cohesive traction-separation relationships may be classified in either non-potential based and potential based formulations.

Within non-potential based models a relationship between the cohesive traction vector acting at the interface and the displacement discontinuity, in the following referred to as displacement jump, is postulated in an ad-hoc manner, cf. eg. Scheider and Brocks [86]. Models falling into that range show some restrictions and limitations, especially from a thermodynamical point of view as discussed in [68]. For instance, van den Bosch et al. [100] proposed a non-potential based cohesive zone model employable for mixed-mode decohesion. However, as shown by the same group, the model is only suitable for small deformations and needs to be extended for finite displacements, see van den Bosch et al. [101]. The authors neither decompose the traction vector nor the displacement jump into normal and shear components which is equivalent to an isotropic interface model. Later on, they suggest an extension of their model to anisotropic interfaces by a decomposition of the displacement jump into a normal and a shear component, cf. van den Bosch et al. [102]. However, one of the main disadvantages of non-potential based cohesive models is that normally two independent models have to be introduced since unloading behaviour is not captured within such models, cf. [101]. This is not in line with the thermodynamically consistent elaboration of material models in the case of classic stress–strain based constitutive models in bulk materials. For instance, in the case of damage–type constitutive laws the reader is referred to Simo and Ju [89]. Furthermore, since such cohesive models are not derived from a potential, they do not guarantee a symmetric tangent matrix and show path dependent behaviour. In [100] it is argued that, due to the irreversibility of cohesive zone laws, the path dependency is physically meaningful and the symmetry requirement for the tangent matrix might be neglected. However, as discussed in [68] symmetry and path dependence are not equivalent, and at least the case of elastic unloading of interfaces described by such cohesive zone laws has to show a symmetric tangent matrix. Anyhow, non-potential based cohesive laws are widespread and often applied to interface modelling.

Nevertheless, due to the aforementioned restrictions and inconsistencies, the focus of this thesis lies on the second main group of so-called potential based cohesive models. Following [68] thermodynamically consistent cohesive models have to be derived from a potential. The idea here is to derive the traction vector as the derivative of a potential function. Famous formulations in that range are for instance Needleman [70], Tvergaard and Hutchinson [99]. Although, numerous widespread potential based cohesive models exist, many of them exhibit restrictions and limitations. The exponential traction-separation law by Xu and Needleman [105] is probably one of the most commonly implemented cohesive zone models. It is based on the definition of an interface potential representing the work done by two surfaces at an interface undergoing a relative separation. The resulting tractions are given as derivative of the potential with respect to this separation. One special feature of this model is the coupling of normal and tangential separation by two varying parameters for the work done by the two opening processes. However, as shown in [100], within the exponential cohesive law in [105] a physically realistic coupling behaviour only can be achieved with equal normal and tangential work of separation parameters. Due to experimental observations, this is unrealistic for most materials. Furthermore, the model is reversible and thereby history independent. This is unsatisfactory since interface models are mostly used in order to capture material failure which is intrinsically a non-conservative process. In order to consider the non-reversibility within the model of [105] an additional cohesive model is required in the case of unloading. Due to this reasons many extensions and improvements exist for the exponential potential based model throughout literature, cf. for instance McGarry et al. [58], Éamonn Ó Máirtín et al. [107].

The PPR-model by Park et al. [79] represents a famous potential based cohesive model. It captures different fracture energies as well as several cohesive strengths in normal and tangential direction. A detailed derivation of the implementation is given in Cerrone et al. [15]. However, the considered potential in the PPR-model just depends on the displacement jump, and therefore the model does not contain a built-in unloading/reloading relation. Certainly, following Spring et al. [91] the PPR model is thermodynamically consistent under the pure loading conditions for which it was designed. Nevertheless, it should be highlighted that this only holds if the crack faces remain parallel during the deformation and if no structural tensors are considered in the potential function. This seems to be unphysical in the case of finite displacements. Furthermore, in [91] a novel thermodynamically consistent coupled unloading/reloading relation for the PPR model under the aforementioned assumption is developed.

In summary, potential based models in line with the previously cited works do still not solve all problems and restrictions discussed for non-potential formulations. A further approach for the thermodynamically consistent derivation of cohesive models has been proposed in Gasser and Holzapfel [32], Mergheim and Steinmann [59], Radulovic et al. [84]. In contrast to the previous potential based models, the Helmholtz free energy density Ψ is taken here as potential function and, apart from the displacement jump, a set of internal variables is also considered. Thereby, the model becomes dependent on the

deformation history. Clearly, this framework holds for loading as well as for unloading. However, further restrictions of modelling anisotropic effects arise in the formulation. To be more precise, modelling anisotropic effects requires the consideration of structural tensors within Ψ . For instance, normal vector $\bar{\mathbf{n}}$ might be chosen in order to decompose the traction vector into a normal and a shear part. Due to the deformation dependence of $\bar{\mathbf{n}}$ an energetically conjugate stress contribution has to be introduced. If this is not the case, the anisotropic formulation would either lead to unphysical dissipation (even in the case of fully elastic deformation), cf. [68], or to an unsymmetric stiffness matrix (also even in the case of fully elastic deformation), cf. [59]. Hence, the approach of anisotropic cohesive zone description in [32] is thermodynamically inconsistent.

This problem might not occur in the case of small displacements where $\bar{\mathbf{n}}$ is assumed to be deformation independent. A thermodynamically consistent cohesive model in the case of small deformations was introduced by Ottosen and Ristinmaa [76]. Dimitri et al. [24] recently proposed a thermodynamically consistent reformulation of the non-potential based model in [100]. Their reformulation includes monolithical loading, unloading, decohesion and contact. However, although the authors of [24] consider $\bar{\mathbf{n}}$ within the Helmholtz free energy density Ψ , they do not consider an additional stress contribution in the stress power due to the change of $\bar{\mathbf{n}}$. As already mentioned, this is only valid if the normal vector does not change during deformation which seems to be physical in the case of small deformations only.

Besides thermodynamical inconsistencies, classic cohesive zone models show further restrictions concerning balance of angular momentum as pointed out by Vossen et al. [103]. It is highlighted that the traction vector has to point into the direction of $[[\mathbf{u}]]$ in the case of large deformations in order to fulfill balance of angular momentum. This formulation is equivalent to an isotropic interface fiber model, cf. [101]. Recently Ottosen et al. [75] pointed out that in classic cohesive zone theory only isotropic models fulfill all fundamental requirements in continuum mechanics. An extension to elastoplasticity leads to further problems concerning material frame indifference which is why the authors of [75] propose a novel extended framework that expands the classic cohesive zone fiber framework by allowing a sliding of the cohesive fiber's corner points within the material configuration. Heitbreder et al. [40] extended the framework with a novel unloading behaviour and re-derived the formulation from a variational point of view. Furthermore, the applicability of the cohesive framework is investigated by means of numerical simulations in [40].

The classic cohesive zone framework is related to non-coherent interfaces that may open during the deformation. However, interfaces can also be assumed as coherent. In the case of coherent interfaces, the deformation is continuous across the interface. To be more precise, the interface may not open during the deformation. In addition to a possible jump of the traction vector acting on the upper and lower side of the interface, coherent interfaces also show in-plane membrane forces in the interface. The general framework for this problem was established by Gurtin and Murdoch [36] and was further developed by Gurtin [34, 35], Murdoch [69]. Many extensions and applica-

tions of the theory may be found in the literature, cf. Javili et al. [49], Kaessmair et al. [52], Steinmann [94] among others. Curvature effects have for instance been studied in Steigmann and Ogden [93] and Chhapadia et al. [17]. A formulation of a geometrically nonlinear theory of higher-gradient elasticity accounting for boundary (surface and curve) energies can be found in Javili et al. [46]. Javili et al. [51] recently proposed an energetically consistent interface linear elasticity theory together with its appropriate stress measures. The theory of surface elasticity has successfully been applied for the analysis of, for instance, grain boundaries and the size effect observed at the nano-scale.

Ottosen et al. [77] recently proposed a novel framework combining the properties of non-coherent interfaces and coherent interfaces at finite displacements. It does not show the inconsistencies and restrictions appearing in classic cohesive zone theory. The framework shows similarities to the work of Mosler and Scheider [68]. The main idea is to consider additional tractions related to membrane-like forces and out-of-plane shear forces acting within the interface, see Fig. 1.1. In summary, the framework allows jumps

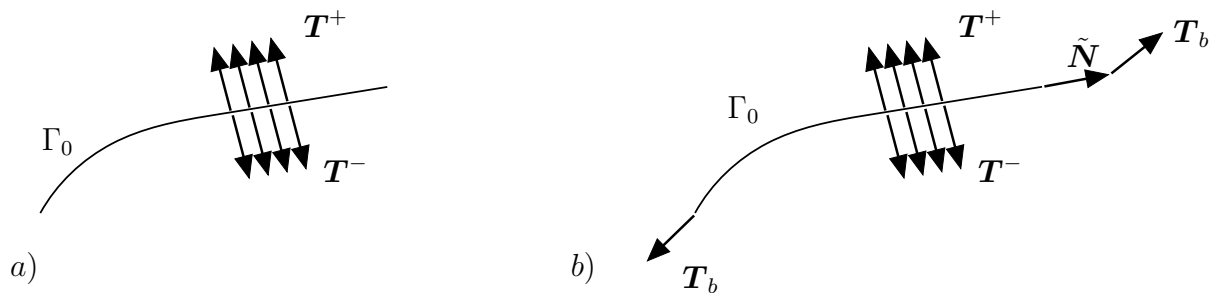


Figure 1.1: Reference configuration of an interface Γ_0 : a) classic cohesive zone approach with tractions T^+ at the upper side and tractions T^- at the lower side of the interface; b) Extended interface framework additionally considering membrane-like and out-of-plane shear tractions T_b along the interface

in the displacement as well as in the tractions. Hence, Javili et al. [50] denote this extension as generalised interface framework. Due to the influence of material interfaces on the macroscopic stress response, an extension of classic bulk homogenisation with interface contributions is introduced in [50] and the arising size effects are investigated. A formulation of the novel framework in a variationally consistent manner can be found in Javili [47], see also Heitbreder et al. [41]. In [41] the applicability of the generalised framework in the case of an anisotropic cohesive zone is investigated where the focus lies on anisotropic material degradation and its numerical implementation.

In summary, generalised interfaces combine the framework of the classic cohesive zone theory for non-coherent interfaces and the theory of surface elasticity for coherent interfaces. Thereby, material anisotropies can for instance be modelled in a thermodynamically consistent way.

Material interfaces can be embedded into the finite element method by assuming them to be located between two adjacent continuum finite elements, cf. Ortiz and Pandolfi [72]. This is especially convenient when the position of the interface is known in advance. Although this type of numerical implementation is well established nowadays, several

questions remain to be answered. For instance, the effect of numerical integration was considered by Schellekens and de Borst [87], convergence issues were analysed by de Borst [22] and locking effects were investigated by Mosler [63]. If, however, the position of the interface is not known in advance – as for cracking – fundamental additional numerical problems arise. A possible solution to this type of so-called free-discontinuity problems is provided by the partition-of-unity concept, cf. Babuška and Melenk [3], Belytschko and Black [9] and Moës et al. [62]. Although free-discontinuity problems are indeed numerically challenging, they do not represent the focus of this thesis.

While the works already cited within the previous paragraph are associated with non-coherent interfaces, finite element implementations for coherent ones are presented by Javili and Steinmann [44, 45].

1.3 Structure of the thesis

As mentioned before, one of the main goals of this thesis is to elaborate interface material models that are consistent with respect to all essential balance laws in physics. In order to introduce the requirements for the consistent elaboration of mechanical material models, Chapter 2 contains a concise review of the fundamentals in continuum mechanics for classic bulk materials. After the formulation of the kinematics, the relevant balance laws are summarised. Subsequently, the focus is on constitutive modelling in the context of variational principles. To be more precise, a framework is introduced that allows the derivation of all fundamental balance laws, boundary conditions, together with the constitutive equations (such as the evolution equations) by minimising an energy potential. Here, hyperelasticity is considered first. Afterwards, the derivation in the case of dissipative materials is summarised.

The relevance of the elaboration of novel interface models is addressed in Chapter 3 where classic cohesive zone models are reviewed. It is highlighted that, while for small displacements the only limitation is that of thermodynamic consistency, in finite displacements, however, the classic theory leads to further problems. It is shown that classic anisotropic cohesive zone models generally are inconsistent with respect to the second law of thermodynamics as well as with respect to balance of angular momentum. Due to the restrictions of modelling shear and anisotropic effects, it turns out that classic cohesive models can be interpreted as fiber models where the traction has to point in the direction of the displacement discontinuity within the interface. The fiber is defined by two points, both with the same material coordinates, on each side of the interface. The concept of traction continuity across the interface is explained from a variational point of view. Furthermore, it is shown that the extension to isotropic damage is straightforward, whereas the extension to elastoplasticity leads to additional problems concerning the principle of material frame indifference.

The aforementioned restrictions serve as a motivation for the first extended cohesive framework presented in Chapter 4. In contrast to classic cohesive zone models, this

extended framework is consistent with respect to the aforementioned points. Since the novel framework abandons the classic fiber interface concept presented in the previous chapter, the interface balance laws have to be derived first. Furthermore, it is pointed out that the relaxation of the fiber concept enables a consistent modelling of elastoplastic interface behaviour. A prototype model of the extended framework is then developed. The prototype model is in line with classic cohesive zone models. One of the key aspects of this chapter is the novel unloading behaviour elaborated afterwards. The underlying idea of this behaviour is the consideration of a fiber with a vanishing bending stiffness resulting in buckling without any energy. Subsequently, the elastoplastic loading and the unloading model are combined and rewritten into a unified framework based on incremental energy minimisation. The capability of the novel model is demonstrated within numerical examples where it is compared to a classic isotropic damage interface model.

A different approach for a generalised consistent interface model is proposed in Chapter 5. Here, the idea is to combine the cohesive zone theory of non-coherent interfaces with the theory of coherent interfaces based on surface elasticity. After the formulation of the generalised interface kinematics, the extended balance laws are derived from a variational point of view. The main point in the elaboration of this extended framework lies in an extended stress power assumption. To be more precise, an additional stress contribution is considered due to the change of the structural tensors during deformation. The novel model enables the consistent modelling of anisotropic interfaces. As a prototype model, a quasi-brittle mixed-mode damage model is introduced. One key feature of the model is the possibility to consider different fracture properties in normal and shear direction. Subsequently, the numerical implementation of the novel interface model is presented. The chapter closes with a numerical example in order to illustrate the advantages of the extended framework compared to classic cohesive zone models. The main outcome is that balance of angular momentum is fulfilled even in the case of an anisotropic interface – in contrast to anisotropic interface modelling in classic cohesive zone theory.

One further key point of this thesis is the investigation of size effects due to material interfaces at different scales. As a consequence, Chapter 6 deals with a homogenisation scheme that allows the analysis of the influence of the novel general interface model on the resulting macroscopic (effective) material response. Therefore, the classic averaging theory known from bulk homogenisation theory is extended in order to account for interface contributions. Subsequently, the numerical implementation of the homogenisation framework is provided in three different ways. To be more precise, it is shown that the macroscopic stresses may be computed based on volume or surface integrals as well as on the vector of internal forces. The capability of the generalised interface framework is highlighted at the end of this chapter within numerical examples. A cubic representative volume element with a spherical inclusion is investigated. The cross-coupled damage model introduced in Chapter 5 enables the modelling of material degradation in different directions within the interface. Furthermore, it is shown that the interaction

of bulk energies and interface energies leads, in a very natural manner, to a complex size effect. It includes the frequently observed „the smaller the stiffer“ relation, but also the less often observed „the smaller the softer“ relation. However, it is highlighted that the overall response is usually a superposition of such relations for with the generalised interface model enables the modelling of complex non-monotonic size effects.

Besides the induced size effect of material interfaces due to the increasing area to volume ratio, further influences like curvature of interfaces become significantly important on smaller scales. In order to capture such phenomena, Chapter 7 deals with an extension of the general interface to higher gradients of the displacement jump and the surface deformation gradient.

This thesis is closed with a short summary and an outlook to future perspectives of the presented interface models.

2 Introduction to continuum mechanics – bulk materials

This chapter gives a short summary of some fundamentals in continuum mechanics and constitutive modelling of bulk materials. Firstly, the kinematics of a geometrically exact description is introduced in Section 2.1. Thereafter, some of the basic balance equations are briefly derived in Section 2.2. Subsequently in Section 2.3 the derivation of constitutive relations is presented from a variational point of view. The concept of hyperelasticity is summarised, where the focus lies on the variational derivation of the mechanical boundary value problem. It is shown afterwards that dissipative material models (for instance elastoplastic models) can also be derived in a variational format.

This chapter neither provides a complete overview of classic continuum mechanics nor a detailed derivation of all presented correlations. It rather introduces the notation and equations that are the basis for the elaboration of consistent interface material models within the following chapters. For further details on relations provided here, the interested reader is referred to the works of Basar and Weichert [7], Bertram [10], Holzapfel [43], Marsden and Hughes [57].

2.1 Kinematics

This section briefly summarises the non-linear kinematics of finite deformation continuum mechanics starting with the motion of a classic bulk material. Consider a continuum body that takes the reference (also called material or Lagrangian) configuration $\mathcal{B}_0 \subset \mathbb{R}^3$ at time $t = 0$. Every material point $P \in \mathcal{B}_0$ is characterised by its Cartesian coordinate $\mathbf{X}(P)$, see Fig. 2.1, where $\mathbf{X} = X^i \mathbf{e}_i$. Henceforth, the Latin index takes the values 1, 2 and 3. Furthermore, \mathbf{e}_i are unit vectors along the X^i -axes. The body deforms under the action of prescribed loads and displacements. The underlying deformation is described by the nonlinear mapping φ , which maps the position $\mathbf{X} \in \mathcal{B}_0$ of material points in the reference configuration to their position $\mathbf{x} \in \mathcal{B}_t$, where \mathcal{B}_t describes the current (also called spatial or Eulerian) configuration of the body at any time t after the deformation, i.e., $\mathbf{x} = \varphi(\mathbf{X}, t)$. The current position $\mathbf{x}(P)$ is determined with respect to the same origin in the Cartesian coordinate system. Hence, it is defined by $\mathbf{x} = x^i \mathbf{e}_i$,

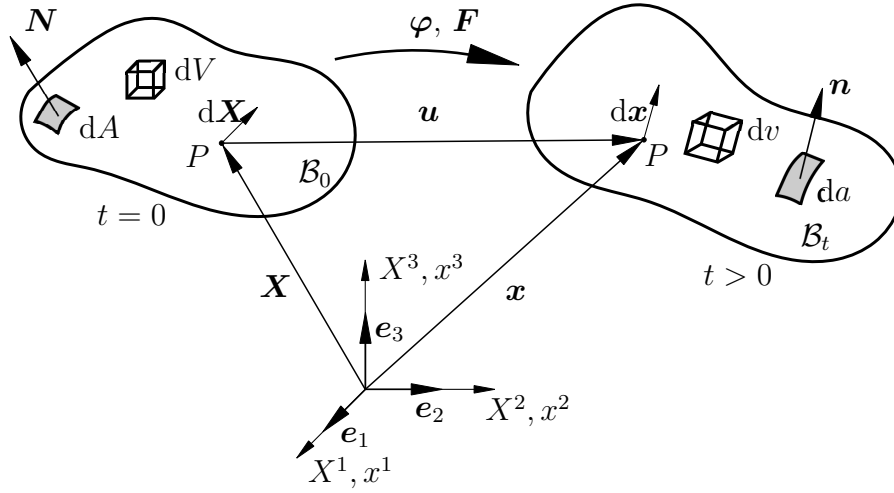


Figure 2.1: Motion of a body without interfaces – reference configuration \mathcal{B}_0 and current configuration \mathcal{B}_t

see Fig. 2.1. The deformation mapping φ is bijective in the interior of the body. The difference between the current and referential coordinate of material points results in the displacement vector

$$\mathbf{u} = \mathbf{x} - \mathbf{X}. \quad (2.1)$$

With the aforementioned assumptions, the local deformation is well defined and can be depicted by the deformation gradient

$$\mathbf{F} := \text{GRAD}(\varphi) = \frac{\partial \varphi}{\partial \mathbf{X}} = \frac{\partial \mathbf{x}}{\partial \mathbf{X}}. \quad (2.2)$$

Accordingly,

$$\text{GRAD}(\bullet) = \frac{\partial(\bullet)}{\partial \mathbf{X}} \quad (2.3)$$

denotes the gradient of quantity (\bullet) with respect to the reference configuration. Since $\varphi|_{\mathcal{B}_0}$ is bijective, the inverse $\varphi^{-1}|_{\mathcal{B}_0}$ exists and it follows that the inverse tensor \mathbf{F}^{-1} exists. By definition it reads

$$\mathbf{F}^{-1} := \text{grad}(\mathbf{X}) = \frac{\partial \mathbf{X}}{\partial \mathbf{x}}, \quad (2.4)$$

where

$$\text{grad}(\bullet) = \frac{\partial(\bullet)}{\partial \mathbf{x}} \quad (2.5)$$

indicates the gradient of (\bullet) with respect to the current configuration. The deformation gradient \mathbf{F} maps an infinitesimal line element $d\mathbf{X}$ in the reference configuration \mathcal{B}_0 , to its deformed counterpart $d\mathbf{x}$ in the current configuration \mathcal{B}_t by means of

$$d\mathbf{x} = \mathbf{F} \cdot d\mathbf{X}. \quad (2.6)$$

Similar relations for the transformation of volume and surface elements from the reference to the current configuration are derived in the following. In order to ensure physically admissible deformation states, the local invertibility condition

$$J = \det(\mathbf{F}) > 0 \quad (2.7)$$

holds. Here, J denotes the Jacobian of the deformation gradient and it connects a current volume element dv and the referential volume element dV as

$$dv = JdV. \quad (2.8)$$

Consider now a referential area element $d\mathbf{A} = \mathbf{N} dA$ where \mathbf{N} denotes its unit normal, see Fig. 2.1. This referential element is transferred to the current area element $d\mathbf{a} = \mathbf{n} da$ with its unit normal \mathbf{n} by means of Nanson's formula

$$\mathbf{n} da = J \mathbf{F}^{-1} \mathbf{N} dA. \quad (2.9)$$

In some cases it is preferable to introduce curvilinear coordinates θ^i . For a detailed derivation of the relations presented in the following, the interested reader is referred to [7]. The curvilinear coordinates θ^i are supposed to be convective. This means that any point of the body is determined by the same values of the coordinates θ^i in the reference as well as in the current configuration. The coordinate curves are subjected to the same deformation as the body and are transformed at time t into a new set of curvilinear coordinates. Thereby, the referential and current placements take the form $\mathbf{X} = \mathbf{X}(\theta^i)$ and $\mathbf{x} = \mathbf{x}(\theta^i, t)$, see Fig. 2.2. This allows the calculation of covariant base vectors related to a point $P \in \mathcal{B}_0$ as

$$\mathbf{G}_i = \mathbf{X}_{,i} = \frac{\partial \mathbf{X}}{\partial \theta^i} = \frac{\partial X^k}{\partial \theta^i} \mathbf{e}_k \quad (2.10)$$

and its contravariant counter part as

$$\mathbf{G}^i = \frac{\partial \theta^i}{\partial X^k} \mathbf{e}^k. \quad (2.11)$$

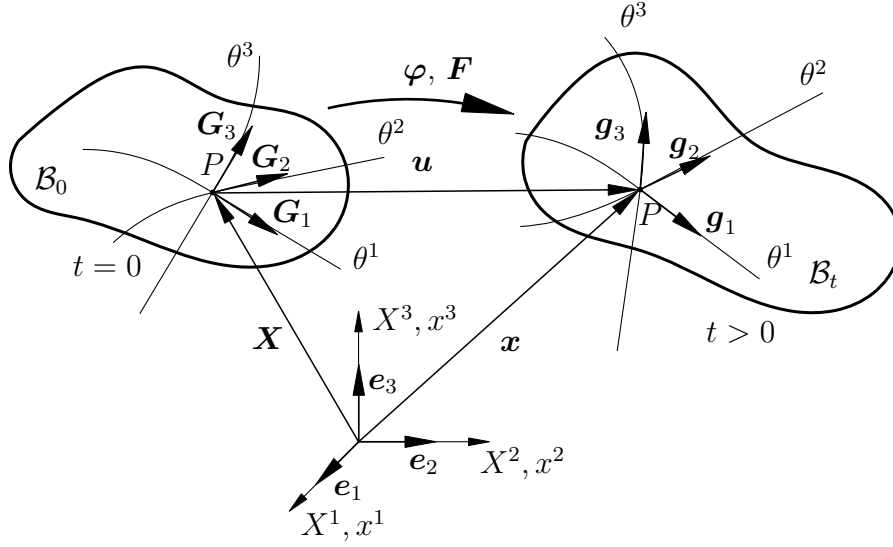


Figure 2.2: Motion of a body without interfaces – reference configuration \mathcal{B}_0 and current configuration \mathcal{B}_t - description of point P with curvilinear coordinates θ^i and referential base vectors \mathbf{G}_i as well as current base vectors \mathbf{g}_i .

Similar relations can be derived for the current configuration \mathcal{B}_t at a fixed time t . To be more precise, the covariant and contravariant base vectors in the current configuration are defined by

$$\mathbf{g}_i = \mathbf{x}_{,i} = \frac{\partial \mathbf{x}}{\partial \theta^i} = \frac{\partial x^k}{\partial \theta^i} \mathbf{e}_k \quad (2.12)$$

and

$$\mathbf{g}^i = \frac{\partial \theta^i}{\partial x^k} \mathbf{e}^k. \quad (2.13)$$

The identity tensors of the referential respectively of the current configuration are constructed with the respective base vectors as

$$\mathbf{I} = \mathbf{G}_i \otimes \mathbf{G}^i \quad \text{and} \quad \mathbf{i} = \mathbf{g}_i \otimes \mathbf{g}^i \quad \text{with} \quad \mathbf{I} = \mathbf{i}. \quad (2.14)$$

The introduction of the base vectors enables the expression of the deformation gradient \mathbf{F} (cf. Eq. (2.2)) and its inverse \mathbf{F}^{-1} (cf. Eq. (2.5)) as

$$\mathbf{F} = \text{GRAD}(\mathbf{x}) = \frac{\partial \mathbf{x}}{\partial \theta^i} \otimes \frac{\partial \theta^i}{\partial \mathbf{X}} = \mathbf{g}_i \otimes \mathbf{G}^i \quad (2.15)$$

and

$$\mathbf{F}^{-1} = \text{grad}(\mathbf{X}) = \frac{\partial \mathbf{X}}{\partial \theta^i} \otimes \frac{\partial \theta^i}{\partial \mathbf{x}} = \mathbf{G}_i \otimes \mathbf{g}^i. \quad (2.16)$$

Thus, the deformation gradient maps the undeformed covariant basis \mathbf{G}_i into the deformed one \mathbf{g}_i by

$$\mathbf{g}_i = \mathbf{F} \cdot \mathbf{G}_i. \quad (2.17)$$

2.2 Balance laws

This section gives a short introduction to some fundamental balance laws in classic continuum mechanics which are used in the following chapters. The derivations presented in this section are limited to bulk bodies without interfaces based on a referential control volume and control boundary, denoted as subsets $\mathcal{V}_0 \subset \mathcal{B}_0$ and $\partial\mathcal{V}_0 \subset \partial\mathcal{B}_0$. The principle of conservation of mass is adopted in the following.

2.2.1 Balance of linear momentum

The conservation of balance of linear momentum states that the sum of prescribed volume forces and prescribed tractions on \mathcal{B}_0 equals the temporal change of linear momentum. In what follows, $\rho_0 \mathbf{B}$ and \mathbf{T}^* represent the referential volumetric body forces and the tractions applied to the surface of the reference body. The corresponding quantities with respect to the current configuration \mathcal{B}_t read $\rho \mathbf{b}$ and \mathbf{t}^* . The resulting referential forces are computed as

$$\mathcal{F} = \int_{\partial\mathcal{V}_0} \mathbf{T}^* \, dA + \int_{\mathcal{V}_0} \rho_0 \mathbf{B} \, dV. \quad (2.18)$$

The linear momentum is denoted by

$$\mathbf{L} = \frac{d}{dt} \int_{\mathcal{V}_0} \rho_0 \boldsymbol{\varphi} \, dV. \quad (2.19)$$

Consequently, with $\dot{\mathbf{L}} = \mathcal{F}$ the global form of balance of linear momentum reads

$$\int_{\mathcal{V}_0} \rho_0 \ddot{\boldsymbol{\varphi}} \, dV = \int_{\mathcal{V}_0} \rho_0 \mathbf{B} \, dV + \int_{\partial\mathcal{V}_0} \mathbf{T}^* \, dA. \quad (2.20)$$

As mentioned above, the principle of conservation of mass, i.e., $\dot{\rho}_0 = 0$, where the superposed dot represents the time derivative, is adopted. The double dot denotes the second material time derivative of the nonlinear deformation map $\boldsymbol{\varphi}$.

Next, the integral-type form (2.20) is re-written into a local form. Therefore, Cauchy's stress theorem is applied that postulates a linear dependency of the stress vector \mathbf{T}^* and the normal vector \mathbf{N} , i.e. $\mathbf{T}^* = \mathbf{P} \cdot \mathbf{N}$. Here and henceforth, \mathbf{P} indicates the first

Piola-Kirchhoff stress tensor. Inserting this relation into Eq. (2.20) and applying the Gauss divergence theorem, the local form of balance of linear momentum results in

$$\rho_0 \ddot{\boldsymbol{\varphi}} = \text{DIV} \mathbf{P} + \rho_0 \mathbf{B} \quad \forall \mathbf{X} \in \mathcal{B}_0, \quad (2.21)$$

where

$$\text{DIV}(\bullet) = \text{GRAD}(\bullet) : \mathbf{I} = \frac{\partial(\bullet)}{\partial \theta^i} \cdot \mathbf{G}^i \quad (2.22)$$

is the divergence operator with respect to \mathbf{X} . Accordingly,

$$\text{div}(\bullet) = \text{grad}(\bullet) : \mathbf{i} = \frac{\partial(\bullet)}{\partial \theta^i} \cdot \mathbf{g}^i \quad (2.23)$$

denotes the divergence operator with respect to the current configuration \mathbf{x} . In the case of quasi-static analysis, dynamic effects are neglected and Eq. (2.21) reduces to

$$\mathbf{0} = \text{DIV} \mathbf{P} + \rho_0 \mathbf{B} \quad \forall \mathbf{X} \in \mathcal{B}_0. \quad (2.24)$$

Remark 1 *Starting with the corresponding spatial quantities of volumetric body forces and applied tractions ($\rho \mathbf{b}$ and \mathbf{t}^*), the local form of balance of linear momentum with respect to the current configuration for quasi-statics reads*

$$\mathbf{0} = \text{div} \boldsymbol{\sigma} + \rho \mathbf{b} \quad \forall \mathbf{x} \in \mathcal{B}_t. \quad (2.25)$$

Here and henceforth, $\boldsymbol{\sigma} = J^{-1} \mathbf{P} \cdot \mathbf{F}^T$ indicates the Cauchy stress tensor.

2.2.2 Balance of angular momentum

The conservation law for balance of angular momentum states that the sum of all moments resulting from prescribed volume forces and prescribed tractions on \mathcal{B}_0 concerning a fixed point P equals the temporal change of angular momentum with respect to point P . The moment \mathcal{M} resulting from $\rho_0 \mathbf{B}$ and \mathbf{T}^* concerning point P is computed as

$$\mathcal{M} = \int_{\mathcal{V}_0} \mathbf{r} \times \rho_0 \mathbf{B} \, dV + \int_{\partial \mathcal{V}_0} \mathbf{r} \times \mathbf{T}^* \, dA, \quad (2.26)$$

where \mathbf{r} denotes the position vector of point P . The total angular momentum \mathbf{M} relative to P is calculated by

$$\mathbf{M} = \int_{\mathcal{V}_0} \mathbf{r} \times \rho_0 \dot{\boldsymbol{\varphi}} \, dV \quad (2.27)$$

and consequently, with $\dot{\mathbf{M}} = \mathcal{M}$ the global form of balance of angular momentum reads

$$\frac{d}{dt} \int_{\mathcal{V}_0} \mathbf{r} \times \rho_0 \dot{\boldsymbol{\varphi}} dV = \int_{\partial\mathcal{V}_0} \mathbf{r} \times \mathbf{T}^* dA + \int_{\mathcal{V}_0} \mathbf{r} \times \rho_0 \mathbf{B} dV. \quad (2.28)$$

After some standard manipulations similar to the procedure in the previous Subsection 2.2.1, the local form of balance of angular momentum can eventually be reduced to

$$\mathbf{P} \cdot \mathbf{F}^T = \mathbf{F} \cdot \mathbf{P}^T. \quad (2.29)$$

Remark 2 From Eq. (2.29) it follows that the second Piola-Kirchhoff stress tensor $\mathbf{S} = \mathbf{F} \cdot \mathbf{P}$ is symmetric. Furthermore, by reformulating the local form of balance of angular momentum with respect to the current configuration, i.e. $\boldsymbol{\sigma} = \boldsymbol{\sigma}^T$, it can be deduced that the Cauchy stress tensor $\boldsymbol{\sigma}$ requires symmetry.

2.2.3 Balance of energy - first law of thermodynamics

This subsection summarises the postulate of energy balance and its local form that corresponds to the first law of thermodynamics. Considering external mechanical power P_{ext} and external thermal power P_{Θ} , balance of energy takes the form

$$\dot{E} + \dot{K} = P_{\text{ext}} + P_{\Theta}, \quad (2.30)$$

where \dot{E} denotes the rate of an energy and where \dot{K} indicates the rate of the kinetic energy of a thermodynamical system. In general, \dot{E} is not necessarily the time derivative of internal energy E . However, experimental observations show that the integral of \dot{E} over a time interval is almost independent of its respective path. Hence, the existence of a material internal energy density U per unit mass can be justified and thereby the internal energy is defined by

$$E(\mathcal{V}_0) = \int_{\mathcal{V}_0} \rho_0 U dV. \quad (2.31)$$

Thus, the rate of the internal energy E simplifies to its material time derivative, i.e.,

$$\dot{E} = \dot{E}. \quad (2.32)$$

For dynamic systems the kinetic energy reads $K = \int_{\mathcal{V}_0} 1/2 \rho_0 \|\dot{\boldsymbol{\varphi}}\|^2 dV$, where $\|\bullet\|$ indicates the Euclidean 2-norm. Equation (2.30) states that the rate of the internal and

the kinetic energy equals the sum of all external powers. According to Eq. (2.18), the external mechanical power reads

$$P_{\text{ext}} = \int_{\partial\mathcal{V}_0} \mathbf{T}^* \cdot \dot{\boldsymbol{\varphi}} \, dA + \int_{\mathcal{V}_0} \rho_0 \mathbf{B} \cdot \dot{\boldsymbol{\varphi}} \, dV. \quad (2.33)$$

The second part contributing to the sum of external power is related to heat. Taking into account a volumetric heat source $\rho_0 R_\Theta$ inside the body and a heat flux \mathbf{Q} across the boundaries, the thermal power is calculated by

$$P_\Theta = - \int_{\partial\mathcal{V}_0} \mathbf{Q} \cdot \mathbf{N} \, dA + \int_{\mathcal{V}_0} \rho_0 R_\Theta \, dV. \quad (2.34)$$

In order to derive a local form of the integral-type balance law (2.30), Gauss's divergence theorem is applied and balance of linear momentum (Eq. (2.21)) is inserted. This procedure leads to

$$\rho_0 \dot{U} = \mathbf{P} : \dot{\mathbf{F}} - \text{DIV} \mathbf{Q} + \rho_0 R_\Theta \quad \forall \mathbf{X} \in \mathcal{B}_0. \quad (2.35)$$

In terms of temperature-independent problems, as is the case in the present work, the rate of the internal energy equals the stress power $\mathbf{P} : \dot{\mathbf{F}}$. Similar to the previous subsections, Eq. (2.35) can be re-written with respect to the current configuration.

2.2.4 Entropy inequality - second law of thermodynamics

The first law of thermodynamics considers the energy transfer within a thermodynamical process. In order to govern the direction of energy transformation, the second law of thermodynamics in form of the Clausius-Duhem inequality is summarised in this subsection. This presentation relies on the works of Truesdell and Toupin [97] and Coleman and Noll [19].

Firstly, by introducing the referential entropy density N per unit mass, the entropy S is defined as

$$S(\mathcal{V}_0) = \int_{\mathcal{V}_0} \rho_0 N \, dV. \quad (2.36)$$

The second law of thermodynamics states that the total entropy production for all thermodynamic processes is never negative. The entropy production is determined by the rate of change of entropy \dot{S} and the rate of entropy input into a certain region of a continuum body. Hence, in form of the Clausius-Duhem inequality, the second law of thermodynamics reads

$$\frac{d}{dt} \int_{\mathcal{V}_0} \rho_0 N \, dV + \int_{\partial\mathcal{V}_0} \frac{\mathbf{Q} \cdot \mathbf{N}}{\Theta} \, dA - \int_{\mathcal{V}_0} \frac{\rho_0 R_\Theta}{\Theta} \, dV \geq 0, \quad (2.37)$$

where $\Theta > 0$ indicates the total temperature in Kelvin. In this form, the entropy flux across the boundary surface is related to the heat flux \mathbf{Q} and the entropy source inside the body is related to the heat source $\rho_0 R_\Theta$. The global integral-type form (2.37) can be re-written into its local form as

$$\rho_0 \dot{N} + \frac{1}{\Theta} \text{DIV}(\mathbf{Q}) - \frac{1}{\Theta^2} \mathbf{Q} \text{GRAD}(\Theta) - \frac{\rho_0 R_\Theta}{\Theta} \geq 0. \quad (2.38)$$

Furthermore, by applying a Legendre-Transformation, see Remark 3, and by using balance of energy (2.35), the Clausius-Duhem inequality can be written in the form

$$\mathcal{D} = \mathbf{P} : \dot{\mathbf{F}} - \rho_0 \left(\dot{\Theta} N + \dot{\psi} \right) - \frac{1}{\Theta} \mathbf{Q} \text{GRAD}(\Theta) \geq 0. \quad (2.39)$$

Here and henceforth, \mathcal{D} is the dissipation of a thermodynamical process and ψ is the Helmholtz free energy, respectively $\dot{\psi}$ is its rate. The present work only regards purely mechanical processes (without thermal effects), and thus the (dissipation) inequality can be presented in the Clausius-Planck form for isothermal processes as

$$\mathcal{D} = \mathbf{P} : \dot{\mathbf{F}} - \dot{\Psi} \geq 0, \quad (2.40)$$

where $\Psi = \rho_0 \psi$ will be considered in the following chapters. Equation (2.40) plays a major role when elaborating thermodynamical consistent material models which are based on the framework of Coleman and Noll [19] and Coleman and Gurtin [18].

Remark 3 *An alternative form of the second law of thermodynamics in terms of the Helmholtz free energy ψ can be derived by applying the Legendre transformation of the type*

$$\psi(\bullet, \Theta) = \inf_N \{U(\bullet, \Theta) - \Theta N\}, \quad (2.41)$$

where Θ and N are thermomechanically dual variables and where (\bullet) is a set of further variables, e.g. the deformation gradient \mathbf{F} . For sufficiently smooth functions the Legendre transformation reads

$$\psi(\bullet, \Theta) = U(\bullet, \Theta) - \Theta N. \quad (2.42)$$

2.3 Variational principles in continuum mechanics

The subsequent section summarises the constitutive modelling in the context of variational principles. To be more precise, a framework is presented that enables the derivation of balance laws, boundary conditions and all unknown state variables directly from minimising an energy potential. Apart from physical and mathematical elegance, the variational derivation of the constitutive framework in continuum mechanics has several

advantages, for instance the possibility of using numerically efficient and robust optimisation schemes in the numerical computations. First, an introduction to hyperelasticity is given, where variational principles are widely used. The well known principle of virtual work and the principle of minimum potential energy is summarised. The latter enables the derivation of balance of linear momentum as well as Neumann boundary conditions by computing the stationary of an energy potential. Subsequently, the focus is on materials showing dissipation. After a brief introduction into plasticity theory, an approach for the derivation of evolution equations for internal variables based on the work of Ortiz and Stainier [74] and Carstensen et al. [14] is presented. The idea is to transfer a rate dependent potential into an incremental variational potential. According to the scope of this work, the focus in this section lies on isothermal quasi-static processes.

2.3.1 Introduction to hyperelasticity

A material is referred to as Cauchy-elastic if the stress tensor only depends on the deformation gradient, i.e. $\mathbf{P}(t, \mathbf{X}) = \mathbf{P}(\mathbf{F}(t, \mathbf{X}))$. For the sake of simplicity, the dependence of \mathbf{P} on \mathbf{X} is not explicitly highlighted in the following. Considering a Cauchy-elastic material, the stress power reads $\mathcal{P} = \mathbf{P} : \dot{\mathbf{F}}$. If the stress power is path-independent, a material is defined as hyperelastic. For such material models the Helmholtz free energy is solely a function of the deformation gradient, i.e. $\psi = \psi(\mathbf{F})$, and identity

$$\Psi(\mathbf{F}) = \rho_0 \psi(\mathbf{F}) \tag{2.43}$$

for the Helmholtz free energy density Ψ , also called strain-energy function, is employed in the following. A hyperelastic process is characterised as perfectly elastic, and due to the reversibility, the local dissipation inequality (2.40) degenerates to an equality with $\mathcal{D} = 0$. The time differentiation of the Helmholtz free energy density reads

$$\dot{\Psi}(\mathbf{F}) = \frac{\partial \Psi}{\partial \mathbf{F}} : \dot{\mathbf{F}} \tag{2.44}$$

and inserting this into Eq. (2.40) leads to

$$\mathcal{D} = \mathbf{P} : \dot{\mathbf{F}} - \dot{\Psi} = \left[\mathbf{P} - \frac{\partial \Psi}{\partial \mathbf{F}} \right] : \dot{\mathbf{F}} = 0. \tag{2.45}$$

It can be deduced that $\Psi(\mathbf{F})$ serves as a potential, whose time derivative equals the stress power and furthermore from which the constitutive relation for the first Piola-Kirchhoff stress tensor follows as

$$\mathbf{P} = \frac{\partial \Psi}{\partial \mathbf{F}}. \tag{2.46}$$

In line with the work of Coleman and Noll [19] and Coleman and Gurtin [18], the stress tensor \mathbf{P} is referred to as thermodynamic force conjugate to deformation gradient \mathbf{F} .

In the case of hyperelasticity it can be shown that, if the Helmholtz energy density fulfills the principle of objectivity also known as material frame indifference, see Truesdell and Noll [98, Section 19, 19A], balance of angular momentum is automatically fulfilled. To be more precise, if Ψ is invariant with respect to an arbitrary rotation \mathbf{Q} as

$$\Psi(\mathbf{F}) = \Psi(\mathbf{Q} \cdot \mathbf{F}) \quad \forall \mathbf{Q} \in \mathcal{SO}3, \quad (2.47)$$

the Helmholtz free energy density can equivalently be defined in dependence of a symmetric tensor \mathbf{C} as

$$\Psi(\mathbf{F}) = \tilde{\Psi}(\mathbf{C}), \quad (2.48)$$

where

$$\mathbf{C} = \mathbf{F}^T \cdot \mathbf{F} \quad (2.49)$$

indicates the right Cauchy-Green deformation tensor. Thus, Piola stress tensor \mathbf{P} can be expressed as

$$\mathbf{P} = 2\mathbf{F} \cdot \frac{\partial \tilde{\Psi}}{\partial \mathbf{C}}. \quad (2.50)$$

Representation (2.50) automatically fulfills the requirement for local form of balance of angular momentum (2.29) (see also Simo and Hughes [90, Chapter 7.1.5.3]).

A hyperelastic material is denoted as isotropic if the response of the material is identical in all directions, see Truesdell and Noll [98, Section 85]. Isotropy is a special class of a material symmetry. For isotropy relation

$$\Psi(\mathbf{C}) = \Psi(\mathbf{Q}^T \cdot \mathbf{C} \cdot \mathbf{Q}) \quad \forall \mathbf{Q} \in \mathcal{SO}3 \quad (2.51)$$

has to hold. In this case the Helmholtz free energy density may be expressed in terms of the invariants of \mathbf{C} (cf. Truesdell and Noll [98, Section 10]), i.e.,

$$\Psi(\mathbf{C}) = \Psi(I_1(\mathbf{C}), I_2(\mathbf{C}), I_3(\mathbf{C})). \quad (2.52)$$

The three invariants of \mathbf{C} read

$$I_1(\mathbf{C}) = \text{tr} \mathbf{C}, \quad (2.53)$$

$$I_2(\mathbf{C}) = \frac{1}{2} [(\text{tr}(\mathbf{C}))^2 - \text{tr}(\mathbf{C}^2)] \quad \text{and} \quad (2.54)$$

$$I_3(\mathbf{C}) = \det \mathbf{C}. \quad (2.55)$$

Instead of the invariants of \mathbf{C} , its eigenvalues can be used as well.

2.3.1.1 Boundary value problem of continuum mechanics

This subsection briefly summarises the boundary value problem (BVP) of continuum mechanics. In line with the scope of the present work, thermal and dynamical effects are neglected in what follows. The mechanical behaviour of an elastic body is described by balance of linear momentum, see Eq. (2.24), and associated boundary conditions that are the Neumann boundary conditions

$$\mathbf{T}^* = \mathbf{P} \cdot \mathbf{N} \quad \forall \mathbf{X} \in \partial_N \mathcal{B}_0 \quad (2.56)$$

and the Dirichlet boundary conditions

$$\varphi = \varphi^* \quad \forall \mathbf{X} \in \partial_D \mathcal{B}_0. \quad (2.57)$$

Here, $\partial_N \mathcal{B}_0$ denotes the Neumann boundary of \mathcal{B}_0 where tractions \mathbf{T}^* are applied. In analogy, $\partial_D \mathcal{B}_0$ indicates the Dirichlet boundary of \mathcal{B}_0 where the deformations are prescribed. Consequently, the BVP reads

$$\begin{aligned} \text{DIV} \mathbf{P} + \rho_0 \mathbf{B} &= \mathbf{0} & \forall \mathbf{X} \in \mathcal{B}_0 \\ \mathbf{T}^* &= \mathbf{P} \cdot \mathbf{N} & \forall \mathbf{X} \in \partial_N \mathcal{B}_0 \\ \varphi &= \varphi^* & \forall \mathbf{X} \in \partial_D \mathcal{B}_0. \end{aligned} \quad (2.58)$$

2.3.1.2 Principle of virtual work

The principle of virtual work can be derived by multiplying local form of balance of linear momentum (2.24) by a vector-valued test function $\boldsymbol{\eta}$ and by integration of the resulting equation over the volume \mathcal{B}_0 . If the space of the test functions \mathcal{V} is sufficiently large, balance of linear momentum is equivalent to

$$\int_{\mathcal{B}_0} \boldsymbol{\eta} \cdot (\text{DIV} \mathbf{P} + \rho_0 \mathbf{B}) \, dV = 0 \quad \forall \boldsymbol{\eta} \in \mathcal{V}. \quad (2.59)$$

Applying Gauss's divergence theorem together with the identity

$$\text{DIV}(\boldsymbol{\eta} \cdot \mathbf{P}) = \boldsymbol{\eta} \cdot \text{DIV} \mathbf{P} + \mathbf{P} : \text{GRAD} \boldsymbol{\eta}, \quad (2.60)$$

Eq. (2.59) can be rewritten as

$$\int_{\mathcal{B}_0} \mathbf{P} : \text{GRAD} \boldsymbol{\eta} \, dV = \int_{\mathcal{B}_0} \rho_0 \boldsymbol{\eta} \cdot \mathbf{B} \, dV + \int_{\partial_N \mathcal{B}_0} \boldsymbol{\eta} \cdot \mathbf{T}^* \, dA \quad \forall \boldsymbol{\eta} \in \mathcal{V}. \quad (2.61)$$

The above equation represents the principle of virtual work. The test function $\boldsymbol{\eta}$ can physically be interpreted as virtual displacement. This allows an interpretation of the left side of Eq. (2.61) as virtual internal work. The right side of Eq. (2.61) appropriately represents the virtual work of external forces.

In the range of finite deformations, $\boldsymbol{\eta}$ is interpreted as a virtual deformation rate. Consequently, Eq. (2.61) sets the virtual internal stress power into relation to virtual external powers, see also Eq. (2.33). As mentioned above, Eq. (2.61) implies balance of linear momentum and the Neumann boundary conditions if the space of \mathcal{V} is large enough.

2.3.1.3 Principle of minimum potential energy

The Boundary Value Problem (BVP), see Subsection 2.3.1.1, can be derived from a minimisation principle, if a total energy potential \mathcal{I} exists for both the stresses and the loads. In the case of hyperelasticity, the total potential of a body can be defined as the sum of the total internal and external energy potential as

$$\mathcal{I}(\boldsymbol{\varphi}) = \mathcal{I}^{\text{int}}(\boldsymbol{\varphi}) + \mathcal{I}^{\text{ext}}(\boldsymbol{\varphi}). \quad (2.62)$$

The total internal energy potential is the integral of the corresponding Helmholtz free energy density $\Psi(\mathbf{F})$. Together with the total external energy potential consisting of contributions from volumetric and externally applied forces, the total energy potential for the body reads

$$\mathcal{I}(\boldsymbol{\varphi}) = \int_{\mathcal{B}_0} \Psi(\mathbf{F}) \, dV - \int_{\mathcal{B}_0} \rho_0 \mathbf{B} \cdot \boldsymbol{\varphi} \, dV - \int_{\partial_N \mathcal{B}_0} \mathbf{T}^* \cdot \boldsymbol{\varphi} \, dA. \quad (2.63)$$

In order to find a state of equilibrium, a stationary point $\delta\mathcal{I} = 0$ can be obtained by a variation of the total potential with respect to the underlying deformation as

$$\delta_{\boldsymbol{\varphi}} \mathcal{I} = \int_{\mathcal{B}_0} \mathbf{P} : \delta \mathbf{F} \, dV - \int_{\mathcal{B}_0} \rho_0 \mathbf{B} \cdot \delta \boldsymbol{\varphi} \, dV - \int_{\partial_N \mathcal{B}_0} \mathbf{T}^* \cdot \delta \boldsymbol{\varphi} \, dA = 0. \quad (2.64)$$

Here, the constitutive relation $\mathbf{P} = \partial_{\mathbf{F}} \Psi$ is substituted and the virtual deformations are defined as $\delta \mathbf{F} = \text{GRAD} \delta \boldsymbol{\varphi}$. Again, by applying an identity of the form (2.60) together with a divergence theorem, variation (2.64) transforms to

$$\delta_{\boldsymbol{\varphi}} \mathcal{I} = - \int_{\mathcal{B}_0} [\text{DIV}(\mathbf{P}) + \rho_0 \mathbf{B}] \cdot \delta \boldsymbol{\varphi} \, dV + \int_{\partial_N \mathcal{B}_0} [\mathbf{P} \cdot \mathbf{N} - \mathbf{T}^*] \cdot \delta \boldsymbol{\varphi} \, dA = 0. \quad (2.65)$$

If the deformation field and the test functions are spanned by the same space (Bubnov-Galerkin scheme), Eq. (2.65) is equivalent to the principle of virtual work (2.61). Consequently, from Eq. (2.65) the local form of balance of linear momentum and the Neumann

boundary conditions (2.58) can be derived. However, the principle of virtual work does not require a potential and is thus more general.

2.3.2 Introduction to plasticity

This section gives a brief introduction to plasticity theory for finite deformations. Further information about the summarised equations and their derivations can for instance be found in Bertram [10], Lubliner [55], Simo and Hughes [90]. The theory is based on the multiplicative split of the deformation gradient into an elastic and a plastic part, i.e.,

$$\mathbf{F} = \mathbf{F}^e \cdot \mathbf{F}^p \quad \text{and} \quad \det(\mathbf{F}^e) > 0, \det(\mathbf{F}^p) > 0. \quad (2.66)$$

Here, \mathbf{F}^e characterises the mapping of the elastic part of the deformation while \mathbf{F}^p describes the irreversible plastic deformations. The idea of the multiplicative decomposition of \mathbf{F} reaches back to the works of Bilby et al. [12] and H. Lee [37] if not further. This decomposition is associated with the introduction of a fictitious, locally incompatible intermediate configuration which is stress free. Based on experimental results, the following plastic deformations are assumed to be isochoric, i.e. $\det \mathbf{F}^p = 1$. The classic approach postulates that the elastic properties of a material do not change with hardening or softening effects. Hence, the Helmholtz energy density is separated into one part related to elastic deformations and into one part associated with internal hardening/softening processes due to the evolution of internal variables, i.e.,

$$\Psi = \Psi^e(\mathbf{F}^e) + \Psi^p(\boldsymbol{\alpha}) = \Psi^e(\mathbf{F}, \mathbf{F}^p) + \Psi^p(\boldsymbol{\alpha}). \quad (2.67)$$

The elastic part of Ψ is assumed to be independent of the processes due to the evolution of $\boldsymbol{\alpha}$, which describes a set of internal strain-like variables correlated to hardening/softening effects. Together with the stress power $\mathcal{P} = \mathbf{P} : \dot{\mathbf{F}}$ and the Helmholtz energy density (2.67), the Clausius-Planck form of the dissipation inequality (2.40) takes the form

$$\mathcal{D} = \mathbf{P} : \dot{\mathbf{F}} - \frac{\partial \Psi}{\partial \mathbf{F}^e} : \dot{\mathbf{F}}^e - \frac{\partial \Psi}{\partial \boldsymbol{\alpha}} \circ \dot{\boldsymbol{\alpha}} \geq 0. \quad (2.68)$$

Inserting the multiplicative split (2.66), and applying the Coleman-Noll procedure leads to the Piola-Kirchhoff stress tensor

$$\mathbf{P} = \frac{\partial \Psi}{\partial \mathbf{F}^e} \cdot [\mathbf{F}^p]^{-T} \quad (2.69)$$

and the reduced dissipation inequality

$$\mathcal{D} = \boldsymbol{\Sigma} : \mathbf{L}^p + \mathbf{Q} \circ \dot{\boldsymbol{\alpha}} \geq 0. \quad (2.70)$$

The first term $\Sigma : \mathbf{L}^p$ is related to the plastic work rate with the Mandel stresses, cf. Mandel [56],

$$\Sigma = [\mathbf{F}^e]^T \cdot \frac{\partial \Psi}{\partial \mathbf{F}^e} \quad (2.71)$$

and the plastic velocity gradient

$$\mathbf{L}^p = \dot{\mathbf{F}}^p \cdot [\mathbf{F}^p]^{-1}. \quad (2.72)$$

Both objects are thermodynamically conjugated and belong to the intermediate configuration. The second term $\mathbf{Q} \circ \dot{\boldsymbol{\alpha}}$ determines the power related to hardening with the stress-like hardening variable

$$\mathbf{Q} = -\frac{\partial \Psi}{\partial \boldsymbol{\alpha}}, \quad (2.73)$$

that is energetically conjugated to $\boldsymbol{\alpha}$. For the definition of the elastic domain, a space of admissible stresses \mathbb{E}_Σ is defined, cf. Lubliner [55]. Here, according to Ineq. (2.70), the stress space \mathbb{E}_Σ is formulated related to the Mandel stresses as

$$\mathbb{E}_\Sigma = \{(\Sigma, \mathbf{Q}) \in \mathbb{R}^{9+n} \mid \phi(\Sigma, \mathbf{Q}) \leq 0\}. \quad (2.74)$$

In order to distinguish between fully elastic and elastoplastic states, a level-set function also known as yield function ($\phi(\Sigma, \mathbf{Q})$) is introduced. Many plasticity models are described by a yield function of the type

$$\phi(\Sigma, \mathbf{Q}) = \Sigma^{\text{eq}}(\Sigma, \mathbf{Q}) - Q_0, \quad (2.75)$$

where Σ^{eq} is an equivalent stress measure and where Q_0 describes an initial strength for the beginning of plastic deformation. Most of the yield functions postulated in practice are positively homogeneous of degree n , see Remark 4.

The constitutive model is completed by choosing suitable evolution equations for the internal variables and the definition of loading/unloading conditions. Following the principle of maximum dissipation for admissible stress states, i.e.,

$$\sup_{\Sigma, \mathbf{Q} \in \mathbb{E}_\Sigma} \{\Sigma : \mathbf{L}^p + \mathbf{Q} \circ \dot{\boldsymbol{\alpha}}\}, \quad (2.76)$$

the evolution equations for the associated plasticity theory are obtained as

$$\mathbf{L}^p = \lambda \frac{\partial \phi}{\partial \Sigma} \quad \text{and} \quad \dot{\boldsymbol{\alpha}} = \lambda \frac{\partial \phi}{\partial \mathbf{Q}}. \quad (2.77)$$

Furthermore, the stress state is admissible if the Karush-Kuhn-Tucker conditions

$$\lambda \geq 0, \quad \phi \leq 0, \quad \lambda\phi = 0 \quad (2.78)$$

are fulfilled. Here, λ denotes the plastic multiplier and conditions (2.78) serve as loading/unloading conditions. The plastic multiplier is calculated from the consistency condition

$$\dot{\phi} = 0. \quad (2.79)$$

Evolution equations of the type (2.77) are denoted as associative flow rules or normality rules, since the rates of the internal variables (together with \mathbf{L}^p) are proportional to the gradient of the yield function. However, these equations are not valid for all types of materials and sometimes have to be generalised. Evolution equations in a more general format are postulated as

$$\mathbf{L}^p = \lambda \frac{\partial g}{\partial \boldsymbol{\Sigma}} \quad \text{and} \quad \dot{\boldsymbol{\alpha}} = \lambda \frac{\partial h}{\partial \mathbf{Q}} \quad (2.80)$$

within the framework of generalised standard materials, see Halphen and Nguyen [39]. Here, the plastic potential g and the hardening potential h define the directions of the rates of \mathbf{L}^p and $\dot{\boldsymbol{\alpha}}$ and the second law of thermodynamics is automatically fulfilled. For more details on generalised standard materials, the interested reader is referred for instance to the work of Hackl [38].

Remark 4 *In those cases where the yield function is postulated as positively homogeneous of degree n , the dissipation can be rewritten as*

$$\mathcal{D} = n\lambda Q_0. \quad (2.81)$$

Remark 5 *The elastic part of the Helmholtz energy is most often taken as $\Psi^e = \Psi^e(\mathbf{C}^e)$, where $\mathbf{C}^e = [\mathbf{F}^e]^T \cdot \mathbf{F}^e$ is the elastic Cauchy-Green deformation tensor in order to fulfill the principle of material frame-indifference. However, \mathbf{C}^e belongs to the intermediate configuration. Consequently, a natural choice of the Helmholtz energy with respect to the reference configuration would be $\Psi^e(\mathbf{F}^e) = \tilde{\Psi}^e(\mathbf{C}^e) \det(\mathbf{F}^p)$. For isochoric deformations one obtains the classic relation $\Psi^e = \Psi^e(\mathbf{C}^e)$.*

2.3.2.1 Standard dissipative media

As shown in Subsection 2.3.1.2, in the case of hyperelasticity all equations characterising the boundary value problem follow a minimisation principle of an energy potential. Thus, the BVP can be formulated in a variational format. For a broad range of different

plasticity models such a variational structure also exists – particularly for associative models, cf. Carstensen et al. [14], Miehe [60], Mosler [64], Mosler and Bruhns [66], Ortiz and Repetto [73], Ortiz and Stainier [74]. Non-associative plasticity, see for instance Mosler and Bruhns [65] as well as thermodynamical coupling, cf. Bartels et al. [6], Fohrmeister et al. [28], Yang et al. [106] has also been investigated from a variational point of view. The present work only considers an isothermal framework. Thus, the goal of this section is to derive a potential of the form (2.63) which defines every aspect of the elastoplastic problem from the previous section, i.e., all unknown state variables follow from the stationary of the potential. Following Carstensen et al. [14], Ortiz and Stainier [74], the functional

$$\tilde{\mathcal{E}}(\dot{\varphi}, \dot{\mathbf{F}}^p, \dot{\boldsymbol{\alpha}}, \boldsymbol{\Sigma}, \mathbf{Q}) = \dot{\Psi}(\dot{\varphi}, \dot{\mathbf{F}}^p, \dot{\boldsymbol{\alpha}}) + \mathcal{D}(\dot{\varphi}, \dot{\mathbf{F}}^p, \dot{\boldsymbol{\alpha}}, \boldsymbol{\Sigma}, \mathbf{Q}) - J(\boldsymbol{\Sigma}, \mathbf{Q}) \quad (2.82)$$

is introduced. Here, $J(\boldsymbol{\Sigma}, \mathbf{Q})$ denotes an indicator function that is defined as

$$J(\boldsymbol{\Sigma}, \mathbf{Q}) := \begin{cases} 0 & \forall (\boldsymbol{\Sigma}, \mathbf{Q}) \in \mathbb{E}_{\boldsymbol{\Sigma}} \\ \infty & \text{else.} \end{cases} \quad (2.83)$$

It is evident that inadmissible stress states are penalised with $J = \infty$. It follows from definition (2.83) that if the stresses are admissible ($\phi(\boldsymbol{\Sigma}, \mathbf{Q}) \leq 0$), potential (2.82) equals the sum of the rate of the Helmholtz energy and the dissipation which represents the stress power, i.e.,

$$\tilde{\mathcal{E}}(\dot{\varphi}, \dot{\mathbf{F}}^p, \dot{\boldsymbol{\alpha}}, \boldsymbol{\Sigma}, \mathbf{Q}) = \mathbf{P} : \dot{\mathbf{F}} := \mathcal{P} \quad \forall (\boldsymbol{\Sigma}, \mathbf{Q}) \in \mathbb{E}_{\boldsymbol{\Sigma}}. \quad (2.84)$$

Clearly, relation (2.84) is only valid in the case of rate-independence. The computation of the stationary conditions of $\tilde{\mathcal{E}}$ leads to

$$\delta_{(\boldsymbol{\Sigma}, \mathbf{Q})} \tilde{\mathcal{E}} = \mathbf{0} \Rightarrow (\mathbf{L}^p, \dot{\boldsymbol{\alpha}}) \in \partial J, \quad (2.85)$$

$$\delta_{(\dot{\boldsymbol{\alpha}})} \tilde{\mathcal{E}} = \mathbf{0} \Rightarrow \mathbf{Q} = -\frac{\partial \Psi}{\partial \dot{\boldsymbol{\alpha}}} \quad \text{and} \quad (2.86)$$

$$\delta_{(\dot{\mathbf{F}}^p)} \tilde{\mathcal{E}} = \mathbf{0} \Rightarrow \boldsymbol{\Sigma} = [\mathbf{F}^e]^T \cdot \frac{\partial \Psi}{\partial \dot{\mathbf{F}}^e}. \quad (2.87)$$

Here, ∂J is the subdifferential of J . According to Eqs. (2.85)-(2.87), the stationary conditions of $\tilde{\mathcal{E}}$ result in the flow rule and in the constitutive relations for \mathbf{Q} and $\boldsymbol{\Sigma}$ as already introduced in the previous section. It can be shown that the stationary condition is mathematically represented by a saddle point problem. To be more precise, $\tilde{\mathcal{E}}$ is minimised with respect to $(\dot{\boldsymbol{\alpha}}, \dot{\mathbf{F}}^p)$ and maximised with respect to $(\boldsymbol{\Sigma}, \mathbf{Q})$. However, as advocated in [74] and [14], it is possible to derive a reduced functional \mathcal{E} whose minimum

yields the evolution equations. Therefore the Legendre-Fenchel transformation of J is introduced as

$$J^*(\mathbf{L}^p, \dot{\boldsymbol{\alpha}}) = \sup\{\boldsymbol{\Sigma} : \mathbf{L}^p + \mathbf{Q} \circ \dot{\boldsymbol{\alpha}} - J(\boldsymbol{\Sigma}, \mathbf{Q}) \mid (\boldsymbol{\Sigma}, \mathbf{Q}) \in \mathbb{E}_{\boldsymbol{\Sigma}}\}. \quad (2.88)$$

Since J^* is homogeneous of degree 1, cf. [14], a maximisation of $\tilde{\mathcal{E}}$ with respect to $(\boldsymbol{\Sigma}, \mathbf{Q})$ leads to the reduced functional

$$\mathcal{E}(\dot{\boldsymbol{\varphi}}, \dot{\mathbf{F}}^p, \dot{\boldsymbol{\alpha}}) = \dot{\Psi}(\dot{\boldsymbol{\varphi}}, \dot{\mathbf{F}}^p, \dot{\boldsymbol{\alpha}}) + J^*(\mathbf{L}^p, \dot{\boldsymbol{\alpha}}). \quad (2.89)$$

Speaking from a physics point of view, \mathcal{E} is still the stress power and J^* represents the dissipation, provided admissible stresses, together with the normality rule, are considered, cf. Mosler and Bruhns [65]. Furthermore, the reduced functional only depends on the rates of the strains and strain-like variables $(\dot{\boldsymbol{\varphi}}, \dot{\mathbf{F}}^p, \dot{\boldsymbol{\alpha}})$. The internal strain-like variables $\dot{\mathbf{F}}^p$ and $\dot{\boldsymbol{\alpha}}$ follow jointly from the stationary of potential \mathcal{E} which itself serves as a reduced functional just depending on the deformation mapping, i.e.,

$$\mathcal{E}_{\text{red}} = \arg \operatorname{stat}_{\{\dot{\mathbf{F}}^p, \dot{\boldsymbol{\alpha}}\}} \mathcal{E}(\dot{\boldsymbol{\varphi}}, \dot{\mathbf{F}}^p, \dot{\boldsymbol{\alpha}}). \quad (2.90)$$

In the case of hyperelasticity, \mathcal{E}_{red} equals the rate of the Helmholtz free energy density, i.e. $\mathcal{E}_{\text{red}}(\dot{\boldsymbol{\varphi}}) = \dot{\Psi}(\dot{\boldsymbol{\varphi}})$, and obviously in this case $\mathcal{E}_{\text{red}}(\dot{\boldsymbol{\varphi}})$ represents the time derivative of a potential. Furthermore, the stress state is defined via

$$\mathbf{P} = \frac{\partial \mathcal{E}_{\text{red}}(\dot{\boldsymbol{\varphi}})}{\partial \dot{\mathbf{F}}}. \quad (2.91)$$

Obviously, under the aforementioned assumptions the standard hyperelastic stress-strain relation $\mathbf{P} = \partial_{\mathbf{F}} \Psi$ is received. It is now relatively straight-forward to extend the principle of minimum potential energy to standard dissipative solids by definition of the functional

$$\mathcal{I}(\boldsymbol{\varphi}) = \arg \operatorname{stat}_{\{\dot{\mathbf{F}}^p, \dot{\boldsymbol{\alpha}}\}} \left[\int_{\mathcal{B}_0} \mathcal{E}(\dot{\boldsymbol{\varphi}}, \dot{\mathbf{F}}^p, \dot{\boldsymbol{\alpha}}) dV - \int_{\mathcal{B}_0} \rho_0 \mathbf{B} \cdot \boldsymbol{\varphi} dV - \int_{\partial_N \mathcal{B}_0} \mathbf{T}^* \cdot \boldsymbol{\varphi} dV \right]. \quad (2.92)$$

The unknown deformation mapping follows as

$$\dot{\boldsymbol{\varphi}} = \arg \operatorname{stat}_{\{\dot{\boldsymbol{\varphi}}\}} \mathcal{I}(\dot{\boldsymbol{\varphi}}). \quad (2.93)$$

A detailed derivation of the relations presented here can be found in [74] and [14].

The presented variational framework implies an efficient numerical implementation. In order to derive such an implementation, the time-continuous functional (2.89) has to

be discretised in time (in analogy to Eq. (2.92)) leading to the time-discretised representation

$$\begin{aligned} & \int_{\mathcal{B}_0} \int_{t_n}^{t_{n+1}} \mathcal{E}(\dot{\boldsymbol{\varphi}}, \dot{\mathbf{F}}^{\text{p}}, \dot{\boldsymbol{\alpha}}) \, dt \, dV \\ & \approx \int_{\mathcal{B}_0} \Psi_{n+1} - \Psi_n + \int_{t_n}^{t_{n+1}} J^* \, dt \, dV := \mathcal{I}_{\text{inc}}(\boldsymbol{\varphi}_{n+1}, \mathbf{F}_{n+1}^{\text{p}}, \boldsymbol{\alpha}_{n+1}). \end{aligned} \quad (2.94)$$

Here, the energy of externally applied forces and tractions is neglected since these do not depend on $\dot{\mathbf{F}}^{\text{p}}$ and $\dot{\boldsymbol{\alpha}}$. In the case where the yield function is assumed to be positively homogeneous of degree one, see Remark 4, the integration of J^* leads to the dissipation $\Delta\lambda Q_0$, where $\Delta\lambda := \int_{t_n}^{t_{n+1}} \lambda \, dt$ is introduced. The incremental potential (2.94) is an approximation of Eq. (2.89) and, accordingly, the strain-like internal variables $(\mathbf{F}_{n+1}^{\text{p}}, \boldsymbol{\alpha}_{n+1})$ are obtained by the stationarity of \mathcal{I}_{inc} as

$$(\mathbf{F}_{n+1}^{\text{p}}, \boldsymbol{\alpha}_{n+1}) = \arg_{\{\mathbf{F}_{n+1}^{\text{p}}, \boldsymbol{\alpha}_{n+1}\}} \text{stat} \quad \mathcal{I}_{\text{inc}}. \quad (2.95)$$

The unknowns \mathbf{F}^{p} and $\boldsymbol{\alpha}$ are defined pointwise. This means that the optimisation problem is restricted to the integration points in the case of a standard finite element formulation. For the calculation of $(\mathbf{F}_{n+1}^{\text{p}}, \boldsymbol{\alpha}_{n+1})$ classic numerical procedures such as Newton's method can be applied. More details on the implementation can be found in [13, 64, 66] among others.

3 Review of classic cohesive zone models

One of the main goals of this thesis is the derivation of a consistent cohesive zone framework that fulfills all fundamental requirements in continuum mechanics. The cohesive zone concept was pioneered by Barenblatt [4, 5] on quasi-brittle materials and by Dugdale [25] on ductile materials. Later on the so-called fictitious crack model was proposed by Hillerborg et al. [42]. The framework of cohesive zone modelling is characterised by a traction-separation law that relates the traction vector with the interface (the crack) opening and sliding. The classic approach does not consider in-plane or out-of-plane membrane forces and there is no discontinuity of the traction vector across the interface.

This chapter gives an introduction to classic cohesive zone models, where the kinematics is described in the first section. In the following course of this chapter it will be shown that the classic approach serves some restrictions and inconsistencies. While for small displacements, the only limitation is that of thermodynamic consistency, in finite displacements, however, the classic theory is exposed to severe further problems. For instance, according to Mosler and Scheider [68], only isotropic classic cohesive zone models are thermodynamically consistent, as shown in Section 3.2. This inhibits the possibility of modelling shear and anisotropic effects. Furthermore, as pointed out by Vossen et al. [103] and Ottosen et al. [75] classic cohesive zone models require collinearity between the traction vector and the displacement discontinuity within the interface. Section 3.3 gives a short review of the derivation of the classic balance laws resulting in traction continuity across the interface and in the collinearity requirement between traction vector and displacement discontinuity. Subsequently, the extension of cohesive zone models with non-elastic deformations is shown. While the embedding of isotropic damage is straightforward, see Section 3.4, the extension to elastoplastic interface models (cf. Section 3.5), encounters further problems, for instance due to the principle of material frame indifference and due to balance of angular momentum, see Ottosen et al. [75].

3.1 Kinematics of non-coherent interfaces

Consider that the bulk body from Section 2.1 now is subdivided into two arbitrary subdomains \mathcal{B}_0^+ and \mathcal{B}_0^- that are bonded via the zero thickness interface Γ_0 , see Fig. 3.1. Since Γ_0 is the common boundary of \mathcal{B}_0^+ and \mathcal{B}_0^- , Γ_0 can also be subdivided into the two

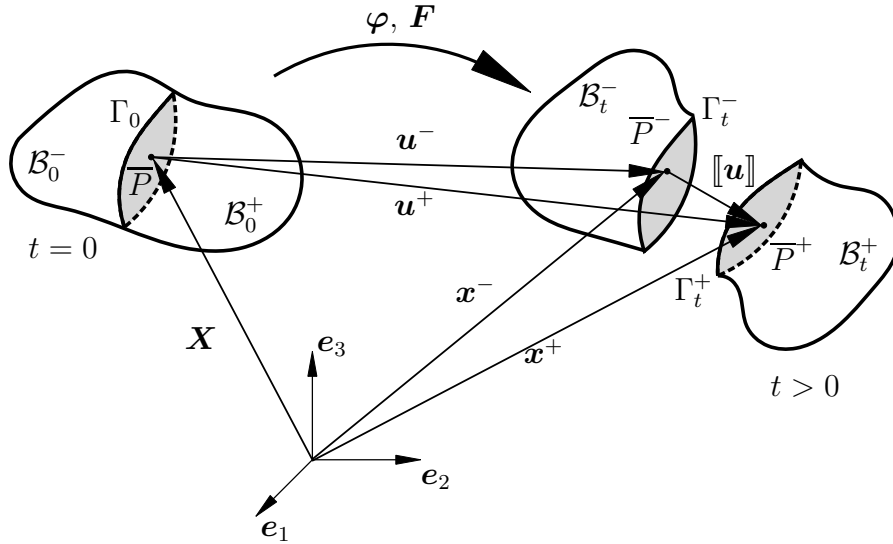


Figure 3.1: Motion of a body with a non-coherent interface – reference configuration \mathcal{B}_0 and current configuration \mathcal{B}_t

surfaces Γ_0^+ and Γ_0^- that coincide geometrically in the reference configuration, i.e. $\Gamma_0^+ = \Gamma_0^- := \Gamma_0$. Furthermore, every material point $\bar{P} \in \Gamma_0$ is described by two coordinates $\mathbf{X}^+(\bar{P}) \in \Gamma_0^+$ and $\mathbf{X}^-(\bar{P}) \in \Gamma_0^-$. In the reference configuration the coordinates are identical, i.e., $\mathbf{X}^+(\bar{P}) = \mathbf{X}^-(\bar{P}) := \mathbf{X}(\bar{P})$, and it follows that $[[\mathbf{X}]] = 0$. The unit normal to the zero thickness reference interface Γ_0 pointing from the minus to the plus side is denoted $\bar{\mathbf{N}}$. Since this work deals with non-coherent interfaces that may open during the deformation, especially points within Γ_0 have to be considered. The sharp interface Γ_0 decomposes into the two surfaces Γ_t^+ and Γ_t^- within the deformed configuration. Hence, deformation mapping φ is discontinuous across Γ_0 . To be more precise, φ is decomposed into φ^+ and φ^- , and it holds that $\varphi^- : \Gamma_0 \rightarrow \Gamma_t^-$ maps points belonging to the lower surface of the interface, and that $\varphi^+ : \Gamma_0 \rightarrow \Gamma_t^+$ maps points belonging to the upper surface of the interface. Accordingly, a material point $\mathbf{X}(\bar{P}) \in \Gamma_0$ decomposes into

$$\mathbf{x}^+(\bar{P}) = \varphi^+(\mathbf{X}(\bar{P})), \quad \mathbf{x}^+(\bar{P}) \in \Gamma_t^+ \quad (3.1)$$

and

$$\mathbf{x}^-(\bar{P}) = \varphi^-(\mathbf{X}(\bar{P})), \quad \mathbf{x}^-(\bar{P}) \in \Gamma_t^- \quad (3.2)$$

As becomes evident from (3.1) and (3.2), it follows that the deformation of non-coherent interfaces results in $\llbracket \boldsymbol{x} \rrbracket \neq 0$ across the interface. This interface discontinuity is related to the discontinuity in the bulk deformation $\llbracket \boldsymbol{\varphi} \rrbracket \neq 0$. Henceforth, this discontinuity is denoted as displacement jump

$$\llbracket \boldsymbol{u} \rrbracket = \boldsymbol{x}^+ - \boldsymbol{x}^-. \quad (3.3)$$

Alternatively, in relation to Eq. (2.1), with \boldsymbol{u}^- representing the displacement field on Γ_t^- and with \boldsymbol{u}^+ representing the displacement field on Γ_t^+ , the displacement jump reads

$$\llbracket \boldsymbol{u} \rrbracket = \boldsymbol{u}^+ - \boldsymbol{u}^-. \quad (3.4)$$

The deformation discontinuity requires further attention. For instance, due to the independence of $\boldsymbol{\varphi}^-$ and $\boldsymbol{\varphi}^+$, the current configuration provides a normal vector \boldsymbol{n}^- on the lower surface Γ_t^- and a normal vector \boldsymbol{n}^+ on the upper surface Γ_t^+ . Consequently, the normal vector $\bar{\boldsymbol{n}}$ across the interface in the deformed configuration is not uniquely defined. In order to solve the non-uniqueness of $\bar{\boldsymbol{n}}$, a fictitious intermediate configuration $\boldsymbol{x}_{(m)}$ – not to be confused with the intermediate configuration in finite strain elastoplasticity – has to be introduced, see Fig. 3.2. According to this description, a

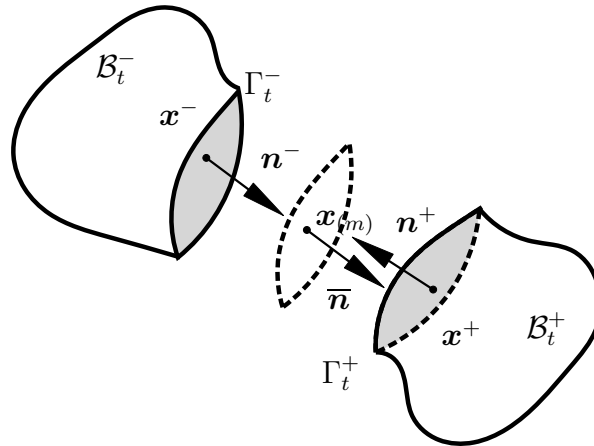


Figure 3.2: Opened material interface (cohesive zone in the deformed configuration) and fictitious intermediate configuration defining the structural tensors (dashed lines) and representing the unique current configuration of the interface Γ_t .

unique representation of the interface within the current configuration is defined as Γ_t . The intermediate configuration $\boldsymbol{x}_{(m)}$ is frequently chosen as the arithmetic average, i.e.,

$$\boldsymbol{x}_{(m)} = \frac{1}{2}(\boldsymbol{x}^+ + \boldsymbol{x}^-), \quad \boldsymbol{x}_{(m)} \in \Gamma_t. \quad (3.5)$$

However, this choice is not mandatory. Further details and a discussion of the choice of $\boldsymbol{x}_{(m)}$ can be found in Mosler and Scheider [68]. This configuration allows the definition

of a normal vector $\bar{\mathbf{n}}$ corresponding to the current configuration of an opened interface in unique manner pointing from Γ_t^- to Γ_t^+ .

3.2 Thermodynamical consistency

In a simple case of reversible cohesive zone models, the Helmholtz free energy density only depends on the displacement jump $\llbracket \mathbf{u} \rrbracket$. Focusing on a purely mechanical problem, the dissipation can be computed from the stress power \mathcal{P} and the rate, respectively the material time derivative of Ψ , see Subsection 2.2.4. The stress power in the classic cohesive zone theory is usually assumed as

$$\mathcal{P} = \mathbf{T} \cdot \dot{\llbracket \mathbf{u} \rrbracket} \quad (3.6)$$

and thus, the dissipation equality for a reversible process, cf. Eq. (2.45), reads

$$\mathcal{D} = \mathbf{T} \cdot \dot{\llbracket \mathbf{u} \rrbracket} - \dot{\Psi}(\llbracket \mathbf{u} \rrbracket) = \left(\mathbf{T} - \frac{\partial \Psi}{\partial \llbracket \mathbf{u} \rrbracket} \right) \cdot \dot{\llbracket \mathbf{u} \rrbracket} = 0. \quad (3.7)$$

Applying the Coleman-Noll procedure leads to the traction vector

$$\mathbf{T} = \frac{\partial \Psi}{\partial \llbracket \mathbf{u} \rrbracket}. \quad (3.8)$$

At first, it is concluded that the stress power equals the time derivative of the Helmholtz energy potential. In order to account for more complex material behaviour, for instance material anisotropies, structural vectors \mathbf{a}_i are considered in many interface models. Such vectors belong to the deformed configuration and refer to the intermediate configuration $\mathbf{x}_{(m)}$. Although the structural vectors may change during the deformation process, most cohesive zone models assume the classic stress power (3.6). However, this causes problems as can be seen in the following example. A special and widespread case of these models uses the midsurface's current normal vector $\bar{\mathbf{n}}$ as structural tensor, i.e.,

$$\Psi = \Psi(\llbracket \mathbf{u} \rrbracket, \bar{\mathbf{n}}). \quad (3.9)$$

This procedure allows a decomposition of the traction vector into a normal part $\mathbf{T}_n = (\mathbf{T} \cdot \bar{\mathbf{n}}) \cdot \bar{\mathbf{n}}$ and a shear part $\mathbf{T}_s = \mathbf{T} - \mathbf{T}_n$. Thereby, a distinction between normal and shear separation is possible and material anisotropies can be captured. In the case of such models, as already mentioned above, the stress power is again mostly assumed as $\mathcal{P} = \mathbf{T} \cdot \dot{\llbracket \mathbf{u} \rrbracket}$ and then the dissipation reads

$$\mathcal{D} = \mathbf{T} \cdot \dot{\llbracket \mathbf{u} \rrbracket} - \dot{\Psi}(\llbracket \mathbf{u} \rrbracket, \bar{\mathbf{n}}) = \left(\mathbf{T} - \frac{\partial \Psi}{\partial \llbracket \mathbf{u} \rrbracket} \right) \cdot \dot{\llbracket \mathbf{u} \rrbracket} - \frac{\partial \Psi}{\partial \bar{\mathbf{n}}} \cdot \dot{\bar{\mathbf{n}}} = 0. \quad (3.10)$$

In general, the displacement jump $\llbracket \mathbf{u} \rrbracket$ and the normal vector $\bar{\mathbf{n}}$ are uncoupled, i.e. $\bar{\mathbf{n}} \neq \bar{\mathbf{n}}(\llbracket \mathbf{u} \rrbracket)$, and applying the Coleman-Noll procedure in turn leads to the traction vector

$$\mathbf{T} = \frac{\partial \Psi}{\partial \llbracket \mathbf{u} \rrbracket}. \quad (3.11)$$

According to

$$\mathcal{D} = -\frac{\partial \Psi}{\partial \bar{\mathbf{n}}} \cdot \dot{\bar{\mathbf{n}}} \neq 0, \quad (3.12)$$

the dissipation does not vanish, although hyperelasticity is assumed. This is certainly a contradiction, and it follows that the stress power assumption $\mathcal{P} = \mathbf{T} \cdot \llbracket \dot{\mathbf{u}} \rrbracket$ leads to thermodynamical inconsistencies for models of the type $\Psi = \Psi(\llbracket \mathbf{u} \rrbracket, \mathbf{a}_i)$. Further details and consequences implied by the classic stress power postulate are discussed in Mosler and Scheider [68] and Ottosen et al. [77].

In the framework of large deformations the structural tensors may evolve during deformation. Therefore, it is unphysical to neglect the change of the normal vector, for instance by assuming the interface facets to remain parallel during deformation. Instead, it turns out that an extended stress power assumption with an additional term accounting for the change in structural tensors has to be considered, see Chapter 5. Resulting from this term, an energetically conjugate stress contribution has to be introduced.

3.3 Balance of linear and angular momentum

The following paragraph summarises the conditions and restrictions of classic cohesive zone models concerning balance of linear and angular momentum. The main points are in accordance to the findings of the works Costanzo [20], Vossen et al. [103] and Ottosen et al. [75]. The classic cohesive zone framework only assumes tractions upon the upper and the lower surface of an interface. With \mathbf{T} denoting the Piola-Kirchhoff traction vector of the reference configuration, \mathbf{T}^+ acts upon the upper surface Γ_0^+ and \mathbf{T}^- acts upon the lower surface Γ_0^- , see Fig. 3.3 for a sketch of the quantities within the current configuration where \mathbf{t} denotes the Cauchy traction vector. Since no further tractions within the interface are considered, it appears that membrane-like surface stresses are excluded in the classic theory. Accordingly, balance of linear momentum reads

$$\mathbf{T}^+ + \mathbf{T}^- = \mathbf{0}, \quad (3.13)$$

which requires traction continuity within the cohesive zone, i.e.,

$$\mathbf{T} := \mathbf{T}^+ = -\mathbf{T}^-. \quad (3.14)$$

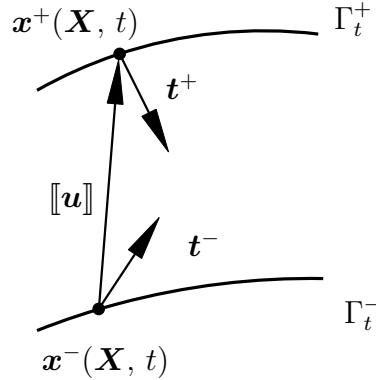


Figure 3.3: Current configuration of an opened cohesive zone with upper surface and tractions Γ_t^+ , \mathbf{t}^+ and lower surface and tractions Γ_t^- , \mathbf{t}^- . The traction vectors do not point in the direction of the displacement jump $[[\mathbf{u}]]$ and thereby generate a resulting moment. Furthermore, balance of linear momentum is not fulfilled.

A detailed discussion about the continuity of the traction vector across the interface can be found in Javili [48]. Since \mathbf{t}^\pm are collinear to the Piola-Kirchhoff traction vectors \mathbf{T}^\pm and considering balance of angular momentum it requires that

$$\mathbf{t} \times [[\mathbf{u}]] = \mathbf{0}, \quad (3.15)$$

which is not the case in the configuration shown in Fig. 3.3. In order to exclude a resulting moment, the traction vector has to be collinear to the displacement jump, i.e.,

$$\mathbf{t} \parallel [[\mathbf{u}]]. \quad (3.16)$$

Using the collinearity between \mathbf{T} and \mathbf{t} , this can be rewritten as

$$\mathbf{T} \parallel [[\mathbf{u}]], \quad (3.17)$$

which is fulfilled for instance if the traction vector can be expressed in the form

$$\mathbf{T} = k[[\mathbf{u}]], \quad (3.18)$$

where k can be any factor. Hence, if the interface is made up of springs or fibers and if the displacement discontinuity $[[\mathbf{u}]]$ is aligned with the respective fiber direction, then conditions (3.16) and (3.17) denote that the traction within the interface has to point into the spring or fiber direction. Thus, classic cohesive zone models can be interpreted as fiber models. The fiber is defined by the two spatial coordinates $\mathbf{x}^-(\mathbf{X}, t)$ and $\mathbf{x}^+(\mathbf{X}, t)$ that are described by the same material coordinate \mathbf{X} , see Fig. 3.3. Furthermore, $\mathbf{T} = \partial_{[[\mathbf{u}]]} \Psi$ holds in the range of these models, see Eq. (3.8). Consequently, it follows from Eq. (3.17) that Ψ has to be isotropic with respect to $[[\mathbf{u}]]$. Isotropy as a special case

of material symmetry is ensured by defining a Helmholtz energy in terms of the length of the displacement jump $\llbracket \mathbf{u} \rrbracket$ as

$$\Psi(\llbracket \mathbf{u} \rrbracket) = \Psi(\|\llbracket \mathbf{u} \rrbracket\|) = \Psi(\Delta). \quad (3.19)$$

This is a contradiction to general anisotropic models of the type $\Psi = \Psi(\llbracket \mathbf{u} \rrbracket, \mathbf{a}_i)$. For this reason and within the classic cohesive zone framework, any anisotropic Helmholtz energy of the type (3.9) is inconsistent with respect to balance of angular momentum.

3.3.1 Variational formulation of balance of linear momentum

In this subsection, the traction continuity for classic cohesive zone models, see Eq. (3.13), is obtained in a variational format. The derivation for hyperelastic interfaces is in line with the one for bulk materials, cf. Subsection 2.3.1.3. Figure 3.4 shows tractions acting

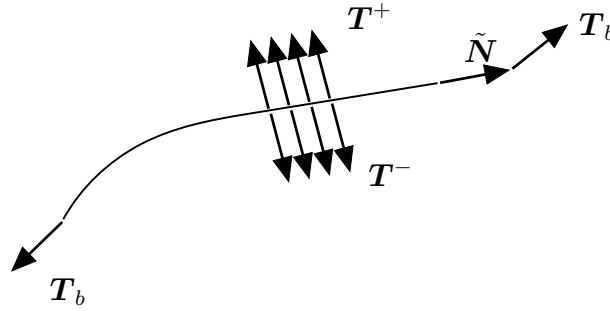


Figure 3.4: Stresses acting on an interface – referential description: Tractions acting at the upper surface $\Gamma_0^+ = \Gamma_0$ are denoted by \mathbf{T}^+ and tractions acting at the lower surface $\Gamma_0^- = \Gamma_0$ are denoted by \mathbf{T}^- . In classic cohesive zone theory, stresses \mathbf{T}_b acting at the boundary of the interface $\partial\Gamma_0$ are neglected.

within an interface in the referential description consisting of tractions \mathbf{T}^+ on the upper surface $\Gamma_0^+ = \Gamma_0$, \mathbf{T}^- on the lower surface $\Gamma_0^- = \Gamma_0$ and membrane like tractions \mathbf{T}_b on the boundary $\partial\Gamma_0$ of the interface. Classic cohesive zone theory does not consider tractions \mathbf{T}_b , see Ottosen et al. [77]. A variational derivation for balance of linear momentum in the general case considering additional interface stresses will be shown in Chapter 5.

Here, the interface potential neglecting tractions \mathbf{T}_b takes the form

$$\bar{\mathcal{I}} = \int_{\Gamma_0} \Psi(\llbracket \mathbf{u} \rrbracket) dA - \int_{\Gamma_0^+ = \Gamma_0} \mathbf{T}^+ \cdot \boldsymbol{\varphi}^+ dA - \int_{\Gamma_0^- = \Gamma_0} \mathbf{T}^- \cdot \boldsymbol{\varphi}^- dA. \quad (3.20)$$

Potential (3.20) consists of energies related to tractions \mathbf{T}^+ and \mathbf{T}^- at the upper and lower side of the interface that follow the bulk motions $\boldsymbol{\varphi}^+$ and $\boldsymbol{\varphi}^-$. In the case of hyperelasticity, the first term in Eq. (3.20) represents the integrated Helmholtz free energy density Ψ , and $\bar{\mathcal{I}}$ is the total potential energy of the interface. Further contributions to the total potential are neglected, see Remark 6. A variation of potential (3.20)

with respect to deformation φ leads to balance of linear momentum. According to the constitutive relation (3.8), the variation of the Helmholtz energy leads to

$$\int_{\Gamma_0} \delta_\varphi \Psi \, dA = \int_{\Gamma_0} \mathbf{T} \cdot \delta[\mathbf{u}] \, dA. \quad (3.21)$$

Taking this into consideration, the variation of Eq. (3.20) takes the form

$$\delta_\varphi \bar{\mathcal{I}} = \int_{\Gamma_0} \left[\mathbf{T} \cdot (\delta \mathbf{x}^+ - \delta \mathbf{x}^-) - \mathbf{T}^+ \cdot \delta \mathbf{x}^+ - \mathbf{T}^- \cdot \delta \mathbf{x}^- \right] dA = 0 \quad \forall \delta \mathbf{x}^-, \delta \mathbf{x}^+, \quad (3.22)$$

where variations

$$\delta[\mathbf{u}] = \delta \mathbf{x}^+ - \delta \mathbf{x}^- \quad \text{and} \quad \delta \varphi^\pm = \delta \mathbf{u}^\pm = \delta \mathbf{x}^\pm \quad (3.23)$$

have been used. Since $\delta \mathbf{x}^-$ and $\delta \mathbf{x}^+$ are independent of each other and arbitrary, Eq. (3.22) is equivalent to the two equations

$$\begin{aligned} -\mathbf{T}^+ + \mathbf{T} = \mathbf{0} &\quad \Rightarrow \quad \mathbf{T}^+ = \mathbf{T} \quad \text{and} \\ -\mathbf{T}^- - \mathbf{T} = \mathbf{0} &\quad \Rightarrow \quad -\mathbf{T}^- = \mathbf{T}^+ := \mathbf{T} \end{aligned} \quad (3.24)$$

that represent balance of linear momentum in the classic cohesive zone framework resulting in traction continuity across the interface.

Remark 6 *For the sake of completeness, interface force densities along and across the interface, comparable to the volumetric contributions $\rho_0 \mathbf{B}$ in the bulk continuum, could have been considered in the total interface potential (3.20). Nevertheless, they would not have led to new findings and have thus been neglected in this work.*

3.4 Extension to isotropic damage

The extension of classic hyperelastic cohesive zone models to isotropic damage is straightforward. This derivation follows the work of Radulovic et al. [84]. The scalar valued damage variable $d \in [0, 1]$ indicates the state of material degradation where $d = 0$ denotes the undamaged initial stage and where $d = 1$ denotes the totally damaged material. With this damage variable, the Helmholtz energy density is assumed to be of the form

$$\Psi = (1 - d) \Psi^e([\mathbf{u}]), \quad (3.25)$$

where Ψ^e describes the elastic part of the undamaged material. In this section, no structural tensors are considered in the Helmholtz energy. In line with classic cohesive

zone theory, the stress power is assumed as $\mathcal{P} = \mathbf{T} \cdot \llbracket \dot{\mathbf{u}} \rrbracket$ and the dissipation inequality, see Eq. (2.40), reads

$$\mathcal{D} = \left(\mathbf{T} - \frac{\partial \Psi}{\partial \llbracket \mathbf{u} \rrbracket} \right) \cdot \llbracket \dot{\mathbf{u}} \rrbracket - \frac{\partial \Psi}{\partial d} \dot{d} \geq 0. \quad (3.26)$$

Evaluating (3.26) for purely elastic unloading ($\mathcal{D} = 0$, $\dot{d} = 0$) generates the classic traction vector

$$\mathbf{T} = \frac{\partial \Psi}{\partial \llbracket \mathbf{u} \rrbracket}. \quad (3.27)$$

Inserting the traction vector (3.27) into the dissipation inequality (3.26) leads to the reduced dissipation as

$$\mathcal{D}_{\text{red}} = -\frac{\partial \Psi}{\partial d} \dot{d} = \Psi^e \dot{d} \geq 0. \quad (3.28)$$

Since $\Psi^e \geq 0$, the second law of thermodynamics is automatically fulfilled if d monotonically increases, respectively if self-healing is avoided, i.e.,

$$\dot{d} \geq 0. \quad (3.29)$$

Furthermore, from Eq. (3.28) it follows that d is thermodynamically conjugate to energy Ψ^e and therefore represents a driving force for damage evolution $d = d(\Psi^e)$. In order to accumulate damage only for increasing energy, the internal variable κ is introduced as

$$d = d(\kappa), \quad \kappa(t_{n+1}) = \max\{\kappa(t_n), \Psi^e(t_{n+1})\}, \quad \kappa(t_0) = \kappa_0. \quad (3.30)$$

Since $\Psi^e = \Psi^e(\llbracket \mathbf{u} \rrbracket)$, an equivalent choice for the driving force would be the displacement jump, i.e., $d = d(\llbracket \mathbf{u} \rrbracket)$.

3.4.1 Variational formulation for isotropic interface damage models

The standard derivation of the isotropic damage cohesive zone framework in line with the Coleman-Noll procedure, see Section 3.4, is widespread. In order to derive a variational structure of the framework and in line with Mosler and Scheider [68], the stress power $\mathcal{P} = \dot{\Psi} + \mathcal{D}$ of the model is considered and integrated over the interface area. Together with externally applied mechanical powers, a resulting potential is built up as

$$\dot{\mathcal{I}} = \int_{\Gamma_0} \left(\dot{\Psi} + \mathcal{D} \right) dA - \mathcal{P}_{\text{ext}}. \quad (3.31)$$

3 Review of classic cohesive zone models

All equations characterising the isotropic interface damage models follow jointly from stationarity of potential (3.31), i.e.,

$$\{\dot{\varphi}, \dot{\kappa}\} = \arg \operatorname{stat}_{\{\dot{\varphi}, \dot{\kappa}\}} \dot{\mathcal{I}}. \quad (3.32)$$

Here, dissipation \mathcal{D} reads

$$\mathcal{D} = \kappa |\dot{d}| = \kappa \frac{\partial d}{\partial \kappa} |\dot{\kappa}| \quad (3.33)$$

and together with Helmholtz energy (3.25) insertion into potential (3.31) leads to

$$\dot{\mathcal{I}} = \int_{\Gamma_0} \left[\frac{\partial \Psi}{\partial \llbracket \mathbf{u} \rrbracket} \cdot \llbracket \dot{\mathbf{u}} \rrbracket - \Psi^e \frac{\partial d}{\partial \kappa} \dot{\kappa} + \kappa \frac{\partial d}{\partial \kappa} |\dot{\kappa}| \right] dA - \mathcal{P}_{\text{ext}}. \quad (3.34)$$

Furthermore, the external interface stress power, cf. Subsection 3.3.1, is inserted as

$$\mathcal{P}_{\text{ext}} = \int_{\Gamma_0} [\mathbf{T}^+ \cdot \dot{\varphi}^+ + \mathbf{T}^- \cdot \dot{\varphi}^-] dA. \quad (3.35)$$

In line with classic cohesive zone theory, interface tractions \mathbf{T}_b are neglected here. The variation of potential (3.31) with respect to velocity field $\dot{\varphi}$ can be computed in a straightforward fashion. Stationarity of (3.31) yields

$$\delta_{\dot{\varphi}} \dot{\mathcal{I}} = \int_{\Gamma_0} [\mathbf{T} \cdot (\delta \dot{\mathbf{u}}^+ - \delta \dot{\mathbf{u}}^-) - \mathbf{T}^+ \cdot \delta \dot{\mathbf{u}}^+ - \mathbf{T}^- \cdot \delta \dot{\mathbf{u}}^-] dA = 0 \quad \forall \delta \dot{\mathbf{u}}^+, \delta \dot{\mathbf{u}}^-, \quad (3.36)$$

where variations

$$\delta \llbracket \dot{\mathbf{u}} \rrbracket = (\delta \dot{\mathbf{u}}^+ - \delta \dot{\mathbf{u}}^-) \quad \text{and} \quad \delta \dot{\varphi}^\pm = \delta \dot{\mathbf{u}}^\pm \quad (3.37)$$

have been used. It becomes obvious that Eq. (3.36) is equivalent to Eq. (3.22) and thereby represents the weak form of equilibrium, respectively balance of linear momentum, see Eq. (3.24). The second stationary condition of potential (3.31) is the one related to a variation of $\dot{\kappa}$ that is obtained as

$$\delta_{\dot{\kappa}} \dot{\mathcal{I}} = \int_{\Gamma_0} \left(-\Psi^e \frac{\partial d}{\partial \kappa} + \partial_{\dot{\kappa}} \mathcal{D} \right) \delta \dot{\kappa} dA = 0 \quad \forall \delta \dot{\kappa}, \quad (3.38)$$

where

$$\partial_{\dot{\kappa}} \mathcal{D} := \begin{cases} \kappa \frac{\partial d}{\partial \kappa} \operatorname{sign}(\dot{\kappa}) & \forall \dot{\kappa} \neq 0 \\ \kappa \frac{\partial d}{\partial \kappa} [-1, 1] & \text{else} \end{cases} \quad (3.39)$$

denotes the subdifferential of \mathcal{D} . Stationary condition (3.38) contains the flow rule for the internal variable. First, in order to avoid healing of the material, $\dot{\kappa} > 0$ holds. Thereby, in the case of damage ($\dot{\kappa} \neq 0$) it follows that

$$\kappa = \Psi^e \quad (3.40)$$

is the driving force for damage evolution. On the other hand, in the case of elastic loading or unloading ($\dot{\kappa} = 0$) it holds that

$$\Psi^e \leq \kappa. \quad (3.41)$$

This is in line with the introduction of the internal variable in the previous section as

$$d = d(\kappa), \quad \kappa(t_{n+1}) = \max\{\kappa(t_n), \Psi^e(t_{n+1})\}, \quad \kappa(t_0) = \kappa_0. \quad (3.42)$$

This equation covers inelastic loading with an evolution of the internal variable as well as elastic unloading.

3.5 Extension to elastoplasticity

3.5.1 Eulerian framework

According to Section 3.3, physically consistent hyperelasticity within the classic cohesive zone framework requires an isotropic Helmholtz energy of the type

$$\Psi(\llbracket \mathbf{u} \rrbracket) = \Psi(\|\llbracket \mathbf{u} \rrbracket\|) = \Psi(\Delta). \quad (3.43)$$

This is the most general format of a classic cohesive zone model that fulfills all fundamental principles since

$$\mathbf{T} = \frac{\partial \Psi}{\partial \Delta} \frac{\llbracket \mathbf{u} \rrbracket}{\Delta}. \quad (3.44)$$

This traction vector is indeed collinear to the displacement jump and the model has the property of a fiber model. It is also observed that this constitutive relation fulfills the principle of frame indifference.

Elastoplastic deformations are then investigated. Most frequently in cohesive zone theory, the displacement jump is additively decomposed into an elastic and a plastic part, i.e.,

$$[[\mathbf{u}]] = [[\mathbf{u}]]^e + [[\mathbf{u}]]^p. \quad (3.45)$$

Although hardening effects have been neglected in this section for the sake of simplicity, they would not have led to further difficulties. Here, the Helmholtz energy depends only on the elastic part of the displacement jump, to be more precise

$$\Psi = \Psi([[\mathbf{u}]]^e). \quad (3.46)$$

Again, the classic stress power assumption $\mathcal{P} = \mathbf{T} \cdot [[\dot{\mathbf{u}}]]$ is used and the dissipation inequality then reads

$$\mathcal{D} = \left(\mathbf{T} - \frac{\partial \Psi}{\partial [[\mathbf{u}]]^e} \right) \cdot [[\dot{\mathbf{u}}]] + \frac{\partial \Psi}{\partial [[\mathbf{u}]]^e} \cdot [[\dot{\mathbf{u}}]]^p \geq 0 \quad (3.47)$$

Application of the Coleman-Noll procedure results in the traction vector as

$$\mathbf{T} = \frac{\partial \Psi}{\partial [[\mathbf{u}]]^e} = \frac{\partial \Psi}{\partial [[\mathbf{u}]]} \quad (3.48)$$

and the reduced dissipation inequality is calculated as

$$\mathbf{T} \cdot [[\dot{\mathbf{u}}]]^p \geq 0. \quad (3.49)$$

Usually the model is completed by defining suitable evolution equations of the type $[[\dot{\mathbf{u}}]]^p = \lambda \mathbf{f}(\mathbf{T})$ where λ is the plastic multiplier. However, this would lead to physically inconsistent models. To be more explicit and following the discussion in Ottosen et al. [75], $[[\dot{\mathbf{u}}]]^p$ is not material frame indifferent (objective). Thus, a naive choice for the evolution equation $[[\dot{\mathbf{u}}]]^p = \lambda \mathbf{f}(\mathbf{T})$ would not lead to objective constitutive models either. Furthermore, plasticity is intrinsically anisotropic. According to Fig. 3.5, the plastic part of the displacement jump $[[\mathbf{u}]]^p$ resulting from the chosen evolution equations does not need to be parallel to $[[\mathbf{u}]]$. Hence, in such a case $[[\mathbf{u}]]^e$ is not collinear to $[[\mathbf{u}]]$. This means, that for isotropic Helmholtz energies of the type

$$\Psi([[\mathbf{u}]]^e) = \Psi(\|[[\mathbf{u}]]^e\|) = \Psi(\Delta^e) \quad (3.50)$$

collinearity between \mathbf{T} and $[[\mathbf{u}]]^e$ is implied by Eq. (3.48). However, since $[[\mathbf{u}]]^e$ is usually not collinear to $[[\mathbf{u}]]$ it also holds that \mathbf{T} does not need to be collinear to $[[\mathbf{u}]]$. However, as stated in Section 3.3, this collinearity is the requirement to fulfill balance of angular momentum. Thus, even an isotropic Helmholtz energy of the type (3.50) does usually not fulfill balance of angular momentum.

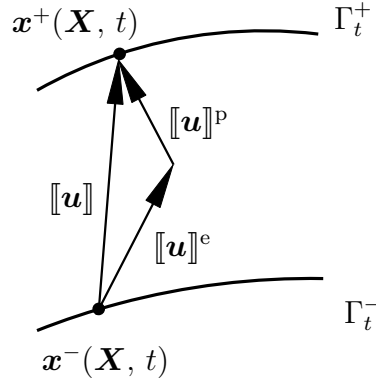


Figure 3.5: Current configuration of an opened cohesive zone with upper surface Γ_t^+ and lower surface Γ_t^- . General case: the displacement jump $[[\mathbf{u}]]$ is additively decomposed into an elastic part $[[\mathbf{u}]]^e$ and a plastic part $[[\mathbf{u}]]^p$.

3.5.2 Lagrangian framework

Alternatively to the Eulerian framework based on the displacement jump $[[\mathbf{u}]]$, cohesive zone models can be described in a Lagrangian framework related to the material displacement jump \mathbf{J} , cf. Garikipati [31] and Armero and Garikipati [2]. It is defined by the pull back operator as

$$\mathbf{J} = \mathbf{F}^{-1} \cdot [[\mathbf{u}]]. \quad (3.51)$$

Here, \mathbf{F} can describe the deformation at the lower, upper or the fictitious midsurface. The classic strong discontinuity approach (SDA) assumes a continuous \mathbf{F} across the interface, cf. [2, 31]. Hence, the results are identical if the deformation gradient of the lower or upper side of the interface is considered in Eq. (3.51). By using a referential description, the requirements for material frame indifference are automatically fulfilled, see Fagerström and Larsson [27]. However, this description is not well suited for several applications due to some important restrictions. First, following Mosler and Scheider [68], the use of \mathbf{J} within constitutive laws implies that the physical displacement jump $[[\mathbf{u}]]$ consists of an additional convective term. To be more precise, from Eq. (3.51) the material time derivative of $[[\mathbf{u}]]$ follows as

$$[[\dot{\mathbf{u}}]] = \dot{\mathbf{F}} \cdot \mathbf{J} + \mathbf{F} \cdot \dot{\mathbf{J}}. \quad (3.52)$$

It is noticeable that an unloading process with $\dot{\mathbf{J}} = \mathbf{0}$ does not automatically imply $[[\dot{\mathbf{u}}]] = \mathbf{0}$ which means that the length of $[[\mathbf{u}]]$ could change even when $\dot{\mathbf{F}} = \mathbf{0}$ holds. A further critical point is emphasised in Ottosen et al. [75]. According to the decomposition

of $[[\mathbf{u}]]$, see Eq. (3.45), the material displacement jump is also additively decomposed, i.e.,

$$\mathbf{J} = \mathbf{J}^e + \mathbf{J}^p. \quad (3.53)$$

In line with the choice for the Helmholtz energy in the Eulerian framework (3.46), the strain-energy is taken as

$$\Psi = \Psi(\mathbf{J}^e). \quad (3.54)$$

By insertion of Eqs. (3.52) and (3.53), the dissipation inequality reads

$$\mathcal{D} = \left(\mathbf{t}_M - \frac{\partial \Psi}{\partial \mathbf{J}^e} \right) \cdot \dot{\mathbf{J}} + \frac{\partial \Psi}{\partial \mathbf{J}^e} \cdot \dot{\mathbf{J}}^p + \mathbf{T} \cdot \dot{\mathbf{F}} \cdot \mathbf{J} \geq 0, \quad (3.55)$$

where the constitutive relation for the traction vector $\mathbf{t}_M = \mathbf{F}^T \cdot \mathbf{T}$ follows as

$$\mathbf{t}_M = \frac{\partial \Psi}{\partial \mathbf{J}^e}. \quad (3.56)$$

It is straightforward to show that \mathbf{t}_M fulfills the principle of material frame indifference, cf. Fagerström and Larsson [27]. In the following, the Helmholtz energy is chosen as

$$\Psi = \frac{1}{2} (\mathbf{J} - \mathbf{J}^p) \cdot \mathbf{K} \cdot (\mathbf{J} - \mathbf{J}^p), \quad (3.57)$$

where \mathbf{K} is a constant symmetric interface stiffness tensor. In this case, the constitutive relation (3.56) leads to the traction vector

$$\mathbf{t}_M = \mathbf{K} \cdot \mathbf{J}^e \quad (3.58)$$

that can be transformed to the classic reference traction vector \mathbf{T} as

$$\mathbf{T} = \mathbf{F}^{-T} \cdot \mathbf{K} \cdot \mathbf{F}^{-1} \cdot ([[\mathbf{u}]] - [[\mathbf{u}]]^p). \quad (3.59)$$

In order to fulfill balance of angular momentum, traction vector \mathbf{T} has to be collinear to the displacement jump $[[\mathbf{u}]]$, which enables an expression of the form (3.18). Considering a purely elastic process with $[[\mathbf{u}]]^p = \mathbf{0}$, condition (3.18) is only fulfilled if $\mathbf{K} = k \mathbf{F}^T \cdot \mathbf{F}$. Applying this expression for the stiffness \mathbf{K} allows the reformulation

$$\mathbf{T} = k ([[\mathbf{u}]] - [[\mathbf{u}]]^p). \quad (3.60)$$

Nonetheless, the condition of a deformation dependent stiffness \mathbf{K} violates the assumption of a constant tensor. Thus, even in the case of elasticity, balance of angular momentum is not fulfilled. Furthermore, in line with the discussion in Subsection 3.5.1 the

plastic deformation jump $[[\mathbf{u}]]^P$ is in general not collinear to $[[\mathbf{u}]]$, see Fig. 3.5. Accepting constitutive relation (3.56), the reduced dissipation inequality takes the form

$$\mathcal{D} = \mathbf{t}_M \cdot \dot{\mathbf{J}}^P + \mathbf{T} \cdot \dot{\mathbf{F}} \cdot \mathbf{J} \geq 0 \quad (3.61)$$

and, even for pure elasticity, the dissipation does not vanish. Following Ottosen et al. [75], the last term in (3.61) is usually neglected and an evolution law for $\dot{\mathbf{J}}^P$ with $\mathbf{t}_M \cdot \dot{\mathbf{J}}^P$ is postulated. In contrast to the Eulerian framework this evolution law fulfills the principle of material frame indifference. However, within this description the dissipation inequality is only fulfilled approximately and the balance of angular momentum still is not fulfilled in general.

4 Consistent cohesive zone framework

I – sliding of the fiber’s corner points

According to the previous chapter, consistent classic cohesive zone models can be interpreted as fiber models, where the traction within the interface has to point into the fiber direction. The fiber is defined by the displacement vector between two spatial coordinates that refer to the same point in the reference configuration. These restrictions limit the possibility of modelling shear and anisotropic effects as well as elastoplasticity within the interface.

This chapter introduces one possibility for an extended consistent cohesive zone framework that was first elaborated in Ottosen et al. [75]. At the beginning, the kinematics of a relaxed fiber concept in the sense that the corner points of the fiber may change during the deformation process is summarised. To be more precise, the fiber no longer links two points that belong to the same material coordinate. Afterwards in Section 4.2 the adjusted balance laws for the extended framework are summarised and the constitutive relations are presented, cf. Section 4.3. Subsequently, a simple model of the generalised framework is introduced in Section 4.4. This prototype model represents a thermodynamically consistent elastoplastic fiber interface model and fulfills all fundamental balance laws. Due to the physical behaviour of fibers under compression, particular attention is given to the unloading behaviour. Therefore, a novel unloading approach is presented in Section 4.5. Subsequently, it is shown that the introduced consistent elastoplastic interface framework can be formulated in a variational format, cf. Section 4.6. At the end of this chapter the consistent elastoplastic fiber model is investigated within numerical simulations. Here, the focus lies on the novel unloading behaviour which is compared to classic damage material models.

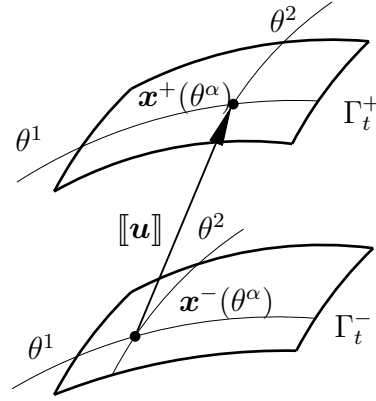


Figure 4.1: Representation of the fiber idea in classic cohesive zone framework. The fiber connecting the lower surface Γ_t^- and the upper surface Γ_t^+ of an opened interface is defined by the two points $\mathbf{x}^-(\theta^\alpha)$ and $\mathbf{x}^+(\theta^\alpha)$, represented by the same material coordinates within the curvilinear coordinate system θ^α . The difference of $\mathbf{x}^-(\theta^\alpha)$ and $\mathbf{x}^+(\theta^\alpha)$ is known as classic displacement jump $[[\mathbf{u}]]$

4.1 Kinematics of the generalised fiber model

Following Section 3.1, the two coinciding crack surfaces of a non-coherent interface in the reference configuration are denoted by

$$\Gamma_0^- = \Gamma_0^-(X^i) \quad \text{and} \quad \Gamma_0^+ = \Gamma_0^+(X^i), \quad (4.1)$$

which are described by the same Cartesian coordinates X^i . Next, a two dimensional curvilinear coordinate system with coordinates θ^α is introduced within the surfaces, i.e., $X^i = X^i(\theta^\alpha)$. Here and henceforth, Greek indices take the values 1 and 2. In the current configuration after crack opening, the reference surface decomposes into the two surfaces Γ_t^- and Γ_t^+ which are characterised by

$$\mathbf{x}^- = \mathbf{x}^-(\theta^\alpha, t) \quad \text{and} \quad \mathbf{x}^+ = \mathbf{x}^+(\theta^\alpha, t). \quad (4.2)$$

In the classic cohesive zone formulation, a fiber connecting the upper and lower surface of an opened interface is always defined by identical material coordinates θ^α on each side of the crack/interface, see Fig. 4.1. The classic displacement jump reads

$$[[\mathbf{u}]] = \mathbf{x}^+(\theta^\alpha, t) - \mathbf{x}^-(\theta^\alpha, t). \quad (4.3)$$

Hence, its directional unit vector is calculated by

$$\mathbf{n}_{[[\mathbf{u}]]} = \frac{[[\mathbf{u}]]}{\|[[\mathbf{u}]]\|}. \quad (4.4)$$

The approach of fixed fiber coordinates is generalised in Ottosen et al. [75]. Instead of always defining a fiber by two fixed material coordinates, the corner points of the fiber are allowed to change during plastic loading. Therefore, the points are defined by independent material coordinates, to be more precise by θ_-^α on the lower surface Γ_0^- and by θ_+^α on the upper surface Γ_0^+ as shown in Fig. 4.2. As mentioned above, the

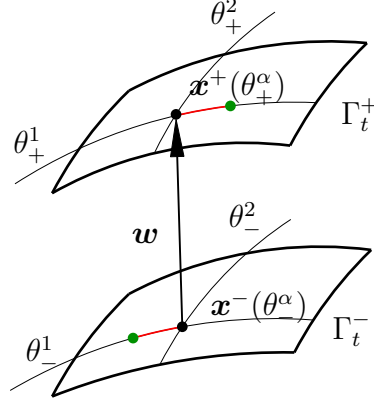


Figure 4.2: Representation of the relaxed fiber idea in the generalised cohesive zone framework. The fiber connecting the lower surface Γ_t^- and the upper surface Γ_t^+ of an opened interface is defined by two points $\mathbf{x}^-(\theta_-^\alpha)$ and $\mathbf{x}^+(\theta_+^\alpha)$, represented by different material coordinates within the curvilinear coordinate system θ_-^α and θ_+^α . The difference of $\mathbf{x}^-(\theta_-^\alpha)$ and $\mathbf{x}^+(\theta_+^\alpha)$ can be interpreted as non-classic displacement jump \mathbf{w} .

redefinition of the starting and the end point of the fiber is associated with elastoplastic deformations. To be more precise, during elastic deformation the fiber is defined by coordinates that belong to the same material point, i.e., initially it holds that

$$\theta_-^\alpha(t=0) = \theta_+^\alpha(t=0) = \theta^\alpha(t=0). \quad (4.5)$$

This approach refers to the classic fiber concept of cohesive zones as sketched in Fig. 4.1. If assumption (4.5) were neglected, different load paths that do not involve a change of the fiber length would be possible and the corresponding stiffness would then be zero. The redefinition of the fiber coordinates is characterised by a sliding of the original material coordinates. An exemplary sliding of the original green fiber points to the redefined black points in the θ^1 direction is outlined by the red lines in Fig. 4.2. In order to obtain a symmetry in the formulation, relations

$$\theta_-^\alpha = \theta^\alpha - c^\alpha \quad \text{and} \quad \theta_+^\alpha = \theta^\alpha + c^\alpha \quad (4.6)$$

are introduced. The sliding of the points (red line in Fig. 4.2) is described by a scalar-valued evolution equation for

$$c^\alpha = c^\alpha(\theta^\beta). \quad (4.7)$$

Since θ^α denotes a fixed material point, the evolution of the coordinates is expressed by

$$\dot{\theta}_-^\alpha = -\dot{c}^\alpha \quad \text{and} \quad \dot{\theta}_+^\alpha = \dot{c}^\alpha. \quad (4.8)$$

Taking all this into consideration, the positions of the fiber starting and end points of the current configuration within the generalised framework read

$$\mathbf{x}^- = \mathbf{x}^-(\theta_-^\alpha, t) \quad \text{and} \quad \mathbf{x}^+ = \mathbf{x}^+(\theta_+^\alpha, t). \quad (4.9)$$

Thereby, the non-classic part of the displacement jump is introduced as

$$\mathbf{w} = \mathbf{x}^+(\theta_+^\alpha, t) - \mathbf{x}^-(\theta_-^\alpha, t), \quad (4.10)$$

see also Fig. 4.2, and its direction is defined by

$$\mathbf{m}_w = \frac{\mathbf{w}}{\|\mathbf{w}\|}. \quad (4.11)$$

In summary, when plasticity has developed, the two surfaces Γ_t^- and Γ_t^+ do not necessarily involve the same material coordinates (in general $\theta_-^\alpha \neq \theta_+^\alpha$). While the classic positions (4.2) result in coinciding reference surfaces $\Gamma_0^- = \Gamma_0^+$, this is not the case in the extended framework. To be more precise, the generalisation of the fiber concept results in different reference crack surfaces during plastic loading, i.e., $\Gamma_0^- \neq \Gamma_0^+$.

The concept of the coordinate sliding for the fiber generalisation as presented in [75] bears some similarities to moving coordinates adopted in contact mechanics, cf. for instance Curnier et al. [21], Pietrzak and Curnier [80]. The idea is to distinguish between a master and a slave surface in the case of contact. The material coordinates on the master surface are the projections of some material points on the slave surface. The material coordinates on the master are allowed to move during loading, as is the case in the generalised fiber concept for cohesive zone models.

4.2 Balance laws of the generalised cohesive zone sliding framework

In the generalised cohesive zone framework introduced in Ottosen et al. [75], the kinematics of a fiber are adjusted by the sliding of points along the crack surfaces. The classic framework of consistent cohesive zone models is expanded by the redefinition of a fiber as a connection between two points described by different material coordinates θ_+^α and θ_-^α . Hence, the generalised balance laws as well as the dissipation inequality have to be re-derived.

4.2.1 Balance of linear momentum

The sliding of nodes is dissipative in nature, cf. [75]. This means that \dot{c}^α is not considered in the stress power. Therefore, only tractions upon the lower and upper surfaces have to be considered in the balance law for linear momentum, cf. Section 3.3 for the classic fiber framework. Thus, the global form reads

$$\int_{\Gamma_t^-} \mathbf{t}^- ds + \int_{\Gamma_t^+} \mathbf{t}^+ ds = \mathbf{0} \quad (4.12)$$

and ds denotes the relevant incremental area of the interface (crack) surface. The area ds_- on the lower interface side Γ_t^- around \mathbf{x}^- can be related to the corresponding area element ds_+ on the upper side Γ_t^+ around \mathbf{x}^+ by

$$ds_+ = j ds_-. \quad (4.13)$$

The factor j is derived in the Appendix A.1 in analogy to [75], cf. Eq. (A.11). Inserting relation (4.13) into Eq. (4.12) yields

$$\int_{\Gamma_t^-} [\mathbf{t}^-(\mathbf{x}^-, t) + j\mathbf{t}^+(\mathbf{x}^+, t)] ds = \mathbf{0}. \quad (4.14)$$

Due to the symmetric definition of the sliding, see Eq. (4.6), the upper position $\mathbf{x}^+(\theta_+^\alpha, t)$ is related to the lower position $\mathbf{x}^-(\theta_-^\alpha, t)$. Finally, the localisation of the global form (4.12) leads to the local form of balance of linear momentum, i.e.,

$$\mathbf{t}^-(\mathbf{x}^-, t) + j\mathbf{t}^+(\mathbf{x}^+, t) = \mathbf{0}. \quad (4.15)$$

4.2.2 Balance of angular momentum

In this subsection balance of angular momentum is considered for the extended fiber concept. Together with the aforementioned preliminaries, the global form of balance of angular momentum reads

$$\int_{\Gamma_t^-} \mathbf{x}^- \times \mathbf{t}^-(\mathbf{x}^-, t) ds + \int_{\Gamma_t^+} \mathbf{x}^+ \times \mathbf{t}^+(\mathbf{x}^+, t) ds = \mathbf{0}, \quad (4.16)$$

which can be reduced by inserting relation (4.13) into a form related to the lower interface surface, i.e.,

$$\int_{\Gamma_t^-} [\mathbf{x}^- \times \mathbf{t}^-(\mathbf{x}^-, t) + j\mathbf{x}^+ \times \mathbf{t}^+(\mathbf{x}^+, t)] ds = \mathbf{0}. \quad (4.17)$$

Application of balance of linear momentum (4.15) leads to the local form of balance of angular momentum for the generalised fiber framework, i.e.,

$$(\mathbf{x}^+ - \mathbf{x}^-) \times \mathbf{t}^- = \mathbf{0}. \quad (4.18)$$

From Eq. (4.18) it can be concluded that the traction vector \mathbf{t}^- has to be collinear to the non-classic displacement jump \mathbf{w} (cf. Eq. (4.10)) in order to fulfill balance of angular momentum. Therefore, it can be expressed in the form

$$\mathbf{t}^-(\mathbf{x}^-, t) = \beta \mathbf{w}, \quad (4.19)$$

where β is any (not necessarily deformation independent) proportionality factor. The Piola-Kirchhoff traction vector \mathbf{T}^- that refers to the lower surface Γ_0^- is collinear to \mathbf{t}^- , cf. \mathbf{t} and \mathbf{T} in the classic fiber framework. This gives rise to the relation

$$\mathbf{T}^- = \gamma \mathbf{w}. \quad (4.20)$$

Here, the connection of \mathbf{t}^- and \mathbf{T}^- through relation

$$\mathbf{T}^- dS_- = \mathbf{t}^- ds \quad (4.21)$$

has been used where dS denotes the incremental area in the reference configuration Γ_0^- .

4.2.3 Second law of thermodynamics

According to Subsection 2.2.4, the second law of thermodynamics in form of the Clausius-Planck inequality plays a major role in the derivation of consistent material models. In the case of isothermal hyperelastic processes, the stress power \mathcal{P} is related to the material time derivative of the Helmholtz energy density $\dot{\Psi}$. Based on the generalised fiber concept, the stress power reads

$$\mathcal{P} = \int_{\Gamma_t^-} \mathbf{t}^-(\mathbf{x}^-, t) \cdot \mathbf{v}^- ds + \int_{\Gamma_t^+} \mathbf{t}^+(\mathbf{x}^+, t) \cdot \mathbf{v}^+ ds, \quad (4.22)$$

where \mathbf{v}^- denotes the velocity of the lower position \mathbf{x}^- for fixed θ_-^α and where \mathbf{v}^+ denotes the velocity of the upper position \mathbf{x}^+ for fixed θ_+^α , i.e., $\dot{\theta}_+^\alpha = \dot{\theta}_-^\alpha = 0$. It holds that

$$\mathbf{v}^- = \frac{\partial \varphi^-}{\partial t} \quad \text{and} \quad \mathbf{v}^+ = \frac{\partial \varphi^+}{\partial t}. \quad (4.23)$$

Together with expression (4.13) and balance of linear momentum (4.15), the stress power can be expressed in terms of the lower traction vector as

$$\mathcal{P} = \int_{\Gamma_t^-} \mathbf{t}^- \cdot [\mathbf{v}^- - \mathbf{v}^+] \, ds. \quad (4.24)$$

Following the collinearity of \mathbf{t} and \mathbf{T} , the stress power can also be defined with respect to the reference configuration as

$$\mathcal{P} = \int_{\Gamma_0^-} \mathbf{T}^- \cdot [\mathbf{v}^- - \mathbf{v}^+] \, dS. \quad (4.25)$$

Similarly to the localisation process for bulk continua, cf. Subsection 2.2.4, the dissipation inequality for the generalised fiber framework in the Clausius-Planck form reads

$$\mathcal{D} = \mathbf{T}^- \cdot [\mathbf{v}^- - \mathbf{v}^+] - \dot{\Psi} = \mathbf{T}^+ \cdot [\mathbf{v}^+ - \mathbf{v}^-] - \dot{\Psi} \geq 0, \quad (4.26)$$

which is formally identical to the dissipation in classic cohesive zone fiber framework, cf. Eq. (3.7) for hyperelasticity.

4.3 Constitutive modelling

4.3.1 Elasticity

As long as the deformations within the cohesive zone are elastic, no fiber sliding occurs. To be more precise, the two crack surfaces Γ_t^- and Γ_t^+ are described by the same material coordinates $\theta_-^\alpha = \theta_+^\alpha = \theta^\alpha$. This is in accordance with the classic fiber cohesive zone framework. It gives rise to the classic displacement jump $[[\mathbf{u}]]$, cf. Eq. (4.3). Therefore, all assumptions and limitations presented in Chapter 3 are valid. Thus, only an isotropic Helmholtz energy of the form

$$\Psi = \Psi(\|[[\mathbf{u}]]\|) = \Psi(\Delta) \quad (4.27)$$

together with a traction vector

$$\mathbf{T} = \frac{\partial \Psi}{\partial \|[[\mathbf{u}]]\|} \frac{[[\mathbf{u}]]}{\|[[\mathbf{u}]]\|} \quad (4.28)$$

can fulfill all fundamental requirements such as balance of angular momentum and material frame indifference.

4.3.2 Elastoplasticity

As mentioned above regarding the range of elastic deformation, the classic fiber concept is still employed. However, from the point when plasticity starts to evolve, the coordinates given by θ^1 and θ^2 are allowed to slide along the surfaces Γ_t^+ and Γ_t^- , cf. Section 4.1. According to Eq. (4.20), balance of angular momentum requires that the traction vector \mathbf{T}^- and the non-standard displacement jump \mathbf{w} have to be collinear in the sense of

$$\mathbf{t}^- \|\mathbf{T}^- = \gamma (\mathbf{x}^+(\theta_+^\alpha) - \mathbf{x}^-(\theta_-^\alpha)) := \gamma \mathbf{w} \neq \gamma \llbracket \mathbf{u} \rrbracket, \quad (4.29)$$

where γ is any proportionality factor. The introduced jump \mathbf{w} is non-standard since it no longer connects two points with identical material coordinates. Hence, after coordinate sliding, \mathbf{w} does not point into the same direction as the classic jump $\llbracket \mathbf{u} \rrbracket$. Within the extended framework, the quantity \mathbf{w}^e represents the elastic part of \mathbf{w} , comparable but not to be confused with $\llbracket \mathbf{u} \rrbracket^e$ in the classic fiber concept. It is assumed that \mathbf{w}^e and \mathbf{w} are collinear. Hence, the elastic part can be expressed as

$$\mathbf{w}^e = \beta \mathbf{w}, \quad (4.30)$$

where β is any factor. According to Fig. 4.3 the length of the non-classic displacement

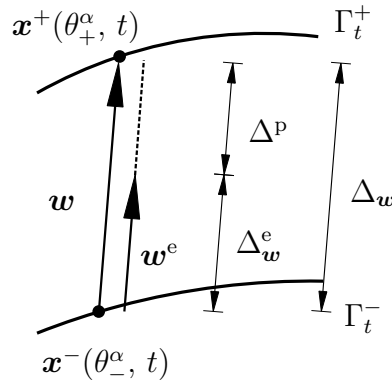


Figure 4.3: Current configuration of an opened cohesive zone with upper surface Γ_t^+ and lower surface Γ_t^- with the generalised fiber concept. The non-classic displacement jump \mathbf{w} (length Δ_w) is defined by $\mathbf{x}^+(\theta_+^\alpha, t)$ and $\mathbf{x}^-(\theta_-^\alpha, t)$ referring to different material coordinates.

jump reads

$$\Delta_w = \|\mathbf{x}^+(\theta_+^\alpha) - \mathbf{x}^-(\theta_-^\alpha)\| \neq \|\llbracket \mathbf{u} \rrbracket\|. \quad (4.31)$$

The corresponding elastic and plastic distances follow as

$$\|\mathbf{w}^e\| = \Delta_w^e = \beta \Delta_w \quad \text{and} \quad \Delta^p = \Delta_w - \Delta_w^e. \quad (4.32)$$

While the direction of the elastic portion \mathbf{w}^e is defined due to the collinearity with the non-classic jump \mathbf{w} , an interpretation of the relation between \mathbf{w}^p and the classic jump $[[\mathbf{u}]]$ is shown in Fig. 4.4. The plastic part of the generalised displacement is calculated

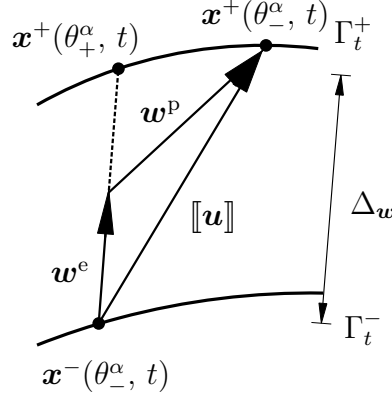


Figure 4.4: Current configuration of an opened cohesive zone with upper surface Γ_t^+ and lower surface Γ_t^- with the classic displacement jump $[[\mathbf{u}]]$. The corresponding decomposition into \mathbf{w}^e and \mathbf{w}^p referring to the generalised fiber concept (sliding of nodes) is sketched.

by

$$\mathbf{w}^p = [[\mathbf{u}]] - \mathbf{w}^e. \quad (4.33)$$

After combining all the introduced relations, Eq. (4.33) can be rewritten as

$$\mathbf{w}^p = \underbrace{\mathbf{x}^+(\theta_+^\alpha, t) - \mathbf{x}^-(\theta_-^\alpha, t)}_{[[\mathbf{u}]]} - \underbrace{\left(1 - \frac{\Delta_w^e}{\Delta_w}\right)}_{\beta \mathbf{w}} (\mathbf{x}^+(\theta_+^\alpha, t) - \mathbf{x}^-(\theta_-^\alpha, t)). \quad (4.34)$$

By including hardening effects, an isotropic Helmholtz energy of type

$$\Psi = \Psi^e(\Delta_w^e) + \Psi^p(\alpha) \quad (4.35)$$

is assumed. From Eq. (4.32) it follows that

$$\dot{\Delta}_w^e = \dot{\Delta}_w - \dot{\Delta}^p. \quad (4.36)$$

Inserting energy (4.35) together with relation (4.36) into the dissipation inequality leads to

$$\mathcal{D} = \mathbf{T}^- \cdot (\mathbf{v}^- - \mathbf{v}^+) - \frac{\partial \Psi}{\partial \Delta_w^e} \dot{\Delta}^p + \frac{\partial \Psi}{\partial \Delta_w} \dot{\Delta}_w + Q(\alpha) \dot{\alpha} \geq 0. \quad (4.37)$$

Here, $Q := -\partial_\alpha \Psi$ is the stress-like internal variable energetically conjugate to α . The assumption for the stress power $\mathcal{P} = \mathbf{T}^- \cdot (\mathbf{v}^- - \mathbf{v}^+) = \mathbf{T}^+ \cdot (\mathbf{v}^+ - \mathbf{v}^-)$ has been introduced

in Subsection 4.2.3. In contrast to the classic fiber concept, the material coordinates of the fiber starting and end point are allowed to slide along the θ^α -axes in the generalised framework. Hence, the material time derivative of the current coordinates is expressed by

$$\dot{\mathbf{x}}^-(\theta_-^\alpha, t) = \frac{\partial \mathbf{x}^-}{\partial t} + \frac{\partial \mathbf{x}^-}{\partial \theta_-^\alpha} \frac{d\theta_-^\alpha}{dt} = \mathbf{v}^- + \mathbf{g}_\alpha^- \dot{\theta}_-^\alpha \quad (4.38)$$

and

$$\dot{\mathbf{x}}^+(\theta_+^\alpha, t) = \frac{\partial \mathbf{x}^+}{\partial t} + \frac{\partial \mathbf{x}^+}{\partial \theta_+^\alpha} \frac{d\theta_+^\alpha}{dt} = \mathbf{v}^+ + \mathbf{g}_\alpha^+ \dot{\theta}_+^\alpha. \quad (4.39)$$

Due to the definition of $\Delta_{\mathbf{w}}$, cf. Eq. (4.31), its material time derivative is computed as

$$\dot{\Delta}_{\mathbf{w}} = \frac{(\mathbf{x}^+ - \mathbf{x}^-)}{\Delta_{\mathbf{w}}} \cdot (\dot{\mathbf{x}}^+ - \dot{\mathbf{x}}^-) = \frac{\mathbf{w}}{\Delta_{\mathbf{w}}} \cdot \left[(\mathbf{v}^+ + \mathbf{g}_\alpha^+ \dot{\theta}_+^\alpha) - (\mathbf{v}^- + \mathbf{g}_\alpha^- \dot{\theta}_-^\alpha) \right]. \quad (4.40)$$

By inserting relations (4.8), (4.38), (4.39) and (4.40) into Eq. (4.37), the dissipation takes the form

$$\left[\mathbf{T}^+ - \frac{\partial \Psi}{\partial \Delta_{\mathbf{w}}^e} \frac{\mathbf{w}}{\Delta_{\mathbf{w}}} \right] \cdot (\mathbf{v}^+ - \mathbf{v}^-) + \frac{\partial \Psi}{\partial \Delta_{\mathbf{w}}^e} \frac{\mathbf{w}}{\Delta_{\mathbf{w}}} \cdot (\mathbf{g}_\alpha^+ + \mathbf{g}_\alpha^-) \dot{c}^\alpha + \frac{\partial \Psi}{\partial \Delta_{\mathbf{w}}^e} \dot{\Delta}^p + Q(\alpha) \dot{\alpha} \geq 0. \quad (4.41)$$

Application of the Coleman-Noll procedure yields the constitutive relation

$$\mathbf{T}^+ = \frac{\partial \Psi}{\partial \Delta_{\mathbf{w}}^e} \frac{\mathbf{w}}{\Delta_{\mathbf{w}}} \quad (4.42)$$

and the reduced dissipation inequality

$$\mathbf{T}^+ \cdot (\mathbf{g}_\alpha^+ + \mathbf{g}_\alpha^-) \dot{c}^\alpha + \frac{\partial \Psi}{\partial \Delta_{\mathbf{w}}^e} \dot{\Delta}^p + Q(\alpha) \dot{\alpha} \geq 0. \quad (4.43)$$

According to Eq. (4.42) it can be concluded that the traction vector \mathbf{T}^+ is collinear to the generalised fiber \mathbf{w} . Therefore, it fulfills the balance of angular momentum as well as the principle of material frame indifference. Next, a physical interpretation of the considered terms in Eq. (4.43) is given. The first part is related to the sliding of the material coordinate \dot{c}^α and the general τ_α may be defined as

$$\tau_\alpha = \mathbf{T}^+ \cdot (\mathbf{g}_\alpha^+ + \mathbf{g}_\alpha^-). \quad (4.44)$$

Taking a closer look to the second part of (4.43), the derivative is expressed as

$$\frac{\partial \Psi}{\partial \Delta_{\mathbf{w}}^e} (\mathbf{m}_{\mathbf{w}} \cdot \mathbf{m}_{\mathbf{w}}) \dot{\Delta}^p = \mathbf{T}^+ \cdot \mathbf{m}_{\mathbf{w}} \dot{\Delta}^p, \quad (4.45)$$

where \mathbf{m}_w is defined as unit vector in the direction of the generalised fiber from $\mathbf{x}^-(\theta_-^\alpha, t)$ to $\mathbf{x}^+(\theta_+^\alpha, t)$, see Eq. (4.11). Introducing σ_m as

$$\sigma_m = \mathbf{T}^+ \cdot \mathbf{m}_w, \quad (4.46)$$

this quantity can be interpreted as the normal stress component within the fiber. The third part of (4.43) is related to hardening/softening effects. The reduced dissipation (4.43) can be rewritten as

$$\tau_\alpha \dot{c}^\alpha + \sigma_m \dot{\Delta}^p + Q(\alpha) \dot{\alpha} \geq 0. \quad (4.47)$$

If the crack surfaces Γ_t^- and Γ_t^+ are parallel then τ_α are tangential shear forces. From the reduced dissipation inequality (4.47) it follows that the fiber normal stress σ_m as well as the generalised shear stress component τ_α are driving forces for the evolution of plasticity.

The model is completed by choosing suitable evolution equations. A thermodynamically consistent framework a priori guaranteeing Ineq. (4.47) is provided by the concept of Generalised Standard Materials (GSM), cf. Halphen and Nguyen [39]. Within this framework, a convex plastic potential $g = g(\sigma_m, \tau_\alpha, Q; \dots)$ is introduced. The gradients of g define the evolution equations as

$$\dot{\Delta}^p = \lambda \frac{\partial g}{\partial \sigma_m}, \quad \dot{c}^\alpha = \lambda \frac{\partial g}{\partial \tau_\alpha} \quad \text{and} \quad \dot{\alpha} = \lambda \frac{\partial g}{\partial Q}, \quad (4.48)$$

where $\lambda \geq 0$ is the plastic multiplier. If potential g is convex and non-negative and contains the origin ($g(\mathbf{0}) = 0$), the dissipation inequality is automatically fulfilled. It bears emphasis that Δ^p , c^α and α are scalar-valued and, thus, their material time derivatives are material frame indifferent. In order to distinguish between fully elastic and elastoplastic deformations, a yield function ϕ is employed. Analogously to the plastic potential g , it depends on σ_m , τ_α and Q , i.e., $\phi = \phi(\sigma_m, \tau_\alpha, Q) \leq 0$. Based on the yield function, loading/unloading conditions can be defined in standard manner as:

$$\lambda \geq 0, \quad \phi \leq 0, \quad \lambda \phi = 0. \quad (4.49)$$

If the sliding of the material coordinates is avoided ($c^\alpha = 0$), the classic fiber concept with identical material coordinates for the starting and end point of the fiber is adopted. This represents a special case of the generalised model for which a consistent elastoplastic prototype model in line with the classic fiber theory is derived in the following section.

4.4 Consistent elastoplastic fiber model – prototype model of the generalised cohesive zone framework

According to Chapter 3, classic cohesive zone models can be interpreted as fiber models and none of the existing classic plasticity-based frameworks fulfills all fundamental requirements of continuum mechanics. So far in this chapter, a generalised framework which extends the classic fiber assumption has been used. In this section the general framework is simplified in the sense that the sliding of the material coordinates is prevented ($c^\alpha = 0$). This leads to the classic fiber concept with identical material coordinates for the corner points of the fiber ($\theta_+^\alpha = \theta_-^\alpha = \theta^\alpha$). In this range, a special case of an elastoplastic prototype fiber model fulfilling all fundamental requirements is presented. The key point of this derivation is the additive decomposition of the displacement jump into an elastic and a plastic part, i.e. $[[\mathbf{u}]] = [[\mathbf{u}]]^e + [[\mathbf{u}]]^p$. Starting with a Helmholtz energy of type

$$\Psi = \Psi([[\mathbf{u}]]^e) \quad (4.50)$$

hardening and softening effects are neglected for now. According to Eq. (3.17), balance of angular momentum in classic fiber models requires that the traction vector \mathbf{T} is collinear to $[[\mathbf{u}]]$. As shown in Subsection 3.5.1, an isotropic Helmholtz energy of the type

$$\Psi([[\mathbf{u}]]^e) = \Psi(\|[[\mathbf{u}]]^e\|) = \Psi(\Delta^e) \quad (4.51)$$

ensures collinearity between \mathbf{T} and $[[\mathbf{u}]]^e$. However, this is not sufficient in order to fulfill balance of angular momentum. Now, the next step is to enforce collinearity between $[[\mathbf{u}]]$ and its plastic part $[[\mathbf{u}]]^p$, see Fig. 4.5. Therefore, an evolution equation that implies

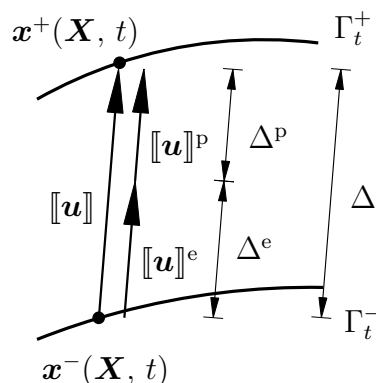


Figure 4.5: Current configuration of an opened cohesive zone with upper surface Γ_t^+ and lower surface Γ_t^- . The displacement jump $[[\mathbf{u}]]$ (length Δ) is decomposed into an elastic part $[[\mathbf{u}]]^e$ (length Δ^e) and a plastic part $[[\mathbf{u}]]^p$ (length Δ^p), that are both taken to be collinear to $[[\mathbf{u}]]$.

$[[\mathbf{u}]] \parallel [[\mathbf{u}]]^p$ has to be chosen. In such a case, $[[\mathbf{u}]]^e$ is collinear to $[[\mathbf{u}]]$ and \mathbf{T} is collinear to

$[[\mathbf{u}]]^e$ leading to the desired collinearity between $[[\mathbf{u}]]$ and \mathbf{T} . According to Fig. 4.5, the lengths of the respective proportions of $[[\mathbf{u}]]$ are given by

$$\Delta = \Delta^e + \Delta^p. \quad (4.52)$$

The direction \mathbf{m} of the displacement jump is introduced, i.e.,

$$\mathbf{m} = \frac{[[\mathbf{u}]]}{\Delta} \quad (4.53)$$

and due to collinearity, the different parts of the displacement jump are rewritten as

$$[[\mathbf{u}]] = \Delta \mathbf{m}, \quad [[\mathbf{u}]]^p = \Delta^p \mathbf{m} \quad \text{and} \quad [[\mathbf{u}]]^e = \Delta^e \mathbf{m}. \quad (4.54)$$

Following these preliminaries, a dissipative material response of the interface should now be considered. To be more precise, hardening and softening effects are accounted for. Therefore, a description with internal state variables is used. Within this framework, a Helmholtz energy of type

$$\Psi = \Psi^e(\Delta^e) + \Psi^p(\alpha) \quad (4.55)$$

is adopted, where α denotes a scalar-valued displacement-like internal variable. According to Eq. (4.55), the elastic response modelled by the first term Ψ^e is assumed to be completely independent of the internal hardening/softening processes reproduced by α . Besides, the second term Ψ^p represents the stored energy due to plastic work. With the additive decomposition $[[\mathbf{u}]] = [[\mathbf{u}]]^e + [[\mathbf{u}]]^p$ the dissipation inequality $\mathcal{D} = \mathcal{P} - \dot{\Psi} \geq 0$ can be written as

$$\mathcal{D} = \left(\mathbf{T} - \frac{\partial \Psi}{\partial [[\mathbf{u}]]^e} \right) \cdot [[\dot{\mathbf{u}}]] + \frac{\partial \Psi}{\partial [[\mathbf{u}]]^e} \cdot [[\dot{\mathbf{u}}]]^p + Q(\alpha) \dot{\alpha} \geq 0. \quad (4.56)$$

In line with the previous section, $Q := -\partial_\alpha \Psi$ is the stress-like internal variable energetically conjugate to α . Application of the Coleman-Noll procedure defines the traction vector

$$\mathbf{T} = \frac{\partial \Psi}{\partial [[\mathbf{u}]]^e} = \frac{\partial \Psi^e}{\partial \Delta^e} \frac{[[\mathbf{u}]]^e}{\Delta^e} \quad (4.57)$$

and the reduced dissipation inequality then becomes

$$\mathbf{T} \cdot [[\dot{\mathbf{u}}]]^p + Q(\alpha) \dot{\alpha} \geq 0. \quad (4.58)$$

Considering collinearity between $[[\mathbf{u}]]^e$, $[[\mathbf{u}]]^p$ and $[[\mathbf{u}]]$, cf. Fig. 4.5, enables a further simplification of the reduced dissipation inequality and a derivation of evolution equations

complying with the second law of thermodynamics. The definitions in Eq. (4.54) allow the derivation of the material time derivative of $[[\mathbf{u}]]^P$ as

$$[[\dot{\mathbf{u}}]]^P = \dot{\Delta}^P \mathbf{m} + \dot{\mathbf{m}} \Delta^P. \quad (4.59)$$

Inserting Eq. (4.59) into the reduced dissipation inequality (4.58) yields

$$(\mathbf{T} \cdot \mathbf{m}) \dot{\Delta}^P + (\mathbf{T} \cdot \dot{\mathbf{m}}) \Delta^P + Q(\alpha) \dot{\alpha} \geq 0. \quad (4.60)$$

Since \mathbf{m} is a unit vector, its time derivative is orthogonal to \mathbf{m} . Using the collinearity between \mathbf{m} and \mathbf{T} , the second term in Eq. (4.60) vanishes ($\dot{\mathbf{m}} \perp \mathbf{T}$). By further introducing the notation $\sigma_m := \mathbf{T} \cdot \mathbf{m}$, the reduced dissipation inequality simplifies to

$$\sigma_m \dot{\Delta}^P + Q(\alpha) \dot{\alpha} \geq 0. \quad (4.61)$$

If the classic cohesive zone model is interpreted as a fiber model, σ_m denotes the normal stress in the classic fiber direction from $\mathbf{x}^-(\mathbf{X}, t)$ to $\mathbf{x}^+(\mathbf{X}, t)$. Clearly, Ineq. (4.61) follows as a special case of the general dissipation inequality (4.47) if sliding is prevented ($\dot{\alpha} = 0$). Thus, this prototype model constitutes a simplified type of the generalised framework in line with the classic cohesive zone framework.

Now the model is completed by choosing suitable evolution equations. According to the previous section, the concept of Generalised Standard Materials (GSM), cf. Halphen and Nguyen [39] is adopted. The convex plastic potential $g(\sigma_m, Q)$ is introduced whose gradients define the evolution equations, i.e.,

$$\dot{\Delta}^P = \lambda \frac{\partial g}{\partial \sigma_m} \quad (4.62)$$

and

$$\dot{\alpha} = \lambda \frac{\partial g}{\partial Q}. \quad (4.63)$$

Again, $\lambda > 0$ is the plastic multiplier. It bears emphasis that Δ^P and α are scalar-valued and, thus, their material time derivatives are material frame indifferent. In order to distinguish between fully elastic and elastoplastic deformations, a yield function ϕ is employed. Analogously to the plastic potential g , it depends on σ_m and Q , i.e., $\phi = \phi(\sigma_m, Q) \leq 0$. Based on the yield function, loading/unloading conditions can be defined in standard manner as

$$\lambda \geq 0, \quad \phi \leq 0, \quad \lambda \phi = 0. \quad (4.64)$$

4.4.1 Elastoplastic prototype model

In line with the theory presented in Section 4.4 a prototype model of the type

$$\Psi(\Delta, \Delta^p, \alpha) = \frac{1}{2} c (\Delta^e)^2 + \Psi^p(\alpha) \quad (4.65)$$

is chosen within the numerical computations presented in Section 4.7. The elastic part Ψ^e is assumed to be quadratic. Since this model represents a fiber model, c is interpreted as the elastic stiffness of the fiber, respectively the spring, connecting $\mathbf{x}^-(\mathbf{X}, t)$ and $\mathbf{x}^+(\mathbf{X}, t)$. Concerning the yield function, the choice

$$\phi(\sigma_m, Q) = \sigma^{\text{eq}} - (Q_0 + Q) \quad (4.66)$$

is made, where σ^{eq} is a positively homogeneous function of degree one and where Q_0 is the initial yield strength of the interface. In the following, an equivalent stress of the type

$$\sigma^{\text{eq}} = |\sigma_m| \quad (4.67)$$

is adopted. By considering associative evolution equations, i.e. $g = \phi$, it follows that

$$\dot{\Delta}^p = \lambda \text{sign}(\sigma_m) \quad (4.68)$$

and

$$\dot{\alpha} = -\lambda = -\dot{\Delta}^p \text{sign}(\sigma_m). \quad (4.69)$$

The plastic part in Eq. (4.65) is represented by an exponential softening model of the type

$$\Psi^p(\alpha) := \mathcal{G}_f \left[1 - \text{Exp} \left(\frac{\alpha Q_0}{\mathcal{G}_f} \right) \right] + Q_0 \alpha, \quad (4.70)$$

and the stress-like internal variable

$$Q = -\frac{\partial \Psi^p}{\partial \alpha} = -Q_0 \left[1 - \text{Exp} \left(\frac{\alpha Q_0}{\mathcal{G}_f} \right) \right], \quad (4.71)$$

where \mathcal{G}_f denotes the fracture energy.

Remark 7 *The fracture energy \mathcal{G}_f follows from the time integration of the stress power $\mathcal{P} = \mathbf{T} \cdot \llbracket \dot{\mathbf{u}} \rrbracket$ as*

$$\mathcal{G}_f = \int_{t=0}^{\infty} \mathbf{T} \cdot \llbracket \dot{\mathbf{u}} \rrbracket dt = \int_{t=0}^{\infty} (\dot{\Psi} + \mathcal{D}) dt. \quad (4.72)$$

According to the presented prototype model from Subsection 4.4.1 the yield function is homogeneous of degree one, leading to a dissipation $\mathcal{D} = \lambda Q_0$. Finally, one obtains the fracture energy as

$$\int_{\alpha=0}^{-\infty} \left(\frac{\partial \Psi^p}{\partial \alpha} - Q_0 \right) d\alpha = \mathcal{G}_f. \quad (4.73)$$

4.4.2 Prototype model including damage

The mechanical properties of the novel elastoplastic prototype model are analysed at the end of this chapter. For the sake of comparison, computations based on a standard isotropic damage cohesive zone model, cf. [84], characterised by Helmholtz energy

$$\Psi(\Delta) = (1 - d) \Psi^e = (1 - d) \frac{1}{2} c \Delta^2 \quad (4.74)$$

are also employed. The material parameters of this model (elastic stiffness of the interface c , fracture energy \mathcal{G}_f and strength Q_0) are chosen according to those of the advocated elastoplastic model, see Subsection 4.4.1.

According to the theory presented in Section 3.4, the isotropic damage variable $d \in [0, 1]$ indicates for $d = 0$ the virgin material, while $d = 1$ is associated with the totally damaged material. In line with the elastoplastic prototype model, c denotes the elastic stiffness of the interface (corresponding to the virgin material). Since d is energetically conjugate to the Helmholtz energy of the virgin material, which in turn depends only on the displacement jump, thermodynamical arguments suggest a damage evolution of the type $d = d(\Delta)$, cf. Section 3.4. However, since the displacement jump is not necessarily monotonic in nature, $d = d(\Delta)$ could lead to self-healing of the material. In order to avoid this, a history variable κ is introduced by means of

$$\kappa(t_{n+1}) = \max\{\kappa(t_n), \Delta(t_{n+1})\}, \quad \kappa(t_0) = \kappa_0. \quad (4.75)$$

The model is completed by a suitable damage evolution law $d = d(\kappa)$, i.e.,

$$d(\kappa) = 1 - \frac{\kappa_0}{\kappa} \text{Exp} \left[-(\kappa - \kappa_0) \frac{Q_0}{\mathcal{G}_f} \right]. \quad (4.76)$$

Here, κ_0 denotes the amplitude of the displacement jump necessary for damage initiation, Q_0 is the strength of the interface (similar to the yield stress for the elastoplastic model) and \mathcal{G}_f represents the fracture energy.

4.5 Novel unloading approach

As far as unloading is concerned, closing of interfaces always requires special attention. Otherwise a non-physical penetration between Γ^- and Γ^+ can occur. A careful review on this problem can be found in literature on contact mechanics. The interested reader is referred to Laursen [54], Wriggers [104]. However, this general problem is not the focus of this work. For this reason, a simple penalty formulation is employed. To be more precise, in the case of penetration, i.e., if $[[\mathbf{u}]] \cdot \bar{\mathbf{n}} < 0$, the interface is assumed to have regained its initial elastic stiffness. However, penetration of the surfaces Γ_t^+ and Γ_t^- is not the only critical problem to be considered.

4.5.1 Preliminaries

As shown in Chapter 3, classic cohesive zone models are fiber models where the traction points into the direction of the fiber, respectively the displacement jump $[[\mathbf{u}]]$. During the opening process of an interface, the fiber is loaded under tension and elastic and plastic deformation parts are collinear, see Section 4.4. Following the previous plasticity concepts, the traction-separation diagram for a representative fiber is shown in Fig. 4.6. Combining the yield criterion with the equivalent stress leads to an isotropic softening

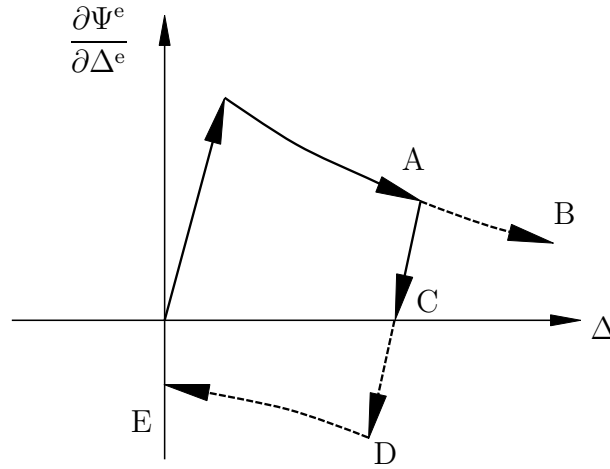


Figure 4.6: Intuitively unphysical traction-separation diagram for the fiber model; thin fibers could not bear compressive stresses (hypothetical load path between CE); furthermore, in point E the direction of the displacement jump is not defined.

model, sketched out in the load path to point A. If loading were continued, it would follow path AB. On the contrary, unloading of the fiber follows path AC to the stress free state of the fiber, where its displacement is fully plastic, e.g. $\Delta = \Delta^p$. The slope of this path is parallel to the initial slope of the elastic area. Following path CD, further unloading results in $\Delta^e < 0$, which would generate compressive stresses within the fiber. Due to isotropic softening, plasticity would again be activated at point D and it would follow

path DE which corresponds to AB. Following such an unloading behaviour, one obtains a singularity in point E. The displacement jump vanishes and consequently its direction \mathbf{m} and traction vector \mathbf{t} are not defined. Physically speaking, this corresponds to a fiber compressed to one point, where the direction of the respective force is not defined. For this reason, a fiber model requires $\mathbf{t}(\llbracket \mathbf{u} \rrbracket = \mathbf{0}) = \mathbf{0}$. Furthermore, thin fibers cannot bear compressive stresses without buckling. Hence, a novel physical meaningful unloading behaviour is introduced in the following.

4.5.2 Novel unloading behaviour - wrinkling of fibers

A physically sound unloading model can be motivated by considering the physical properties of fibers: If a thin fiber is loaded under compression, it buckles. If one further assumes a vanishing bending stiffness (sufficiently thin fibers), compressive stresses are inadmissible. Similar ideas have also been successfully applied in order to study wrinkling in membranes, cf. Epstein [26], Mosler and Cirak [67], Pipkin [81, 82, 83]. Application of this assumption leads to the traction-separation diagram in Fig. 4.7, where load path

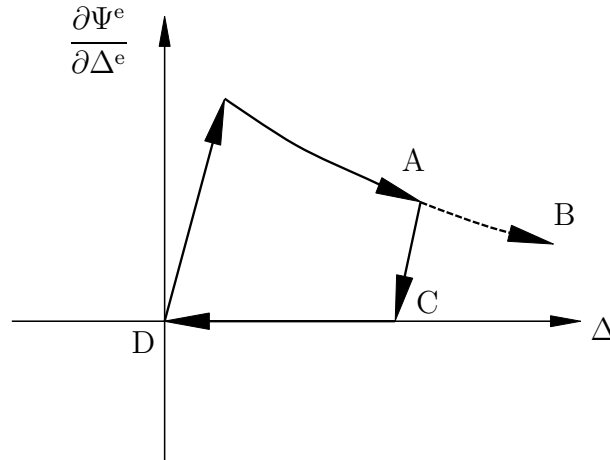


Figure 4.7: Load displacement diagram of the novel unloading model related to fiber wrinkling with stress free relaxation of the fiber to the deformation free state (load path CD).

CD captures the stress free relaxation of the fiber to the deformation free state with $\mathbf{t}(\llbracket \mathbf{u} \rrbracket = 0) = \mathbf{0}$. Wrinkling in membranes is captured by a wrinkling strain. In analogy thereto, a wrinkling proportion $\llbracket \mathbf{u} \rrbracket^w$ adjusts the displacement jump in the case of unloading, i.e.,

$$\llbracket \mathbf{u} \rrbracket = \llbracket \mathbf{u} \rrbracket^e + \llbracket \mathbf{u} \rrbracket^p - \llbracket \mathbf{u} \rrbracket^w. \quad (4.77)$$

Thereby, the buckling of fibers under compression is captured in the presented cohesive zone framework. In analogy to Section 4.4, all proportions of the displacement jump are collinear leading to the additive decomposition

$$\Delta = \Delta^e + \Delta^p - \Delta^w, \quad (4.78)$$

where $\Delta^w := \|\llbracket \mathbf{u} \rrbracket^w\|$. The underlying idea of the wrinkling portion of Δ is sketched out in Fig. 4.8. First, a fiber is loaded under tension and the fiber displacement decomposes

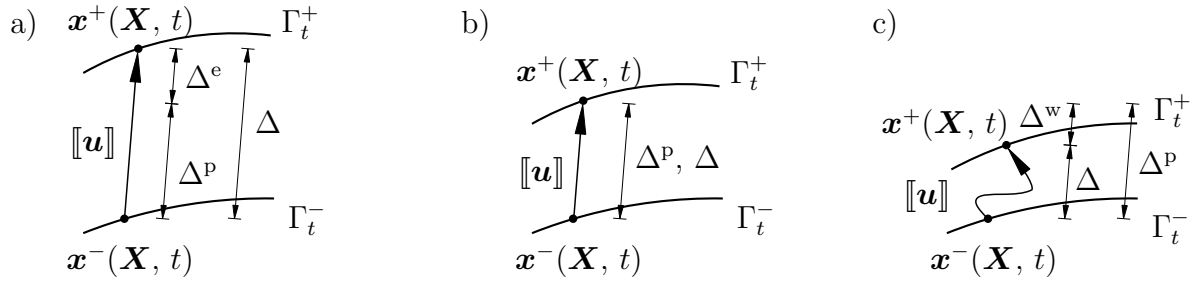


Figure 4.8: Graphical explanation for the unloading process within the fiber model including wrinkling: a) a fiber under tensile loading where the fiber stretch decomposes into an elastic and a plastic part; b) unloading of the fiber to the stress free state, where the fiber stretch is purely plastic; c) a further compression of the fiber would result in a negative elastic stretch $\Delta^e < 0$, respectively in a compressive stress. However, this does not seem to be realistic since thin fibers would show buckling and consequently vanishing stresses. The wrinkling approach precisely depicts this process by enforcing vanishing stresses through $\Delta^e = \Delta - \Delta^p + \Delta^w = 0$. Since under compression it holds that $\Delta - \Delta^p < 0$, the condition $\Delta^w > 0$ has to be fulfilled.

into an elastic and a plastic part, e.g. $\Delta = \Delta^e + \Delta^p$, see Fig. 4.8 a). Then the fiber undergoes elastic unloading until the hole deformation is purely plastic, e.g. $\Delta = \Delta^p$, see Fig. 4.8 b). According to Subsection 4.5.1, compressive stresses within the fiber due to $\Delta^e < 0$ should be excluded since the fiber would start to buckle. This process is precisely captured by the wrinkling related stretching part of the fiber Δ^w . Physically speaking, Δ^w describes the change in the length of the fiber under buckling. Since under compression of the fiber it holds that $\Delta - \Delta^p < 0$, the condition

$$\Delta^w \geq 0 \quad (4.79)$$

is implied, see Fig. 4.8 c). Inserting Eq. (4.78) into the Helmholtz energy density of the elastoplastic prototype model (4.65) gives

$$\Psi(\Delta, \Delta^p, \Delta^w, \alpha) = \Psi^e(\Delta^e) + \Psi^p(\alpha). \quad (4.80)$$

As shown in [26, 67, 81–83] this potential includes the wrinkling conditions in a variational format. To be more explicit, the wrinkling/buckling displacement jump can be computed by minimising Eq. (4.80) subjected to the constraint (4.79), i.e.,

$$\Delta^w = \arg \inf_{\Delta^w \geq 0} \Psi(\Delta, \Delta^p, \Delta^w, \alpha). \quad (4.81)$$

This can be seen by computing the necessary condition for stationarity resulting in

$$\frac{\partial \Psi}{\partial \Delta^w} = \frac{\partial \Psi^e}{\partial \Delta^w} = \frac{\partial \Psi^e}{\partial \Delta^e} = \sigma_m \geq 0. \quad (4.82)$$

Accordingly, the variational principle (4.81) naturally enforces tensile stresses.

A closed-form solution of the variational problem (4.81) providing further insights can be derived by enforcing the following two physically sound constraints:

- (1) $\Psi^e(\Delta^e) = 0 \Leftrightarrow \Delta^e = 0$,
- (2) $\Psi^e(\Delta^e)$ is monotonically increasing.

Suppose $\Delta - \Delta^p < 0$. Without buckling, this case would correspond to compressive stresses in the fiber. With $\Delta^w \geq 0$, the closed-form solution of the variational problem (4.81) reads

$$\Delta - \Delta^p < 0 \quad \Rightarrow \quad \Delta^w = \Delta^p - \Delta > 0, \Delta^e = 0, \Psi^e = 0, \sigma_m = 0. \quad (4.83)$$

The closed-form solution in the case of a positive elastic part of the jump reads

$$\Delta - \Delta^p > 0 \quad \Rightarrow \quad \Delta^w = 0, \Delta^e = \Delta - \Delta^p > 0, \Psi^e > 0, \sigma_m > 0. \quad (4.84)$$

Wrinkling is therefore not active. The solution follows from the monotony of Ψ^e , i.e., $\Delta^w > 0$ would lead to a further increase in energy.

4.6 Variational structure of the cohesive zone framework

As shown in the previous section, buckling of the fibers can be written in a variational format. For a broad range of different plasticity models such a variational structure also exists, cf. Section 2.3. For this reason, the combination of fiber buckling and fiber plasticity could have a variational structure as well. For wrinkling in membranes the variational structure was shown in Mosler and Cirak [67].

In order to derive a variational structure and in line with [67], the stress power $\mathcal{P} = \mathbf{T} \cdot \dot{[\mathbf{u}]} = \dot{\Psi} + \mathcal{D}$ of the model is considered. Assuming associative evolution equations and a yield function given by Eq. (4.66), combined with the equivalent stress (4.67), the dissipation reduces to $\mathcal{D} = \lambda Q_0 \geq 0$ and the stress power can then be written as

$$\mathcal{P} = \dot{\Psi} + \lambda Q_0. \quad (4.85)$$

According to Eq. (2.89) for classic bulk materials, the interface stress power (4.85) can be interpreted as a functional in terms of $[[\dot{\mathbf{u}}]]$, λ and $\dot{\Delta}^w$, i.e.,

$$\mathcal{E}([[\dot{\mathbf{u}}]], \dot{\Delta}^w, \lambda) = \dot{\Psi}([[\dot{\mathbf{u}}]], \dot{\Delta}^w, \lambda) + \lambda Q_0. \quad (4.86)$$

The variational structure

$$(\dot{\Delta}^w, \lambda) = \arg \operatorname{stat}_{\{\dot{\Delta}^w \geq 0, \lambda \geq 0\}} \mathcal{E}([[\dot{\mathbf{u}}]], \dot{\Delta}^w, \lambda) \quad (4.87)$$

can be shown by computing the stationary conditions. With

$$\dot{\Psi} = \sigma_m \left(\dot{\Delta} - \dot{\Delta}^p + \dot{\Delta}^w \right) - Q \dot{\alpha} = \sigma_m \left(\dot{\Delta} - \lambda \partial_{\sigma_m} \phi + \dot{\Delta}^w \right) + Q \lambda \quad (4.88)$$

the stationary conditions associated with Eq. (4.87) result in

$$\frac{\partial \mathcal{E}}{\partial \lambda} = -\sigma_m \partial_{\sigma_m} \phi + Q + Q_0 = -\phi \geq 0 \quad (4.89)$$

and

$$\frac{\partial \mathcal{E}}{\partial \dot{\Delta}^w} = \sigma_m \geq 0. \quad (4.90)$$

Accordingly, the model is indeed variational, i.e., it contains the yield function (4.89) as well as the constraint corresponding to buckling of the fibers (4.90). Furthermore, the reduced energy

$$\mathcal{E}_{\text{red}}([[\dot{\mathbf{u}}]]) = \inf_{\dot{\Delta}^w \geq 0, \lambda \geq 0} \mathcal{E}([[\dot{\mathbf{u}}]], \dot{\Delta}^w, \lambda) \quad (4.91)$$

serves as a quasi hyperelastic potential defining the stress state via

$$\mathbf{T} = \frac{\partial \mathcal{E}_{\text{red}}([[\dot{\mathbf{u}}]])}{\partial [[\dot{\mathbf{u}}]]}. \quad (4.92)$$

In addition to its elegance, the presented variational framework implies an efficient numerical implementation. In order to derive such an implementation, the time-continuous functional $\mathcal{E}([[\dot{\mathbf{u}}]], \lambda, \dot{\Delta}^w)$ is discretised in time (time interval $t \in [t_n; t_{n+1}]$) leading to the time-discrete approximation

$$\bar{\mathcal{I}}([[\mathbf{u}]]_{n+1}, \Delta \lambda, \Delta_{n+1}^w) = \int_{t_n}^{t_{n+1}} \mathcal{E}([[\dot{\mathbf{u}}]], \lambda, \dot{\Delta}^w) dt = \Psi_{n+1} - \Psi_n + \Delta \lambda Q_0, \quad (4.93)$$

where $\Delta\lambda := \int_{t_n}^{t_{n+1}} \lambda \, dt$. The discrete counterparts corresponding to the stationary conditions (4.89) and (4.90) of the time-continuous problem are

$$\frac{\partial \bar{\mathcal{I}}}{\partial \Delta\lambda} = - [\sigma_m \partial_{\sigma_m} \phi]_{|_{n+1}} + Q|_{n+1} + Q_0 = -\phi_{n+1} \geq 0 \quad (4.94)$$

and

$$\frac{\partial \bar{\mathcal{I}}}{\partial \Delta^w} = \sigma_m|_{n+1} \geq 0. \quad (4.95)$$

Within the numerical implementation, such implicit constraints are solved by means of a classic predictor-corrector algorithm similar to the one advocated in [67]. In the case of plastic loading or buckling, the implicit problems $\phi_{n+1} = 0$ and $\sigma_m|_{n+1} = 0$ are solved by means of a Newton iteration giving asymptotically a quadratic convergence. Finally, the stress update is performed in the standard manner

$$\mathbf{T} = \frac{\partial}{\partial \llbracket \mathbf{u} \rrbracket_{n+1}} \left\{ \inf_{\Delta\lambda \geq 0, \Delta_{n+1}^w \geq 0} \bar{\mathcal{I}} \right\}. \quad (4.96)$$

4.7 Numerical examples

This section deals with numerical structural analyses. Such analyses serve two purposes. First, efficiency and accuracy of the proposed numerical implementation is checked. Secondly and more importantly, the mechanical properties characterising the novel fiber-like cohesive zone model are studied. For all computations, the L-shape shown in Fig. 4.9 is considered. While quadratic displacement-driven 10-node tetrahedron finite elements, together with a standard neo-Hooke-type model, are employed for the bulk material, the novel interface model is incorporated into standard quadratic displacement-driven 12-node interface models (6 nodes on each side), cf. Ortiz and Pandolfi [72]. The material parameters of the cohesive zone model summarised in Fig. 4.9 correspond to the prototype presented in Subsection 4.4.1 and the elastic parameters (μ and λ) are identical to those adopted in Radulovic et al. [84]. According to the employed interface implementation [72], cohesive zones can only open between existing bulk elements and, thus, the geometry of the cohesive zones is biased by the finite element discretisation. However, it bears emphasis that the respective constitutive model can also be implemented within the framework of the embedded strong discontinuity approach or the extended finite element method not showing this bias, cf. [84]. In any case, the mesh bias is not the focus of this work. First, the influence of the discretisation is analysed. For that purpose, the L-shape is computed with a coarse mesh (see Fig. 4.10 left) and with a fine mesh (see Fig. 4.10 right). Figure 4.10 shows the deformed configurations (displacements are magnified). It can be seen that both meshes lead to a curved cohesive zone surface, similar to the geometry reported in [84]. Furthermore, the mesh bias is almost negli-

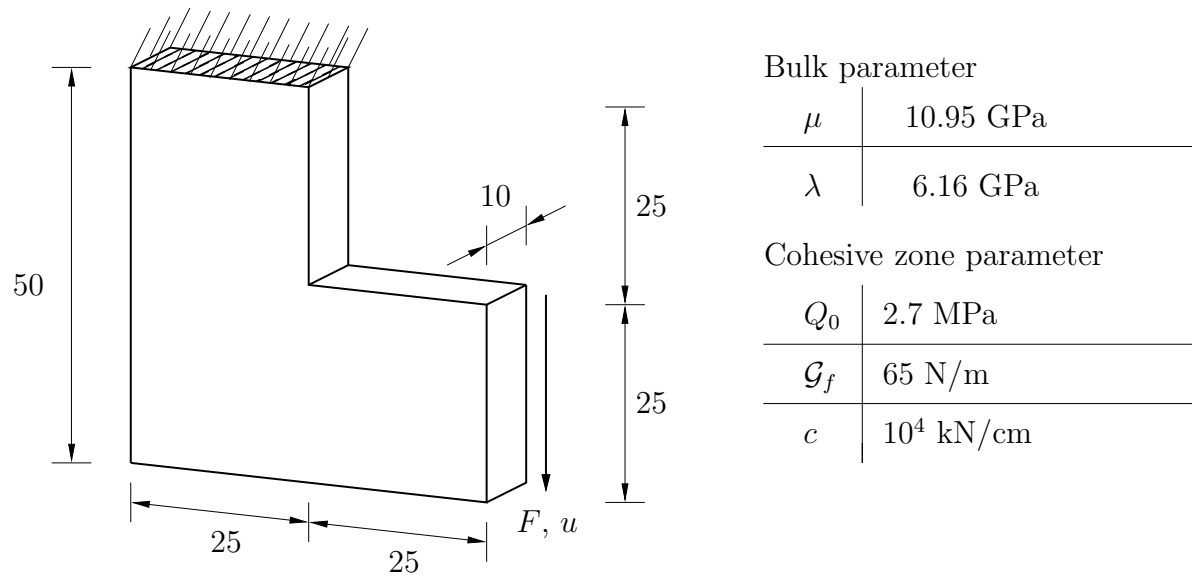


Figure 4.9: L-shaped structure: dimensions [cm], boundary conditions and material parameters (see Eq. (4.70)) used within the numerical analysis, cf. [84].

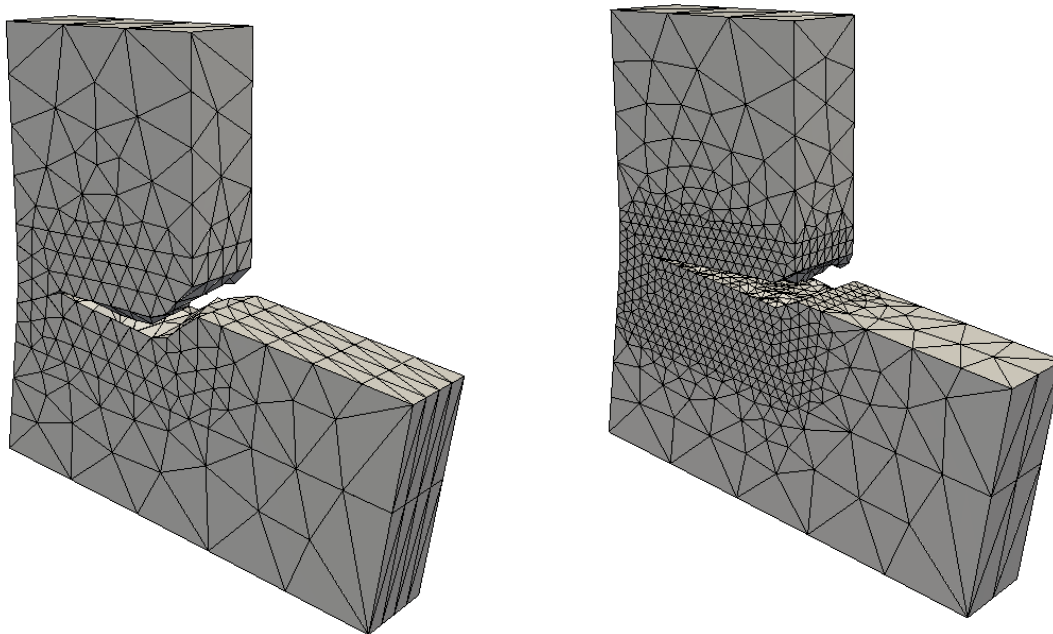


Figure 4.10: L-shaped structure: deformed discretisations as computed by means of the proposed cohesive zone model. left: coarse mesh; right: fine mesh. The geometry and the material parameters are summarised in Fig. 4.9. magnification factor: 150

gible for the two different tetrahedron discretisations. The load-displacement diagrams corresponding to the two computations are summarised in Fig. 4.11. Again, only a slight

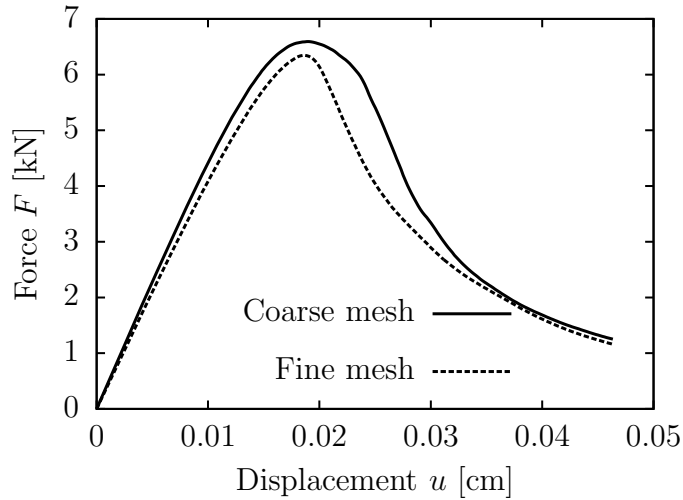


Figure 4.11: L-shaped structure: load-displacement diagrams as computed by means of the proposed cohesive zone model: coarse mesh (continuous line) and fine mesh (dashed line). The geometry and the material parameters are summarised in Fig. 4.9.

influence of the discretisation on the predicted mechanical response can be observed.

The properties of the novel cohesive zone model are then studied. Since the coarse mesh and the fine mesh lead to almost identical results, only the coarser mesh is considered in the following. For comparison purposes, the computations are also performed by using the scalar-valued damage cohesive zone presented in Subsection 4.4.2. The material parameters of this model (elastic stiffness of the interface, fracture energy and strength) are chosen according to those of the respective elastoplastic model.

A comparison between the elastoplastic model and the classic damage model shows that both models lead to exponential softening during loading. Furthermore, both predict the same strength of the interface and the same fracture energy. As a matter of fact, the damage evolution (4.76) has been designed such that both models lead to identical results for monotonic loading and for a uniaxial stress state. For this reason, major differences between both models are expected only during unloading. In order to activate local unloading, the L-shape is first loaded and subsequently, displacement-driven unloaded.

The deformed L-shaped structures as predicted by the two constitutive models are shown in Fig. 4.12. Such configurations correspond to the maximum prescribed displacement $u_{\max} = 0.025$ cm. It can be seen that both constitutive models lead to almost

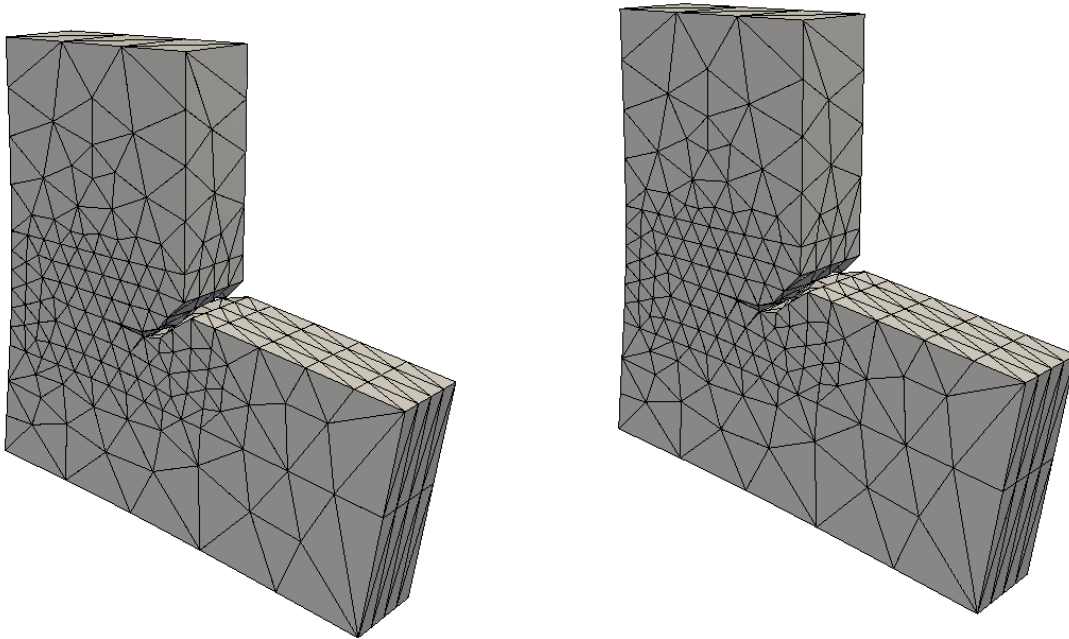


Figure 4.12: L-shaped structure: deformed configuration as computed by means of the proposed cohesive zone model (left diagram) compared to the deformed configuration as computed by means of a scalar-valued damage model (right diagram). The geometry and the material parameters are summarised in Fig. 4.9. magnification factor: 250

identical results. This is not surprising, since the local deformation paths which the material points experience are monotonic (almost no unloading). Consequently, the differences between elastoplasticity and damage theory are not pronounced. Similarly, the predicted load-displacement diagrams corresponding to the two different models also agree reasonably, see Fig. 4.13. While this is expected for loading, the good agreement for unloading seems to be surprising at first glance. To be more precise, the results obtained by the novel elastoplastic cohesive zone models look counterintuitive. For instance, no plastic deformations remain after unloading. The reason for this non-standard behaviour seems to be related to the buckling mode included in the model: In the case of unloading, the tensile stresses within the opened cohesive zones decrease and finally, the buckling kinematics is active leading to zero stresses – as for a fully damaged material point. This conjecture is confirmed by means of Fig. 4.14. As can be seen, some material points show the unloading behaviour according to classic elastoplasticity (picture at the bottom right in Fig. 4.14), while other material points show wrinkling (picture at the top right in Fig. 4.14). The global structural unloading response is thus a superposition of these two different effects.

The aforementioned superposition is explained schematically in Fig. 4.15 and in Fig. 4.16. Figure 4.15 depicts local loading-unloading diagrams in the equivalent traction-displacement-jump space for two different material points (upper and lower row). The horizontal axis is associated with time. Accordingly, the first material point

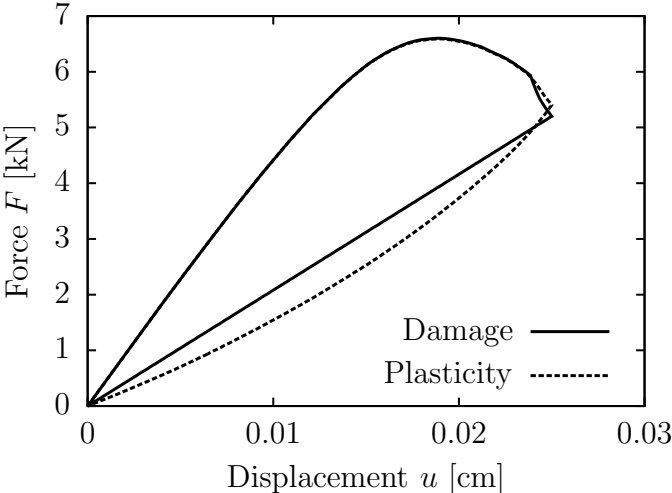


Figure 4.13: L-shaped structure: load-displacement diagram as computed by means of the proposed cohesive zone model (continuous line) compared to the load-displacement diagram as computed by means of a scalar-valued damage model (dashed line). The geometry and the material parameters are summarised in Fig. 4.9.

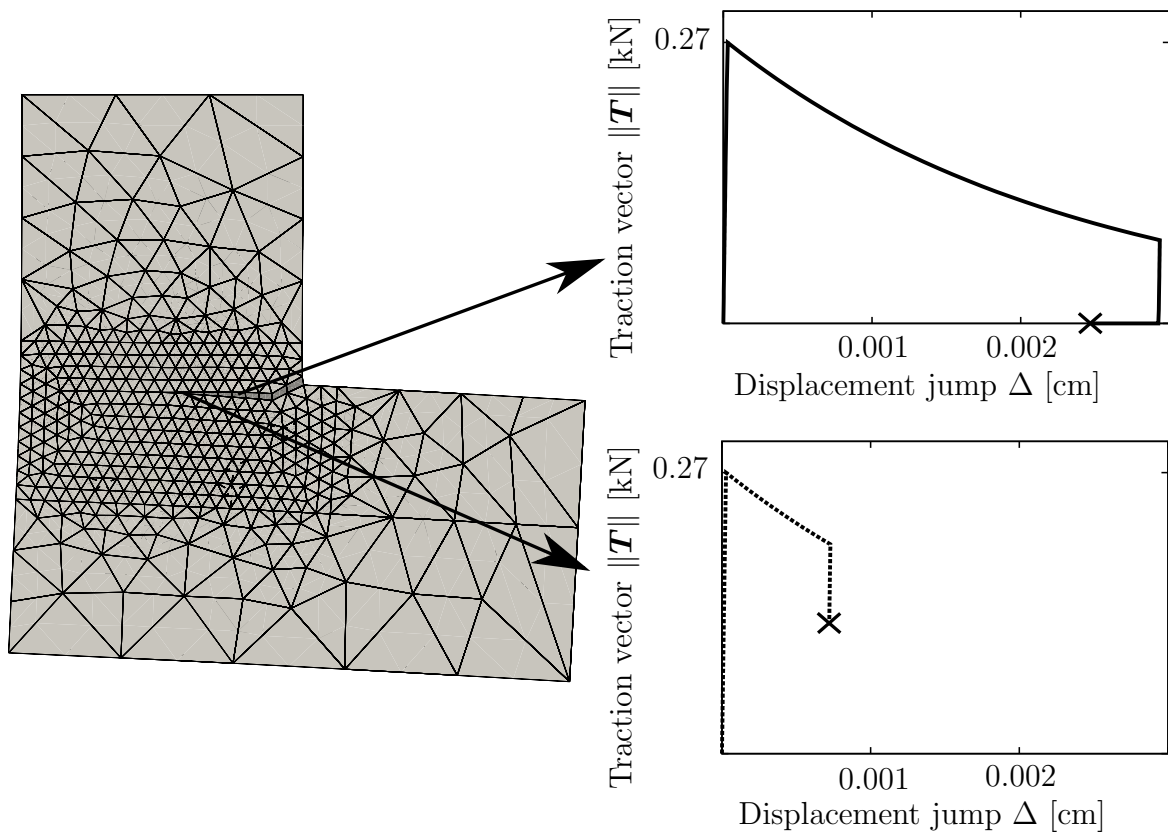


Figure 4.14: L-shaped structure: (left) deformed structure and visualisation of the crack; (right) equivalent traction separation diagram for two different Gauss points on the crack; (top right) Gauss point showing unloading according to wrinkling in the final state; (bottom right): Gauss point showing unloading according to plasticity theory in the final state

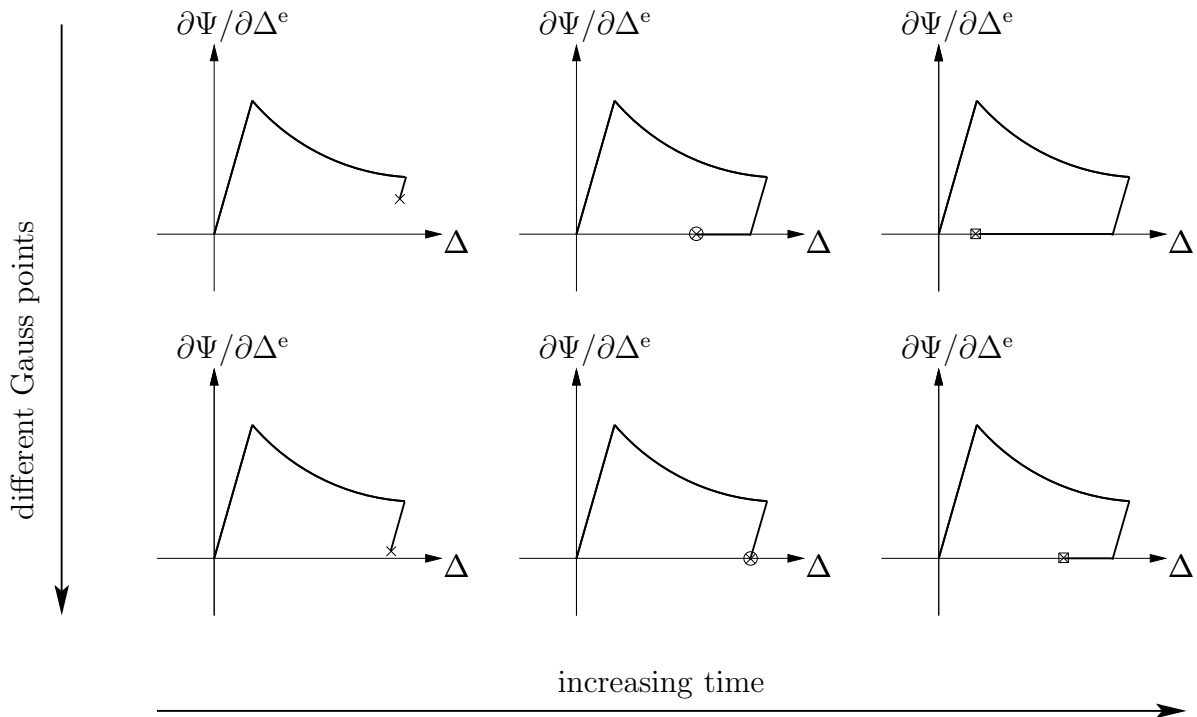


Figure 4.15: Schematic local load-displacement diagrams (equivalent traction vs. equivalent displacement jump) for two different Gauss points (upper and lower row) at three different time steps (from left to right)

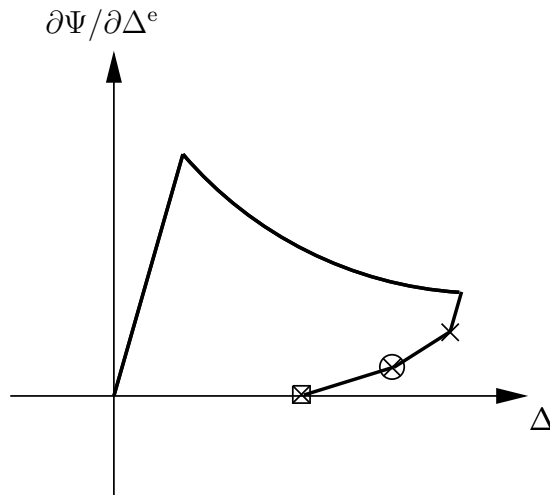


Figure 4.16: Schematic illustration of the structural response by means of a load-displacement diagram resulting from the local loading-unloading behaviour of two different material points according to Fig. 4.15

(upper row) unloads in line with elastoplasticity theory in the first time step (upper left diagram). Subsequently, wrinkling is observed (middle and right upper diagrams). Similarly, the second material point follows the classic elastoplastic unloading behaviour in the first time step (bottom left diagram). During the second time step (bottom middle diagram), the same elastoplastic unloading behaviour is observed. Only during the final step (bottom right diagram) wrinkling is active. If these two material points belong to the same structure, the structural response is conceptually obtained by superposition of the different diagrams. Such a superposition is shown in Fig. 4.16. In line with the behaviour of the two material points, the standard elastoplastic unloading behaviour can also be seen at the structural level during the first loading stage. Likewise, wrinkling-like behaviour is visible for the third loading step. However, the interesting loading step is step two, where the different material points correspond to different unloading responses, see the middle diagrams in Fig. 4.15. In this case, superposition leads to a smooth transition between elastoplasticity and damage theory (the circle in Fig. 4.16). This is precisely the effect explaining the diagram in Fig. 4.13.

5 Consistent cohesive zone framework II – coupling with surface elasticity

This chapter presents a generalised consistent interface framework based on an extended stress power assumption. To be more precise, the change of the structural tensors is accounted for in this chapter. This results in a further stress contribution besides the classic traction vector within the interface.

The idea is to combine the framework of classic non-coherent interfaces investigated in the previous chapter with the theory of coherent interfaces. The general framework for coherent interfaces is based on surface elasticity established by Gurtin [34, 35], Gurtin and Murdoch [36], Murdoch [69] and further developed by Steinmann [94], Javili et al. [49], Kaessmair et al. [52] and recently by Javili et al. [51]. The combination of the cohesive zone and coherent interface theory was first established in Ottosen et al. [77], see also Javili et al. [50] and Javili [47]. The change of structural tensors is considered within the stress power. Thereby, the derived interface framework is thermodynamically consistent and allows the investigation of shear and anisotropic effects what is not the case for classic cohesive zone fiber models.

After a short introduction to the generalised kinematics in Section 5.1, the balance laws for the generalised interface framework are derived from a variational point of view in Section 5.2. Subsequently, the framework is extended with an anisotropic damage model and a quasi-brittle prototype model is introduced in Section 5.3. Afterwards, the numerical implementation of the proposed framework is introduced. At the end of this chapter, numerical investigations are presented that show the advantages of the extended interface framework in contrast to classic cohesive zone models.

5.1 Kinematics of coherent interfaces - introduction to surface elasticity

This section introduces the kinematics of surfaces, respectively coherent interfaces, related to surface elasticity theory established in Gurtin and Murdoch [36], Murdoch [69]. According to Section 3.1, the kinematics describe the motion of particles within the

reference interface Γ_0 to the current configuration of the interface Γ_t . Mathematically, the surface Γ_0 is understood as a two-dimensional submanifold in \mathbb{R}^3 . The essential difference to the previous two chapters is that the interface may not open during the deformation process. To be more precise the interface is assumed to be coherent and the jump of the motion across the interface vanishes, i.e. $[[\boldsymbol{\varphi}]] = \mathbf{0}$. Thereby, only in-plane deformations within the interface can be captured. As mentioned before, a point \bar{P} lying within Γ_0 is described by $\mathbf{X}(\bar{P})$. During the deformation, the material point does not decompose into two different spatial configurations as in non-coherent interface theory, see Eqs. (3.1) and (3.2). Here, the motion from its referential to its unique spatial configuration is denoted as $\bar{\boldsymbol{\varphi}}$ and the position is labelled as $\bar{\mathbf{x}}$. In order to deliver a relation for the notation of surface elasticity and the kinematics of non-coherent interfaces introduced in Section 3.1, it is assumed that

$$\bar{\mathbf{x}}(\bar{P}) = \mathbf{x}_{(m)}(\bar{P}) = \bar{\boldsymbol{\varphi}}(\mathbf{X}(\bar{P})), \quad \mathbf{x}_{(m)}(\bar{P}) \in \Gamma_t. \quad (5.1)$$

Furthermore, the motion of the interface follows the motion of the bulk as $\bar{\boldsymbol{\varphi}} = \boldsymbol{\varphi}|_{\Gamma_0}$. In order to describe the in-plane deformation, curvilinear coordinates θ^1 and θ^2 are introduced. Thereby, points belonging to the undeformed interface Γ_0 are denoted by $\mathbf{X}(\theta^\alpha)$, where the Greek index runs from 1 to 2, see Fig. 5.1. The covariant tangential

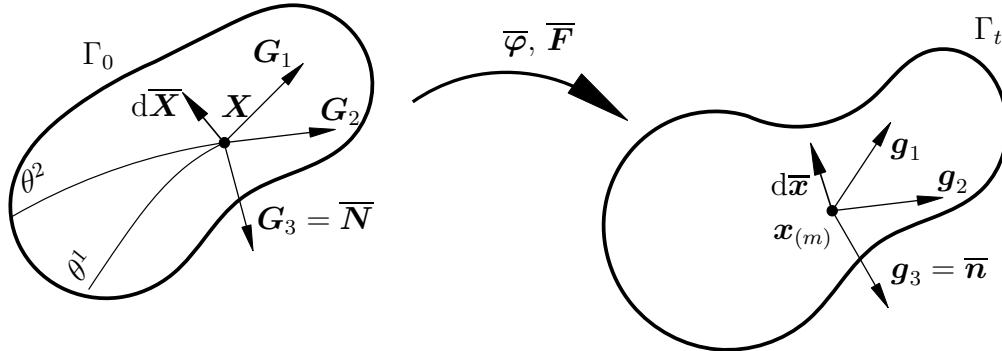


Figure 5.1: Motion of a surface – reference configuration Γ_0 and current configuration Γ_t . The deformation mapping $\bar{\boldsymbol{\varphi}}$ maps points \mathbf{X} belonging to Γ_0 to their current counterparts $\mathbf{x}_{(m)}$ in Γ_t .

base vectors of the reference configuration \mathbf{G}_α are given by

$$\mathbf{G}_\alpha = \mathbf{X}_{,\alpha} = \frac{\partial \mathbf{X}}{\partial \theta^\alpha}, \quad (5.2)$$

which allow the definition of the unit normal vector

$$\bar{\mathbf{N}} = \frac{\mathbf{G}_1 \times \mathbf{G}_2}{|\mathbf{G}_1 \times \mathbf{G}_2|} = \mathbf{G}^3 \quad (5.3)$$

and it follows that $\mathbf{G}_3 = \mathbf{G}^3$. The base vectors \mathbf{G}_1 , \mathbf{G}_2 and \mathbf{G}_3 then constitute a right-handed system, see Fig. 5.1. The normal vector $\bar{\mathbf{N}}$ points from the lower interface side

Γ_0^- to the upper interface side Γ_0^+ . Having introduced the deformation, the tangential base vectors of the deformed configuration of a coherent interface read

$$\mathbf{g}_\alpha = \mathbf{x}_{(m),\alpha} = \frac{\partial \mathbf{x}_{(m)}}{\partial \theta^\alpha}. \quad (5.4)$$

The unit normal vector $\bar{\mathbf{n}}$ is given by

$$\bar{\mathbf{n}} = \frac{\mathbf{g}_1 \times \mathbf{g}_2}{|\mathbf{g}_1 \times \mathbf{g}_2|} = \mathbf{g}^3, \quad (5.5)$$

where it follows that $\mathbf{g}_3 = \mathbf{g}^3$. Having set up the notation, the surface deformation gradient $\bar{\mathbf{F}}$ is introduced as

$$\bar{\mathbf{F}} := \overline{\text{GRAD}}(\mathbf{x}_{(m)}) = \frac{\partial \mathbf{x}_{(m)}}{\partial \mathbf{X}} = \frac{\partial \mathbf{x}_{(m)}}{\partial \theta^\alpha} \otimes \frac{\partial \theta^\alpha}{\partial \mathbf{X}} = \mathbf{g}_\alpha \otimes \mathbf{G}^\alpha. \quad (5.6)$$

Accordingly,

$$\overline{\text{GRAD}}(\bullet) = \frac{\partial(\bullet)}{\partial \theta^\alpha} \otimes \frac{\partial \theta^\alpha}{\partial \mathbf{X}} \quad (5.7)$$

denotes the surface gradient of quantity (\bullet) with respect to the referential configuration and \mathbf{G}^α are the contravariant base vectors of Γ_0 . In relation to Eq. (2.16), the inverse of the surface deformation gradient $\bar{\mathbf{F}}^{-1}$ also exists and reads

$$\bar{\mathbf{F}}^{-1} = \overline{\text{grad}}(\mathbf{X}) = \frac{\partial \mathbf{X}}{\partial \theta^\alpha} \otimes \frac{\partial \theta^\alpha}{\partial \mathbf{x}_{(m)}} = \mathbf{G}_\alpha \otimes \mathbf{g}^\alpha, \quad (5.8)$$

where

$$\overline{\text{grad}}(\bullet) = \frac{\partial(\bullet)}{\partial \theta^\alpha} \otimes \frac{\partial \theta^\alpha}{\partial \mathbf{x}_{(m)}} = \frac{\partial(\bullet)}{\partial \theta^\alpha} \otimes \mathbf{g}^\alpha \quad (5.9)$$

defines the surface gradient of (\bullet) with respect to the current configuration. Analogously to the bulk, the surface deformation gradient $\bar{\mathbf{F}}$ is a linear deformation map of line elements $d\bar{\mathbf{X}}$ within the reference surface Γ_0 to their counterpart $d\bar{\mathbf{x}}$ within the current configuration of the surface Γ_t , i.e.,

$$d\bar{\mathbf{x}} = \bar{\mathbf{F}} \cdot d\bar{\mathbf{X}}. \quad (5.10)$$

As already mentioned, this chapter presents a generalised interface theory. The kinematics of non-coherent cohesive zone models are combined with the kinematics of coherent interfaces based on surface elasticity theory as introduced in this section. Thereby, modelling of shear and anisotropic effects in a thermodynamically consistent matter is

possible. The balance laws and constitutive relations for the extended interface framework are derived in the following sections.

5.2 Balance laws of the generalised interface framework

5.2.1 Preliminaries

According to Sections 3.1 and 5.1, the kinematics of the generalised interface depend on the displacement jump $[[\mathbf{u}]]$ and on the surface deformation gradient $\overline{\mathbf{F}}$. It bears emphasis that such variables are independent of each other. To be more precise, $\overline{\mathbf{F}}$ cannot be computed if $[[\mathbf{u}]]$ is known, i.e., $\overline{\mathbf{F}} \neq \overline{\mathbf{F}}([[\mathbf{u}]])$ and vice versa, if $\overline{\mathbf{F}}$ is known, $[[\mathbf{u}]]$ cannot be computed, i.e., $[[\mathbf{u}]] \neq [[\mathbf{u}]](\overline{\mathbf{F}})$. This mathematical independence is also comprehensible from a physics point of view. While $[[\mathbf{u}]]$ describes the opening of an interface (e.g., the crack opening), $\overline{\mathbf{F}}$ captures the in-plane deformation of the interface. Thus, they are related to different physical effects and consequently, the aforementioned independence is expected. Since the opening and the in-plane deformation of an interface are independent, a Helmholtz energy Ψ that should capture both effects has to depend on $[[\mathbf{u}]]$ as well as on $\overline{\mathbf{F}}$. Focusing on hyperelasticity for now, and in line with Javili et al. [50], Ottosen et al. [77], an energy of type

$$\Psi = \Psi([[\mathbf{u}]], \overline{\mathbf{F}}, \boldsymbol{\alpha}) \quad (5.11)$$

is therefore adopted in the following. Here, $\boldsymbol{\alpha}$ is a set of suitable internal variables capturing inelastic effects such as hardening/softening due to plasticity or material degradation due to microcracking. Alternatively, this choice can also be motivated by modelling anisotropies. Taking material anisotropies into consideration, the Helmholtz energy has to be extended with structural tensors \mathbf{a}_i to $\Psi = \Psi([[\mathbf{u}]], \mathbf{a}_i, \boldsymbol{\alpha})$. For instance, in order to distinguish between mode-I and mode-II or mode-III failure, the normal vector of the interface $\overline{\mathbf{n}} = \mathbf{g}_3$ has to enter the Helmholtz energy, i.e., $\Psi = \Psi([[\mathbf{u}]], \overline{\mathbf{n}}, \boldsymbol{\alpha})$, see Eq. (3.9). However, \mathbf{g}_3 is a function in terms of the tangential vector \mathbf{g}_1 and \mathbf{g}_2 which, in turn, can be computed by means of surface deformation gradient $\overline{\mathbf{F}}$, cf. Eq. (5.6). In summary, $\Psi = \Psi([[\mathbf{u}]], \overline{\mathbf{n}}, \boldsymbol{\alpha}) = \hat{\Psi}([[\mathbf{u}]], \overline{\mathbf{F}}, \boldsymbol{\alpha})$ and thus energy $\Psi([[\mathbf{u}]], \overline{\mathbf{n}}, \boldsymbol{\alpha})$ depicts a special case in the range of general interfaces represented by Helmholtz energy (5.11). Consequently, the incorporation of surface deformation gradient $\overline{\mathbf{F}}$ can either be motivated by the independence of $\overline{\mathbf{F}}$ on $[[\mathbf{u}]]$ or by the introduction of structural tensors/vectors such as $\overline{\mathbf{n}} = \mathbf{g}_3$.

An alternative, equivalent representation of Helmholtz energy (5.11) can be derived considering material time derivative

$$\dot{\overline{\mathbf{F}}} = \dot{\mathbf{g}}_\alpha \otimes \mathbf{G}^\alpha \quad (5.12)$$

of the surface deformation gradient, cf Eq. (5.6). Accordingly, the only deformation-dependent variables entering $\overline{\mathbf{F}}$ are the tangent vectors \mathbf{g}_α . They can therefore be considered as structural tensors \mathbf{a}_i for a Helmholtz energy of type

$$\Psi = \Psi(\llbracket \mathbf{u} \rrbracket, \mathbf{g}_\alpha, \boldsymbol{\alpha}). \quad (5.13)$$

This choice is indeed a different, but nevertheless equivalent representation of Eq. (5.11). Helmholtz energies (5.11) and (5.13) both represent descriptions for general interfaces.

5.2.2 Work conjugacy and second law of thermodynamics

Based on Helmholtz energy (5.11) or (5.13), the stresses dual to $\llbracket \mathbf{u} \rrbracket$ and $\overline{\mathbf{F}}$, or those dual to $\llbracket \mathbf{u} \rrbracket$ and \mathbf{g}_α can be derived by applying the classic Coleman-Noll procedure. For that purpose and focusing on representation (5.11), the variables conjugate to $\llbracket \mathbf{u} \rrbracket$ and $\overline{\mathbf{F}}$ are introduced first. They are denoted by $\overline{\mathbf{T}}$ and $\overline{\mathbf{P}}$. Assuming that $\boldsymbol{\alpha}$ is exclusively related to dissipative effects – in line with standard (local) plasticity theory or damage mechanics – the stress power reads

$$\mathcal{P} = \overline{\mathbf{T}} \cdot \llbracket \dot{\mathbf{u}} \rrbracket + \overline{\mathbf{P}} : \dot{\overline{\mathbf{F}}}, \quad (5.14)$$

where $\overline{\mathbf{T}}$ is a traction vector dual to $\llbracket \mathbf{u} \rrbracket$ and where $\overline{\mathbf{P}}$ is a stress tensor dual to $\overline{\mathbf{F}}$. In analogy to bulk materials, $\overline{\mathbf{P}}$ is denoted as first Piola-Kirchhoff interface stress tensor. The new variable $\overline{\mathbf{T}}$ has to be introduced, since it will turn out that $\mathbf{T}^+ \neq -\mathbf{T}^- \neq \overline{\mathbf{T}}$ in general.

Alternatively, and starting from Eq. (5.13), the stress power takes the format

$$\mathcal{P} = \overline{\mathbf{T}} \cdot \llbracket \dot{\mathbf{u}} \rrbracket + \mathbf{A}^\alpha \cdot \dot{\mathbf{g}}_\alpha, \quad (5.15)$$

where the stresses \mathbf{A}^α dual to \mathbf{g}_α are related to $\overline{\mathbf{P}}$ by $\mathbf{A}^\alpha = \overline{\mathbf{P}} \cdot \mathbf{G}^\alpha$. This relation follows from inserting Eq. (5.12) into Eq. (5.14) and by comparing the result to Eq. (5.15).

According to representations (5.11) and (5.14), the dissipation of the generalised isothermal interface model takes the form

$$\mathcal{D} = \mathcal{P} - \dot{\Psi} = \left[\overline{\mathbf{T}} - \frac{\partial \Psi}{\partial \llbracket \mathbf{u} \rrbracket} \right] \cdot \llbracket \dot{\mathbf{u}} \rrbracket + \left[\overline{\mathbf{P}} - \frac{\partial \Psi}{\partial \overline{\mathbf{F}}} \right] : \dot{\overline{\mathbf{F}}} + \mathbf{Q} \cdot \dot{\boldsymbol{\alpha}} \geq 0, \quad (5.16)$$

where $\mathbf{Q} := -\partial \Psi / \partial \boldsymbol{\alpha}$ is the internal variable dual to $\boldsymbol{\alpha}$. Adopting the classic Coleman-Noll procedure leads to the stresses dual to $\llbracket \mathbf{u} \rrbracket$ and $\overline{\mathbf{F}}$ as

$$\overline{\mathbf{T}} = \frac{\partial \Psi}{\partial \llbracket \mathbf{u} \rrbracket} \quad (5.17)$$

and

$$\overline{\mathbf{P}} = \frac{\partial \Psi}{\partial \overline{\mathbf{F}}}. \quad (5.18)$$

Here, the analogy to the Piola-Kirchhoff bulk stress tensor (2.46) is obvious. The components of $\overline{\mathbf{P}}$ are calculated as $\overline{\mathbf{P}} = P^{\alpha i} \mathbf{g}^i \otimes \mathbf{G}_\alpha$, cf. [77]. Hence, it holds that $\overline{\mathbf{P}} \cdot \mathbf{G}^3 = \overline{\mathbf{P}} \cdot \mathbf{G}_3 = \mathbf{0}$ and $\overline{\mathbf{P}}$ is a superficial tensor, see Gurtin [35, Section 15a]. Due to Javili et al. [46] the superficiality is the consequence of a first-order continuum theory. The obtained stresses give rise to the reduced dissipation inequality

$$\mathcal{D} = \mathbf{Q} \cdot \dot{\boldsymbol{\alpha}} \geq 0. \quad (5.19)$$

In what follows, representations (5.13) and (5.15) are considered – a representation in terms of $[[\mathbf{u}]]$ and \mathbf{g}_α . Based on this choice, the dissipation of an isothermal model can be computed as (see also [77])

$$\mathcal{D} = \mathcal{P} - \dot{\Psi} = \left[\overline{\mathbf{T}} - \frac{\partial \Psi}{\partial [[\mathbf{u}]]} \right] \cdot [[\dot{\mathbf{u}}]] + \left[\mathbf{A}^\alpha - \frac{\partial \Psi}{\partial \dot{\mathbf{g}}_\alpha} \right] \cdot \dot{\mathbf{g}}_\alpha + \mathbf{Q} \cdot \dot{\boldsymbol{\alpha}} \geq 0. \quad (5.20)$$

Again by applying the Coleman-Noll procedure, the stresses dual to $[[\mathbf{u}]]$ and \mathbf{g}_α are obtained as

$$\overline{\mathbf{T}} = \frac{\partial \Psi}{\partial [[\mathbf{u}]]} \quad (5.21)$$

and

$$\mathbf{A}^\alpha = \frac{\partial \Psi}{\partial \dot{\mathbf{g}}_\alpha}. \quad (5.22)$$

In turn, stress contributions (5.21) and (5.22) again lead to the reduced dissipation inequality (5.19).

Remark 8 *It bears emphasis that Ineq. (5.20) indeed represents the most general case – as far as assumed stress power (5.15) is concerned. For instance, Ineq. (5.20) also encompasses plasticity theories. In this case and in line with [75], internal variables $\boldsymbol{\alpha}$ would also include certain plasticity related displacement jumps.*

5.2.3 Balance of linear momentum

In order to derive balance of linear momentum in the case of general interfaces, a variational point of view is adopted here. A similar derivation can be found in the work by Javili [47]. As will be shown, the variational framework leads to a compact and direct derivation. In this subsection hyperelasticity is considered. In analogy to the principle

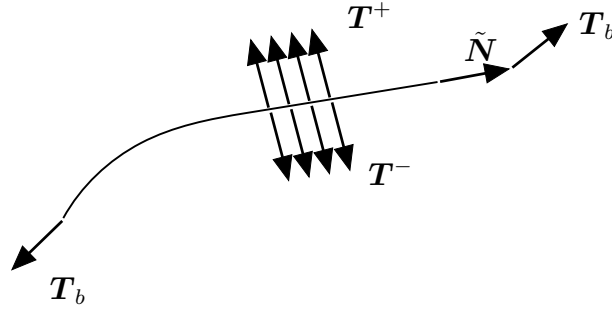


Figure 5.2: Stresses acting on an interface – referential description: Tractions acting at the upper surface $\Gamma_0^+ = \Gamma_0$ are denoted by \mathbf{T}^+ , tractions acting at the lower surface $\Gamma_0^- = \Gamma_0$ are denoted by \mathbf{T}^- , stresses acting at the boundary of the interface $\partial\Gamma_0$ are denoted by \mathbf{T}_b . The normal vector of the boundary of the interface is denoted by $\tilde{\mathbf{N}}$.

of minimum potential energy for bulk materials (cf. Subsection 2.3.1.3), the starting point of the variational re-derivation is the total potential energy of the interface

$$\begin{aligned} \bar{\mathcal{I}} = & \int_{\Gamma_0} \Psi([\mathbf{u}], \mathbf{g}_\alpha) \, dA \\ & - \int_{\Gamma_0^+ = \Gamma_0} \mathbf{T}^+ \cdot \boldsymbol{\varphi}^+ \, dA - \int_{\Gamma_0^- = \Gamma_0} \mathbf{T}^- \cdot \boldsymbol{\varphi}^- \, dA - \oint_{\partial\Gamma_0} \mathbf{T}_b \cdot \boldsymbol{\varphi}_{(m)} \, d\mathcal{L}. \end{aligned} \quad (5.23)$$

The first term represents the total Helmholtz energy. According to Fig. 5.2, the external potential consists of energies related to tractions \mathbf{T}^+ and \mathbf{T}^- . The motions of the upper and lower side of the interface follow the bulk motions $\boldsymbol{\varphi}^+$ and $\boldsymbol{\varphi}^-$. Moreover, as an extension to the classic cohesive zone framework, the tractions \mathbf{T}_b prescribed on the boundary $d\mathcal{L}$ are also considered here. It bears emphasis that \mathbf{T}^+ and \mathbf{T}^- are standard tractions showing the physical unit force/area, while stresses \mathbf{T}_b show the physical unit force/length.

In order to compute the variation of $\bar{\mathcal{I}}$, the term depending on the Helmholtz energy is considered first. Applying the constitutive relations (5.21) and (5.22), its variation yields

$$\int_{\Gamma_0} \delta_\varphi \Psi([\mathbf{u}], \mathbf{g}_\alpha) \, dA = \int_{\Gamma_0} [\bar{\mathbf{T}} \cdot \delta[\mathbf{u}] + \mathbf{A}^\alpha \cdot \delta\mathbf{g}_\alpha] \, dA. \quad (5.24)$$

By employing the identity

$$\overline{\text{DIV}}(\delta\mathbf{x}_{(m)} \cdot \bar{\mathbf{P}}) = \delta\mathbf{x}_{(m)} \cdot \overline{\text{DIV}} \bar{\mathbf{P}} + \mathbf{A}^\alpha \cdot \delta\mathbf{g}_\alpha, \quad (5.25)$$

which depends on the surface divergence operator

$$\overline{\text{DIV}}(\bullet) = \frac{\partial(\bullet)}{\partial\theta^\alpha} \cdot \mathbf{G}^\alpha, \quad (5.26)$$

Eq. (5.24) can be rewritten as

$$\int_{\Gamma_0} \delta_{\varphi} \Psi(\llbracket \mathbf{u} \rrbracket, \mathbf{g}_{\alpha}) \, dA = \int_{\Gamma_0} [\overline{\mathbf{T}} \cdot \delta \llbracket \mathbf{u} \rrbracket + \overline{\text{DIV}} (\overline{\mathbf{P}} \cdot \delta \mathbf{x}_{(m)}) - \overline{\text{DIV}} \overline{\mathbf{P}} \cdot \delta \mathbf{x}_{(m)}] \, dA. \quad (5.27)$$

Now, the surface Gauss theorem, cf. for instance Gurtin and Murdoch [36], Steinmann [94],

$$\int_{\Gamma_0} \overline{\text{DIV}} (\delta \mathbf{x}_{(m)} \cdot \overline{\mathbf{P}}) \, dA = \oint_{\partial \Gamma_0} \delta \mathbf{x}_{(m)} \cdot (\overline{\mathbf{P}} \cdot \tilde{\mathbf{N}}) \, d\mathcal{L} - \int_{\Gamma_0} \overline{K} \delta \mathbf{x}_{(m)} \cdot \overline{\mathbf{P}} \cdot \overline{\mathbf{N}} \, dA, \quad (5.28)$$

is inserted into Eq. (5.27). Here, the second term in Eq. (7.16) concerning the curvature \overline{K} vanishes due to the superficiality property $\overline{\mathbf{P}} \cdot \overline{\mathbf{N}} = \mathbf{0}$ of the Piola-Kirchhoff interface stress. Furthermore, the Cauchy-type relation $\mathbf{T}_b = \overline{\mathbf{P}} \cdot \tilde{\mathbf{N}}$ – in line with bulk materials – is employed. The variation of potential (5.23) with respect to the deformation φ simplifies to

$$\delta_{\varphi} \overline{\mathcal{I}} = \int_{\Gamma_0} \left[\overline{\mathbf{T}} \cdot (\delta \mathbf{x}^+ - \delta \mathbf{x}^-) - \mathbf{T}^+ \cdot \delta \mathbf{x}^+ - \mathbf{T}^- \cdot \delta \mathbf{x}^- - \frac{1}{2} \overline{\text{DIV}} \overline{\mathbf{P}} \cdot (\delta \mathbf{x}^+ + \delta \mathbf{x}^-) \right] \, dA = 0 \quad \forall \delta \mathbf{x}^+, \delta \mathbf{x}^-, \quad (5.29)$$

where the variations

$$\delta \llbracket \mathbf{u} \rrbracket = \delta \mathbf{x}^+ - \delta \mathbf{x}^- \quad \text{and} \quad \delta \varphi^{\pm} = \delta \mathbf{u}^{\pm} = \delta \mathbf{x}^{\pm} \quad (5.30)$$

have been used. Since $\delta \mathbf{x}^-$ and $\delta \mathbf{x}^+$ are independent of each other and arbitrary, Eq. (5.29) is equivalent to the two equations

$$-\frac{1}{2} \overline{\text{DIV}} \overline{\mathbf{P}} - \mathbf{T}^+ + \overline{\mathbf{T}} = \mathbf{0} \quad (5.31)$$

and

$$-\frac{1}{2} \overline{\text{DIV}} \overline{\mathbf{P}} - \mathbf{T}^- - \overline{\mathbf{T}} = \mathbf{0}. \quad (5.32)$$

These are the Euler-Lagrange equations associated with potential (5.23). Since these cannot be compared easily to existing frameworks, they are reformulated next. For that purpose, Eq. (5.31) is added to Eq. (5.32) yielding

$$\mathbf{T}^+ + \mathbf{T}^- + \overline{\text{DIV}} \overline{\mathbf{P}} = \mathbf{0}. \quad (5.33)$$

This equation is equivalent to the local form of balance of linear momentum as derived in [77] and [47]. Equation (5.33) shows that trivial identity $\mathbf{T}^+ = -\mathbf{T}^-$, cf. Eq. (3.13),

is only fulfilled in the classic framework, i.e., if the Helmholtz energy only depends on the displacement jump $[[\mathbf{u}]]$ – and not also on structural tensors like base vectors \mathbf{g}_α . Finally, by subtracting Eq. (5.32) from Eq. (5.31) one obtains

$$\bar{\mathbf{T}} = \frac{1}{2} (\mathbf{T}^+ - \mathbf{T}^-), \quad (5.34)$$

which is the averaged traction vector conjugate to $[[\mathbf{u}]]$.

Remark 9 *As an alternative to the considered variational principle and to the principle of virtual work, one can also start from postulating the external mechanical power, cf. Javili et al. [50]. In this case, invariance principles such as those in Noll [71] and Beatty [8] can be applied. Again, this would eventually lead to strong form (5.33).*

5.2.4 Balance of angular momentum

The goal of this subsection is to derive the balance of angular momentum for the extended interface framework from a variational point of view – in line with the derivation in Ottosen et al. [77]. According to (local) bulk material models, balance of angular momentum can be enforced point-wise by choosing a suitable Helmholtz energy. To be more precise, it was shown in [77] that an invariance of the Helmholtz energy with respect to arbitrary isometries – also known as material objectivity or frame indifference from a physics point of view – is sufficient in order to fulfill balance of angular momentum point-wise, cf. Subsection 2.3.1 for bulk materials. In the case of hyperelasticity, the aforementioned invariance reads

$$\Psi(\mathbf{Q} \cdot [[\mathbf{u}]], \mathbf{Q} \cdot \mathbf{g}_\alpha) = \Psi([[\mathbf{u}]], \mathbf{g}_\alpha) \quad \forall \mathbf{Q} \in SO(3), \quad (5.35)$$

where \mathbf{Q} is an arbitrarily proper orthogonal matrix. In line with classic invariance principles, cf. Green and Rivlin [33], Noll [71] (see also Del Piero [23]), it can be shown that invariance of the power with respect to a change of observer is equivalent to balance of linear and angular momentum. Consequently, any objective Helmholtz energy Ψ automatically fulfills balance of angular momentum. In order to derive the local form of balance of angular momentum for the extended interface framework, the material time derivative of Eq. (5.35) is computed as

$$\begin{aligned} & \frac{\partial \Psi(\mathbf{Q} \cdot [[\mathbf{u}]], \mathbf{Q} \cdot \mathbf{g}_\alpha)}{\partial \mathbf{Q}} : \dot{\mathbf{Q}} \\ &= \left[\frac{\partial \Psi(\mathbf{Q} \cdot [[\mathbf{u}]], \mathbf{Q} \cdot \mathbf{g}_\alpha)}{\partial(\mathbf{Q} \cdot [[\mathbf{u}]])} \cdot \frac{\partial(\mathbf{Q} \cdot [[\mathbf{u}]])}{\partial \mathbf{Q}} + \frac{\partial \Psi(\mathbf{Q} \cdot [[\mathbf{u}]], \mathbf{Q} \cdot \mathbf{g}_\alpha)}{\partial(\mathbf{Q} \cdot \mathbf{g}_\alpha)} \cdot \frac{\partial(\mathbf{Q} \cdot \mathbf{g}_\alpha)}{\partial \mathbf{Q}} \right] : \dot{\mathbf{Q}} = 0. \end{aligned} \quad (5.36)$$

Clearly, in the case of hyperelasticity the material time derivative of Ψ is equivalent to the internal stress power. By applying the relations

$$\frac{\partial \Psi}{\partial(\mathbf{Q} \cdot \llbracket \mathbf{u} \rrbracket)} = \frac{\partial \Psi}{\partial \llbracket \mathbf{u} \rrbracket} \cdot \mathbf{Q}^T \quad \text{and} \quad \frac{\partial \Psi}{\partial(\mathbf{Q} \cdot \mathbf{g}_\alpha)} = \frac{\partial \Psi}{\partial \mathbf{g}_\alpha} \cdot \mathbf{Q}^T \quad (5.37)$$

together with the constitutive relations (5.21) and (5.22), Eq. (5.36) is reformulated to

$$\llbracket \overline{\mathbf{T}} \otimes \llbracket \mathbf{u} \rrbracket + \mathbf{A}^\alpha \otimes \mathbf{g}_\alpha \rrbracket : \boldsymbol{\Omega} = 0, \quad (5.38)$$

where $\boldsymbol{\Omega} = \mathbf{Q}^T \cdot \dot{\mathbf{Q}}$ denotes the spin tensor. Since $\boldsymbol{\Omega}$ is skew symmetric, it is implied that the term within the square brackets is symmetric. Then, following [77] and using arguments similar to, for instance, Bertram [10, p. 31], Eq. (5.38) is fulfilled, if and only if

$$\llbracket \mathbf{u} \rrbracket \times \overline{\mathbf{T}} + \mathbf{g}_\alpha \times \mathbf{A}^\alpha = \mathbf{0}. \quad (5.39)$$

Equation (5.39) represents the local form of balance of angular momentum for the extended general interface framework. Accordingly, in a classic cohesive zone framework $\mathbf{A}^\alpha = \mathbf{0}$ which implies collinearity between $\llbracket \mathbf{u} \rrbracket$ and $\overline{\mathbf{T}}$, i.e., a fiber model, cf. Eq. (3.15).

In what follows, condition (5.35) is a priori fulfilled by considering suitable invariants. A possible choice for such invariants is

$$I_1 = \llbracket \mathbf{u} \rrbracket \cdot \llbracket \mathbf{u} \rrbracket, \quad I_2 = \llbracket \mathbf{u} \rrbracket \cdot (\mathbf{g}_1 \otimes \mathbf{g}^1) \cdot \llbracket \mathbf{u} \rrbracket, \quad I_3 = \llbracket \mathbf{u} \rrbracket \cdot (\mathbf{g}_2 \otimes \mathbf{g}^2) \cdot \llbracket \mathbf{u} \rrbracket \quad (5.40)$$

and

$$\overline{\mathbf{C}} = \overline{\mathbf{F}}^T \cdot \overline{\mathbf{F}} = (\mathbf{g}_\alpha \cdot \mathbf{g}_\beta) \mathbf{G}^\alpha \otimes \mathbf{G}^\beta. \quad (5.41)$$

Due to the symmetry of $\overline{\mathbf{C}}$, the total number of (independent) invariants is six. Three of those are related to an anisotropic cohesive zone-like model (see Eq. (5.40)), while the remaining three are associated with the deformation of the mid-surface (see Eq. (5.41)). The derivatives of such invariants necessary for the implementation are summarised in Appendix B.1.

5.3 Prototype model – a quasi-brittle mixed-mode damage model

In this section, a prototype model is presented which falls into the range of the constitutive framework elaborated before. It is a mixed-mode quasi-brittle damage model which accounts for the different physics associated with mode-I and mode-II/III failure.

For instance, different fracture energies and material strengths can be chosen for the aforementioned failure modes.

In order to derive the prototype model, the Helmholtz energy is additively decomposed into energies related to the relevant failure modes. In line with Mosler and Scheider [68], Ottosen et al. [75] and Ottosen et al. [77], a Helmholtz energy of type

$$\Psi = \sum_{i=1}^n \Psi_i(\llbracket \mathbf{u} \rrbracket, \mathbf{g}_\alpha, \boldsymbol{\alpha}) \quad (5.42)$$

is thus postulated. For a mixed-mode model distinguishing between mode-I failure (index n – failure in normal direction of the interface) and mode-II/III failure (index t – failure in tangential direction of the interface), Eq. (5.42) simplifies to

$$\Psi = \Psi_n(\llbracket \mathbf{u} \rrbracket, \mathbf{g}_\alpha, \boldsymbol{\alpha}) + \Psi_t(\llbracket \mathbf{u} \rrbracket, \mathbf{g}_\alpha, \boldsymbol{\alpha}). \quad (5.43)$$

Material degradation / failure of the considered interface is realised by a degradation of the material's stiffness through scalar-valued damage parameters. Such parameters are denoted by

- $d_n^{(n)}$: degradation in normal direction due to loading in normal direction
- $d_t^{(t)}$: degradation in tangential direction due to loading in tangential direction
- $d_n^{(t)}$: degradation in normal direction due to loading in tangential direction
- $d_t^{(n)}$: degradation in tangential direction due to loading in normal direction.

Since all $d_i^{(j)} \in [0; 1]$ are scalar-valued, they are a priori invariant with respect to a change of observer. According to this invariance, Eq. (5.35) indeed guarantees material frame indifference of the Helmholtz energy. In order to couple failure in normal and failure in tangential direction (cross softening), and in order to enforce an effective damage parameter within the range $[0; 1]$, a multiplicative decomposition of the effective damage parameter is used. To be more precise, a Helmholtz energy of type

$$\Psi = (1 - d_n^{(n)})(1 - d_n^{(t)}) \Psi_n^0(\llbracket \mathbf{u} \rrbracket, \mathbf{g}_\alpha) + (1 - d_t^{(n)})(1 - d_t^{(t)}) \Psi_t^0(\llbracket \mathbf{u} \rrbracket, \mathbf{g}_\alpha) \quad (5.44)$$

is assumed. Since $d_i^{(j)} \in [0; 1]$, the effective parameters $(1 - d_n^{(n)})(1 - d_n^{(t)})$ and $(1 - d_t^{(n)})(1 - d_t^{(t)})$ indeed belong to the same interval – as required by physics. The energies $\Psi_n^0(\llbracket \mathbf{u} \rrbracket, \mathbf{g}_\alpha)$ and $\Psi_t^0(\llbracket \mathbf{u} \rrbracket, \mathbf{g}_\alpha)$ in Eq. (5.44) are the Helmholtz energies due to mode-I and mode-II/III loading associated with the virgin undamaged material (the superscript 0 signals the undamaged state).

Energies $\Psi_n^0(\llbracket \mathbf{u} \rrbracket, \mathbf{g}_\alpha)$ and $\Psi_t^0(\llbracket \mathbf{u} \rrbracket, \mathbf{g}_\alpha)$ are defined next. For that purpose, invariants

$$I_1 = \llbracket \mathbf{u} \rrbracket \cdot \llbracket \mathbf{u} \rrbracket, \quad I_2 = \llbracket \mathbf{u} \rrbracket \cdot (\mathbf{g}_1 \otimes \mathbf{g}^1) \cdot \llbracket \mathbf{u} \rrbracket, \quad I_3 = \llbracket \mathbf{u} \rrbracket \cdot (\mathbf{g}_2 \otimes \mathbf{g}^2) \cdot \llbracket \mathbf{u} \rrbracket \quad (5.45)$$

are introduced. Here, the contravariant vectors \mathbf{g}^β being dual to \mathbf{g}_α have been used, i.e., $\mathbf{g}^\beta \cdot \mathbf{g}_\alpha = \delta_\alpha^\beta$. Accordingly, the mixed-variant invariants (5.45) are not only invariant with respect to isometries (as required by the principle of material objectivity), but also invariant with respect to arbitrary isomorphisms. Consequently, if Helmholtz energies $\Psi_n^0(\llbracket \mathbf{u} \rrbracket, \mathbf{g}_\alpha)$ and $\Psi_t^0(\llbracket \mathbf{u} \rrbracket, \mathbf{g}_\alpha)$ are written in terms of such invariants, the resulting potential is spatially covariant. This property implies material frame indifference which, in turn, implies balance of angular momentum (point-wise), cf. Subsection 5.2.4 (see also Remark 10). As the energy associated with mode-I loading should depend on the normal component of the displacement jump $\llbracket \mathbf{u} \rrbracket \cdot \bar{\mathbf{n}} = \llbracket \mathbf{u} \rrbracket \cdot \mathbf{g}_3 = \llbracket \mathbf{u} \rrbracket \cdot \mathbf{g}^3$ which is related to invariants (5.45) by $I_1 - I_2 - I_3 = \llbracket \mathbf{u} \rrbracket \cdot (\mathbf{g}_3 \otimes \mathbf{g}^3) \cdot \llbracket \mathbf{u} \rrbracket$, ansatz

$$\Psi_n^0 = \Psi_n^0(I_1 - I_2 - I_3) \quad (5.46)$$

is made. With respect to the numerical examples presented in Section 6.4, the simplest possible choice – a quadratic energy (quadratic with respect to the displacement jump)

$$\Psi_n^0 = \frac{1}{2} c_n (I_1 - I_2 - I_3) \quad (5.47)$$

is considered. Here, c_n is the elastic stiffness of the interface in normal direction. Analogously to Eq. (5.47), the energy due to failure in tangential direction (represented by the quadratic invariants I_2 and I_3), is defined by

$$\Psi_t^0 = \Psi_t^0(I_2, I_3). \quad (5.48)$$

Assuming the same mechanical response in both tangential directions and again a quadratic representation of the Helmholtz energy,

$$\Psi_t^0 = \frac{1}{2} c_t (I_2 + I_3) \quad (5.49)$$

is chosen for the numerical examples. It is shown explicitly in [77] that choices (5.47) and (5.49) imply a cohesive model where, in addition to traditional cohesive fiber forces, also out-of-plane membrane forces exist.

The model is completed by suitable evolution equations for $d_i^{(j)}$. Since the reduced dissipation inequality (5.19) resulting from general Helmholtz energy (5.44) reads

$$\mathcal{D} = (1 - d_n^{(t)}) \Psi_n^0 \dot{d}_n^{(n)} + (1 - d_n^{(n)}) \Psi_n^0 \dot{d}_n^{(t)} + (1 - d_t^{(n)}) \Psi_t^0 \dot{d}_t^{(t)} + (1 - d_t^{(t)}) \Psi_t^0 \dot{d}_t^{(n)} \geq 0 \quad (5.50)$$

and since factor $(1 - d_i^{(j)}) \Psi_k^0 \geq 0$ is non-negative for all four terms occurring in this inequality, a sufficient condition in order to fulfill the second law of thermodynamics is

$$\dot{d}_i^{(j)} \geq 0. \quad (5.51)$$

Speaking in terms of physics, Ineq. (5.51) prohibits self-healing. In line with Simo and Ju [89], a suitable evolution equation guaranteeing Ineq. (5.51) is postulated in terms of variables being dual to $d_i^{(j)}$. According to Ineq. (5.51), $d_i^{(j)}$ is dual to Ψ_i^0 (and a prefactor). For this reason, ansatz $d_i^{(j)} = d_i^{(j)}(\Psi_i^0)$ is made. Again, by following standard continuum damage mechanics (cf. [89]), Ineq. (5.51) is enforced by choosing a monotonously increasing function $d_i^{(j)} = d_i^{(j)}(\Psi_i^0)$ and by replacing non-monotonous energies Ψ_i^0 by their maximum value, i.e.,

$$d_i^{(j)} = d_i^{(j)}(\kappa_j), \quad \kappa_{j_{n+1}} = \max\{\kappa_{j_n}; \Psi_{j_{n+1}}\}. \quad (5.52)$$

Within the numerical examples presented in Section 6.4 a function of the type

$$d_i^{(j)}(\kappa_j) = 1 - \sqrt{\frac{\kappa_{j_0}}{\kappa_j}} \exp \left[- (\sqrt{\kappa_j} - \sqrt{\kappa_{j_0}}) \frac{Q_{0_j}}{\sqrt{1/2} c_j \mathcal{G}_{f_j}} \right] \quad (5.53)$$

is chosen, cf. Radulovic et al. [84]. Here, κ_{j_0} denotes the value of energy Ψ_j^0 that has to be reached for damage initiation, Q_{0_j} is the strength of the interface and \mathcal{G}_{f_j} represents the interface's fracture energy. The parameters can be adjusted individually for failure in normal (mode-I) and failure in tangential (mode-II/III) direction. A summary of the prototype model is given in Tab. 5.1.

Remark 10 *Energies (5.46) and (5.48) are material covariant, i.e., they are invariant with respect to an arbitrary change of frame. This is a stronger condition as the one implied by the principle of material frame indifference, which is – mathematically speaking – an invariance with respect to isometries (with respect to the deformed configuration). If only material frame indifference is to be fulfilled, invariants (5.45) can be replaced by rotationally invariant invariants*

$$I_1 = \llbracket \mathbf{u} \rrbracket \cdot \llbracket \mathbf{u} \rrbracket, \quad I_2 = \llbracket \mathbf{u} \rrbracket \cdot \mathbf{g}_1, \quad I_3 = \llbracket \mathbf{u} \rrbracket \cdot \mathbf{g}_2. \quad (5.54)$$

However, it bears emphasis that an in-plane stretch of the interface leading to a change in \mathbf{g}_α would in this case lead to a change in I_2 and I_3 and thus, to a change in energy (5.48) as well. For this reason, if only the jump is to be decomposed into a normal and a shear part without taking into account energy due to stretching of the interface, invariants (5.45) should be employed. They are invariant with respect to a stretch of the interface.

Remark 11 *Since Helmholtz energy (5.46) due to mode-I loading depends quadratically on the displacement jump ($I_1 - I_2 - I_3 = \llbracket \mathbf{u} \rrbracket \cdot (\mathbf{g}_3 \otimes \mathbf{g}^3) \cdot \llbracket \mathbf{u} \rrbracket$), damage would occur under tension as well as under compression, cf. Eq. (5.52). Certainly, the latter is unphysical.*

Table 5.1: Summary of the prototype model

- Total Helmholtz energy

$$\Psi = (1 - d_n^{(n)})(1 - d_n^{(t)}) \Psi_n^0([\mathbf{u}], \mathbf{g}_\alpha) + (1 - d_t^{(n)})(1 - d_t^{(t)}) \Psi_t^0([\mathbf{u}], \mathbf{g}_\alpha)$$

- Elastic parts of Helmholtz energy

- Due to mode-I loading

$$\Psi_n^0 = \frac{1}{2} c_n (I_1 - I_2 - I_3)$$

- Due to mode-II/III loading

$$\Psi_t^0 = \frac{1}{2} c_t (I_2 + I_3)$$

- Damage criterion and evolution

- Due to mode-I loading

$$\kappa_{n_{n+1}} = \max\{\kappa_{n_n}; \Psi_{n_{n+1}}\}$$

$$d_n^{(n)}(\kappa_n) = 1 - \sqrt{\frac{\kappa_{n_0}}{\kappa_n}} \exp\left[-(\sqrt{\kappa_n} - \sqrt{\kappa_{n_0}}) Q_{0_n} / \left(\sqrt{1/2} c_n \mathcal{G}_{f_n}\right)\right]$$

$$d_t^{(n)}(\kappa_n) = 1 - \sqrt{\frac{\kappa_{n_0}}{\kappa_n}} \exp\left[-(\sqrt{\kappa_n} - \sqrt{\kappa_{n_0}}) Q_{0_n} / \left(\sqrt{1/2} c_n \mathcal{G}_{f_n}\right)\right]$$

- Due to mode-II/III loading

$$\kappa_{t_{n+1}} = \max\{\kappa_{t_n}; \Psi_{t_{n+1}}\}$$

$$d_t^{(n)}(\kappa_t) = 1 - \sqrt{\frac{\kappa_{t_0}}{\kappa_t}} \exp\left[-(\sqrt{\kappa_t} - \sqrt{\kappa_{t_0}}) Q_{0_t} / \left(\sqrt{1/2} c_t \mathcal{G}_{f_t}\right)\right]$$

$$d_t^{(t)}(\kappa_t) = 1 - \sqrt{\frac{\kappa_{t_0}}{\kappa_t}} \exp\left[-(\sqrt{\kappa_t} - \sqrt{\kappa_{t_0}}) Q_{0_t} / \left(\sqrt{1/2} c_t \mathcal{G}_{f_t}\right)\right]$$

- Model parameters:

$$c_n, c_t, Q_{0_n}, \mathcal{G}_{f_n}, \kappa_{n_0} = \frac{1}{2} \frac{Q_{0_n}^2}{c_n}, Q_{0_t}, \mathcal{G}_{f_t}, \kappa_{t_0} = \frac{1}{2} \frac{Q_{0_t}^2}{c_t}$$

For this reason, the loading type is checked first by condition $\llbracket \mathbf{u} \rrbracket \cdot \mathbf{n} \geq 0$. If this condition is met, energy (5.44) is used. Otherwise (crack closure), it is replaced by

$$\Psi = \Psi_n^0(\llbracket \mathbf{u} \rrbracket, \mathbf{g}_\alpha) + (1 - d_t^{(n)})(1 - d_t^{(t)}) \Psi_t^0(\llbracket \mathbf{u} \rrbracket, \mathbf{g}_\alpha). \quad (5.55)$$

Consequently, an initial undamaged state is considered for mode-I loading and, therefore, if the normal stiffness c_n entering Ψ_n^0 is chosen to be large enough, a physically inadmissible overlapping of the upper and the lower interface surfaces cannot occur. Mathematically, this corresponds to a penalty-like formulation. In line with this assumption, damage evolution due to mode-I loading is suppressed, i.e., κ_n is fixed as constant, cf. Eq. (5.52). With regard to mode-II/III failure, damage variable κ_t may still evolve under compression.

5.3.1 Numerical implementation

This subsection deals with the numerical implementation of the proposed framework for the description of interfaces. According to Eq. (5.44), the general structure of the underlying Helmholtz energy is of type

$$\Psi = \Psi(\boldsymbol{\varphi}, \boldsymbol{\alpha}), \quad (5.56)$$

where $\boldsymbol{\varphi} := (\boldsymbol{\varphi}_-, \boldsymbol{\varphi}_+)$ describes the deformation of the interface (its upper and its lower surfaces correlated to the affiliated bulk deformation, cf. Section 3.1) and where $\boldsymbol{\alpha}$ denotes a set of internal variables (such as the damage variables $d_i^{(j)}$ as introduced in the previous section). Since $\boldsymbol{\varphi}$ contains the kinematics of the upper and the lower surfaces of the interface, displacement jump $\llbracket \mathbf{u} \rrbracket$ as well as tangential base vectors \mathbf{g}_α can be computed from $\boldsymbol{\varphi}$. To be more explicit,

$$\llbracket \mathbf{u} \rrbracket = \boldsymbol{\varphi}_+ - \boldsymbol{\varphi}_- \quad , \quad \mathbf{g}_\alpha = \frac{\partial}{\partial \theta^\alpha} \left(\frac{1}{2}(\boldsymbol{\varphi}_- + \boldsymbol{\varphi}_+) \right). \quad (5.57)$$

According to Subsection 5.2.4, balance of angular momentum can be enforced point-wise by choosing the Helmholtz energy to be material frame indifferent. Likewise, the second law can be fulfilled by using suitable evolution equations. The only balance law which cannot be fulfilled a priori is balance of linear momentum. According to Subsection 5.2.3, this law is equivalent to a vanishing first variation of the total energy with respect to the deformation (if the internal variables are kept fixed). With $\boldsymbol{\varphi} := (\boldsymbol{\varphi}_-, \boldsymbol{\varphi}_+)$, the stored energy of the interface can be written as

$$\overline{\mathcal{I}}(\boldsymbol{\varphi}, \boldsymbol{\alpha}) = \int_{\mathcal{I}_0} \Psi(\boldsymbol{\varphi}, \boldsymbol{\alpha}) \, dA. \quad (5.58)$$

In order to compute Energy (5.58), a spatial finite element discretisation is employed. The respective triangulation by means of interface elements reads

$$\mathcal{I}_0 \approx \mathcal{I}_0^h = \bigcup_{e=1}^{nIE} \mathcal{I}_0^e, \quad (5.59)$$

where nIE denotes the number of interface elements. Within each of the nIE elements, an isoparametric ansatz is made. Accordingly, the reference configuration and its deformed counterpart are approximated as

$$\begin{aligned} \mathbf{X}_- = \mathbf{X}_+ \approx \mathbf{X}(\boldsymbol{\theta}) &= \sum_{i=1}^{nNIE} N^{(i)}(\boldsymbol{\theta}) \mathbf{X}^{(i)}, & (5.60) \\ \left. \begin{aligned} \mathbf{x}_-(\boldsymbol{\theta}) &\approx \sum_{i=1}^{nNIE} N^{(i)}(\boldsymbol{\theta}) \mathbf{x}_-^{(i)} \\ \mathbf{x}_+(\boldsymbol{\theta}) &\approx \sum_{i=1}^{nNIE} N^{(i)}(\boldsymbol{\theta}) \mathbf{x}_+^{(i)} \end{aligned} \right\} &=: \mathbf{x}_\pm(\boldsymbol{\theta}) \approx \sum_{i=1}^{nNIE} N^{(i)}(\boldsymbol{\theta}) \mathbf{x}_\pm^{(i)} & (5.61) \end{aligned}$$

where $N^{(i)}$ are shape functions depending on natural coordinates $\boldsymbol{\theta}$ and where $nNIE$ denotes the number of nodes on the lower side of an interface element (respectively, on the upper side). The unknowns in this representation are $\mathbf{x}_\pm^{(i)} = (\mathbf{x}_-^{(i)}, \mathbf{x}_+^{(i)})$: the coordinates of the nodes with respect to the deformed configuration. Based on approximations (5.61), the deformed mid-surface of the interface (denoted by $\mathbf{x}_{(m)}$) as well as the displacement jump are obtained as

$$\mathbf{x}_{(m)}(\boldsymbol{\theta}) = \sum_{i=1}^{nNIE} \frac{1}{2} N^{(i)}(\boldsymbol{\theta}) \left(\mathbf{x}_-^{(i)} + \mathbf{x}_+^{(i)} \right), \quad \llbracket \mathbf{u} \rrbracket(\boldsymbol{\theta}) \approx \sum_{i=1}^{nNIE} N^{(i)}(\boldsymbol{\theta}) \left(\mathbf{x}_+^{(i)} - \mathbf{x}_-^{(i)} \right). \quad (5.62)$$

Furthermore, the approximation of tangential base vectors \mathbf{G}_α and \mathbf{g}_α is given by

$$\mathbf{G}_\alpha(\boldsymbol{\theta}) \approx \sum_{i=1}^{nNIE} \frac{\partial N^{(i)}(\boldsymbol{\theta})}{\partial \theta^\alpha} \mathbf{X}^{(i)}, \quad \frac{\partial \bar{\varphi}}{\partial \theta^\alpha} \approx \mathbf{g}_\alpha(\boldsymbol{\theta}) = \sum_{i=1}^{nNIE} \frac{1}{2} \frac{\partial N^{(i)}(\boldsymbol{\theta})}{\partial \theta^\alpha} \left(\mathbf{x}_-^{(i)} + \mathbf{x}_+^{(i)} \right). \quad (5.63)$$

By inserting such approximations into energy (5.58), $\bar{\mathcal{I}}$ becomes a function in terms of \mathbf{x}_\pm — to be more precise, a function in terms of the nodal unknowns $\mathbf{x}_\pm^{(i)}$. For this reason, the computation of the first variation of $\bar{\mathcal{I}}$ with respect to the deformation requires the

variation of the unknown field \mathbf{x}_\pm . By using a Bubnov-Galerkin scheme, this variation is approximated in standard manner by means of

$$\delta \mathbf{x}_+ \approx \delta \mathbf{x}_+(\boldsymbol{\theta}) = \sum_{i=1}^{nNIE} N^{(i)}(\boldsymbol{\theta}) \delta \mathbf{x}_+^{(i)}, \quad \delta \mathbf{x}_- \approx \delta \mathbf{x}_-(\boldsymbol{\theta}) = \sum_{i=1}^{nNIE} N^{(i)}(\boldsymbol{\theta}) \delta \mathbf{x}_-^{(i)}. \quad (5.64)$$

With such approximations, the aforementioned first variation results in

$$\begin{aligned} \delta_\varphi \bar{\mathcal{I}}(\varphi) &= \int_{\mathcal{I}_0} \delta_\varphi \Psi \, dA = \int_{\mathcal{I}_0} \left[\frac{\partial \Psi}{\partial [\mathbf{u}]} \cdot \delta [\mathbf{u}] + \frac{\partial \Psi}{\partial \mathbf{g}_\alpha} \cdot \delta \mathbf{g}_\alpha \right] dA \\ &= \bigcup_{e=1}^{nIE} \int_{\mathcal{I}_0^e} \left\{ \frac{\partial \Psi}{\partial [\mathbf{u}]} \cdot \left[\sum_{i=1}^{nNIE} N^{(i)}(\boldsymbol{\theta}) \left(\delta \mathbf{x}_+^{(i)} - \delta \mathbf{x}_-^{(i)} \right) \right] + \right. \\ &\quad \left. \frac{\partial \Psi}{\partial \mathbf{g}_\alpha} \cdot \left[\sum_{i=1}^{nNIE} \frac{1}{2} \frac{\partial N^{(i)}(\boldsymbol{\theta})}{\partial \theta^\alpha} \left(\delta \mathbf{x}_-^{(i)} + \delta \mathbf{x}_+^{(i)} \right) \right] dA \right\}. \end{aligned} \quad (5.65)$$

By introducing the vector of internal forces $\mathbf{R}_\pm^{(i)} = (\mathbf{R}_-^{(i)}, \mathbf{R}_+^{(i)})$ corresponding to node i of the considered finite element at the lower (-) or at the upper (+) surface of the interface, Eq. (5.65) can be rewritten as

$$\delta_\varphi \bar{\mathcal{I}}(\varphi) = \bigcup_{e=1}^{nIE} \left[\sum_i^{nNIE} \mathbf{R}_-^{(i)} \cdot \delta \mathbf{x}_-^{(i)} + \sum_i^{nNIE} \mathbf{R}_+^{(i)} \cdot \delta \mathbf{x}_+^{(i)} \right] =: \bigcup_{e=1}^{nIE} \sum_i^{nNIE} \mathbf{R}_\pm^{(i)} \cdot \delta \mathbf{x}_\pm^{(i)}. \quad (5.66)$$

Consequently, a comparison between Eq. (5.66) and Eq. (5.65) yields

$$\mathbf{R}_\pm^{(i)} = \int_{\mathcal{I}_0} \left[\pm N^{(i)} \frac{\partial \Psi}{\partial [\mathbf{u}]} + \underbrace{\frac{1}{2} \frac{\partial N^{(i)}}{\partial \theta^\alpha} \frac{\partial \Psi}{\partial \mathbf{g}_\alpha}}_{\text{Summation over } \alpha} \right] dA. \quad (5.67)$$

Assembling all elemental contributions – including those related to bulk elements and prescribed forces – leads to the global residual vector $[\mathbf{R}]$. With this notation, the approximated weak form of equilibrium reads $[\mathbf{R}] = \mathbf{0}$. This equation depends on all unknown nodal positions with respect to the deformed configuration such as $\mathbf{x}_\pm^{(i)}$.

In order to find the solution $[\mathbf{R}] = \mathbf{0}$, a Newton-Raphson scheme is employed. Therefore, the consistent linearisation of the system is needed. Starting from Eq. (5.66), the general structure of this linearisation due to the interface's contribution is

$$\Delta_\varphi (\delta_\varphi \bar{\mathcal{I}}) = \bigcup_{e=1}^{nIE} \sum_{i=1}^{nNIE} \delta \mathbf{x}_\pm^{(i)} \cdot \Delta \mathbf{R}_\pm^{(i)}. \quad (5.68)$$

Considering residual (5.67), the linearisation of $\mathbf{R}_\pm^{(i)}$ shows the format

$$\Delta \mathbf{R}_\pm^{(i)} = \int_{\mathcal{I}_0} \left[\pm N^{(i)} \Delta \left(\frac{\partial \Psi}{\partial \llbracket \mathbf{u} \rrbracket} \right) + \frac{1}{2} \frac{\partial N^{(i)}(\boldsymbol{\theta})}{\partial \theta^\alpha} \Delta \left(\frac{\partial \Psi}{\partial \mathbf{g}_\alpha} \right) \right] dA. \quad (5.69)$$

The linearisations involved in Eq. (5.69) can be computed as

$$\Delta \left(\frac{\partial \Psi}{\partial \llbracket \mathbf{u} \rrbracket} \right) = \frac{\partial^2 \Psi}{\partial \llbracket \mathbf{u} \rrbracket \otimes \partial \llbracket \mathbf{u} \rrbracket} \cdot \Delta \llbracket \mathbf{u} \rrbracket + \frac{\partial^2 \Psi}{\partial \llbracket \mathbf{u} \rrbracket \otimes \partial \mathbf{g}_\alpha} \cdot \Delta \mathbf{g}_\alpha + \frac{\partial^2 \Psi}{\partial \llbracket \mathbf{u} \rrbracket \otimes \partial \boldsymbol{\alpha}} \cdot \Delta \boldsymbol{\alpha} \quad (5.70)$$

and

$$\Delta \left(\frac{\partial \Psi}{\partial \mathbf{g}_\alpha} \right) = \frac{\partial^2 \Psi}{\partial \mathbf{g}_\alpha \otimes \partial \mathbf{g}_\beta} \cdot \Delta \mathbf{g}_\beta + \frac{\partial^2 \Psi}{\partial \mathbf{g}_\alpha \otimes \partial \llbracket \mathbf{u} \rrbracket} \cdot \Delta \llbracket \mathbf{u} \rrbracket + \frac{\partial^2 \Psi}{\partial \mathbf{g}_\alpha \otimes \partial \boldsymbol{\alpha}} \cdot \Delta \boldsymbol{\alpha}. \quad (5.71)$$

It bears emphasis that the variation of internal variables $\boldsymbol{\alpha}$ has now indeed to be included. While the linearisations of $\llbracket \mathbf{u} \rrbracket$ and \mathbf{g}_β are obvious, i.e.,

$$\Delta \llbracket \mathbf{u} \rrbracket(\boldsymbol{\theta}) \approx \sum_{i=1}^{nNIE} N^{(i)}(\boldsymbol{\theta}) \left(\Delta \mathbf{x}_+^{(i)} - \Delta \mathbf{x}_-^{(i)} \right) \quad (5.72)$$

and

$$\Delta \mathbf{g}_\beta(\boldsymbol{\theta}) \approx \sum_{i=1}^{nNIE} \frac{1}{2} \frac{\partial N^{(i)}(\boldsymbol{\theta})}{\partial \theta^\beta} \left(\Delta \mathbf{x}_-^{(i)} + \Delta \mathbf{x}_+^{(i)} \right), \quad (5.73)$$

the linearisation of internal variables $\boldsymbol{\alpha}$ follows from linearising the constitutive update algorithm – in line with, e.g., the classic return-mapping algorithm in computational plasticity theory. This is shown next.

According to Eq. (5.52), if loading is signalled (non-vanishing damage evolution), identity

$$\kappa_j = \kappa_j(\Psi_j(\llbracket \mathbf{u} \rrbracket, \mathbf{g}_\alpha)) \quad (5.74)$$

holds true. This is an explicit function which relates internal variables κ_j to the deformation mapping (through $\llbracket \mathbf{u} \rrbracket$ and \mathbf{g}_α). A generalisation of this relation is

$$\boldsymbol{\alpha} = \boldsymbol{\alpha}(\llbracket \mathbf{u} \rrbracket, \mathbf{g}_\alpha). \quad (5.75)$$

Without going into too much detail, for implicitly defined constitutive models, Eq. (5.75), has to be replaced by the implicit relation

$$\mathcal{R} = \mathcal{R}(\boldsymbol{\alpha}, \llbracket \mathbf{u} \rrbracket, \mathbf{g}_\alpha) = \mathbf{0}. \quad (5.76)$$

For Eq. (5.75) as well as for Eq. (5.76), the linearisation of $\boldsymbol{\alpha}$ eventually results in

$$\Delta \boldsymbol{\alpha} = \Delta \boldsymbol{\alpha} (\Delta [\mathbf{u}], \Delta \mathbf{g}_\alpha). \quad (5.77)$$

Finally by inserting Eqs. (5.70) and (5.71), together with sensitivities (5.77) and approximations (5.72) and (5.73), into Eq. (5.69), the linearisation of $\mathbf{R}_\pm^{(i)}$ can be transferred into the compact notation

$$\Delta \mathbf{R}_\pm^{(i)} = \int_{\mathcal{I}_0} \sum_{j=1}^{nNIE} \left(\mathbf{K}_{(\pm+)}^{(ij)} \cdot \Delta \mathbf{x}_+^{(j)} + \mathbf{K}_{(\pm-)} \cdot \Delta \mathbf{x}_-^{(j)} \right) dA. \quad (5.78)$$

Here, \mathbf{K} is the stiffness matrix. In matrix notation it shows the structure

$$\mathbf{K}^{(ij)} = \begin{bmatrix} \mathbf{K}_{--}^{(ij)} & \mathbf{K}_{-+}^{(ij)} \\ \mathbf{K}_{+-}^{(ij)} & \mathbf{K}_{++}^{(ij)} \end{bmatrix} = \begin{bmatrix} \frac{d\mathbf{R}_-^{(i)}}{d\mathbf{x}_-^{(j)}} & \frac{d\mathbf{R}_-^{(i)}}{d\mathbf{x}_+^{(j)}} \\ \frac{d\mathbf{R}_+^{(i)}}{d\mathbf{x}_-^{(j)}} & \frac{d\mathbf{R}_+^{(i)}}{d\mathbf{x}_+^{(j)}} \end{bmatrix}. \quad (5.79)$$

Within this subsection, the generic implementation of the proposed framework for interfaces has been given. Further details — and the required derivatives — are provided in Appendix B.1. It is important to observe that the linearisation process relies on some non-trivial differentials.

Remark 12 *The integrals in Eq. (5.67) and Eq. (5.69) are computed numerically by employing a standard Gauss-type integration. For this reason, the proper number of integration points has to be chosen. Since quadratic interface elements are used, i.e., 6 nodes at the lower and 6 nodes at the upper part of the interface, the resulting stiffness matrix is a 36×36 matrix (12 nodes \times 3 Dofs = 36). Furthermore, the interface element shows 18 zero energy modes. This follows from setting $\mathbf{x}_-^{(i)} = \mathbf{x}_+^{(i)}$ which results in a vanishing displacement jump, and by observing that this coupling implies 18 independent nodal degrees of freedom. Since the stiffness matrix is a 36×36 matrix and since the interface shows 18 zero energy modes, the stiffness matrix has a rank of 18. Focusing on isotropic hyperelasticity for the sake of illustration, the interface stiffness matrix simplifies to*

$$\mathbf{K}_{\pm\pm}^{(ij)} = \int_{\mathcal{I}_0} \left[(\pm N^{(i)}) \frac{\partial^2 \Psi}{\partial [\mathbf{u}] \otimes \partial [\mathbf{u}]} (\pm N^{(j)}) \right] dA. \quad (5.80)$$

Accordingly, the integrand is represented by a matrix with a rank lower or equal to 3, since $\partial^2 \Psi / (\partial [\mathbf{u}] \otimes \partial [\mathbf{u}])$ is a 3×3 -matrix. Consequently, a necessary condition for the stiffness matrix to have a rank of 18 is a Gauss integration by means of 6 integration points. The same number also follows from postulating that product $N^{(i)} N^{(j)}$ should

be integrated exactly. Clearly, the proposed interface model is not isotropic. However, the respective stiffness matrix also shows terms of the type $N^{(i)} N^{(j)}$. Furthermore, the matrix connecting $\bar{\mathbf{T}}$ and $\llbracket \mathbf{u} \rrbracket$ as well as the one connecting \mathbf{A}^α and \mathbf{g}_α are 3×3 matrices. For this reason, a numerical integration by means of 6 Gauss points is indeed reasonable. However, it should not be ignored that a full Gauss integration may lead to numerical oscillations as reported in Svenning [96]. Fortunately, such instabilities have not been observed in the numerical examples.

5.4 Numerical investigation of balance of angular momentum

This section presents a comparison of numerical results within the classic fiber cohesive zone and the extended general interface framework derived in this chapter. To be more explicit, an anisotropic interface Helmholtz energy is considered. It will be shown that this leads to inconsistencies concerning fundamental physical laws within a classic fiber cohesive zone model. In contrast thereto the generalised interface model is indeed consistent in terms of physics. As shown in Subsection 5.3.1, the novel generalised interface model is characterised by residuum

$$[\mathbf{R}_\pm^{(i)}]_{\text{gen}} = \int_{\mathcal{I}_0} \left[\pm N^{(i)} \frac{\partial \Psi}{\partial \llbracket \mathbf{u} \rrbracket} + \frac{1}{2} \frac{\partial N^{(i)}}{\partial \theta^\alpha} \frac{\partial \Psi}{\partial \mathbf{g}_\alpha} \right] dA = \int_{\mathcal{I}_0} \left[\pm N^{(i)} \bar{\mathbf{T}} + \frac{1}{2} \frac{\partial N^{(i)}}{\partial \theta^\alpha} \mathbf{A}^\alpha \right] dA \quad (5.81)$$

while the second term is ignored in the classic framework, i.e.,

$$[\mathbf{R}_\pm^{(i)}]_{\text{cla}} = \int_{\mathcal{I}_0} \left[\pm N^{(i)} \frac{\partial \Psi}{\partial \llbracket \mathbf{u} \rrbracket} \right] dA = \int_{\mathcal{I}_0} [\pm N^{(i)} \mathbf{T}] dA. \quad (5.82)$$

With these preliminaries one example with two comparative numerical simulations is presented in the following. The L-shape structure already known from Section 4.7 is investigated. For the bulk material, quadratic displacement-driven 10-node tetrahedron finite elements together with a standard Neo-Hooke-type model are employed. The bulk material parameters are identical to the parameters used in Section 4.7. However, the discretisation is different since the crack path is prescribed for a better understanding of the influence of the opening process of the interface, see Fig. 5.3. The crack face where the standard quadratic displacement-driven 12-node interface elements, cf. Ortiz and Pandolfi [72], are implemented is plotted in red colour. In order to show the advantages of the generalised interface framework, the anisotropic Helmholtz energy

$$\Psi = \Psi(\llbracket \mathbf{u} \rrbracket, \mathbf{g}_\alpha) = \frac{1}{2} c_n (I_1 - I_2 - I_3) + \frac{1}{2} c_t (I_2 + I_3) \quad (5.83)$$

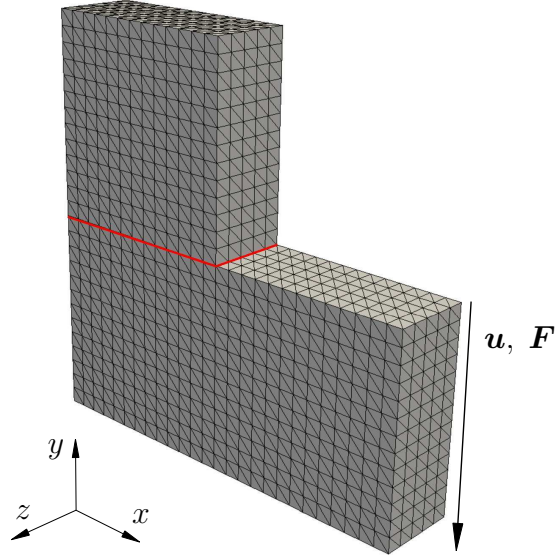


Figure 5.3: L-shape structure: undeformed discretisation with prescribed crack path. Within the red marked surface interface elements are implemented. The displacement vector \mathbf{u} is prescribed and the corresponding force vector \mathbf{F} arises.

is considered. Here, $c_n = 10^2$ kN/cm and $c_t = 2 \cdot 10^4$ kN/cm denote the interface stiffness in normal, respectively shear direction and the invariants I_1 , I_2 and I_3 were introduced in (5.45).

Since the differences between the classic and the generalised framework require the consideration of large deformations, a displacement of $u = 30$ cm is prescribed. The displacement is prescribed in 30 time steps. In order to find the solution in the both cases $[\mathbf{R}]_{\text{gen}} = \mathbf{0}$ and $[\mathbf{R}]_{\text{cla}} = \mathbf{0}$, a Newton-Raphson scheme is employed. In line with the underlying theory, the generalised model leads to a vanishing angular momentum, i.e.,

$$[\mathbf{M}]_{\text{gen}} = \sum_{i=1}^{n_n} [\mathbf{R}]_{\text{gen}}^{(i)} \times \mathbf{x}^{(i)} = \mathbf{0}, \quad (5.84)$$

where n_n denotes the number of nodes of the model. The amplitude of the corresponding force is

$$\|\mathbf{F}_{\text{gen}}\| = 20,329 \text{ kN}. \quad (5.85)$$

The force \mathbf{F}_{gen} refers to the edge where the displacement is prescribed, see Fig. 5.3. By way of contrast, the classic approach applied to the anisotropic constitutive model yields a resulting angular momentum

$$[\mathbf{M}]_{\text{cla}} = \sum_{i=1}^{n_n} [\mathbf{R}]_{\text{cla}}^{(i)} \times \mathbf{x}^{(i)} = \begin{bmatrix} -0.67 \\ 0.38 \\ -83,164.92 \end{bmatrix} \text{ kN cm} \neq \mathbf{0} \quad (5.86)$$

with

$$\|[\mathbf{M}]_{\text{cla}}\| = 83,164 \text{ kN cm}. \quad (5.87)$$

This is inconsistent in terms of physics. The amplitude of the corresponding force is

$$\|\mathbf{F}_{\text{cla}}\| = 20,175 \text{ kN}. \quad (5.88)$$

It turns out that the difference between the corresponding forces in the classic case $\|\mathbf{F}\|_{\text{cla}}$ and in the generalised model $\|\mathbf{F}\|_{\text{gen}}$ is negligible. However, the non-vanishing angular momentum is not consistent in terms of physics. In order to give a relation for this, the resultant moment about point \mathbf{X}_P is considered, see Fig. 5.4. Related to this

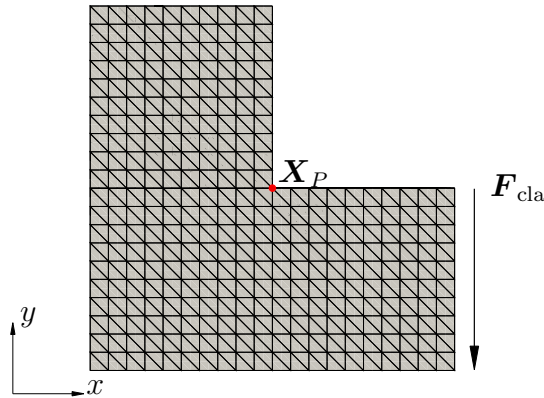


Figure 5.4: L-shape structure: corresponding force vector \mathbf{F}_{cla} and edge point \mathbf{X}_P . The resultant moment on this point is considered in order to give a relation for the error arising with classic cohesive zone theory.

point, the corresponding force \mathbf{F}_{cla} generates a resultant angular momentum of $\|\mathbf{F}_{\text{cla}}\| \cdot \|[-25, 0, 0]\| \text{ cm} = 504,375 \text{ kNcm}$. It is noteworthy that there is a factor of six between the corresponding moment appearing at the L-shape corner and the resultant angular momentum from the simulation with the classic cohesive fiber framework. Hence, the resultant angular momentum is not negligible and has a high influence on the real material behaviour.

A further graphical illustration of the problems arising with classic cohesive zone theory within this example is shown in Fig. 5.5. It shows the deformed configuration of

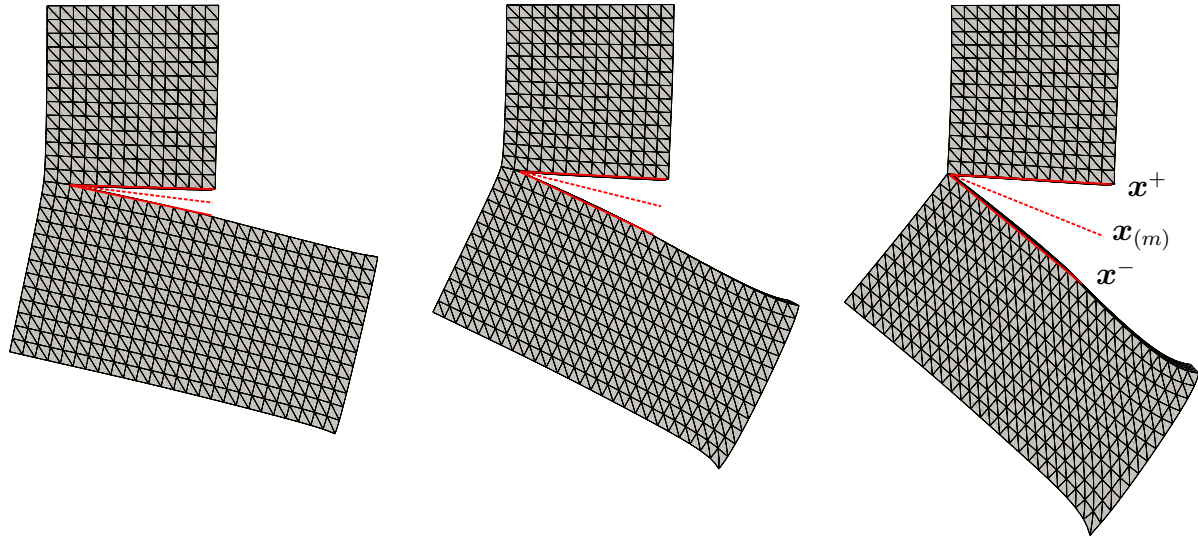


Figure 5.5: L-shape structure: deformed configuration with red marked upper and lower crack surface as well as fictitious mid-surface (dashed line) at three different time steps – left configuration after 10 time steps ($u = 10$ cm), middle configuration after 20 time steps ($u = 20$ cm) and left picture after 30 time steps ($u = 30$ cm).

the L-shape structure at three different time steps. The upper and lower crack surfaces are marked by red lines, while the fictitious mid-surface is indicated with the red dashed line. It becomes clear that even after 10 time steps the assumption of parallel crack faces, as it is the case in small deformations, is no longer valid. Since the structural tensors, for instance the normal vector $\bar{\mathbf{n}}$, are related to the current mid-surface (dashed red line), their adjustment during deformation is not negligible in the case of large displacements.

6 Size effects due to material interfaces

Cohesive zone models are most frequently applied to the analysis of cracking at the macroscale. However, they certainly can also be used at the microscale, e.g., for the description of microcracks or debonding between different constituents, cf. Javili et al. [50]. This application is very interesting from a materials science point of view, since the coupling of bulk materials and interface materials naturally introduces a length scale in the resulting response and, thus, a size-effect can be modelled. Such an example will be studied in this chapter. In order to define the effective mechanical response due to the interaction between bulk and interface materials at the microscale, a novel computational homogenisation scheme is presented. This scheme allows the analysis of the influence of material interfaces on the resulting macroscopic (effective) material response. It is shown by numerical examples that the interaction of bulk energies and interface energies leads, in a very natural manner, to a complex size effect. It includes the frequently observed „the smaller the stiffer“ relation, but also the less often observed „the smaller the softer“ relation. However, since the overall response is usually a superposition of such relations, the effective properties cannot generally be characterised by one of the aforementioned limiting relations.

6.1 Preliminaries

In the following, a representative volume element (RVE) containing bulk materials and material interfaces is considered, cf. Fig. 6.1. Quantities belonging to the macroscopic scale are denoted by $(\bullet)^M$. The kinematics and constitutive relations for the macroscale follow the correlations presented in Chapter 2 for classic bulk materials. Thus, the focus is on the microscopic scale. For a unified review of several homogenisation theories, the interested reader is referred to Saeb et al. [85] and the references cited therein. The solution of the mechanical problem characterising the microscale is governed by balance of linear momentum, i.e.,

$$\text{DIV} \mathbf{P} = \mathbf{0} \quad \forall \mathbf{X} \in \mathcal{B}_0 \tag{6.1}$$

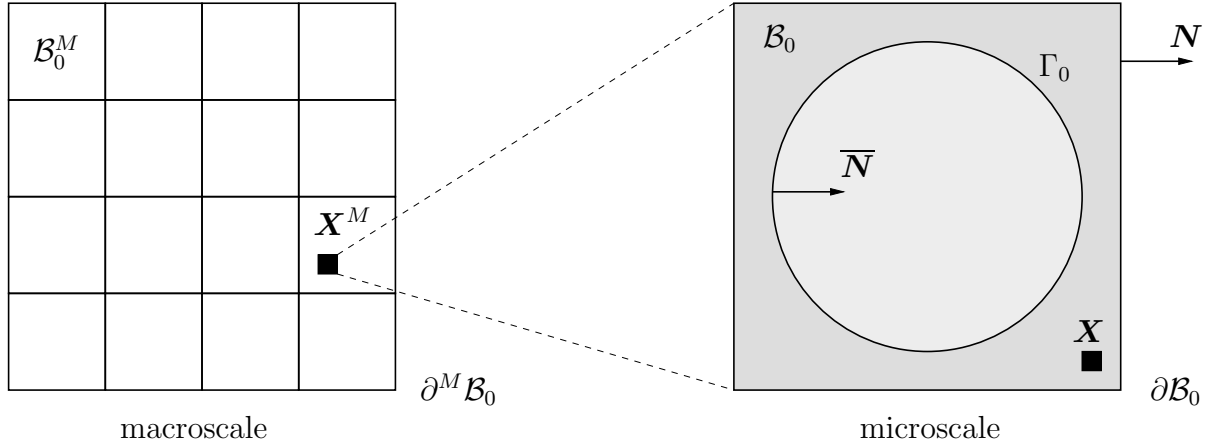


Figure 6.1: Sketch of the multiscale (two-scale) homogenisation problem: Left hand side: macroscopic problem (respective variables are denoted by $(\bullet)^M$). A representative volume element (right hand side) is assigned to each macroscopic material point \mathbf{X}^M . The representative volume element consists of an inclusion embedded in a matrix. The bulk materials are separated by a general interface with normal vector $\bar{\mathbf{N}}$.

for all points belonging to bulk materials and

$$\overline{\text{DIV}} \bar{\mathbf{P}} + (\mathbf{T}^+ + \mathbf{T}^-) = \mathbf{0} \quad \forall \mathbf{X} \in \Gamma_0 \quad (6.2)$$

for all points belonging to the material interface, cf. Subsection 5.2.3. In Eqs. (6.1) and (6.2), \mathbf{P} is the classic first Piola-Kirchhoff stress tensor at microscale, $\bar{\mathbf{P}}$ represents its interfacial counterpart, \mathbf{T}^+ and \mathbf{T}^- denote the Piola-Kirchhoff traction vectors acting at the interface as introduced in the previous chapters. According to Eqs. (6.1) and (6.2), vanishing external body forces have been assumed for the sake of simplicity. However, they could be accounted for in a straightforward manner.

6.2 Average theorems for interface homogenisation

Up to now, the boundary conditions at the microscale have been implicitly assumed as given. Clearly, they are related to the macroscopic problem. In order to couple the deformation at the microscale to that at the macroscale, the standard ansatz

$$\mathbf{F}^M := \frac{1}{\mathcal{V}_0} \int_{\partial \mathcal{B}_0} \mathbf{x} \otimes \mathbf{N} \, dA, \quad (6.3)$$

is adopted in [50]. Here, \mathcal{V}_0 denotes the total volume of the RVE, respectively of the matrix and the inclusion. Since this ansatz is based on the deformation at the boundary of the RVE, the effect of material interfaces cannot be explicitly seen – if the interfaces do not cross the boundary as shown in Fig. 6.1. However, the case of interfaces crossing the

boundaries has to be excluded anyway, since it would neither comply with the assumed periodicity (see next paragraph) nor with the assumption of scale separation. Following [50], Eq. (6.3) can be rewritten as

$$\mathbf{F}^M := \frac{1}{\mathcal{V}_0} \int_{\mathcal{B}_0} \mathbf{F} \, dV + \frac{1}{\mathcal{V}_0} \int_{\Gamma_0} \llbracket \mathbf{u} \rrbracket \otimes \mathbf{N} \, dA \quad (6.4)$$

by using the gradient theorem. By doing so, the classic first term (volume averaging) is obtained, together with the non-standard second term associated with the displacement discontinuity. Clearly, for coherent interfaces without displacement jumps, Eq. (6.4) reduces to the classic average deformation gradient theorem.

In a similar manner, the homogenisation of the stress tensor can be derived. For that purpose – and in line with Eq. (6.3) – the ansatz

$$\mathbf{P}^M := \frac{1}{\mathcal{V}_0} \int_{\partial \mathcal{B}_0} \mathbf{T}^* \otimes \mathbf{X} \, dA, \quad (6.5)$$

is made which can be transformed into the equivalent equation

$$\mathbf{P}^M := \frac{1}{\mathcal{V}_0} \int_{\mathcal{B}_0} \mathbf{P} \, dV + \frac{1}{\mathcal{V}_0} \int_{\Gamma_0} \overline{\mathbf{P}} \, dA. \quad (6.6)$$

Accordingly, one obtains the classic first term (volume averaging) again, together with a non-classic part corresponding to the material interface. However, while the non-standard term related to averaging of the deformation gradient (6.4) shows the displacement jump, the non-standard term related to averaging of the stress tensor (6.6) contains the interface stress tensor $\overline{\mathbf{P}}$. As a consequence, the influence of a classic cohesive zone model characterised by a Helmholtz energy of type $\Psi = \Psi(\llbracket \mathbf{u} \rrbracket)$ (which implies $\overline{\mathbf{P}} = \mathbf{0}$) can only be seen in the averaging of the deformation gradient. By way of contrast, an interface model of type $\Psi = \Psi(\overline{\mathbf{F}})$ falling into the range of Gurtin & Murdoch's framework [36] (which implies $\llbracket \mathbf{u} \rrbracket = \mathbf{0}$) can only be seen in the averaging of the stress tensor. Since general interface models as presented in Chapter 5 can be interpreted as a non-trivial coupling of the aforementioned models, both non-standard terms have to be considered.

In a classic homogenisation scheme, incremental energy equivalence between the micro- and the macroscale is imposed by the Hill-Mandel condition, i.e.,

$$\mathbf{P}^M : \dot{\mathbf{F}}^M = \frac{1}{\mathcal{V}_0} \int_{\partial \mathcal{B}_0} \mathbf{T}^* \cdot \dot{\mathbf{x}} \, dA. \quad (6.7)$$

The classic representation of the Hill-Mandel condition as surface integral does not need to be modified in the presence of interfaces, cf. [50]. Suitable boundary conditions

are therefore derived, starting with representation (6.7). This derivation is in line with Schröder [88, Chapter 3]. Relation (6.7) can therefore be expressed equivalently as

$$\frac{1}{\mathcal{V}_0} \int_{\partial\mathcal{B}_0} \mathbf{T}^* \cdot \dot{\mathbf{x}} \, dA - \mathbf{P}^M : \dot{\mathbf{F}}^M + \underbrace{\mathbf{P}^M : \dot{\mathbf{F}}^M - \mathbf{P}^M : \dot{\mathbf{F}}^M}_{=0} = 0. \quad (6.8)$$

According to Eqs. (6.3) and (6.5) and considering the gradient theorem

$$\frac{1}{\mathcal{V}_0} \int_{\partial\mathcal{B}_0} \mathbf{N} \otimes \mathbf{X} \, dA = \frac{1}{\mathcal{V}_0} \int_{\mathcal{B}_0} [\text{GRAD}(\mathbf{X})]^T \, dV = \frac{1}{\mathcal{V}_0} \int_{\mathcal{B}_0} \mathbf{I} \, dV = \mathbf{I} \quad (6.9)$$

the second, third and last terms in Eq. (6.8) can be rewritten as

$$\begin{aligned} \mathbf{P}^M : \dot{\mathbf{F}}^M &= \mathbf{P}^M : \frac{1}{\mathcal{V}_0} \int_{\partial\mathcal{B}_0} \dot{\mathbf{x}} \otimes \mathbf{N} \, dA = \frac{1}{\mathcal{V}_0} \int_{\partial\mathcal{B}_0} (\mathbf{P}^M \cdot \mathbf{N}) \cdot \dot{\mathbf{x}} \, dA, \\ \mathbf{P}^M : \dot{\mathbf{F}}^M &= \frac{1}{\mathcal{V}_0} \int_{\partial\mathcal{B}_0} \mathbf{T}^* \otimes \mathbf{X} \, dA : \dot{\mathbf{F}}^M = \frac{1}{\mathcal{V}_0} \int_{\partial\mathcal{B}_0} \mathbf{T}^* \cdot (\dot{\mathbf{F}}^M \cdot \mathbf{X}) \, dA, \\ \mathbf{P}^M : \dot{\mathbf{F}}^M &= \mathbf{P}^M \cdot \frac{1}{\mathcal{V}_0} \int_{\mathcal{B}_0} [\text{GRAD}(\mathbf{X})]^T \, dV \cdot \dot{\mathbf{F}}^M = \int_{\partial\mathcal{B}_0} (\dot{\mathbf{F}}^M \cdot \mathbf{X}) \cdot (\mathbf{P}^M \cdot \mathbf{N}) \, dA. \end{aligned} \quad (6.10)$$

Inserting relation (6.10) into (6.8) leads to the Hill-Mandel condition in the form

$$\frac{1}{\mathcal{V}_0} \int_{\partial\mathcal{B}_0} (\mathbf{T}^* - \mathbf{P}^M \cdot \mathbf{N}) \cdot (\dot{\mathbf{x}} - \dot{\mathbf{F}}^M \cdot \mathbf{X}) \, dA = 0. \quad (6.11)$$

Following the derivation for suitable boundary conditions presented in [50], Eq. (6.11) is also valid if the RVE contains interfaces. Nevertheless, the equivalent volume integral for the classic condition has to be extended in order to account for interfaces. The extended energy equivalence equation between the macro- and the microscale including interfaces reads

$$\mathbf{P}^M : \dot{\mathbf{F}}^M = \frac{1}{\mathcal{V}_0} \int_{\mathcal{B}_0} \mathbf{P} : \dot{\mathbf{F}} \, dV + \frac{1}{\mathcal{V}_0} \int_{\Gamma_0} \overline{\mathbf{P}} : \dot{\overline{\mathbf{F}}} \, dA + \frac{1}{\mathcal{V}_0} \int_{\Gamma_0} \overline{\mathbf{T}} \cdot \llbracket \dot{\mathbf{u}} \rrbracket \, dA. \quad (6.12)$$

Here, the relation

$$\frac{1}{\mathcal{V}_0} \int_{\partial\mathcal{B}_0} \mathbf{T}^* \cdot \dot{\mathbf{x}} \, dA = \frac{1}{\mathcal{V}_0} \int_{\mathcal{B}_0} \mathbf{P} : \dot{\mathbf{F}} \, dV + \frac{1}{\mathcal{V}_0} \int_{\Gamma_0} \overline{\mathbf{P}} : \dot{\overline{\mathbf{F}}} \, dA + \frac{1}{\mathcal{V}_0} \int_{\Gamma_0} \overline{\mathbf{T}} \cdot \llbracket \dot{\mathbf{u}} \rrbracket \, dA, \quad (6.13)$$

has been taken from [50], where a detailed derivation of (6.13) can be found. As already mentioned, suitable boundary conditions for the microscopic problem can be determined

by fulfilling the Hill-Mandel condition (6.11). As shown in [50], the Hill-Mandel condition including interfaces is represented as

$$\begin{aligned} \mathbf{P}^M : \dot{\mathbf{F}}^M - \frac{1}{\mathcal{V}_0} \int_{\mathcal{B}_0} \mathbf{P} : \dot{\mathbf{F}} \, dV + \frac{1}{\mathcal{V}_0} \int_{\Gamma_0} \bar{\mathbf{P}} : \dot{\bar{\mathbf{F}}} \, dA + \frac{1}{\mathcal{V}_0} \int_{\Gamma_0} \bar{\mathbf{T}} \cdot \llbracket \dot{\mathbf{u}} \rrbracket \, dA = \\ \frac{1}{\mathcal{V}_0} \int_{\partial \mathcal{B}_0} (\mathbf{T}^* - \mathbf{P}^M \cdot \mathbf{N}) \cdot (\dot{\mathbf{x}} - \dot{\mathbf{F}}^M \cdot \mathbf{X}) \, dA. \end{aligned} \quad (6.14)$$

Obviously, the Hill-Mandel condition is satisfied if the right-hand side of Eq. (6.12) vanishes, which is equivalent to fulfilling Eq. (6.11). According to [50] admissible boundary conditions are the ones already known from classic homogenisation. Thus, linear displacement boundary conditions ($\mathbf{x} = \mathbf{F}^M \cdot \mathbf{X}$) as well as constant traction boundary conditions ($\mathbf{T}^* = \mathbf{P}^M \cdot \mathbf{N}$) agree with Eq. (6.14). A third class of boundary conditions involves periodic boundary conditions. To be more precise, the classic choice

$$\mathbf{x} = \mathbf{F}^M \cdot \mathbf{X} + \mathbf{w} \quad (6.15)$$

is made. As a consequence, the deformation map at the microscale consists of a part reflecting the macroscopic deformation gradient, as well as of a part allowing for fluctuations \mathbf{w} . The fluctuations are enforced to be periodic at the boundaries of the RVE, i.e. $\mathbf{w}^+ = \mathbf{w}^-$. From Eq. (6.15) it follows that

$$\dot{\mathbf{x}} = \dot{\mathbf{F}}^M \cdot \mathbf{X} + \dot{\mathbf{w}}. \quad (6.16)$$

Inserting this into Eq. (6.7) leads to

$$\mathbf{P}^M : \dot{\mathbf{F}}^M = \frac{1}{\mathcal{V}_0} \int_{\partial \mathcal{B}_0} \mathbf{T}^* \cdot (\dot{\mathbf{F}}^M \cdot \mathbf{X}) \, dA + \frac{1}{\mathcal{V}_0} \int_{\partial \mathcal{B}_0^+} \mathbf{T}^{*+} \cdot \dot{\mathbf{w}}^+ \, dA + \frac{1}{\mathcal{V}_0} \int_{\partial \mathcal{B}_0^-} \mathbf{T}^{*-} \cdot \dot{\mathbf{w}}^- \, dA. \quad (6.17)$$

Since the fluctuations are periodic, it holds that $\dot{\mathbf{w}}^+ = \dot{\mathbf{w}}^-$. Furthermore, the tractions are anti-periodic, i.e. $\mathbf{T}^{*+} = -\mathbf{T}^{*-}$. Thereby, it follows that

$$\frac{1}{\mathcal{V}_0} \int_{\partial \mathcal{B}_0^+} \mathbf{T}^{*+} \cdot \dot{\mathbf{w}}^+ \, dA + \frac{1}{\mathcal{V}_0} \int_{\partial \mathcal{B}_0^-} \mathbf{T}^{*-} \cdot \dot{\mathbf{w}}^- \, dA = \frac{1}{\mathcal{V}_0} \int_{\partial \mathcal{B}_0^+} (\mathbf{T}^{*+} - \mathbf{T}^{*+}) \cdot \dot{\mathbf{w}} \, dA = 0. \quad (6.18)$$

Following [50, 88] the resulting terms in Eq. (6.17) fulfill the Hill-Mandel condition.

6.3 Numerical implementation

This section deals with the numerical implementation of the homogenisation scheme presented in Section 6.2. For the prolongation condition, Eq. (6.15) is employed. By

doing so, macroscopic deformation gradient \mathbf{F}^M defines the boundary conditions – up to the periodic fluctuation \mathbf{w} . This step is identical to the one for classic bulk materials. For this reason, no additional implementation effort is required – provided a code for bulk materials exists. For the same reason, no further explanation seems necessary.

Having defined the boundary conditions, the mechanical problem associated with the microscale can be computed. For that purpose, strong forms (6.1) and (6.2) are approximated by means of the finite element method. The solution of the resulting set of nonlinear equations gives the deformation mapping which, in turn, allows the computation of the stresses at the microscale.

The computational scheme is completed by an averaging step which yields the macroscopic stresses. This step is usually based on Eq. (6.5) or Eq. (6.6).

6.3.1 Computation of macroscopic stresses based on volume integrals

In this work, representation (6.6) is considered. A straightforward evaluation of this equation by means of numerical integration leads to

$$\mathbf{P}^M = \mathbf{P}^{MB} + \mathbf{P}^{MI} \approx \frac{1}{\mathcal{V}_0} \left[\sum_{i=1}^{nBE} \sum_{j=1}^{nGPB} \mathbf{P}^{(ij)} V^{(ij)} + \sum_{i=1}^{nIE} \sum_{j=1}^{nGPI} \bar{\mathbf{P}}^{(ij)} A^{(ij)} \right]. \quad (6.19)$$

Here, nBE denotes the number of bulk elements, $nGPB$ is the number of Gauss points per Bulk element and $V^{(ij)}$ is a weighting coefficient (volume) due to the numerical integration. Analogously, nIE is the number of interface elements, $nGPI$ the number of Gauss points per interface element and $A^{(ij)}$ a weighting coefficient (area) due to the numerical integration.

6.3.2 Computation of macroscopic stresses based on surface integrals

As an alternative to Eq. (6.19), one could also start from the surface-specific representation (6.5). This choice has the advantage that existing bulk homogenisation codes do not have to be modified at all – if they are based on Eq. (6.5) and if none of the interfaces crosses the boundary of the RVE. In this case, the macroscopic stresses can be computed as

$$\mathbf{P}^M \approx \frac{1}{\mathcal{V}_0} \sum_{i=1}^{nSE} \sum_{j=1}^{nGPB} \left[\mathbf{P}^{(ij)} \cdot \mathbf{N}^{(ij)} \right] \otimes \mathbf{X}^{(ij)} A^{(ij)}, \quad (6.20)$$

where nSE denotes the number of bulk facets joining the facet of the RVE, $nGPB$ is the number of Gauss points necessary for the numerical integration, $\mathbf{X}^{(ij)}$ is the referential

coordinate of the considered Gauss point and A^{ij} is a weighting coefficient (area) due to the numerical integration. Furthermore, \mathbf{N} represents the normal vector at the boundary of the considered RVE.

6.3.3 Computation of macroscopic stresses based on the vector of internal forces

Finally, a third possibility of computing the macroscopic stresses is elaborated. In order to follow this third possibility, the finite element approximation of Eq. (6.5) is considered. The contribution of node (i) of one finite element having one facet at the boundary of the RVE reads (only bulk elements are at the boundary of the RVE)

$$\mathbf{P}^M \approx \frac{1}{\mathcal{V}_0} \left\{ \int (\mathbf{P} \cdot \mathbf{N}) N^{(i)} dA \right\} \otimes \mathbf{X}^{(i)}, \quad (6.21)$$

where the reference configuration of the aforementioned facet is approximated by $\mathbf{X} \approx \sum_{i \in \partial RVE} N^{(i)} \mathbf{X}^{(i)}$. Here, $N^{(i)}$ are the shape functions and $\mathbf{X}^{(i)}$ are the nodal positions. Clearly, representation (6.21) is related to the vector of internal forces. In order to show this explicitly, the weak form of equilibrium for bulk elements is rewritten first

$$\int_{\Omega} \mathbf{P} \cdot \text{GRAD} \delta \mathbf{x} dV \stackrel{\text{DIV} \mathbf{P} = 0}{=} \int_{\partial \Omega} \mathbf{T}^* \cdot \delta \mathbf{x} dV \quad (6.22)$$

and subsequently approximated by means of finite elements. The contribution resulting from a single finite element is given by (with $\delta \mathbf{x} \approx \sum_i N^{(i)} \delta \mathbf{x}^{(i)}$)

$$\int_{\Omega} \mathbf{P} \cdot \text{GRAD} \delta \mathbf{x} dV \approx \sum_i \left\{ \int (\mathbf{P} \cdot \mathbf{N}) N^{(i)} dA \right\} \cdot \delta \mathbf{x}^{(i)} =: \sum_i \mathbf{R}^{(i)} \cdot \delta \mathbf{x}^{(i)}. \quad (6.23)$$

By comparing Eq. (6.23) to Eq. (6.21) an alternative representation of the macroscopic stress tensor can be derived, i.e.,

$$\mathbf{P}^M \approx \frac{1}{\mathcal{V}_0} \sum_i^{\text{elements}} \sum_j^{\text{nodes}} \mathbf{R}^{(i)} \otimes \mathbf{X}^{(j)}. \quad (6.24)$$

Since the assembled contributions of all points belonging to the interior of the RVE vanish, only nodes at the boundary of the RVE contribute to Eq. (6.24), i.e.,

$$\mathbf{P}^M \approx \frac{1}{\mathcal{V}_0} \sum_i^{\text{elements}} \sum_j^{\text{nodes}} \mathbf{R}^{(i)} \otimes \mathbf{X}^{(j)} = \frac{1}{\mathcal{V}_0} \sum_i^{\text{elements}} \sum_j^{\text{nodes} \cap \partial RVE} \mathbf{R}^{(i)} \otimes \mathbf{X}^{(j)}. \quad (6.25)$$

For this reason and depending on the implementation, one can either consider all nodes or only those belonging to the boundary of the RVE.

6.4 Numerical Examples

This section deals with numerical analyses of the influence of general material interfaces on the macroscopic response. The focus is on two different aspects: (a) anisotropy of the interface model, i.e., mode-I failure vs. mode-II/III failure; (b) the size effect induced by general material interfaces. For all computations, a representative volume element consisting of a cube with a spherical inclusion is considered, see Fig. 6.2.

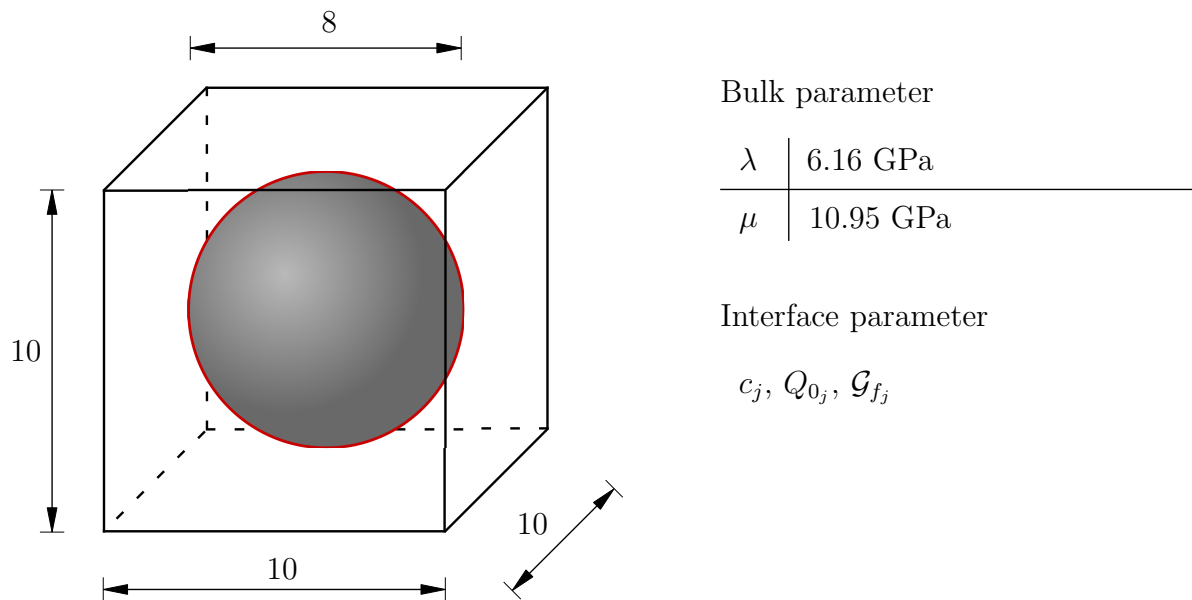


Figure 6.2: Numerical analysis of an RVE consisting of a spherical inclusion embedded in a matrix. The bulk materials are separated by a general interface: geometry and bulk material parameters, cf. [84]. The interface parameters according to Tab. 5.1 are summarised on page 110 corresponding to the depicted degradation mechanism j .

The bulk material is discretised by means of standard 10-node quadratic displacement-driven tetrahedron finite elements, while standard 12-node quadratic displacement-driven interface elements (6 nodes on each side) are used for the interface between the inclusion and the surrounding matrix, cf. Ortiz and Pandolfi [72]. Additional interfaces resulting from cracks in the inclusion or in the matrix are not considered. Since the focus of this work is on material interfaces, a standard Neo-Hooke model with identical elastic material parameters for the matrix and the inclusion is chosen for the bulk materials (the respective Lamé parameters are denoted by λ and μ , see Fig. 6.2). The RVE shown in

Fig. 6.2 is subjected to uniaxial strain. The respective macroscopic deformation gradient reads

$$\mathbf{F}^M = \begin{bmatrix} 1.05 & 0 & 0 \\ 0 & 1 & 0 \\ 0 & 0 & 1 \end{bmatrix}, \quad (6.26)$$

i.e., the maximum engineering strains have an amplitude of 5%. The load is applied in five equidistant load steps in the hyperelastic model and in 50 equidistant load steps in the simulations including damage. Periodic boundary conditions are enforced, cf. Eq. (6.15).

6.4.1 Analysis of the anisotropy induced by the general interface model

First, a purely hyperelastic interface is investigated for different stiffnesses in normal direction (the respective stiffness is denoted by c_n) and in shear direction (the respective stiffness is denoted by c_t). The Helmholtz energy of the elastic interface reads

$$\Psi = \Psi(\llbracket \mathbf{u} \rrbracket, \mathbf{g}_\alpha) = \frac{1}{2} c_n (I_1 - I_2 - I_3) + \frac{1}{2} c_t (I_2 + I_3), \quad (6.27)$$

where the invariants are defined as

$$I_1 = \llbracket \mathbf{u} \rrbracket \cdot \llbracket \mathbf{u} \rrbracket, \quad I_2 = \llbracket \mathbf{u} \rrbracket \cdot (\mathbf{g}_1 \otimes \mathbf{g}^1) \cdot \llbracket \mathbf{u} \rrbracket \quad \text{and} \quad I_3 = \llbracket \mathbf{u} \rrbracket \cdot (\mathbf{g}_2 \otimes \mathbf{g}^2) \cdot \llbracket \mathbf{u} \rrbracket. \quad (6.28)$$

The following two limiting cases are considered:

- (a) Isotropic hyperelasticity with $c_n = c_t = 10^8 \text{ kN/cm}^3 \gg 0$
Homogeneous problem; matrix without an inclusion
- (b) Isotropic hyperelasticity with $c_n = c_t = 10^{-1} \text{ kN/cm}^3 \approx 0$
Matrix with a spherical pore

Case (a) characterises a perfect interface which cannot open. Since the bulk materials (inclusion and matrix) have been assumed to be identical, this case is equivalent to an RVE consisting only of a matrix without an inclusion, i.e., a homogeneous problem. By way of contrast, the inclusion is not connected to the matrix in case (b). Consequently, it corresponds to a matrix with a pore whose diameter is identical to the one of the inclusion. Clearly, these cases are indeed limiting cases. To be more precise, the response of a realistic interface model is bounded by such cases.

In addition to the purely isotropic and hyperelastic interface, several computations based on different damage models were also performed. To be more precise, the following three different models are compared:

(c) Isotropic mixed-mode fiber model:

$$\Psi = (1 - d) \frac{1}{2} c \|\llbracket \mathbf{u} \rrbracket\|^2$$

$$Q_0 = 270\text{MPa}, \quad \mathcal{G}_f = 650\text{kN/m}$$

(d) Anisotropic damage in normal direction (mode-I)

with out-of-plane membrane forces:

$$\Psi = (1 - d_n^{(n)}) \frac{1}{2} [c_n (I_1 - I_2 - I_3) + c_t (I_2 + I_3)]$$

$$Q_{0n} = 270\text{MPa}, \quad \mathcal{G}_{fn} = 650\text{kN/m}$$

(e) Anisotropic damage in shear direction (mode-II/III)

with out-of-plane membrane forces:

$$\Psi = (1 - d_t^{(t)}) \frac{1}{2} [c_n (I_1 - I_2 - I_3) + c_t (I_2 + I_3)]$$

$$Q_{0t} = 270\text{MPa}, \quad \mathcal{G}_{ft} = 650\text{kN/m}$$

For the isotropic damage model, the elastic stiffness is chosen as $c = 10^4 \text{ kN/cm}^3$, while $c_n = 2 \cdot 10^4 \text{ kN/cm}^3 = 2 c_t$ is set for the anisotropic damage models. Furthermore, the driving force conjugate to d is the total elastic energy $\Psi^0 = 1/2c \llbracket \mathbf{u} \rrbracket \cdot \llbracket \mathbf{u} \rrbracket$ in the isotropic damage model (c). By way of contrast, $d_n^{(n)}$ and $d_t^{(t)}$ are only governed by the normal part Ψ_n^0 of the total elastic energy (model (d)) and the tangential part Ψ_t^0 of the total elastic energy (model (e)) in the case of the anisotropic damage models, see Tab. (5.1). It has to be noted that in the case of crack closure, the models have to be slightly modified, see Remark 11. However, the crack closure effect is only of minor importance for the analysed RVE and as a consequence it could be neglected.

Figure 6.3 shows the macroscopic stress (11-component of the first Piola-Kirchhoff stress tensor) plotted over the macroscopic deformation gradient (11-component of the deformation gradient subtracted by 1). According to Fig. 6.3, model (a) and model (b) define the limiting cases: case (a) represents a perfect interface being equivalent to a homogeneous matrix with neither a pore nor an inclusion. By way of contrast, model (b) is associated with a pore in a matrix (no connection between the inclusion and the matrix). Consequently, model (a) defines the stiffest response while model (b) spans the softest response. All damage models (model (c), (d) and (e) described on page 110) are bounded by the aforementioned limiting cases. Furthermore, since the initial stiffness of the damage models is identical to that of the perfect interface, all damage models agree with model (a) during the first loading stage. When damage initiates, a deviation towards the pore-like model (b) can be observed. Since the same damage function $d(\kappa)$ as well as the same initial value of the internal variables κ have been chosen for all damage models, damage starts first in the isotropic damage model, since the total elastic energy Ψ^0 is always larger than the respective normal part Ψ_n^0 or the tangential part Ψ_t^0 of it. Furthermore, damage due to mode-I separation is more pronounced than damage due to mode-II/III separation. This was indeed expected for the analysed RVE under the considered loading.

The stronger effect of mode-I separation compared to that of mode-II/III separation can also be seen in Tab. 6.1: The normal component of the displacement jump is indeed

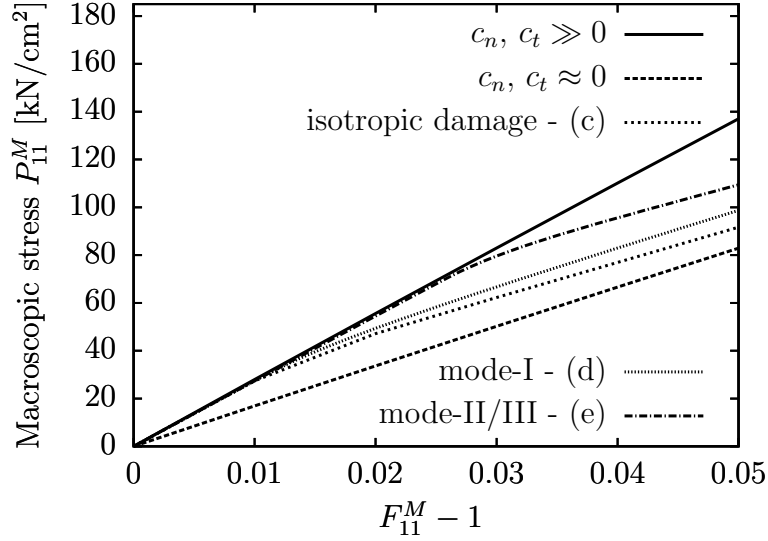


Figure 6.3: Numerical analysis of an RVE consisting of a spherical inclusion embedded in a matrix. The bulk materials are separated by a general interface: macroscopic stress (11-component of the first Piola-Kirchhoff stress tensor) plotted over macroscopic engineering strain (11-component of the deformation gradient subtracted by 1). Comparison between purely hyperelastic models (model (a) and model (b) on page 109) and damage models (model (c) and model (d) and model (e) on page 110)


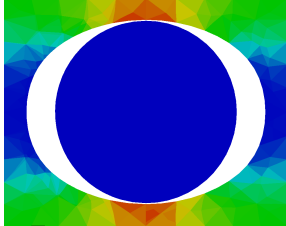
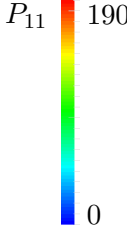
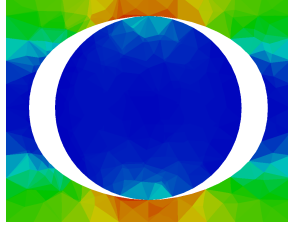
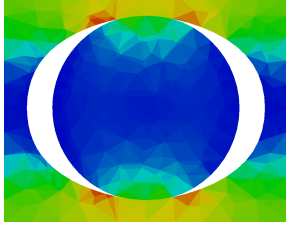
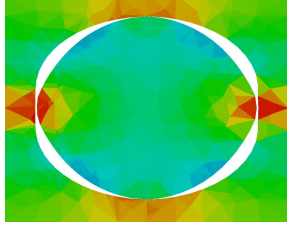
larger than its shear counterpart. The figures in Tab. 6.1 show the deformed RVE at the final stage of deformation. The colours are associated with the value of the 11-component of the first Piola-Kirchhoff stress tensor. According to the figures in Tab. 6.1 and as expected, higher stresses are observed below and above the inclusion for all models, i.e., in regions which are farthest away from those showing a fully softened response. In the case of model (e), high stress peaks can also be seen on the left as well as on the right hand side of the inclusion. In such zones the shear deformation within the interfaces is zero due to symmetry of the problem. Thus, damage caused by shearing does not evolve in this case.

Furthermore, Tab. 6.1 confirms that model (a) indeed corresponds to a homogeneous matrix.

6.4.2 Analysis of the size effect induced by interface models

While the energies associated with bulk materials scale with respect to volume, energies corresponding to interfaces scale with respect to area. The non-trivial superposition of both such scaling in the analysed RVE results in a size effect, cf. Javili et al. [50]. This size effect is analysed in the following section. For that purpose, geometrically equivalent RVEs are considered and the length of the cube is varied (from $l = 0.01$ cm up to $l = 100$ cm). The results are compared to the following three size independent limiting cases: (1) perfect interface behaviour resulting in an RVE with a homogeneous

Table 6.1: Numerical analysis of an RVE consisting of a spherical inclusion embedded in a matrix. The bulk materials are separated by a general interface: distribution of the stresses (component P_{11} [kN/cm^2] of the first Piola-Kirchhoff stress tensor) at a cut through the middle of the cube at the end of the simulation time (five times magnified deformation). Models (a) and (b) are described on page 109, while models (c), (d) and (e) are described on page 110

Hyperelasticity	 <p>(a) - perfect interface</p>	 <p>(b) - pore</p>	 <p>P_{11} 190 0</p>
Damage	 <p>(c) - isotropic</p>	 <p>(d) - mode-I</p>	 <p>(e) - mode-II</p>

stress state, (2) zero-stiffness interface leading to a pore like behaviour and (3) a rigid inclusion.

Regarding the interface, the following different constitutive models are considered:

- (1) Anisotropic hyperelastic cohesive zone model

with out-of-plane membrane forces:

$$\Psi_{\text{coh}}(\llbracket \mathbf{u} \rrbracket, \mathbf{g}_\alpha) = \frac{1}{2} [c_n (I_1 - I_2 - I_3) + c_t (I_2 + I_3)]$$

$$c_n = 2 \cdot 10^4 \text{ kN}/\text{cm}^3, c_t = 10^4 \text{ kN}/\text{cm}^3$$

- (2) Isotropic surface elasticity theory (cf. Javili et al. [50]):

$$\Psi_{\text{ela}}(\mathbf{g}_\alpha) = \frac{1}{2} \mu [\text{tr} \overline{\mathbf{C}} - 2 - 2 \ln (\det \overline{\mathbf{F}})]$$

$$\mu = 10^3 \text{ kN}/\text{cm}$$

- (3) General interface

with out-of-plane membrane forces:

$$\Psi = \frac{1}{2} [c_n (I_1 - I_2 - I_3) + c_t (I_2 + I_3)] + \frac{1}{2} \mu [\text{tr} \overline{\mathbf{C}} - 2 - 2 \ln (\det \overline{\mathbf{F}})]$$

$$c_n = 2 \cdot 10^4 \text{ kN}/\text{cm}^3, c_t = 10^4 \text{ kN}/\text{cm}^3, \mu = 10^3 \text{ kN}/\text{cm}$$

A systematic analysis of the size effect resulting from different interface models can also be found in [50]. However, only isotropic models are considered within the cited work. The present thesis extends this analysis to anisotropic interface models.

6.4.2.1 Loading case I – Uniaxial strain

In order to quantify the size effect, the macroscopic stresses P_{11}^M corresponding to the final strain with magnitude $F_{11}^M - 1 = 0.05$ are plotted in Fig. 6.4 as a function in terms

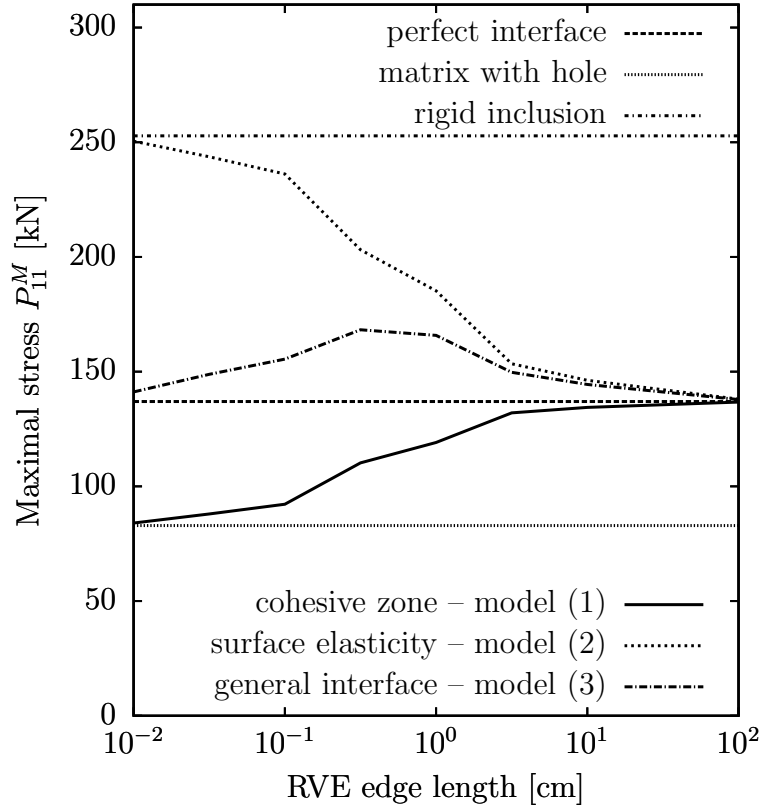


Figure 6.4: Numerical analysis of an RVE consisting of a spherical inclusion embedded in a matrix. Load case: uniaxial strain. Macroscopic stresses P_{11}^M at $F_{11}^M - 1 = 0.05$ as a function in terms of the RVE's size (l). The material models are defined on page 112 and page 109.

of the RVE's size l . First, the anisotropic cohesive model (model (1)) is investigated.

In line with [50], the effect "the smaller the softer" is observed for the cohesive interface model (model (1)). A cohesive zone interface can be interpreted as containing elastic springs normal to the interface and infinitely compliant springs along the interface. The latter shows that cohesive zone models do not capture in-plane deformation. They only resist against the opening process. To be more precise, the energy of a cohesive zone is not affected by a pure stretch of the interface. Thus, including cohesive zone interfaces into the boundary of the matrix and the inclusion leads to an interpretation

of including further springs in series. This leads to a more compliant material behaviour which becomes dominant at small scales. Therefore, the two limiting cases being $l \rightarrow 0$ and $l \rightarrow \infty$ correspond to a pore ($l \rightarrow 0$) in a matrix and to a homogeneous matrix without a hole ($l \rightarrow \infty$). It bears emphasis that this effect does not depend on the ratio of the chosen stiffness values. To be more precise, in the case of decreasing RVE size the cohesive interface model converges to a final value P_{11}^M that corresponds to the behaviour of a cube with a pore. In contrast to that, an increasing RVE size converges to a final stress value P_{11}^M corresponding to the behaviour of a homogeneous cube since the interface influence is negligible for large RVE sizes.

The coherent surface elasticity model (model (2)) shows a size effect in the opposite direction, i.e., a "the smaller the stiffer" relation. According to Section 5.1, coherent interfaces may exhibit a jump within the tractions ($[[\mathbf{t}]] \neq \mathbf{0}$), while the displacement is continuous across the interface ($[[\mathbf{u}]] = \mathbf{0}$). Physically speaking the interface resists against an expansion of its area. This behaviour can be represented by an infinitely stiff spring across and an elastic spring along the interface with the elastic stiffness μ . Including such interface behaviour into the boundary of matrix and inclusion leads to an interpretation of including further parallel springs. Again, for sufficiently large RVEs, the interface behaviour does not influence the overall material response. The model converges to a perfect interface (homogeneous matrix without a hole). However, the effect of the additional springs becomes more pronounced on small scales. For small RVEs, the overall material response becomes stiffer due to the additional parallel springs and the increasing area to volume ratio. The limiting case being $l \rightarrow 0$ corresponds to a rigid inclusion embedded in an elastic matrix, cf. [50]. This becomes obvious since the interface model converges to a final stress value P_{11}^M corresponding to the behaviour of a RVE with a rigid inclusion.

Finally, the coupled model (model (3)) which can be understood as a non-trivial superposition of model (1) and model (2) shows a more complex, non-monotonous size effect. Model (3) can suffer a jump in the tractions ($[[\mathbf{t}]] \neq \mathbf{0}$) as well as in the deformation ($[[\mathbf{u}]] \neq \mathbf{0}$). Thus, the interface behaviour is represented by elastic springs across and along the interface. Each of the two directions across and along the interface has its own stiffness. In turn, sufficiently large RVEs converge to a homogeneous matrix without a hole – in line with model (1) and model (2). Decreasing the RVE's size then leads to a "the smaller the stiffer" effect first. However, if the RVE's size is decreased further, a "the smaller the softer" relation is obtained. Furthermore, the limiting case related to $l \rightarrow 0$ is not obvious and depends on the stiffness ratio of the material parameters – in contrast to model (1) and model (2). In summary, no general statement concerning the size effect induced by model (3) can thus be given. To be more precise, the size effect can be designed and fine-tuned for a certain application by carefully coupling cohesive zone models (model (1)) with surface elasticity theory (model (2)).

6.4.2.2 Loading case II – Simple shear

Finally, the inclusion embedded in a matrix is re-analysed for the load case "simple shear". The respective macroscopic deformation gradient reads

$$\mathbf{F}^M = \begin{bmatrix} 1 & 0.05 & 0 \\ 0 & 1 & 0 \\ 0 & 0 & 1 \end{bmatrix}. \quad (6.29)$$

The obtained size effect is again investigated by comparing the macroscopic stresses obtained for different RVEs with different edge lengths. The results are summarised in Fig. 6.5. According to Fig. 6.5, the cohesive interface model (model (1)) again shows an

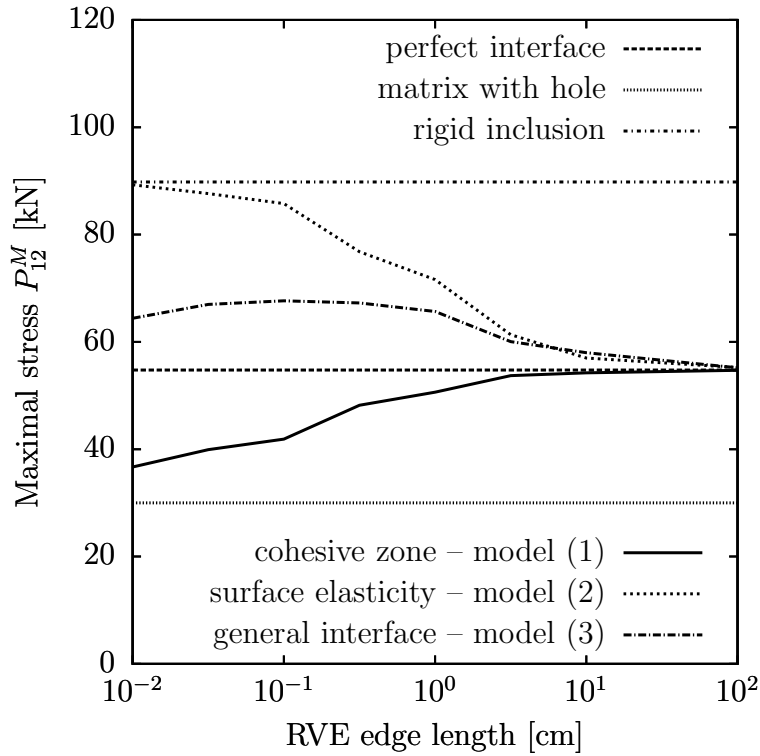


Figure 6.5: Numerical analysis of an RVE consisting of a spherical inclusion embedded in a matrix. Load case: simple shear. Macroscopic stresses P_{12}^M at $F_{12}^M = 0.05$ as a function in terms of the RVE's size (l). The material models are defined on page 112 and page 109.

effect of the type "the smaller the softer", while the coherent surface elasticity model (model (2)) yields a size effect of the type "the smaller the stiffer" again. Furthermore and in line with the previous example, the coupled model (model (3)) leads to a more complex, non-monotonous size effect.

7 Higher-order interfaces

The coupling of bulk materials and interface materials naturally introduces a length scale in the resulting response. Thus, a size-effect can be modelled. According to the previous chapter, several size-effects can be investigated and understood at small length scales by invoking the concept of cohesive zone theory, surface elasticity or the non-trivial combination of the both – also known as generalised interface theory, cf. [50]. So far, the presented interface theories are of first order. To be more precise, only displacement jump $[[\mathbf{u}]]$ and surface deformation gradient $\overline{\mathbf{F}}$ enter the model. However, higher-order interface gradients could also be of high interest concerning size effects. For instance it is known that bulk materials exhibit internal length scales if higher deformation gradients are considered in the material model. This idea goes back at least to the work of Mindlin [61] on elastic solids. It has been intensively expanded through the last decades since then. However, gradient enhancement in bulk materials is not the focus of this thesis. The interested reader is referred to Bertram [11] and the references cited therein. The cited manuscript gives a concise overview of gradient enhanced bulk theory. In this chapter some investigations of gradient enhanced interface models are presented.

First, the surface gradient of the displacement jump is considered. It is studied if the incorporation of $\overline{\text{GRAD}}[[\mathbf{u}]]$ into the interface Helmholtz energy leads to further physical effects in the material response. Furthermore, the motivation of taking $\overline{\text{GRAD}}[[\mathbf{u}]]$ into account lies in a novel homogenisation approach. To be more precise, it is investigated if the behaviour of a cohesive interface finite element can be described completely by a single point when an averaged displacement jump $[[\mathbf{u}]]_M$ and its gradient $\overline{\text{GRAD}}_M[[\mathbf{u}]]$ are known, see Fig. 7.1. In general, opening of a material interface can be captured by interface elements in numerical simulations, cf. [72]. A typical RVE is schematically shown in the middle of Fig. 7.1. For simplicity the figure shows a two-dimensional view of the interface. The RVE illustrated in the middle of the figure is loaded in mode-I direction. The interface elements are implemented along the expected crack path. If the framework is based on a minimisation principle, a potential is required. The classic way of calculating the potential is by spatial integration of a local interface model $\Psi = \Psi([[\mathbf{u}]])$, see Fig. 7.1 (left). In Fig. 7.1 (left), $[[\mathbf{u}]]_{(1)}$ and $[[\mathbf{u}]]_{(2)}$ denote the displacement jumps between upper and lower coordinates of $\mathbf{x}_{(1)}$ respectively $\mathbf{x}_{(2)}$. The goal of the first part of this chapter is to investigate if the behaviour computed by this

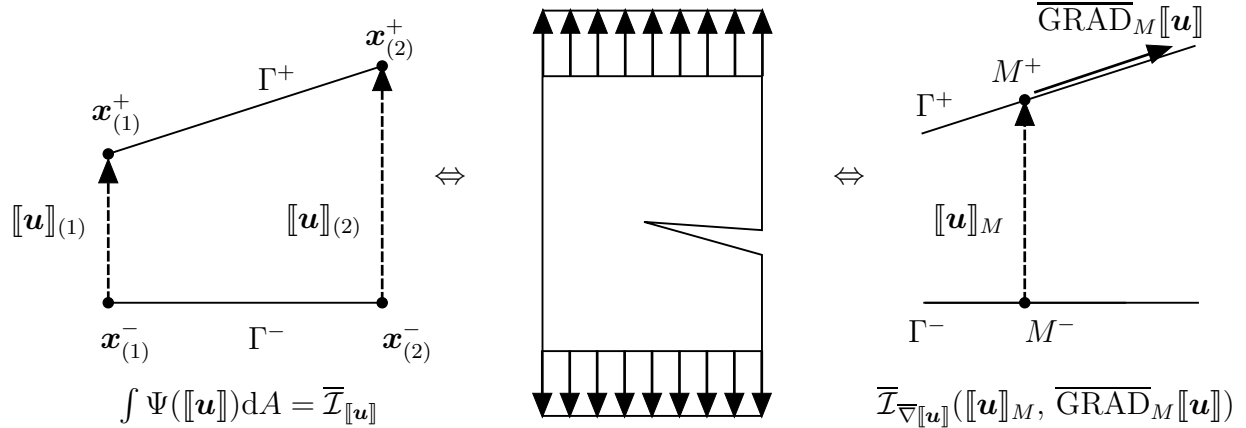


Figure 7.1: Graphical illustration of a homogenisation approach: An open interface (see RVE in the middle) can be represented by spatial integration of a local model (left side, $\Psi \neq \Psi(\overline{\text{GRAD}}_M[[\mathbf{u}]])$) or equivalently by an effective model of type $\Psi = \Psi([\mathbf{u}]_M, \overline{\text{GRAD}}_M[[\mathbf{u}]])$ in one material point

procedure can be captured by an effective model in one single material point represented by potential $\overline{\mathcal{I}}_{\nabla[[\mathbf{u}]}}([\mathbf{u}]_M, \overline{\text{GRAD}}_M[[\mathbf{u}]])$, i.e.,

$$\int \Psi([\mathbf{u}]) \, dA \stackrel{?}{=} \overline{\mathcal{I}}_{\nabla[[\mathbf{u}]}}([\mathbf{u}]_M, \overline{\text{GRAD}}_M[[\mathbf{u}]]) \, A, \quad (7.1)$$

where A denotes the area of the interface element. Here, $[[\mathbf{u}]]_M$ is an effective displacement jump averaged over the element and $\overline{\text{GRAD}}_M[[\mathbf{u}]]$ is its effective surface gradient. The interface behaviour is thereby reduced to one single material point which would be helpful in homogenisation theory. For the sake of comparison, additional energy potential $\overline{\mathcal{I}} = \overline{\mathcal{I}}([\mathbf{u}]_{(i)} \cdot [\mathbf{u}]_{(j)})$ is postulated and compared to both models sketched out before. Here, $[[\mathbf{u}]]_{(i)}$ denotes the displacement jump at point (i) .

The second part of this chapter deals with the enhancement of the surface elasticity theory. According to Chapter 5, the theory based on the work of Gurtin and Murdoch [36] is independent of the curvature of the surface/interface. To be more precise, no flexural resistance is considered. An important expansion of this was developed by Steigmann and Ogden [92, 93]. Here, the Gurtin–Murdoch theory is generalised to incorporate a flexural stiffness of the surface into the material behaviour. This was further studied for instance by Chhapadia et al. [17] in order to capture the curvature dependence of surfaces. The theory was applied to the investigation of nano structures, see Gao et al. [29, 30]. In Javili et al. [46] the interaction between higher-order interface and bulk theories is investigated. It is shown that, in order to have an interface energy depending on the total (surface) deformation gradient, the bulk energy needs to be a function of at least the first derivative of the bulk deformation gradient.

The enhancement of the interface with $\overline{\text{GRAD}}(\overline{\mathbf{F}})$ intrinsically includes curvature effects to the interface behaviour. This is investigated in this chapter. It is shown that the mean curvature of a surface can be represented as a covariant function of $\overline{\mathbf{F}}$ and

$\overline{\text{GRAD}}(\overline{\mathbf{F}})$. The balance of angular of momentum is thereby automatically fulfilled for the enhanced model.

7.1 Enhancement with the gradient of the displacement jump

7.1.1 Preliminaries – Objectivity requirements

Starting from the general interface model, an extension in order to account for the gradient of the displacement jump leads to the respective Helmholtz energy of type

$$\Psi = \Psi(\llbracket \mathbf{u} \rrbracket, \mathbf{g}_\alpha, \overline{\nabla} \llbracket \mathbf{u} \rrbracket). \quad (7.2)$$

Here, $\overline{\nabla} \llbracket \mathbf{u} \rrbracket$ is the surface gradient of $\llbracket \mathbf{u} \rrbracket$ with respect to the reference configuration, i.e., $\overline{\nabla} \llbracket \mathbf{u} \rrbracket$ describes the change of the displacement jump along the interface surface. Compared to the definition of the surface gradient within the considered curvilinear setting, cf. Eq. (5.7), it reads

$$\overline{\nabla} \llbracket \mathbf{u} \rrbracket = \overline{\text{GRAD}} \llbracket \mathbf{u} \rrbracket = \frac{\partial \llbracket \mathbf{u} \rrbracket}{\partial \theta^\alpha} \otimes \frac{\partial \theta^\alpha}{\partial \mathbf{X}} = \frac{\partial \llbracket \mathbf{u} \rrbracket}{\partial \theta^\alpha} \otimes \mathbf{G}^\alpha. \quad (7.3)$$

For this extended framework, objectivity (frame indifference) requires

$$\Psi(\llbracket \mathbf{u} \rrbracket, \mathbf{g}_1, \mathbf{g}_2, \overline{\nabla} \llbracket \mathbf{u} \rrbracket) = \Psi(\mathbf{Q} \cdot \llbracket \mathbf{u} \rrbracket, \mathbf{Q} \cdot \mathbf{g}_1, \mathbf{Q} \cdot \mathbf{g}_2, \mathbf{Q} \cdot \overline{\nabla} \llbracket \mathbf{u} \rrbracket) \quad \forall \mathbf{Q} \in SO3, \quad (7.4)$$

since the gradient of the displacement jump transforms under an observer transformation according to

$$\{\overline{\nabla} \llbracket \mathbf{u} \rrbracket\}^* = \mathbf{Q} \cdot \overline{\nabla} \llbracket \mathbf{u} \rrbracket. \quad (7.5)$$

Evidently, by applying the same procedure as outlined in the previous chapters, one obtains the objective representation of Helmholtz energy (7.97) as

$$\Psi = \Psi(I_1, I_2, I_3, \overline{\mathbf{C}}, \mathbf{g}_1 \cdot \overline{\nabla} \llbracket \mathbf{u} \rrbracket, \mathbf{g}_2 \cdot \overline{\nabla} \llbracket \mathbf{u} \rrbracket, \llbracket \mathbf{u} \rrbracket \cdot \overline{\nabla} \llbracket \mathbf{u} \rrbracket, (\overline{\nabla} \llbracket \mathbf{u} \rrbracket)^T \cdot \overline{\nabla} \llbracket \mathbf{u} \rrbracket). \quad (7.6)$$

Hence, an objective isotropic energy including the surface gradient of $\llbracket \mathbf{u} \rrbracket$ has to be of the form

$$\begin{aligned} \Psi(\llbracket \mathbf{u} \rrbracket, \mathbf{g}_\alpha, \overline{\nabla} \llbracket \mathbf{u} \rrbracket) &= \Psi(I_1, I_2, I_3, \text{tr}(\overline{\mathbf{C}}), \overline{\det}(\overline{\mathbf{C}}), \|\mathbf{g}_1 \cdot \overline{\nabla} \llbracket \mathbf{u} \rrbracket\|, \\ &\|\mathbf{g}_2 \cdot \overline{\nabla} \llbracket \mathbf{u} \rrbracket\|, \|\llbracket \mathbf{u} \rrbracket \cdot \overline{\nabla} \llbracket \mathbf{u} \rrbracket\|, \text{tr}(\overline{\nabla}^T \llbracket \mathbf{u} \rrbracket \cdot \overline{\nabla} \llbracket \mathbf{u} \rrbracket), \overline{\det}(\overline{\nabla}^T \llbracket \mathbf{u} \rrbracket \cdot \overline{\nabla} \llbracket \mathbf{u} \rrbracket)). \end{aligned} \quad (7.7)$$

7.1.2 Balance of linear momentum

In this subsection the balance of linear momentum for the gradient extended interface framework is derived in variational manner. In analogy to the principle of minimum potential energy for bulk materials (cf. Subsection 2.3.1.3), the starting point of the variational derivation is the total potential energy of the interface

$$\begin{aligned} \bar{\mathcal{I}} = & \int_{\Gamma_0} \Psi([\mathbf{u}], \bar{\nabla}[\mathbf{u}]) \, dA - \int_{\Gamma_0^+} \mathbf{T}^+ \cdot \boldsymbol{\varphi}^+ \, dA - \int_{\Gamma_0^-} \mathbf{T}^- \cdot \boldsymbol{\varphi}^- \, dA \\ & - \oint_{\partial\Gamma_0^+} \mathbf{T}_b^+ \cdot \boldsymbol{\varphi}^+ \, d\mathcal{L} - \oint_{\partial\Gamma_0^-} \mathbf{T}_b^- \cdot \boldsymbol{\varphi}^- \, d\mathcal{L}. \end{aligned} \quad (7.8)$$

The first term represents the total Helmholtz energy. In contrast to the general interface (cf. Subsection 5.2.3) additional tractions \mathbf{T}_b are separated into one part at the upper and one part at the lower interface surface, cf. Fig. 7.2. First, the variation of Ψ with

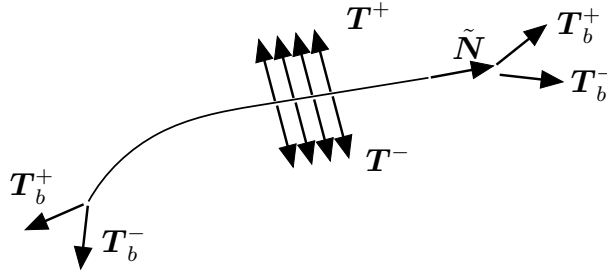


Figure 7.2: Stresses acting on an interface – referential description: Tractions acting at the upper surface $\Gamma_0^+ = \Gamma_0$ are denoted by \mathbf{T}^+ , tractions acting at the lower surface $\Gamma_0^- = \Gamma_0$ are denoted by \mathbf{T}^- , stresses acting at the boundary of the interface $\partial\Gamma_0$ are denoted by \mathbf{T}_b . The normal vector of the boundary of the interface is denoted by $\tilde{\mathbf{N}}$.

respect to deformation $\boldsymbol{\varphi}$ is considered as

$$\int_{\Gamma_0} \delta_{\boldsymbol{\varphi}} \Psi([\mathbf{u}], \bar{\nabla}[\mathbf{u}]) \, dA = \int_{\Gamma_0} \left[\frac{\partial \Psi}{\partial [\mathbf{u}]} \cdot \delta[\mathbf{u}] + \frac{\partial \Psi}{\partial \bar{\nabla}[\mathbf{u}]} : \delta \bar{\nabla}[\mathbf{u}] \right] \, dA. \quad (7.9)$$

Since the surface gradient of $[\mathbf{u}]$ is defined as

$$\bar{\nabla}[\mathbf{u}] = \frac{\partial [\mathbf{u}]}{\partial \theta^\alpha} \otimes \mathbf{G}^\alpha = \frac{\partial \mathbf{x}^+}{\partial \theta^\alpha} \otimes \mathbf{G}^\alpha - \frac{\partial \mathbf{x}^-}{\partial \theta^\alpha} \otimes \mathbf{G}^\alpha = \bar{\mathbf{F}}^+ - \bar{\mathbf{F}}^-, \quad (7.10)$$

one obtains

$$\delta \bar{\nabla}[\mathbf{u}] = \delta \bar{\mathbf{F}}^+ - \delta \bar{\mathbf{F}}^-. \quad (7.11)$$

Hence, variation (7.9) can be rewritten as

$$\int_{\Gamma_0} \delta_\varphi \Psi([\mathbf{u}], \overline{\nabla}[\mathbf{u}]) \, dA = \int_{\Gamma_0} \left[\overline{\mathbf{T}} \cdot \delta[\mathbf{u}] + \tilde{\mathbf{P}} : \left(\delta \overline{\mathbf{F}}^+ - \delta \overline{\mathbf{F}}^- \right) \right] \, dA, \quad (7.12)$$

where the definitions

$$\overline{\mathbf{T}} = \frac{\partial \Psi}{\partial [\mathbf{u}]} \quad \text{and} \quad \tilde{\mathbf{P}} = \frac{\partial \Psi}{\partial \overline{\nabla}[\mathbf{u}]} \quad (7.13)$$

are applied. Hence, $\tilde{\mathbf{P}}$ represents a stress tensor that is thermodynamically conjugate to $\overline{\nabla}[\mathbf{u}]$. Taking into consideration that $\delta \overline{\mathbf{F}}^\pm = \overline{\text{GRAD}} \delta \varphi^\pm$, identity

$$\tilde{\mathbf{P}} : \overline{\mathbf{F}}^\pm = \tilde{\mathbf{P}} : \overline{\text{GRAD}} \delta \varphi^\pm = \overline{\text{DIV}} \left(\delta \varphi^\pm \cdot \tilde{\mathbf{P}} \right) - \delta \varphi^\pm \cdot \overline{\text{DIV}} \tilde{\mathbf{P}} \quad (7.14)$$

holds true. By inserting this identity into (7.12) one obtains

$$\begin{aligned} & \int_{\Gamma_0} \left[\overline{\mathbf{T}} \cdot \delta[\mathbf{u}] + \tilde{\mathbf{P}} : \left(\delta \overline{\mathbf{F}}^+ - \delta \overline{\mathbf{F}}^- \right) \right] \, dA = \\ & \int_{\Gamma_0} \left[\overline{\mathbf{T}} \cdot \delta[\mathbf{u}] + \overline{\text{DIV}} \left(\delta \varphi^+ \cdot \tilde{\mathbf{P}} \right) - \delta \varphi^+ \cdot \overline{\text{DIV}} \tilde{\mathbf{P}} - \overline{\text{DIV}} \left(\delta \varphi^- \cdot \tilde{\mathbf{P}} \right) + \delta \varphi^- \cdot \overline{\text{DIV}} \tilde{\mathbf{P}} \right] \, dA. \end{aligned} \quad (7.15)$$

Next, interface divergence theorem

$$\int_{\Gamma_0} \overline{\text{DIV}} \left(\delta \varphi^\pm \cdot \tilde{\mathbf{P}} \right) \, dA = \oint_{\partial \Gamma_0} \delta \varphi^\pm \cdot \left(\tilde{\mathbf{P}} \cdot \tilde{\mathbf{N}}^\pm \right) \, d\mathcal{L} - \int_{\Gamma_0} \overline{K} \delta \varphi^\pm \cdot \tilde{\mathbf{P}} \cdot \overline{\mathbf{N}}^\pm \, dA, \quad (7.16)$$

is introduced. Following the same arguments as for the superficiality of $\overline{\mathbf{P}}$, stress tensor $\tilde{\mathbf{P}}$ is also superficial. Consequently, it holds that $\tilde{\mathbf{P}} \cdot \overline{\mathbf{N}}^\pm = 0$. Taking all the aforementioned relations into consideration and requiring the variation of potential (7.8) with respect to the deformation φ to be zero it follows that

$$\begin{aligned} \delta_\varphi \overline{\mathcal{I}} &= \int_{\Gamma_0} \overline{\mathbf{T}} \cdot (\delta \mathbf{x}^+ - \delta \mathbf{x}^-) \, dA \\ &- \int_{\Gamma_0^+} \mathbf{T}^+ \cdot \delta \mathbf{x}^+ \, dA - \int_{\Gamma_0^-} \mathbf{T}^- \cdot \delta \mathbf{x}^- \, dA \\ &+ \oint_{\partial \Gamma_0^+} \delta \mathbf{x}^+ \cdot \left(\tilde{\mathbf{P}} \cdot \tilde{\mathbf{N}}^+ \right) \, d\mathcal{L} - \int_{\Gamma_0^+} \delta \mathbf{x}^+ \cdot \overline{\text{DIV}} \tilde{\mathbf{P}} \, dA - \oint_{\partial \Gamma_0^+} \mathbf{T}_b^+ \cdot \delta \mathbf{x}^+ \, d\mathcal{L} \\ &- \oint_{\partial \Gamma_0^-} \delta \mathbf{x}^- \cdot \left(\tilde{\mathbf{P}} \cdot \tilde{\mathbf{N}}^- \right) \, d\mathcal{L} + \int_{\Gamma_0^-} \delta \mathbf{x}^- \cdot \overline{\text{DIV}} \tilde{\mathbf{P}} \, dA - \oint_{\partial \Gamma_0^-} \mathbf{T}_b^- \cdot \delta \mathbf{x}^- \, d\mathcal{L} = 0. \end{aligned} \quad (7.17)$$

Again, variations

$$\delta[\mathbf{u}] = \delta\mathbf{x}^+ - \delta\mathbf{x}^- \quad \text{and} \quad \delta\varphi^\pm = \delta\mathbf{u}^\pm = \delta\mathbf{x}^\pm \quad (7.18)$$

have been used. Since $\delta\mathbf{x}^-$ and $\delta\mathbf{x}^+$ are independent of each other and arbitrary, Eq. (7.17) is equivalent to

$$\overline{\mathbf{T}} - \mathbf{T}^+ - \overline{\text{DIV}} \tilde{\mathbf{P}} = \mathbf{0} \quad (7.19)$$

$$-\overline{\mathbf{T}} - \mathbf{T}^- + \overline{\text{DIV}} \tilde{\mathbf{P}} = \mathbf{0}, \quad (7.20)$$

$$\mathbf{T}_b^+ = \tilde{\mathbf{P}} \cdot \tilde{\mathbf{N}}^+ \quad \text{on } \partial\Gamma_0^+ \quad (7.21)$$

and

$$\mathbf{T}_b^- = -\tilde{\mathbf{P}} \cdot \tilde{\mathbf{N}}^- \quad \text{on } \partial\Gamma_0^-. \quad (7.22)$$

These are the Euler-Lagrange equations associated with potential (7.8). Since these cannot be compared easily to existing frameworks, they are reformulated next – in line with Subsection 5.2.3. For that purpose, Eq. (7.19) is added to Eq. (7.20) yielding

$$\mathbf{T}^+ = -\mathbf{T}^-. \quad (7.23)$$

By subtracting Eq. (7.20) from Eq. (7.19) one obtains under consideration of Eq. (7.23)

$$\overline{\mathbf{T}} - \mathbf{T}^+ - \overline{\text{DIV}} \tilde{\mathbf{P}} = \mathbf{0}. \quad (7.24)$$

By comparing Eq. (7.24) to balance of linear momentum for the generalised interface model (Eq. (5.33)), one can clearly see the strong analogy. This analogy is due to $\overline{\text{GRAD}}[\mathbf{u}] = \overline{\mathbf{F}}^+ - \overline{\mathbf{F}}^-$, i.e., only deformation gradients $\overline{\mathbf{F}}^+$ and $\overline{\mathbf{F}}^-$ enter the new model - similarly as in generalised interface model with $\Psi = \Psi([\mathbf{u}], \overline{\mathbf{F}})$.

7.2 Interface models in homogenisation theory

The idea is to describe the energy arising from one interface element by means of an effective model in one single material point. Therefore, an opening process with $\overline{\text{GRAD}}[\mathbf{u}] \neq \mathbf{0}$ is required, cf. Fig. 7.1. Now, the two following possibilities are compared:

- a) Classic local standard model with potential $\overline{\mathcal{I}}_{[\mathbf{u}]} = \int \Psi([\mathbf{u}]) \, dA$
- b) Enhanced gradient model with potential $\overline{\mathcal{I}}_{\nabla[\mathbf{u}]} = \overline{\mathcal{I}}_{\nabla[\mathbf{u}]}([\mathbf{u}]_M, \overline{\text{GRAD}}_M[\mathbf{u}])$

In order to compare the two approaches some assumptions have to be introduced. The investigation of approach a) reduces to one triangle interface element with six nodes – three on each side, see Fig. 7.3. A linear ansatz (representing a linear interface element

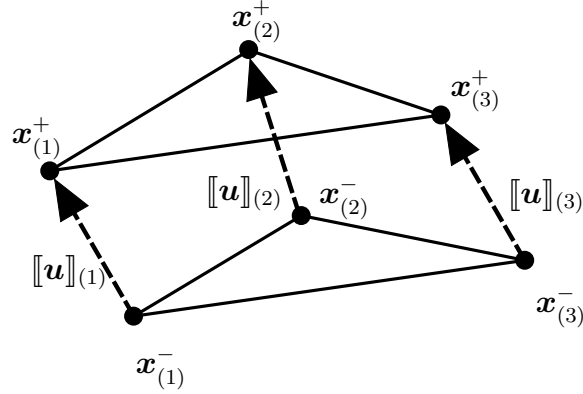


Figure 7.3: Linear triangle interface element with three nodes on the upper side and with three nodes on the lower side

with 3 nodes) for the displacement jump is chosen, i.e.,

$$[[\mathbf{u}]](\mathbf{X}) \approx \sum_{i=1}^3 N^{(i)} [[\mathbf{u}]]_{(i)}. \quad (7.25)$$

As a consequence

$$\overline{\nabla} [[\mathbf{u}]] \approx \sum_{i=1}^3 [[\mathbf{u}]]_{(i)} \otimes \overline{\text{GRAD}} N^{(i)} = \sum_{i=1}^3 [[\mathbf{u}]]_{(i)} \otimes N_{,\alpha}^{(i)} \mathbf{G}^\alpha. \quad (7.26)$$

The approximation of $[[\mathbf{u}]]$ by affine functions leads to a spatially constant gradient, i.e., $\overline{\text{GRAD}} [[\mathbf{u}]] = \text{const.}$

The kinematics of the displacement jump can also be described by an averaged (effective) jump $[[\mathbf{u}]]_M$ and the averaged (effective) gradient along the surface as

$$[[\mathbf{u}]](\mathbf{X}) = [[\mathbf{u}]]_M + \overline{\text{GRAD}}_M [[\mathbf{u}]] \cdot (\mathbf{X} - \mathbf{X}_M) \quad (7.27)$$

with

$$[[\mathbf{u}]]_M = \sum_{i=1}^3 N^{(i)}|_{\mathbf{X}_M} [[\mathbf{u}]]_{(i)} \quad (7.28)$$

and \mathbf{X}_M as the coordinate of the center of gravity. Clearly, in the case of a linear interpolation of $[[\mathbf{u}]]$, cf. Eq. (7.25), $\overline{\text{GRAD}}_M [[\mathbf{u}]]$ is spatially constant. Furthermore, a spatially constant stiffness parameter is considered as it is the case in classic quadratic cohesive model $\Psi([[\mathbf{u}]]) = 1/2 c [[\mathbf{u}]] \cdot [[\mathbf{u}]]$ with $c \neq c(\mathbf{X})$.

7.2.1 Preliminaries for the local interface model

This subsection elaborates an energy potential by spatial integration of a local interface model of type $\Psi = \Psi(\llbracket \mathbf{u} \rrbracket)$, see Fig. 7.1 (left). Following the procedure in order to obtain an objective interface model, the Helmholtz energy takes the form

$$\Psi = \Psi(\llbracket \mathbf{u} \rrbracket \cdot \llbracket \mathbf{u} \rrbracket) = \Psi(I_1). \quad (7.29)$$

Since energy (7.29) just depends on a scalar invariant it is intrinsically isotropic. As mentioned above the displacement jump is approximated by affine functions. From the requirement for objectivity (7.29) and the linear approximation of $\llbracket \mathbf{u} \rrbracket$ it follows that the energy potential of the discretised element $\bar{\mathcal{I}}_{\llbracket \mathbf{u} \rrbracket}$ can be represented as a function of the displacement jumps at the interface's nodes, i.e.,

$$\begin{aligned} \int \Psi(\llbracket \mathbf{u} \rrbracket \cdot \llbracket \mathbf{u} \rrbracket) dA &\approx \int \Psi \left(\sum_i \sum_j N^{(i)} N^{(j)} (\llbracket \mathbf{u} \rrbracket_{(i)} \cdot \llbracket \mathbf{u} \rrbracket_{(j)}) \right) dA \\ &= \bar{\mathcal{I}}_{\llbracket \mathbf{u} \rrbracket}(\llbracket \mathbf{u} \rrbracket_{(i)} \cdot \llbracket \mathbf{u} \rrbracket_{(j)}). \end{aligned} \quad (7.30)$$

Furthermore, it is assumed that energy potential $\bar{\mathcal{I}}_{\llbracket \mathbf{u} \rrbracket}$ can be approximated by a Taylor series, i.e.,

$$\begin{aligned} \bar{\mathcal{I}}_{\llbracket \mathbf{u} \rrbracket}(\llbracket \mathbf{u} \rrbracket_{(i)} \cdot \llbracket \mathbf{u} \rrbracket_{(j)}) &\approx a_0^{\text{el}} + \sum_i \sum_j a_{ij}^{\text{el}} (\llbracket \mathbf{u} \rrbracket_{(i)} \cdot \llbracket \mathbf{u} \rrbracket_{(j)}) + \\ &\sum_i \sum_j \sum_k \sum_l a_{ijkl}^{\text{el}} (\llbracket \mathbf{u} \rrbracket_{(i)} \cdot \llbracket \mathbf{u} \rrbracket_{(j)}) (\llbracket \mathbf{u} \rrbracket_{(k)} \cdot \llbracket \mathbf{u} \rrbracket_{(l)}) + \dots, \end{aligned} \quad (7.31)$$

with coefficients

$$a_{ij}^{\text{el}} = c_I^{\text{el}} \int \int N^{(i)} N^{(j)} dA \quad \text{and} \quad a_{ijkl}^{\text{el}} = c_{II}^{\text{el}} \int \int N^{(i)} N^{(j)} N^{(k)} N^{(l)} dA. \quad (7.32)$$

Here, c_I^{el} denotes one stiffness parameter concerned with contributions $(\llbracket \mathbf{u} \rrbracket_{(i)} \cdot \llbracket \mathbf{u} \rrbracket_{(j)})$ and c_{II}^{el} describes the stiffness related to $(\llbracket \mathbf{u} \rrbracket_{(i)} \cdot \llbracket \mathbf{u} \rrbracket_{(j)}) (\llbracket \mathbf{u} \rrbracket_{(k)} \cdot \llbracket \mathbf{u} \rrbracket_{(l)})$. Coefficients a_{ij}^{el} , a_{ijkl}^{el} and all further higher order contributions depend on the class of shape functions. Due to the commutativity, the following symmetry holds true

$$a_{ij}^{\text{el}} = a_{ji}^{\text{el}}. \quad (7.33)$$

Furthermore, all permutations within a_{ijkl}^{el} are commutative. Due to the commutativity of the scalar product equal contributions in $(\llbracket \mathbf{u} \rrbracket_{(i)} \cdot \llbracket \mathbf{u} \rrbracket_{(j)})$ are collected. For instance in the case of a six node triangle interface element with three nodes on the upper side

and with three nodes on the lower side (cf. Fig. 7.3), the possible combinations reduce from nine to six scalar product combinations, i.e.,

$$\llbracket \mathbf{u} \rrbracket_{(ij)} = \left[\llbracket \mathbf{u} \rrbracket_{(1)} \cdot \llbracket \mathbf{u} \rrbracket_{(1)}, \llbracket \mathbf{u} \rrbracket_{(1)} \cdot \llbracket \mathbf{u} \rrbracket_{(2)}, \llbracket \mathbf{u} \rrbracket_{(1)} \cdot \llbracket \mathbf{u} \rrbracket_{(3)}, \llbracket \mathbf{u} \rrbracket_{(2)} \cdot \llbracket \mathbf{u} \rrbracket_{(2)}, \llbracket \mathbf{u} \rrbracket_{(2)} \cdot \llbracket \mathbf{u} \rrbracket_{(3)}, \llbracket \mathbf{u} \rrbracket_{(3)} \cdot \llbracket \mathbf{u} \rrbracket_{(3)} \right] \quad (7.34)$$

The same holds equivalently for higher order terms.

By additionally taking all assumptions presented in Subsection 7.2 into consideration the following equivalence arises:

$$\int \Psi(\llbracket \mathbf{u} \rrbracket) \, dA \Rightarrow \bar{\mathcal{I}}_{\llbracket \mathbf{u} \rrbracket}(\llbracket \mathbf{u} \rrbracket_{(i)} \cdot \llbracket \mathbf{u} \rrbracket_{(j)}) \quad (7.35)$$

To be more explicit it seems obvious that spatial integration of the local interface model just depending on $\llbracket \mathbf{u} \rrbracket$ always leads to a potential in dependence of the nodes' jumps scalar products ($\llbracket \mathbf{u} \rrbracket_{(i)} \cdot \llbracket \mathbf{u} \rrbracket_{(j)}$). However, since there are six different possible combinations, a general potential in dependence of ($\llbracket \mathbf{u} \rrbracket_{(i)} \cdot \llbracket \mathbf{u} \rrbracket_{(j)}$) shows six different material parameters. Clearly, this cannot be captured by a local model with just one material parameter.

7.2.2 Preliminaries of the effective interface model

This subsection presents certain invariants that allow the definition of an objective effective interface energy depending on averaged jump $\llbracket \mathbf{u} \rrbracket_M$ and averaged gradient $\overline{\text{GRAD}}_M \llbracket \mathbf{u} \rrbracket$.

Following the objectivity requirement of the extended energy (7.6), invariants are defined by means of different relations between $\llbracket \mathbf{u} \rrbracket_M$ and $\overline{\text{GRAD}}_M \llbracket \mathbf{u} \rrbracket$. To be more precise, the invariants are defined by means of

$$\llbracket \mathbf{u} \rrbracket_M \cdot \llbracket \mathbf{u} \rrbracket_M \rightarrow \hat{I}_1, \quad (7.36)$$

$$\llbracket \mathbf{u} \rrbracket_M \cdot \overline{\text{GRAD}}_M \llbracket \mathbf{u} \rrbracket \approx \sum_{i=1}^n (\llbracket \mathbf{u} \rrbracket_M \cdot \llbracket \mathbf{u} \rrbracket_{(i)}) N_{,\alpha}^{(i)} \mathbf{G}^\alpha \rightarrow \hat{I}_2, \hat{I}_3 \quad (7.37)$$

and

$$\overline{\nabla}^T \llbracket \mathbf{u} \rrbracket \cdot \overline{\nabla} \llbracket \mathbf{u} \rrbracket \approx \sum_{i=1}^n \sum_{j=1}^n (\llbracket \mathbf{u} \rrbracket_{(i)} \cdot \llbracket \mathbf{u} \rrbracket_{(j)}) N_{,\alpha}^{(i)} N_{,\beta}^{(j)} \mathbf{G}^\alpha \otimes \mathbf{G}^\beta \rightarrow \hat{I}_4, \hat{I}_5, \hat{I}_6, \quad (7.38)$$

where the symmetry of the scalar products has been accounted for. Insertion of the linear approximation (7.25) into the combination of $\llbracket \mathbf{u} \rrbracket_M$ and $\overline{\text{GRAD}}_M \llbracket \mathbf{u} \rrbracket$, see (7.36) - (7.38), leads to six invariants, i.e.

$$\hat{I}_1 = \llbracket \mathbf{u} \rrbracket_M \cdot \llbracket \mathbf{u} \rrbracket_M = \hat{I}_1(\llbracket \mathbf{u} \rrbracket_{(i)} \cdot \llbracket \mathbf{u} \rrbracket_{(j)}) \quad (7.39)$$

$$\hat{I}_2 = \sum_{i=1}^n (\llbracket \mathbf{u} \rrbracket_{(i)} \cdot \llbracket \mathbf{u} \rrbracket_M) N_{,1}^{(i)} = \hat{I}_2(\llbracket \mathbf{u} \rrbracket_{(i)} \cdot \llbracket \mathbf{u} \rrbracket_{(j)}), \quad (7.40)$$

$$\hat{I}_3 = \sum_{i=1}^n (\llbracket \mathbf{u} \rrbracket_{(i)} \cdot \llbracket \mathbf{u} \rrbracket_M) N_{,2}^{(i)} = \hat{I}_3(\llbracket \mathbf{u} \rrbracket_{(i)} \cdot \llbracket \mathbf{u} \rrbracket_{(j)}), \quad (7.41)$$

$$\hat{I}_4 = \sum_{i=1}^n \sum_{j=1}^n (\llbracket \mathbf{u} \rrbracket_{(i)} \cdot \llbracket \mathbf{u} \rrbracket_{(j)}) N_{,1}^{(i)} N_{,1}^{(j)} = \hat{I}_4(\llbracket \mathbf{u} \rrbracket_{(i)} \cdot \llbracket \mathbf{u} \rrbracket_{(j)}), \quad (7.42)$$

$$\hat{I}_5 = \sum_{i=1}^n \sum_{j=1}^n (\llbracket \mathbf{u} \rrbracket_{(i)} \cdot \llbracket \mathbf{u} \rrbracket_{(j)}) N_{,1}^{(i)} N_{,2}^{(j)} = \hat{I}_5(\llbracket \mathbf{u} \rrbracket_{(i)} \cdot \llbracket \mathbf{u} \rrbracket_{(j)}) \quad \text{and} \quad (7.43)$$

$$\hat{I}_6 = \sum_{i=1}^n \sum_{j=1}^n (\llbracket \mathbf{u} \rrbracket_{(i)} \cdot \llbracket \mathbf{u} \rrbracket_{(j)}) N_{,2}^{(i)} N_{,2}^{(j)} = \hat{I}_6(\llbracket \mathbf{u} \rrbracket_{(i)} \cdot \llbracket \mathbf{u} \rrbracket_{(j)}). \quad (7.44)$$

Using invariants $\hat{I}_1 - \hat{I}_6$, an objective interface potential of the form

$$\overline{\mathcal{I}}_{\nabla \llbracket \mathbf{u} \rrbracket}(\llbracket \mathbf{u} \rrbracket_M, \overline{\text{GRAD}}_M \llbracket \mathbf{u} \rrbracket) = \overline{\mathcal{I}}_{\nabla \llbracket \mathbf{u} \rrbracket}(\hat{I}_1, \hat{I}_2, \hat{I}_3, \hat{I}_4, \hat{I}_5, \hat{I}_6) \quad (7.45)$$

can be formulated. It bears emphasis that potential (7.45) does not need to be isotropic since it is not of form (7.7), see Remark 13.

Focussing on an affine displacement field (spatially constant gradient of displacement jump), see Fig. 7.3, invariants $\hat{I}_1 - \hat{I}_6$ can be rewritten in terms of the six different scalar products $\llbracket \mathbf{u} \rrbracket_{(i)} \cdot \llbracket \mathbf{u} \rrbracket_{(j)}$, i.e.,

$$\begin{bmatrix} \hat{I}_1 \\ \hat{I}_2 \\ \hat{I}_3 \\ \hat{I}_4 \\ \hat{I}_5 \\ \hat{I}_6 \end{bmatrix} = \underbrace{\begin{bmatrix} 1/9 & 2/9 & 2/9 & 1/9 & 2/9 & 1/9 \\ -1/3 & 0 & -1/3 & 1/3 & 1/3 & 0 \\ -1/3 & -1/3 & 0 & 0 & 1/3 & 1/3 \\ 1 & -2 & 0 & 1 & 0 & 0 \\ 1 & -1 & -1 & 0 & 1 & 0 \\ 1 & 0 & -2 & 0 & 0 & 1 \end{bmatrix}}_{\mathbf{A}} \cdot \begin{bmatrix} \llbracket \mathbf{u} \rrbracket_{(1)} \cdot \llbracket \mathbf{u} \rrbracket_{(1)} \\ \llbracket \mathbf{u} \rrbracket_{(1)} \cdot \llbracket \mathbf{u} \rrbracket_{(2)} \\ \llbracket \mathbf{u} \rrbracket_{(1)} \cdot \llbracket \mathbf{u} \rrbracket_{(3)} \\ \llbracket \mathbf{u} \rrbracket_{(2)} \cdot \llbracket \mathbf{u} \rrbracket_{(2)} \\ \llbracket \mathbf{u} \rrbracket_{(2)} \cdot \llbracket \mathbf{u} \rrbracket_{(3)} \\ \llbracket \mathbf{u} \rrbracket_{(3)} \cdot \llbracket \mathbf{u} \rrbracket_{(3)} \end{bmatrix}. \quad (7.46)$$

By inverting matrix \mathbf{A} , one obtains

$$\begin{bmatrix} \llbracket \mathbf{u} \rrbracket_{(1)} \cdot \llbracket \mathbf{u} \rrbracket_{(1)} \\ \llbracket \mathbf{u} \rrbracket_{(1)} \cdot \llbracket \mathbf{u} \rrbracket_{(2)} \\ \llbracket \mathbf{u} \rrbracket_{(1)} \cdot \llbracket \mathbf{u} \rrbracket_{(3)} \\ \llbracket \mathbf{u} \rrbracket_{(2)} \cdot \llbracket \mathbf{u} \rrbracket_{(2)} \\ \llbracket \mathbf{u} \rrbracket_{(2)} \cdot \llbracket \mathbf{u} \rrbracket_{(3)} \\ \llbracket \mathbf{u} \rrbracket_{(3)} \cdot \llbracket \mathbf{u} \rrbracket_{(3)} \end{bmatrix} = \begin{bmatrix} 1 & -2/3 & -2/3 & 1/9 & 2/9 & 1/9 \\ 1 & 1/3 & -2/3 & -2/9 & -1/9 & 1/9 \\ 1 & -2/3 & 1/3 & 1/9 & -1/9 & -2/9 \\ 1 & 4/3 & -2/3 & 4/9 & -4/9 & 1/9 \\ 1 & 1/3 & 1/3 & -2/9 & 5/9 & -2/9 \\ 1 & -2/3 & 4/3 & 1/9 & -4/9 & 4/9 \end{bmatrix} \cdot \begin{bmatrix} \hat{I}_1 \\ \hat{I}_2 \\ \hat{I}_3 \\ \hat{I}_4 \\ \hat{I}_5 \\ \hat{I}_6 \end{bmatrix}, \quad (7.47)$$

which allows the representation of $\overline{\mathcal{I}}_{\nabla[\mathbf{u}]}$ as

$$\overline{\mathcal{I}}_{\nabla[\mathbf{u}]}(\hat{I}_1, \hat{I}_2, \hat{I}_3, \hat{I}_4, \hat{I}_5, \hat{I}_6) = \overline{\mathcal{I}}_{\nabla[\mathbf{u}]}(\llbracket \mathbf{u} \rrbracket_{(i)} \cdot \llbracket \mathbf{u} \rrbracket_{(j)}). \quad (7.48)$$

Thus, every model in terms of $\llbracket \mathbf{u} \rrbracket_M$ and $\overline{\text{GRAD}}_M[\mathbf{u}]$ can be rewritten into an equivalent model in terms of $(\llbracket \mathbf{u} \rrbracket_{(i)} \cdot \llbracket \mathbf{u} \rrbracket_{(j)})$ and vice versa.

According to the Taylor approximation of $\overline{\mathcal{I}}_{\nabla[\mathbf{u}]}(\llbracket \mathbf{u} \rrbracket_{(i)} \cdot \llbracket \mathbf{u} \rrbracket_{(j)})$, cf. Eq. (7.31), effective energy $\overline{\mathcal{I}}_{\nabla[\mathbf{u}]}(\llbracket \mathbf{u} \rrbracket_M, \overline{\text{GRAD}}_M[\mathbf{u}])$ can also be represented as a combination of the jump scalar products as

$$\begin{aligned} \overline{\mathcal{I}}_{\nabla[\mathbf{u}]}(\llbracket \mathbf{u} \rrbracket_{(i)} \cdot \llbracket \mathbf{u} \rrbracket_{(j)}) &= c_0^{\text{eff}} + \sum_i \sum_j c_{ij}^{\text{eff}} (\llbracket \mathbf{u} \rrbracket_{(i)} \cdot \llbracket \mathbf{u} \rrbracket_{(j)}) + \\ &\sum_i \sum_j \sum_k \sum_l c_{ijkl}^{\text{eff}} (\llbracket \mathbf{u} \rrbracket_{(i)} \cdot \llbracket \mathbf{u} \rrbracket_{(j)}) (\llbracket \mathbf{u} \rrbracket_{(k)} \cdot \llbracket \mathbf{u} \rrbracket_{(l)}) + \dots, \end{aligned} \quad (7.49)$$

where the coefficients c_{ij}^{eff} and c_{ijkl}^{eff} can be chosen arbitrarily. However, due to the commutativity of the scalar product it holds that

$$c_{ij}^{\text{eff}} = c_{ji}^{\text{eff}} \quad (7.50)$$

and c_{ijkl}^{eff} shows the major and the minor symmetry, i.e., $c_{ijkl}^{\text{eff}} = c_{ijlk}^{\text{eff}} = c_{jikl}^{\text{eff}} = c_{jilk}^{\text{eff}}$. In summary, in the case of the gradient enhanced model the equivalence follows as

$$\overline{\mathcal{I}}_{\nabla[\mathbf{u}]}(\llbracket \mathbf{u} \rrbracket_M, \overline{\text{GRAD}}_M[\mathbf{u}]) \Leftrightarrow \overline{\mathcal{I}}_{\nabla[\mathbf{u}]}(\llbracket \mathbf{u} \rrbracket_{(i)} \cdot \llbracket \mathbf{u} \rrbracket_{(j)}). \quad (7.51)$$

7.2.3 Comparison of the different approaches

Within Subsections 7.2.1 and 7.2.2, two representations of integrated local energy $\overline{\mathcal{I}}_{\nabla[\mathbf{u}]} = \int \Psi(\llbracket \mathbf{u} \rrbracket) dA$ and effective potential $\overline{\mathcal{I}}_{\nabla[\mathbf{u}]}(\llbracket \mathbf{u} \rrbracket_M, \overline{\text{GRAD}}_M[\mathbf{u}])$ have been derived. These two descriptions are now compared to generic potential

$$\overline{\mathcal{I}} = \overline{\mathcal{I}}(\llbracket \mathbf{u} \rrbracket_{(i)} \cdot \llbracket \mathbf{u} \rrbracket_{(j)}). \quad (7.52)$$

Evidently, this energy is a priori frame indifferent. If it is assumed that the energy potential (7.52) can be approximated by a Taylor series, i.e.,

$$\begin{aligned} \bar{\mathcal{I}}(\llbracket \mathbf{u} \rrbracket_{(i)} \cdot \llbracket \mathbf{u} \rrbracket_{(j)}) &\approx b_0 + \sum_i \sum_j b_{ij} (\llbracket \mathbf{u} \rrbracket_{(i)} \cdot \llbracket \mathbf{u} \rrbracket_{(j)}) + \\ &\sum_i \sum_j \sum_k \sum_l b_{ijkl} (\llbracket \mathbf{u} \rrbracket_{(i)} \cdot \llbracket \mathbf{u} \rrbracket_{(j)}) (\llbracket \mathbf{u} \rrbracket_{(k)} \cdot \llbracket \mathbf{u} \rrbracket_{(l)}) + \dots, \end{aligned} \quad (7.53)$$

the coefficients b_0 , b_{ij} and b_{ijkl} may be chosen arbitrarily. Due to the commutativity it holds – nevertheless – that $b_{ij} = b_{ji}$ and $b_{ijkl} = b_{ijlk} = b_{jilk} = b_{jlik}$, see Tab. 7.1

Table 7.1: Overview of the different approaches

$\Psi = \Psi(\llbracket \mathbf{u} \rrbracket)$		
Linear approximation of $\llbracket \mathbf{u} \rrbracket$: $\llbracket \mathbf{u} \rrbracket(\mathbf{X}) \approx \sum_i N^{(i)} \llbracket \mathbf{u} \rrbracket_{(i)}$		
objectivity + spatial integration	dependence on combina- tions of scalar products of node jumps $(\llbracket \mathbf{u} \rrbracket_{(i)} \cdot \llbracket \mathbf{u} \rrbracket_{(j)})$	objectivity + averaging leading to effec- tive jump $\llbracket \mathbf{u} \rrbracket_M$ and its gradient $\bar{\nabla} \llbracket \mathbf{u} \rrbracket$
$\int \Psi(\llbracket \mathbf{u} \rrbracket) \, dA = \bar{\mathcal{I}}_{\llbracket \mathbf{u} \rrbracket}$	generic potential $\bar{\mathcal{I}}$	$\bar{\mathcal{I}}_{\bar{\nabla} \llbracket \mathbf{u} \rrbracket}(\llbracket \mathbf{u} \rrbracket_M, \bar{\nabla} \llbracket \mathbf{u} \rrbracket_M)$
Potential can be approximated by a Taylor series		
$\bar{\mathcal{I}}_{\llbracket \mathbf{u} \rrbracket}(\llbracket \mathbf{u} \rrbracket_{(i)} \cdot \llbracket \mathbf{u} \rrbracket_{(j)}) =$ $a_0^{\text{el}} +$ $\sum_{ij} a_{ij}^{\text{el}} (\llbracket \mathbf{u} \rrbracket_{(i)} \cdot \llbracket \mathbf{u} \rrbracket_{(j)}) +$ $\sum_{ijkl} a_{ijkl}^{\text{el}}$ $(\llbracket \mathbf{u} \rrbracket_{(i)} \cdot \llbracket \mathbf{u} \rrbracket_{(j)})$ $(\llbracket \mathbf{u} \rrbracket_{(k)} \cdot \llbracket \mathbf{u} \rrbracket_{(l)}) + \dots$	$\bar{\mathcal{I}}(\llbracket \mathbf{u} \rrbracket_{(i)} \cdot \llbracket \mathbf{u} \rrbracket_{(j)}) =$ $b_0 +$ $\sum_{ij} b_{ij} (\llbracket \mathbf{u} \rrbracket_{(i)} \cdot \llbracket \mathbf{u} \rrbracket_{(j)}) +$ $\sum_{ijkl} b_{ijkl}$ $(\llbracket \mathbf{u} \rrbracket_{(i)} \cdot \llbracket \mathbf{u} \rrbracket_{(j)})$ $(\llbracket \mathbf{u} \rrbracket_{(k)} \cdot \llbracket \mathbf{u} \rrbracket_{(l)}) + \dots$	$\bar{\mathcal{I}}_{\bar{\nabla} \llbracket \mathbf{u} \rrbracket}(\llbracket \mathbf{u} \rrbracket_{(i)} \cdot \llbracket \mathbf{u} \rrbracket_{(j)}) =$ $c_0^{\text{eff}} +$ $\sum_{ij} c_{ij}^{\text{eff}} (\llbracket \mathbf{u} \rrbracket_{(i)} \cdot \llbracket \mathbf{u} \rrbracket_{(j)}) +$ $\sum_{ijkl} c_{ijkl}^{\text{eff}}$ $(\llbracket \mathbf{u} \rrbracket_{(i)} \cdot \llbracket \mathbf{u} \rrbracket_{(j)})$ $(\llbracket \mathbf{u} \rrbracket_{(k)} \cdot \llbracket \mathbf{u} \rrbracket_{(l)}) + \dots$
Number of unknowns		
$a_{ij}^{\text{el}} = a_I^{\text{el}} \int \int N^{(i)} N^{(j)} \, dA$ $a_{ijkl}^{\text{el}} =$ $a_{II}^{\text{el}} \int \int N^{(i)} N^{(j)} N^{(k)} N^{(l)} \, dA,$	$b_{ij} = b_{ji},$ $b_{ijkl} = b_{ijlk} = b_{jilk} = b_{jlik},$	$c_{ij}^{\text{eff}} = c_{ji}^{\text{eff}},$ $c_{ijkl}^{\text{eff}} = c_{ijlk}^{\text{eff}} = c_{jilk}^{\text{eff}} = c_{jlik}^{\text{eff}},$
$\mathbb{X}_{\llbracket \mathbf{u} \rrbracket} = \{a_0, a_I^{\text{el}}, a_{II}^{\text{el}}, \dots\}$ $\#(\mathbb{X}_{\llbracket \mathbf{u} \rrbracket}) = 1 + 1 + 1 + \dots$	$\mathbb{X} = \{b_0, b_{ij}, b_{ijkl}, \dots\}$ $\#(\mathbb{X}) = 1 + 6 + 21 + \dots$	$\mathbb{X}_{\bar{\nabla} \llbracket \mathbf{u} \rrbracket} = \{c_0^{\text{eff}}, c_{ij}^{\text{eff}}, c_{ijkl}^{\text{eff}}, \dots\}$ $\#(\mathbb{X}_{\bar{\nabla} \llbracket \mathbf{u} \rrbracket}) = 1 + 6 + 21 + \dots$
$\bar{\mathcal{I}}_{\llbracket \mathbf{u} \rrbracket}(\llbracket \mathbf{u} \rrbracket_{(i)} \cdot \llbracket \mathbf{u} \rrbracket_{(j)})$	$\stackrel{(7.35)}{\Rightarrow} \bar{\mathcal{I}}(\llbracket \mathbf{u} \rrbracket_{(i)} \cdot \llbracket \mathbf{u} \rrbracket_{(j)})$	$\stackrel{(7.51)}{\Leftrightarrow} \bar{\mathcal{I}}_{\bar{\nabla} \llbracket \mathbf{u} \rrbracket}(\llbracket \mathbf{u} \rrbracket_{(i)} \cdot \llbracket \mathbf{u} \rrbracket_{(j)})$

7.2.3.1 Example for equivalence with one material parameter

Spatial integration of the local interface model leads to an energy potential $\bar{\mathcal{I}}_{[\mathbf{u}]}([\mathbf{u}]_{(i)} \cdot [\mathbf{u}]_{(j)})$ where the coefficients a_{ij}^{el} and a_{ijkl}^{el} are prescribed due to the integration of the shape functions, see Eq. (7.32). Furthermore, the commutativity of the scalar product is applied. Thereby, contributions $[\mathbf{u}]_{(i)} \cdot [\mathbf{u}]_{(j)}$ reduce from nine to six different combinations while the higher order contributions $([\mathbf{u}]_{(i)} \cdot [\mathbf{u}]_{(j)}) ([\mathbf{u}]_{(k)} \cdot [\mathbf{u}]_{(l)})$ reduce from 81 to 21 different combinations.

In this subsection, the classic local cohesive zone model with just one spatially constant material parameter μ is investigated, i.e.,

$$\Psi = \Psi([\mathbf{u}]) = \frac{1}{2} \mu [\mathbf{u}] \cdot [\mathbf{u}]. \quad (7.54)$$

Spatial integration and insertion of the linear ansatz (7.25) lead to energy potential

$$\begin{aligned} \int \psi([\mathbf{u}]) \, dA &\approx \int_{\Delta} \frac{1}{2} \mu \left(\sum_{i=1}^3 \sum_{j=1}^3 N^{(i)} N^{(j)} [\mathbf{u}]_{(i)} \cdot [\mathbf{u}]_{(j)} \right) \det \mathbf{J}_{\xi} \, dA_{\xi} \\ &= \frac{1}{2} \sum_1^3 \sum_1^3 \underbrace{\int_{\Delta} \mu N^{(i)} N^{(j)} \det \mathbf{J}_{\xi} \, dA_{\xi}}_{a_{ij}^{\text{el}}} [\mathbf{u}]_{(i)} \cdot [\mathbf{u}]_{(j)} \\ &= \frac{1}{2} A \left(\frac{1}{6} \mu [\mathbf{u}]_{(1)}^2 + 2 \frac{1}{12} \mu [\mathbf{u}]_{(1)} \cdot [\mathbf{u}]_{(2)} + 2 \frac{1}{12} \mu [\mathbf{u}]_{(1)} \cdot [\mathbf{u}]_{(3)} + \right. \\ &\quad \left. \frac{1}{6} \mu [\mathbf{u}]_{(2)}^2 + 2 \frac{1}{12} \mu [\mathbf{u}]_{(2)} \cdot [\mathbf{u}]_{(3)} + \frac{1}{6} \mu [\mathbf{u}]_{(3)}^2 \right) \\ &= \frac{1}{12} A \mu \left([\mathbf{u}]_{(1)}^2 + [\mathbf{u}]_{(1)} \cdot [\mathbf{u}]_{(2)} + [\mathbf{u}]_{(1)} \cdot [\mathbf{u}]_{(3)} + [\mathbf{u}]_{(2)}^2 + [\mathbf{u}]_{(2)} \cdot [\mathbf{u}]_{(3)} + [\mathbf{u}]_{(3)}^2 \right) \\ &= \bar{\mathcal{I}}_{[\mathbf{u}]}([\mathbf{u}]_{(i)} \cdot [\mathbf{u}]_{(j)}). \end{aligned} \quad (7.55)$$

Using the commutativity of the scalar product, all stiffness contributions for the different scalar product combinations $[\mathbf{u}]_{(i)} \cdot [\mathbf{u}]_{(j)}$ are identical. The comparison to ansatz (7.31) results in $a_0^{\text{el}} = 0$ and $a_{ij}^{\text{el}} = 1/12 \mu$.

Alternatively, energy potential (7.55) can also be represented by an effective gradient enhanced model $\bar{\mathcal{I}}_{\nabla[\mathbf{u}]}([\mathbf{u}]_{(i)} \cdot [\mathbf{u}]_{(j)})$. In this case, the inverse coefficient matrix from Eq. (7.47) has to be evaluated for energy ansatz (7.54). This leads to

$$\begin{aligned} \bar{\mathcal{I}}_{\nabla[\mathbf{u}]}([\mathbf{u}]_M, \overline{\text{GRAD}}_M[\mathbf{u}]) &= \bar{\mathcal{I}}_{\nabla[\mathbf{u}]}([\mathbf{u}]_{(i)} \cdot [\mathbf{u}]_{(j)}) \\ &= \bar{\mathcal{I}}_{\nabla[\mathbf{u}]}(\hat{I}_1, \hat{I}_2, \hat{I}_3, \hat{I}_4, \hat{I}_5, \hat{I}_6) = \left[\frac{1}{2} \lambda \hat{I}_1 + \frac{1}{36} \lambda (\hat{I}_4 - \hat{I}_5 + \hat{I}_6) \right] A \end{aligned}$$

$$= \frac{1}{12} A \lambda \left(\llbracket \mathbf{u} \rrbracket_{(1)}^2 + \llbracket \mathbf{u} \rrbracket_{(1)} \cdot \llbracket \mathbf{u} \rrbracket_{(2)} + \llbracket \mathbf{u} \rrbracket_{(1)} \cdot \llbracket \mathbf{u} \rrbracket_{(3)} + \llbracket \mathbf{u} \rrbracket_{(2)}^2 + \llbracket \mathbf{u} \rrbracket_{(2)} \cdot \llbracket \mathbf{u} \rrbracket_{(3)} + \llbracket \mathbf{u} \rrbracket_{(3)}^2 \right). \quad (7.56)$$

Accordingly, by choosing $\mu = \lambda$, Eq. (7.56) is equivalent to Eq. (7.55). It can be shown in a straightforward manner, that the same inclusion also holds for higher-order models and thus,

$$\overline{\mathcal{I}}_{\llbracket \mathbf{u} \rrbracket}(\llbracket \mathbf{u} \rrbracket_{(i)} \cdot \llbracket \mathbf{u} \rrbracket_{(j)}) \Rightarrow \overline{\mathcal{I}}_{\nabla \llbracket \mathbf{u} \rrbracket}(\llbracket \mathbf{u} \rrbracket_M, \overline{\text{GRAD}}_M \llbracket \mathbf{u} \rrbracket) A. \quad (7.57)$$

7.2.3.2 Example for more than one material parameter

As shown in the previous subsection, equivalence (7.57) holds in the case of one spatially constant material parameter. In contrast to that, this subsection shows with a simple example that equivalence (7.57) is not valid from the opposite direction. A quadratic counter example is given by energy

$$\begin{aligned} \overline{\mathcal{I}}_{\nabla \llbracket \mathbf{u} \rrbracket} &= \overline{\mathcal{I}}_{\nabla \llbracket \mathbf{u} \rrbracket}(\llbracket \mathbf{u} \rrbracket_M, \overline{\text{GRAD}}_M \llbracket \mathbf{u} \rrbracket) \\ &= \frac{1}{2} \left[\lambda_1 \llbracket \mathbf{u} \rrbracket_M \cdot \llbracket \mathbf{u} \rrbracket_M + \lambda_2 (\overline{\text{GRAD}}_M \llbracket \mathbf{u} \rrbracket : \overline{\text{GRAD}}_M \llbracket \mathbf{u} \rrbracket) \right] \\ &= \frac{1}{2} A \left[\left(\frac{\lambda_1}{9} + 2 \lambda_2 \right) \llbracket \mathbf{u} \rrbracket_{(1)}^2 + \left(\frac{\lambda_1}{9} - 2 \lambda_2 \right) \llbracket \mathbf{u} \rrbracket_{(1)} \cdot \llbracket \mathbf{u} \rrbracket_{(2)} \right. \\ &\quad \left. \left(\frac{\lambda_1}{9} - 2 \lambda_2 \right) \llbracket \mathbf{u} \rrbracket_{(1)} \cdot \llbracket \mathbf{u} \rrbracket_{(3)} + \left(\frac{\lambda_1}{9} + \lambda_2 \right) \llbracket \mathbf{u} \rrbracket_{(2)}^2 \right. \\ &\quad \left. + \left(\frac{1}{9} \lambda_1 \right) \llbracket \mathbf{u} \rrbracket_{(2)} \cdot \llbracket \mathbf{u} \rrbracket_{(3)} + \left(\frac{\lambda_1}{9} + \lambda_2 \right) \llbracket \mathbf{u} \rrbracket_{(3)}^2 \right]. \end{aligned} \quad (7.58)$$

It becomes obvious that potential (7.58) cannot be captured by a local model with only one material parameter μ . To be more explicit, by rewriting this equation into generic form

$$\begin{aligned} &\overline{\mathcal{I}}_{\nabla \llbracket \mathbf{u} \rrbracket}(\llbracket \mathbf{u} \rrbracket_{(i)} \cdot \llbracket \mathbf{u} \rrbracket_{(j)}) \\ &= \left(c_{11}^{\text{eff}} \llbracket \mathbf{u} \rrbracket_{(1)}^2 + c_{12}^{\text{eff}} \llbracket \mathbf{u} \rrbracket_{(1)} \cdot \llbracket \mathbf{u} \rrbracket_{(2)} + c_{13}^{\text{eff}} \llbracket \mathbf{u} \rrbracket_{(1)} \cdot \llbracket \mathbf{u} \rrbracket_{(3)} + \right. \\ &\quad \left. c_{22}^{\text{eff}} \llbracket \mathbf{u} \rrbracket_{(2)}^2 + c_{23}^{\text{eff}} \llbracket \mathbf{u} \rrbracket_{(2)} \cdot \llbracket \mathbf{u} \rrbracket_{(3)} + c_{33}^{\text{eff}} \llbracket \mathbf{u} \rrbracket_{(3)}^2 \right) \end{aligned} \quad (7.59)$$

and by comparing the coefficients, one obtains

$$c_{11}^{\text{eff}} = \frac{1}{2} \left(\frac{\lambda_1}{9} + 2 \lambda_2 \right), \quad c_{12}^{\text{eff}} = c_{13}^{\text{eff}} = \frac{1}{2} \left(\frac{\lambda_1}{9} - 2 \lambda_2 \right),$$

$$c_{22}^{\text{eff}} = c_{33}^{\text{eff}} = \frac{1}{2} \left(\frac{\lambda_1}{9} + \lambda_2 \right), \quad c_{23}^{\text{eff}} = \frac{1}{2} \left(\frac{1}{9} \lambda_1 \right). \quad (7.60)$$

Clearly, this set of equations does not have a solution. Consequently, in general it is not possible to create an arbitrary generic potential by integration of a local model with just one material parameter leading to equivalence

$$\bar{\mathcal{I}}_{\llbracket \mathbf{u} \rrbracket}(\llbracket \mathbf{u} \rrbracket_{(i)} \cdot \llbracket \mathbf{u} \rrbracket_{(j)}) \stackrel{(7.35)}{\Rightarrow} \bar{\mathcal{I}}(\llbracket \mathbf{u} \rrbracket_{(i)} \cdot \llbracket \mathbf{u} \rrbracket_{(j)}) \stackrel{(7.51)}{\Leftrightarrow} \bar{\mathcal{I}}_{\nabla \llbracket \mathbf{u} \rrbracket}(\llbracket \mathbf{u} \rrbracket_{(i)} \cdot \llbracket \mathbf{u} \rrbracket_{(j)}). \quad (7.61)$$

7.2.4 Possibilities to expand the equivalence

As shown in the previous subsection, it is not possible to generate an arbitrary generic potential of the form $\bar{\mathcal{I}}_{\llbracket \mathbf{u} \rrbracket}(\llbracket \mathbf{u} \rrbracket_{(i)} \cdot \llbracket \mathbf{u} \rrbracket_{(j)})$ from spatial integration of a local model with just one single material parameter.

As a possible expansion, a spatial distribution of the material parameter in the local interface model μ is investigated next. Since the generic model (7.59) shows six model parameters for a quadratic energy, six different material parameters are also required for the local model. As a consequence, the material parameters are discretised by quadratic shape functions $\tilde{N}^{(i)}$ leading to

$$\mathbf{a}_I^{\text{el}}(\mathbf{X}) \approx \sum_i^6 \tilde{N}^{(i)} \tilde{c}^{(i)}. \quad (7.62)$$

Thereby, the integration off the local model reads

$$\begin{aligned} \int_{\Delta} \Psi(\llbracket \mathbf{u} \rrbracket \cdot \llbracket \mathbf{u} \rrbracket) dA &\approx \int_{\Delta} \frac{1}{2} \left(\sum_i \sum_j \sum_k \tilde{N}^{(i)} N^{(j)} N^{(k)} \tilde{c}^{(i)} \llbracket \mathbf{u} \rrbracket_{(j)} \cdot \llbracket \mathbf{u} \rrbracket_{(k)} \right) \det \mathbf{J}_{\xi} dA_{\xi} \\ &= \frac{1}{2} A \begin{bmatrix} \llbracket \mathbf{u} \rrbracket_{(1)} \cdot \llbracket \mathbf{u} \rrbracket_{(1)} \\ \llbracket \mathbf{u} \rrbracket_{(1)} \cdot \llbracket \mathbf{u} \rrbracket_{(2)} \\ \llbracket \mathbf{u} \rrbracket_{(1)} \cdot \llbracket \mathbf{u} \rrbracket_{(3)} \\ \llbracket \mathbf{u} \rrbracket_{(2)} \cdot \llbracket \mathbf{u} \rrbracket_{(2)} \\ \llbracket \mathbf{u} \rrbracket_{(2)} \cdot \llbracket \mathbf{u} \rrbracket_{(3)} \\ \llbracket \mathbf{u} \rrbracket_{(3)} \cdot \llbracket \mathbf{u} \rrbracket_{(3)} \end{bmatrix} \cdot \underbrace{\begin{pmatrix} \begin{bmatrix} 1/30 & -1/90 & -1/90 & 1/15 & 1/45 & 1/15 \\ 0 & 0 & -1/90 & 4/45 & 2/45 & 2/45 \\ 0 & -1/90 & 0 & 2/45 & 2/45 & 4/45 \\ -1/90 & 1/30 & -1/90 & 1/15 & 1/15 & 1/45 \\ -1/90 & 0 & 0 & 2/45 & 4/45 & 2/45 \\ -1/90 & -1/90 & 1/30 & 1/45 & 1/15 & 1/15 \end{bmatrix} \\ \begin{bmatrix} \tilde{c}^{(1)} \\ \tilde{c}^{(2)} \\ \tilde{c}^{(3)} \\ \tilde{c}^{(4)} \\ \tilde{c}^{(5)} \\ \tilde{c}^{(6)} \end{bmatrix} \end{pmatrix}}_B \end{aligned} \quad (7.63)$$

leading to a potential with six material parameters. On the other hand, postulating a general quadratic effective potential yields

$$\bar{\mathcal{I}}_{\nabla \llbracket \mathbf{u} \rrbracket}(\llbracket \mathbf{u} \rrbracket_M, \nabla \llbracket \mathbf{u} \rrbracket)$$

$$\begin{aligned}
 &= \overline{\mathcal{I}}_{\nabla[\mathbf{u}]}(\hat{I}_1, \hat{I}_2, \hat{I}_3, \hat{I}_4, \hat{I}_5, \hat{I}_6) = \left[\hat{k}^{(1)} \hat{I}_1 + \hat{k}^{(2)} \hat{I}_2 + \hat{k}^{(3)} \hat{I}_3 + \hat{k}^{(4)} \hat{I}_4 + \hat{k}^{(5)} \hat{I}_5 + \hat{k}^{(6)} \hat{I}_6 \right] \\
 &= \overline{\mathcal{I}}_{\nabla[\mathbf{u}]}([\mathbf{u}]_{(i)} \cdot [\mathbf{u}]_{(j)}) \approx \\
 &\frac{1}{2} \begin{bmatrix} [\mathbf{u}]_{(1)} \cdot [\mathbf{u}]_{(1)} \\ [\mathbf{u}]_{(1)} \cdot [\mathbf{u}]_{(2)} \\ [\mathbf{u}]_{(1)} \cdot [\mathbf{u}]_{(3)} \\ [\mathbf{u}]_{(2)} \cdot [\mathbf{u}]_{(2)} \\ [\mathbf{u}]_{(2)} \cdot [\mathbf{u}]_{(3)} \\ [\mathbf{u}]_{(3)} \cdot [\mathbf{u}]_{(3)} \end{bmatrix} \cdot \underbrace{\begin{pmatrix} \begin{bmatrix} 1/9 & -1/3 & -1/3 & 1 & 1 & 1 \\ 2/9 & 0 & -1/3 & -2 & -1 & 0 \\ 2/9 & -1/3 & 0 & 0 & -1 & -2 \\ 1/9 & 1/3 & 0 & 1 & 0 & 0 \\ 2/9 & 1/3 & 1/3 & 0 & 1 & 0 \\ 1/9 & 0 & 1/3 & 0 & 0 & 1 \end{bmatrix} \cdot \begin{bmatrix} \hat{k}^{(1)} \\ \hat{k}^{(2)} \\ \hat{k}^{(3)} \\ \hat{k}^{(4)} \\ \hat{k}^{(5)} \\ \hat{k}^{(6)} \end{bmatrix} \\ \mathbf{C} \end{pmatrix} \cdot \quad (7.64)
 \end{aligned}$$

Since matrix \mathbf{B} as well as matrix \mathbf{C} are invertible, both models can be transferred to each other in the case of a quadratic relation of the displacement jump and a spatial distribution of the material parameter, i.e.,

$$\int \Psi([\mathbf{u}]) \, dA \Leftrightarrow \overline{\mathcal{I}}_{\nabla[\mathbf{u}]}([\mathbf{u}]_M, \overline{\text{GRAD}}_M[\mathbf{u}]) \, A \quad (\text{for quadratic energies}). \quad (7.65)$$

However, equivalence (7.65) is only valid under the aforementioned assumptions. Furthermore, the inversion of matrix \mathbf{B} and \mathbf{C} provides information about the choice of material parameters, see Remark 14.

An extension to higher-order energies is not possible. For instance, in the case of a fourth order potential $([\mathbf{u}]_{(i)} \cdot [\mathbf{u}]_{(j)}) ([\mathbf{u}]_{(k)} \cdot [\mathbf{u}]_{(l)})$, one has 21 material parameters. In this case, the stiffness of the respective local model would be approximated by

$$\mathbf{a}_{II}^{\text{el}}(\mathbf{X}) = \sum_{m=1}^{21} \hat{N}^{(m)} \hat{c}^{(m)}. \quad (7.66)$$

A detailed overview of the shape functions is given in Appendix C.1. In analogy to Eq. (7.63), integration of the local energy takes the form

$$\begin{aligned}
 &\int_{\Delta} \Psi([\mathbf{u}] \cdot [\mathbf{u}])^2 \, dA \approx \\
 &\int_{\Delta} \frac{1}{2} \left(\sum_{m=1}^{21} \sum_{i=1}^3 \sum_{j=1}^3 \sum_{k=1}^3 \sum_{l=1}^3 \hat{N}^{(m)} N^{(i)} N^{(j)} N^{(k)} N^{(l)} \hat{c}^{(m)} \right. \\
 &\left. ([\mathbf{u}]_{(i)} \cdot [\mathbf{u}]_{(j)}) ([\mathbf{u}]_{(k)} \cdot [\mathbf{u}]_{(l)}) \right) \det \mathbf{J}_{\xi} \, dA_{\xi} = \frac{1}{2} A [\mathbf{u}]_{(ijkl)} \cdot \mathbb{D} \cdot \hat{\mathbf{c}}. \quad (7.67)
 \end{aligned}$$

Here, $[\mathbf{u}]_{(ijkl)}$ represents a vector with the 21 different scalar product combinations of node jumps, \mathbb{D} is a 21×21 matrix including the several stiffness pre-factors arising from

the integration and $\hat{\mathbf{c}}$ denotes the vector with the 21 stiffness contributions. A detailed representation is given in Appendix C.1.

It can be shown that matrix \mathbb{D} is not invertible due to the commutativity of the product of the shape functions. For instance, it holds that

$$\int N^{(i)} N^{(j)} N^{(k)} N^{(l)} dA = \int N^{(i)} N^{(k)} N^{(j)} N^{(l)} dA. \quad (7.68)$$

However, it also holds that

$$([\mathbf{u}]_{(i)} \cdot [\mathbf{u}]_{(j)}) ([\mathbf{u}]_{(k)} \cdot [\mathbf{u}]_{(l)}) \neq ([\mathbf{u}]_{(i)} \cdot [\mathbf{u}]_{(k)}) ([\mathbf{u}]_{(j)} \cdot [\mathbf{u}]_{(l)}). \quad (7.69)$$

Consequently, in general local potential $\bar{\mathcal{I}}_{[\mathbf{u}]}$ does not follow from $\bar{\mathcal{I}}_{\nabla[\mathbf{u}]}$ since the local model provides identical stiffness values to several contributions due to commutativity of the shape functions.

7.2.5 Physical interpretation of the interface contributions

In the previous subsection it was shown that the equivalence between the integration of a local interface model with a spatial distribution of the material parameter and the gradient enhanced effective model is only valid in the case of quadratic dependence of the displacement jump $[\mathbf{u}]$. From a physics point of view this is not surprising, since the local approach cannot capture different stiffness values for all different physical modes. In the case of $(i) = (j)$, the contributions are related to the length of the fiber connecting nodes with identical material coordinates in the reference configuration, see Fig. 7.4 (left). In contrast, if $(i) \neq (j)$, the contributions are related to the angle between

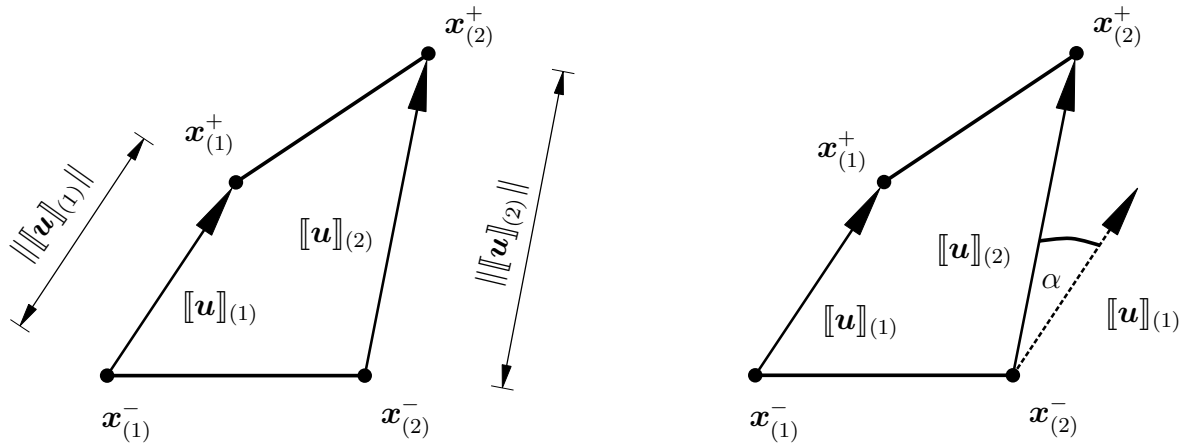


Figure 7.4: Two-dimensional interface element with four nodes (two on each side of the interface). Left side: Graphical interpretation of the contributions $[\mathbf{u}]_{(i)} \cdot [\mathbf{u}]_{(j)}$ if $(i) = (j)$ – length of the fiber. Right side: Graphical interpretation of the contributions $[\mathbf{u}]_{(i)} \cdot [\mathbf{u}]_{(j)}$ if $(i) \neq (j)$ – angle between the fibers.

two different fibers, see Fig. 7.4 (right), i.e.,

$$[[\mathbf{u}]]_{(i)} \cdot [[\mathbf{u}]]_{(j)} = \|[[\mathbf{u}]]_{(i)} \| \|[[\mathbf{u}]]_{(j)} \| \cos \angle([[\mathbf{u}]]_{(i)}, [[\mathbf{u}]]_{(j)}) \quad (7.70)$$

with $\angle([[\mathbf{u}]]_{(i)}, [[\mathbf{u}]]_{(j)})$ denoting the angle between $[[\mathbf{u}]]_{(i)}$ and $[[\mathbf{u}]]_{(j)}$. Thus, Eq. (7.69) compares contributions with different physical modes, although they are described by the same material stiffness, see Eq. (7.68). For instance, the contribution

$$([[\mathbf{u}]]_{(1)} \cdot [[\mathbf{u}]]_{(1)}) ([[\mathbf{u}]]_{(2)} \cdot [[\mathbf{u}]]_{(2)}) \quad (7.71)$$

describes the relation of two node jump lengths while contribution

$$([[\mathbf{u}]]_{(1)} \cdot [[\mathbf{u}]]_{(2)}) ([[\mathbf{u}]]_{(1)} \cdot [[\mathbf{u}]]_{(2)}) \quad (7.72)$$

is related to the change of the angle between two fibers. Thus, they can be characterised by different stiffness values in general, while integration of the local model yields identical stiffness values for both contributions due to Eq. (7.68).

Remark 13 *An isotropic model of type $\Psi([[\mathbf{u}]])$ does not imply an isotropic model of type $\Psi([[\mathbf{u}]]_M, \overline{GRAD}_M[[\mathbf{u}]])$. First, a quadratic Helmholtz energy just depending on the displacement jump $[[\mathbf{u}]]$ (classic framework) is considered, i.e.,*

$$\Psi([[\mathbf{u}]]) = \frac{1}{2} c [[\mathbf{u}]] \cdot [[\mathbf{u}]], \quad (7.73)$$

where approximation (7.27) for the displacement jump vector is used. Thereby, energy (7.73) takes the form

$$\Psi = \frac{1}{2} c [[\mathbf{u}]]_M + \overline{GRAD}_M[[\mathbf{u}]] \cdot (\mathbf{X} - \mathbf{X}_M) \cdot [[\mathbf{u}]]_M + \overline{GRAD}_M[[\mathbf{u}]] \cdot (\mathbf{X} - \mathbf{X}_M) \quad (7.74)$$

with $\mathbf{X}_M = \mathbf{0}$, see Fig. 7.5. An integration of Ψ over the element area leads to

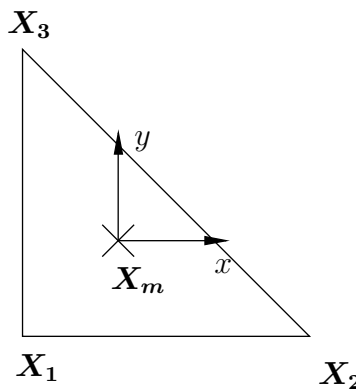


Figure 7.5: Linear triangle element

$$\int \Psi \, dA = \frac{1}{2} c \left[\llbracket \mathbf{u} \rrbracket_M \cdot \llbracket \mathbf{u} \rrbracket_M A + 2 \overline{GRAD}_M^T \llbracket \mathbf{u} \rrbracket \cdot \llbracket \mathbf{u} \rrbracket_M \cdot \underbrace{\int \mathbf{X} \, dA}_{=0} \right] \quad (7.75)$$

$$+ \left(\overline{GRAD}_M^T \llbracket \mathbf{u} \rrbracket \cdot \overline{GRAD}_M \llbracket \mathbf{u} \rrbracket \right) : \underbrace{\int \mathbf{X} \otimes \mathbf{X} \, dA}_{\mathbf{I}}, \quad (7.76)$$

where the second term vanishes due to the position of the coordinate system in the center of gravity. Accordingly, starting from an isotropic energy depending on $\llbracket \mathbf{u} \rrbracket$ leads to an anisotropic energy depending on $\llbracket \mathbf{u} \rrbracket_M$ and $\overline{\nabla} \llbracket \mathbf{u} \rrbracket_M$. The anisotropy is related to tensor \mathbf{I} (tensor of moment of inertia).

Remark 14 The inversion of matrices \mathbf{B} and \mathbf{C} in Eqs. (7.63) and (7.64) provides information about the choice of the material parameter. To be more explicit, the simple choice of $\hat{k}^{(i)} = 1$ leading to

$$\overline{\mathcal{I}}_{\overline{\nabla} \llbracket \mathbf{u} \rrbracket}(\hat{I}_1, \hat{I}_2, \hat{I}_3, \hat{I}_4, \hat{I}_5, \hat{I}_6) = \left[\hat{I}_1 + \hat{I}_2 + \hat{I}_3 + \hat{I}_4 + \hat{I}_5 + \hat{I}_6 \right] \quad (7.77)$$

yields the following equivalent material parameter $\tilde{c}^{(i)}$ for the local model (units are ignored here):

$$\begin{aligned} \tilde{c}^{(1)} &= 258.667, \quad \tilde{c}^{(2)} = -101.333, \quad \tilde{c}^{(3)} = -101.333 \\ \tilde{c}^{(4)} &= -171.333, \quad \tilde{c}^{(5)} = 143.667, \quad \tilde{c}^{(6)} = 33.6667 \end{aligned} \quad (7.78)$$

It follows that, although both models are equivalent, this does not mean that the models are meaningful from a physics point of view since negative stiffness values are from a physics point of view - at least - questionable.

7.3 Gradient of surface deformation gradient

7.3.1 Motivation

As presented in Chapter 6 complex non-monotonic size effects can be captured with the generalised interface framework combining the displacement jump $[[\mathbf{u}]]$ and the surface deformation gradient $\overline{\mathbf{F}}$. However, the influence of curvature effects is not considered. Especially at small scales curvature effects can highly influence the material behaviour. An extension of surface elasticity theory with curvature effects was shown, for instance in [92, 93] and further elaborated in [17]. In this section it is investigated as to how curvature effects can be captured within the interface by incorporation of the surface gradient of $\overline{\mathbf{F}}$ into the Helmholtz energy. Firstly, it is shown by a simple example why this could be of high interest at small length scales. For that purpose, different energies are compared in order to investigate the influence of displacement jump $[[\mathbf{u}]]$, surface deformation gradient $\overline{\mathbf{F}}$ and the gradient of $\overline{\mathbf{F}}$. A spherical RVE with reference radius $r = R$ is chosen, where φ and θ describe the curvilinear coordinates θ^1 and θ^2 , see Fig. 7.6. A point P lying on the reference surface of the sphere is described by spherical

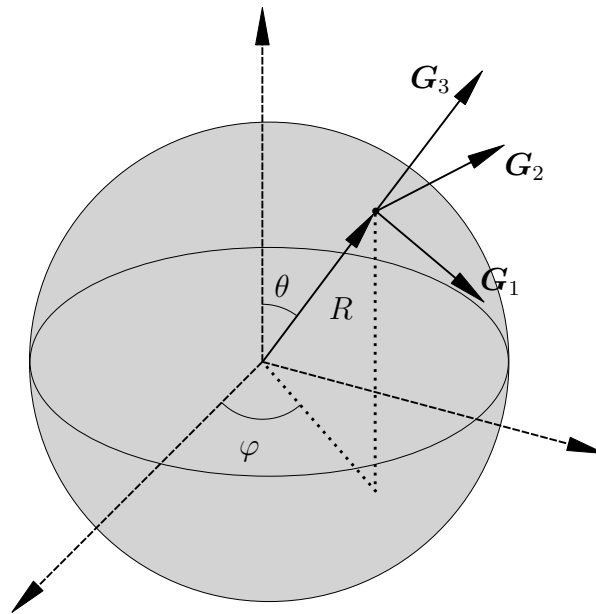


Figure 7.6: Reference configuration of the sphere with covariant base vectors \mathbf{G}_1 , \mathbf{G}_2 and \mathbf{G}_3

coordinates, i.e.,

$$\mathbf{X}(R, \varphi, \theta) = \begin{bmatrix} R \sin(\theta) \cos(\varphi) \\ R \sin(\theta) \sin(\varphi) \\ R \cos(\theta) \end{bmatrix}. \quad (7.79)$$

The tangential base vectors of the reference configuration are calculated by

$$\mathbf{G}_1 = \frac{\partial \mathbf{X}}{\partial \varphi} \quad \text{and} \quad \mathbf{G}_2 = \frac{\partial \mathbf{X}}{\partial \theta} \quad (7.80)$$

and the unit normal vector $\mathbf{N} = \mathbf{G}_3$ simplifies to \mathbf{X}/R . The sphere undergoes a uniform expansion by applying displacement $\llbracket u \rrbracket$ to the initial radius R . The current configuration is thus computed

$$\mathbf{x} = \mathbf{X} + \llbracket u \rrbracket \mathbf{e}_r. \quad (7.81)$$

For this deformation, the surface deformation gradient reads

$$\overline{\mathbf{F}}(\llbracket u \rrbracket) = \frac{\partial \mathbf{x}(\llbracket u \rrbracket)}{\partial \theta^\alpha} \otimes \frac{\partial \theta^\alpha}{\partial \mathbf{X}} \quad (7.82)$$

and its gradient

$$\overline{\text{GRAD}}(\overline{\mathbf{F}})(\llbracket u \rrbracket) = \frac{\partial^2 \mathbf{x}(\llbracket u \rrbracket)}{\partial \theta^\alpha \partial \theta^\beta} \otimes \mathbf{G}^\alpha \otimes \mathbf{G}^\beta + \frac{\partial \mathbf{x}(\llbracket u \rrbracket)}{\partial \theta^\alpha} \otimes \frac{\partial \mathbf{G}^\alpha}{\partial \theta^\beta} \otimes \mathbf{G}^\beta. \quad (7.83)$$

First, an isotropic quadratic energy $\psi(\llbracket u \rrbracket) = 1/2 \tilde{c} \llbracket u \rrbracket^2$ is analysed. The Helmholtz energy is integrated over the sphere surface, i.e.,

$$\tilde{\Psi}_{\llbracket u \rrbracket} = \tilde{\Psi}^{\text{eff}}(\llbracket u \rrbracket) = \int \frac{1}{2} \tilde{c} \llbracket u \rrbracket^2 \underbrace{\mathbf{e}_r \cdot \mathbf{e}_r}_{=1} dA = 2 \pi c R^2 \llbracket u \rrbracket^2, \quad (7.84)$$

where R denotes the initial radius of the sphere and the material parameter \tilde{c} characterises a stiffness. In the case of a fully reversible material response, the energetically dual force results in

$$\tilde{F}_{\llbracket u \rrbracket} = \frac{d\tilde{\Psi}_{\llbracket u \rrbracket}}{d\llbracket u \rrbracket} = 4 \pi c R^2 \llbracket u \rrbracket. \quad (7.85)$$

Next, an energy depending on $\overline{\mathbf{F}}$ is investigated. It is given by

$$\Psi(\overline{\mathbf{F}}) = \frac{1}{2} \hat{c} (\overline{\mathbf{F}} : \overline{\mathbf{F}} - 2 - 2 \ln [\overline{\det}(\overline{\mathbf{F}})]). \quad (7.86)$$

It is a Neo-Hooke-like energy which vanishes for the undeformed configuration, the respective stresses also vanish in the undeformed configuration and converges to infinity, if the sphere is either compressed to a point or increased up to infinity. Integration yields

$$\hat{\Psi}_{\overline{\mathbf{F}}} = \hat{\Psi}(\overline{\mathbf{F}}) = \hat{\Psi}^{\text{eff}}(\llbracket u \rrbracket) = \int \frac{1}{2} \hat{c} (\overline{\mathbf{F}} : \overline{\mathbf{F}} - 2 - 2 \ln [\overline{\det}(\overline{\mathbf{F}})]) dA$$

$$= \pi \hat{c} \left[\llbracket u \rrbracket (\llbracket u \rrbracket + 4R) - 4R^2 \ln \left(\frac{(2R + \llbracket u \rrbracket)^2}{4R^2} \right) \right]. \quad (7.87)$$

The material parameter \hat{c} characterises again a stiffness. The energetically dual force reads

$$\hat{F}_{\overline{\mathbf{F}}} = \frac{d\hat{\Psi}_{\overline{\mathbf{F}}}}{d\llbracket u \rrbracket} = \pi \hat{c} \llbracket u \rrbracket \left(\frac{4R + \llbracket u \rrbracket}{R + \frac{1}{2}\llbracket u \rrbracket} \right). \quad (7.88)$$

Finally, an energy depending on $\overline{\text{GRAD}}(\overline{\mathbf{F}})$, respectively the current mean curvature h is investigated. It is assumed that the reference configuration of the sphere has no initial energy, i.e.,

$$\overline{\Psi}(\overline{\mathbf{F}}, \overline{\text{GRAD}}(\overline{\mathbf{F}})) = \bar{c} (h - H)^2, \quad (7.89)$$

where \bar{c} denotes a bending stiffness and where H is the mean curvature of the reference configuration. The integration over the sphere surface leads to

$$\begin{aligned} \overline{\Psi}_{\overline{\text{GRAD}}(\overline{\mathbf{F}})} &= \overline{\Psi}(\overline{\mathbf{F}}, \overline{\text{GRAD}}(\overline{\mathbf{F}})) = \overline{\Psi}^{\text{eff}}(\llbracket u \rrbracket) \\ &= \int \frac{\tilde{c} \llbracket u \rrbracket^2}{r^2 (2r + \llbracket u \rrbracket)^2} dA = \frac{4\pi \bar{c} \llbracket u \rrbracket^2}{(\llbracket u \rrbracket + 2R)^2}. \end{aligned} \quad (7.90)$$

The energetically dual force results now in

$$\overline{F}_{\overline{\text{GRAD}}(\overline{\mathbf{F}})} = \frac{d\overline{\Psi}_{\overline{\text{GRAD}}(\overline{\mathbf{F}})}}{d\llbracket u \rrbracket} = \frac{16\pi \bar{c} r \llbracket u \rrbracket}{(2r + \llbracket u \rrbracket)^3}. \quad (7.91)$$

Next, the different types of surface energies and the conjugate forces are compared. For that reason the stiffness parameters are chosen as

$$\tilde{c} = 100 \frac{\text{N}}{\text{cm}^3}, \quad \hat{c} = 3300 \frac{\text{N}}{\text{cm}} \quad \text{and} \quad \bar{c} = 40000 \text{ Ncm} \quad (7.92)$$

and the initial radius of the sphere is set to $R = 10$ cm. The evaluation of the energies and the corresponding forces versus $\llbracket u \rrbracket/R$ are plotted in Fig. 7.7 and Fig. 7.8.

It can be seen that all energies and forces vanish in the reference configuration. Furthermore, and in contrast to $\hat{\Psi}$ and $\overline{\Psi}$, energy $\tilde{\Psi}$ quadratically depending on $\llbracket u \rrbracket$ is finite and thus unphysical if the sphere is compressed to a point ($\llbracket u \rrbracket/R = -1$). In the case of $\llbracket u \rrbracket/R \rightarrow \infty$, $\tilde{\Psi}$ and $\hat{\Psi}$ also converge to infinity. By ways of contrast energy $\overline{\Psi}$ saturates and thus the respective force approaches zero for $\llbracket u \rrbracket/R \rightarrow \infty$. This is expected, since the curvature of the deformed configuration vanishes in this case. It can be seen that especially on small sizes the curvature highly influences the energy and the respective

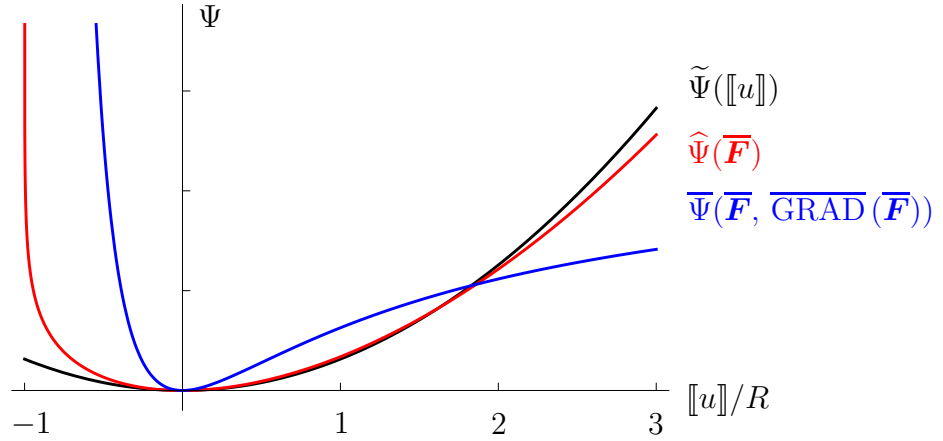


Figure 7.7: Sphere undergoing deformation in radial direction: Energies depending on $[[u]]/R$

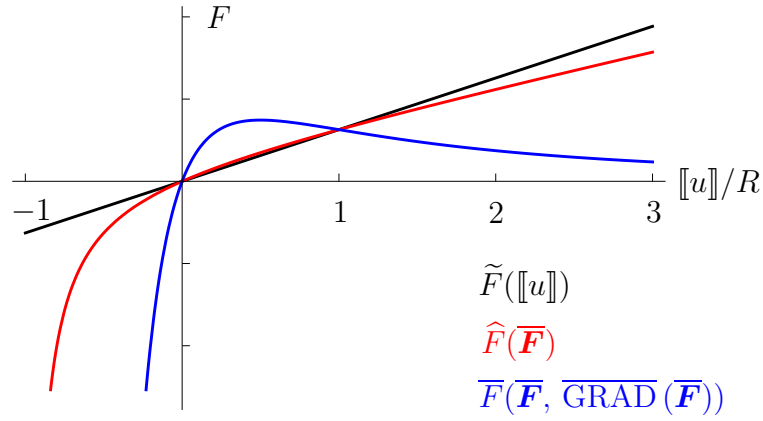


Figure 7.8: Sphere undergoing deformation in radial direction: Reaction forces depending on $[[u]]/R$

force. Therefore, it seems to be promising to further investigate the curvature influence to capture additional size effects on small length scales.

7.3.2 Kinematics

According to Chapter 5, in the case of non-coherent interfaces the surface deformation gradient is related to the coordinates $\mathbf{x}_{(m)}$ located in the fictitious mid-surface and is defined as

$$\overline{\mathbf{F}} := \overline{\text{GRAD}}(\mathbf{x}_{(m)}) = \frac{\partial \mathbf{x}_{(m)}}{\partial \mathbf{X}} = \frac{\partial \mathbf{x}_{(m)}}{\partial \theta^\alpha} \otimes \frac{\partial \theta^\alpha}{\partial \mathbf{X}} = \mathbf{g}_\alpha \otimes \mathbf{G}^\alpha. \quad (7.93)$$

It follows then

$$\overline{\mathbf{F}}^T = \mathbf{G}^\alpha \otimes \mathbf{g}_\alpha, \quad \overline{\mathbf{F}}^{-1} = \mathbf{G}_\alpha \otimes \mathbf{g}^\alpha \quad \text{and} \quad \overline{\mathbf{F}}^{-T} = \mathbf{g}^\alpha \otimes \mathbf{G}_\alpha. \quad (7.94)$$

Accordingly, the surface gradient of $\overline{\mathbf{F}}$ is calculated by

$$\overline{\text{GRAD}}(\overline{\mathbf{F}}) = \frac{\partial \overline{\mathbf{F}}}{\partial \theta^\beta} \otimes \mathbf{G}^\beta = \frac{\partial (\mathbf{g}_\alpha \otimes \mathbf{G}^\alpha)}{\partial \theta^\beta} \otimes \mathbf{G}^\beta, \quad (7.95)$$

which leads to

$$\overline{\text{GRAD}}(\overline{\mathbf{F}}) = \mathbf{g}_{\alpha,\beta} \otimes \mathbf{G}^\alpha \otimes \mathbf{G}^\beta + \mathbf{g}_\alpha \otimes \mathbf{G}_{,\beta}^\alpha \otimes \mathbf{G}^\beta. \quad (7.96)$$

Here and henceforth $[(\bullet), \beta]$ denotes the partial derivative of (\bullet) with respect to the coordinate θ^β .

7.3.3 Objectivity requirements

In the case of the general interface model an extension in order to account for the gradient of $\overline{\mathbf{F}}$ leads to the respective Helmholtz energy of type

$$\Psi = \Psi(\llbracket \mathbf{u} \rrbracket, \overline{\mathbf{F}}, \overline{\text{GRAD}}(\overline{\mathbf{F}})). \quad (7.97)$$

For this extended framework, objectivity (frame indifference) requires

$$\Psi(\llbracket \mathbf{u} \rrbracket, \overline{\mathbf{F}}, \overline{\text{GRAD}}(\overline{\mathbf{F}})) = \Psi(\mathbf{Q} \cdot \llbracket \mathbf{u} \rrbracket, \mathbf{Q} \cdot \overline{\mathbf{F}}, \mathbf{Q} \cdot \overline{\text{GRAD}}(\overline{\mathbf{F}})) \quad \forall \mathbf{Q} \in SO3, \quad (7.98)$$

since the surface gradient of $\overline{\mathbf{F}}$ transforms under an observer transformation according to

$$\{\overline{\text{GRAD}}(\overline{\mathbf{F}})\}^* = \mathbf{Q} \cdot \overline{\text{GRAD}}(\overline{\mathbf{F}}). \quad (7.99)$$

In order to fulfill the principle of objectivity, or to be more precise the principle of material covariance, the Helmholtz energy density has to be of the form

$$\Psi = \Psi(\llbracket \mathbf{u} \rrbracket \cdot \llbracket \mathbf{u} \rrbracket, \overline{\mathbf{F}} \cdot \llbracket \mathbf{u} \rrbracket, \overline{\text{GRAD}}(\overline{\mathbf{F}}) \cdot \llbracket \mathbf{u} \rrbracket, \overline{\mathbf{F}}^T \cdot \overline{\mathbf{F}}, \overline{\mathbf{F}}^{-1} \cdot \overline{\text{GRAD}}(\overline{\mathbf{F}}), \overline{\text{GRAD}}^T(\overline{\mathbf{F}}) \cdot \overline{\text{GRAD}}(\overline{\mathbf{F}})). \quad (7.100)$$

The contributions in (7.100) are then analysed in detail. Since the focus is on bending effects, the influence of $\llbracket \mathbf{u} \rrbracket$ -terms is neglected. Following standard notation in bulk materials and as already introduced in Subsection 5.2.4, the first term in Eq. (7.100) that does not depend on $\llbracket \mathbf{u} \rrbracket$ is the Cauchy-Green surface tensor, i.e.,

$$\overline{\mathbf{C}} = \overline{\mathbf{F}}^T \cdot \overline{\mathbf{F}} = (\mathbf{g}_\alpha \cdot \mathbf{g}_\beta) \mathbf{G}^\alpha \otimes \mathbf{G}^\beta = g_{\alpha\beta} \mathbf{G}^\alpha \otimes \mathbf{G}^\beta. \quad (7.101)$$

The contribution $\overline{\mathbf{F}}^{-1} \cdot \overline{\text{GRAD}}(\overline{\mathbf{F}})$ is sometimes referred to as configuration tensor, c.f. Bertram [11], in bulk materials. It can be rewritten as

$$\begin{aligned}\overline{\mathbf{K}}_{\text{sur}} &= \overline{\mathbf{F}}^{-1} \cdot \overline{\text{GRAD}}(\overline{\mathbf{F}}) \\ &= (\mathbf{g}_{\alpha,\beta} \cdot \mathbf{g}^\gamma) \mathbf{G}_\gamma \otimes \mathbf{G}^\alpha \otimes \mathbf{G}^\beta + \mathbf{G}_\alpha \otimes \mathbf{G}_{,\beta}^\alpha \otimes \mathbf{G}^\beta.\end{aligned}\quad (7.102)$$

In order to derive the fourth order tensor arising from the last contribution, $\overline{\text{GRAD}}^T(\overline{\mathbf{F}})$ is introduced in index notation as

$$\left(\overline{\text{GRAD}}^T(\overline{\mathbf{F}})\right)_{nmi} = \frac{\partial \overline{F}_{im}}{\partial \overline{X}_n}.\quad (7.103)$$

This leads to representation

$$\begin{aligned}\overline{\text{GRAD}}^T(\overline{\mathbf{F}}) \cdot \overline{\text{GRAD}}(\overline{\mathbf{F}}) &= (\mathbf{g}_{\alpha,\beta} \cdot \mathbf{g}_{\gamma,\delta}) [\mathbf{G}^\beta \otimes \mathbf{G}^\alpha \otimes \mathbf{G}^\gamma \otimes \mathbf{G}^\delta] \\ &\quad + (\mathbf{g}_{\alpha,\beta} \cdot \mathbf{g}_\gamma) [\mathbf{G}^\beta \otimes \mathbf{G}^\alpha \otimes \mathbf{G}_{,\delta}^\gamma \otimes \mathbf{G}^\delta] \\ &\quad + (\mathbf{g}_\alpha \cdot \mathbf{g}_{\gamma,\delta}) [\mathbf{G}^\beta \otimes \mathbf{G}_{,\beta}^\alpha \otimes \mathbf{G}^\gamma \otimes \mathbf{G}^\delta] \\ &\quad + (\mathbf{g}_\alpha \cdot \mathbf{g}_\gamma) [\mathbf{G}^\beta \otimes \mathbf{G}_{,\beta}^\alpha \otimes \mathbf{G}_{,\delta}^\gamma \otimes \mathbf{G}^\delta].\end{aligned}\quad (7.104)$$

7.3.4 Symmetry properties of $\overline{\text{GRAD}}(\overline{\mathbf{F}})$

Following Steinmann [95], in the case of convective coordinates the deformation gradient of the bulk deformation gradient \mathbf{F} can be expressed as

$$\text{GRAD}(\mathbf{F}) = (\gamma_{jk}^i - \Gamma_{jk}^i) \mathbf{g}_i \otimes \mathbf{G}^j \otimes \mathbf{G}^k,\quad (7.105)$$

where γ_{jk}^i and Γ_{jk}^i denote Christoffel symbols defined as

$$\gamma_{jk}^i = \mathbf{g}_{j,k} \cdot \mathbf{g}^i \quad \text{and} \quad -\Gamma_{jk}^i = \mathbf{G}_{,j}^i \cdot \mathbf{G}_k.\quad (7.106)$$

Since $\text{GRAD}(\mathbf{F})$ maps tensors in the $\theta^1 - \theta^2 - \theta^3$ -space it holds that

$$\text{GRAD}(\mathbf{F}) : \mathbf{A} = \text{GRAD}(\mathbf{F}) : \mathbf{A}^T \quad \forall \mathbf{A}, \mathbf{A}^T \in \text{span}\{\mathbf{G}_i\}.\quad (7.107)$$

In analogy to (7.105), an equivalent representation of $\overline{\text{GRAD}}(\overline{\mathbf{F}})$ is introduced as

$$\overline{\text{GRAD}}(\overline{\mathbf{F}}) = \overline{\gamma}_{\alpha\beta}^k \mathbf{g}_k \otimes \mathbf{G}^\alpha \otimes \mathbf{G}^\beta - \overline{\Gamma}_{\beta k}^\alpha \mathbf{g}_\alpha \otimes \mathbf{G}^k \otimes \mathbf{G}^\beta.\quad (7.108)$$

Here, the Christoffel surface symbols are denoted as

$$\overline{\gamma}_{\alpha\beta}^k = \mathbf{g}_{\alpha,\beta} \cdot \mathbf{g}^k \quad \text{and} \quad -\overline{\Gamma}_{\beta k}^\alpha = \mathbf{G}_{,\beta}^\alpha \cdot \mathbf{G}_k.\quad (7.109)$$

Since $\overline{\text{GRAD}}(\overline{\mathbf{F}})$ maps tensors in the θ^1 - θ^2 -plane, respectively superficial tensors, definition (7.108) simplifies to

$$\overline{\text{GRAD}}(\overline{\mathbf{F}}) = \overline{\gamma}_{\alpha\beta}^k \mathbf{g}_k \otimes \mathbf{G}^\alpha \otimes \mathbf{G}^\beta - \overline{\Gamma}_{\beta\delta}^\alpha \mathbf{g}_\alpha \otimes \mathbf{G}^\delta \otimes \mathbf{G}^\beta. \quad (7.110)$$

To be more precise, it holds that

$$\begin{aligned} d\overline{\mathbf{x}} &= \overline{\mathbf{F}} \cdot d\overline{\mathbf{X}} \quad d\overline{\mathbf{x}} \in \text{span}\{\mathbf{g}_\alpha\} \quad , \quad d\overline{\mathbf{X}} \in \text{span}\{\mathbf{G}_\alpha\} \\ d\overline{\mathbf{F}} &= \overline{\text{GRAD}}(\overline{\mathbf{F}}) : d\overline{\mathbf{X}}. \end{aligned} \quad (7.111)$$

Regarding the symmetry properties of $\overline{\text{GRAD}}(\overline{\mathbf{F}})$ it holds that

$$\overline{\text{GRAD}}(\overline{\mathbf{F}}) : \overline{\mathbf{A}} = \overline{\text{GRAD}}(\overline{\mathbf{F}}) : \overline{\mathbf{A}}^T \quad \forall \overline{\mathbf{A}}, \overline{\mathbf{A}}^T \in \text{span}\{\mathbf{G}_\alpha\}. \quad (7.112)$$

Here, $\overline{\mathbf{A}} = A^{\alpha\beta} \mathbf{G}_\alpha \otimes \mathbf{G}_\beta$ is an arbitrary tensor. A detailed derivation is given in Appendix D.1.

7.3.5 On the relation between the mean curvature and $\overline{\text{GRAD}}(\overline{\mathbf{F}})$

The goal of this subsection is to show that the mean curvature h of the current configuration of a manifold can be represented as a covariant function of $\overline{\mathbf{F}}$ and $\overline{\text{GRAD}}(\overline{\mathbf{F}})$. Thereby, it is ensured that an energy depending of h automatically fulfills the principle of material covariance and equivalently the balance of angular momentum. Throughout the literature many different curvature terms and definitions exist, cf. for instance Kühnel [53], Steinmann [95]. Here, the mean curvature is defined as the arithmetic mean of the principal curvatures. To be more precise the reference mean curvature is defined as

$$H = \frac{1}{2}(K_1 + K_1) \quad (7.113)$$

while for the current configuration it follows that

$$h = \frac{1}{2}(k_1 + k_2). \quad (7.114)$$

Here, K_1 , K_2 , k_1 and k_2 denote the principle curvatures in the reference, respectively in the current configuration. Furthermore, the Laplacian operator applied to manifolds, also known as Laplace-Beltrami operator, is introduced as

$$\overline{\Delta}_{\mathbf{X}}(\mathbf{X}) = \overline{\text{DIV}}(\overline{\text{GRAD}}(\mathbf{X})) = -2H\overline{\mathbf{N}}. \quad (7.115)$$

Thus, $\overline{\Delta}_{\mathbf{x}}$ yields the reference mean curvature H of a surface, where $\overline{\mathbf{N}}$ denotes the unit normal vector at the considered point. Likewise, the current mean curvature is calculated by

$$\overline{\Delta}_{\mathbf{x}} = \overline{\text{div}}(\overline{\text{grad}}(\mathbf{x})) = -2h\overline{\mathbf{n}}. \quad (7.116)$$

Hence, the current mean curvature h follows as

$$\| -h\overline{\mathbf{n}} \| = \frac{1}{2} \| \overline{\text{div}}(\overline{\text{grad}}(\mathbf{x})) \| = h \quad (7.117)$$

In order to see the relation between the Laplace-Beltrami operator and $\overline{\text{GRAD}}(\overline{\mathbf{F}})$ the following transformed equation is introduced:

$$\overline{\text{div}}(\overline{\text{grad}}(\mathbf{x})) = \left[\overline{\text{GRAD}}(\overline{\mathbf{F}}) \cdot \overline{\mathbf{F}}^{-1} \right] : \overline{\mathbf{F}}^{-1} + \overline{\mathbf{F}} \cdot \left[\overline{\text{GRAD}}(\overline{\mathbf{F}}^{-1}) : \overline{\mathbf{F}}^{-T} \right]. \quad (7.118)$$

A detailed derivation of Eq. (7.118) can be found in Appendix D.2. By doing so, the current mean curvature h follows as

$$h = \frac{1}{2} \left\| \left[\overline{\text{GRAD}}(\overline{\mathbf{F}}) \cdot \overline{\mathbf{F}}^{-1} \right] : \overline{\mathbf{F}}^{-1} + \overline{\mathbf{F}} \cdot \left[\overline{\text{GRAD}}(\overline{\mathbf{F}}^{-1}) : \overline{\mathbf{F}}^{-T} \right] \right\|. \quad (7.119)$$

In order to further simplify Eq. (7.119), identity

$$\overline{\text{GRAD}}(\overline{\mathbf{F}}^{-1} \cdot \overline{\mathbf{F}}) = \overline{\text{GRAD}}(\overline{\mathbf{I}}) \quad (7.120)$$

holds in general. It bears emphasis that

$$\overline{\text{GRAD}}(\overline{\mathbf{I}}) \neq \mathbf{0} \quad (7.121)$$

Equation (7.120) allows the expression of term $\overline{\text{GRAD}}(\overline{\mathbf{F}}^{-1})$ as

$$\overline{\text{GRAD}}(\overline{\mathbf{F}}^{-1}) : \overline{\mathbf{i}} = \overline{\text{GRAD}}(\overline{\mathbf{I}}) : \overline{\mathbf{F}}^{-1} - \overline{\mathbf{F}}^{-1} \cdot \overline{\text{GRAD}}(\overline{\mathbf{F}}) : \overline{\mathbf{F}}^{-1}, \quad (7.122)$$

where

$$[\mathbf{A} \cdot \mathbf{B}]_{iml} = [\mathbf{A}]_{ijl} [\mathbf{B}]_{jm}. \quad (7.123)$$

A detailed derivation is given in Appendix D.3. Furthermore, due to the symmetry properties of $\overline{\text{GRAD}}(\overline{\mathbf{F}}^{-1})$ it holds that

$$\left[\overline{\text{GRAD}}(\overline{\mathbf{F}}^{-1}) : \overline{\mathbf{i}} \right] : \overline{\mathbf{F}}^{-T} = \overline{\text{GRAD}}(\overline{\mathbf{F}}^{-1}) : \overline{\mathbf{F}}^{-T}, \quad (7.124)$$

cf. Appendix D.4. By inserting relations (7.122) and (7.124), Eq. (7.119) transforms to

$$h = \frac{1}{2} \left\| \left[\overline{\text{GRAD}}(\overline{\mathbf{F}}) \cdot \overline{\mathbf{F}}^{-1} \right] : \overline{\mathbf{F}}^{-1} + \overline{\mathbf{F}} \cdot \left[\left(\overline{\text{GRAD}}(\overline{\mathbf{I}}) \cdot \overline{\mathbf{F}}^{-1} - \overline{\mathbf{F}}^{-1} \cdot \overline{\text{GRAD}}(\overline{\mathbf{F}}) \cdot \overline{\mathbf{F}}^{-1} \right) : \overline{\mathbf{F}}^{-T} \right] \right\|. \quad (7.125)$$

It now becomes apparent that

$$h = h(\overline{\mathbf{F}}, \overline{\text{GRAD}}(\overline{\mathbf{F}}), \overline{\text{GRAD}}(\overline{\mathbf{I}})) \quad \text{with} \quad \overline{\text{GRAD}}(\overline{\mathbf{I}}) = \text{const.} \quad (7.126)$$

As a consequence, h indeed depends on $\overline{\mathbf{F}}$ and $\overline{\text{GRAD}}(\overline{\mathbf{F}})$. Essentially, Eq. (D.17) can be interpreted as a push forward of H .

The next step is to show that mean curvature (D.17) is a covariant function. To be more precise it has to be shown that

$$h(\overline{\mathbf{F}}, \overline{\text{GRAD}}(\overline{\mathbf{F}}), \overline{\text{GRAD}}(\overline{\mathbf{I}})) = h(\overline{\mathbf{C}}, \overline{\mathbf{F}}^{-1} \cdot \overline{\text{GRAD}}(\overline{\mathbf{F}}), \overline{\text{GRAD}}(\overline{\mathbf{F}})^T \cdot \overline{\text{GRAD}}(\overline{\mathbf{F}}), \dots). \quad (7.127)$$

For that purpose mean curvature h is re-written as

$$h = \frac{1}{2} \|\mathbf{a} + \mathbf{b} - \mathbf{c}\| = \frac{1}{2} \sqrt{(\mathbf{a} + \mathbf{b} - \mathbf{c}) \cdot (\mathbf{a} + \mathbf{b} - \mathbf{c})} \quad (7.128)$$

with

$$\mathbf{a} = \left[\overline{\text{GRAD}}(\overline{\mathbf{F}}) \cdot \overline{\mathbf{F}}^{-1} \right] : \overline{\mathbf{F}}^{-1}, \quad (7.129)$$

$$\mathbf{b} = \overline{\mathbf{F}} \cdot \left[\left(\overline{\text{GRAD}}(\overline{\mathbf{I}}) \cdot \overline{\mathbf{F}}^{-1} \right) : \overline{\mathbf{F}}^{-T} \right] \quad \text{and} \quad (7.130)$$

$$\mathbf{c} = \overline{\mathbf{F}} \cdot \left[\left(-\overline{\mathbf{F}}^{-1} \cdot \overline{\text{GRAD}}(\overline{\mathbf{F}}) \cdot \overline{\mathbf{F}}^{-1} \right) : \overline{\mathbf{F}}^{-T} \right]. \quad (7.131)$$

Now it is investigated if the coefficients arising from (7.128) are covariant. For that purpose one has to show that

$$\mathbf{a} \cdot \mathbf{a} = \mathbf{a} \cdot \mathbf{a}(\overline{\mathbf{C}}, \overline{\mathbf{F}}^{-1} \cdot \overline{\text{GRAD}}(\overline{\mathbf{F}}), \overline{\text{GRAD}}(\overline{\mathbf{F}})^T \cdot \overline{\text{GRAD}}(\overline{\mathbf{F}}), \overline{\text{GRAD}}(\overline{\mathbf{I}})), \quad (7.132)$$

$$\mathbf{a} \cdot \mathbf{b} = \mathbf{a} \cdot \mathbf{b}(\overline{\mathbf{C}}, \overline{\mathbf{F}}^{-1} \cdot \overline{\text{GRAD}}(\overline{\mathbf{F}}), \overline{\text{GRAD}}(\overline{\mathbf{F}})^T \cdot \overline{\text{GRAD}}(\overline{\mathbf{F}}), \overline{\text{GRAD}}(\overline{\mathbf{I}})), \quad (7.133)$$

$$\mathbf{a} \cdot \mathbf{c} = \mathbf{a} \cdot \mathbf{c}(\overline{\mathbf{C}}, \overline{\mathbf{F}}^{-1} \cdot \overline{\text{GRAD}}(\overline{\mathbf{F}}), \overline{\text{GRAD}}(\overline{\mathbf{F}})^T \cdot \overline{\text{GRAD}}(\overline{\mathbf{F}}), \overline{\text{GRAD}}(\overline{\mathbf{I}})), \quad (7.134)$$

$$\mathbf{b} \cdot \mathbf{b} = \mathbf{b} \cdot \mathbf{b}(\overline{\mathbf{C}}, \overline{\mathbf{F}}^{-1} \cdot \overline{\text{GRAD}}(\overline{\mathbf{F}}), \overline{\text{GRAD}}(\overline{\mathbf{F}})^T \cdot \overline{\text{GRAD}}(\overline{\mathbf{F}}), \overline{\text{GRAD}}(\overline{\mathbf{I}})), \quad (7.135)$$

$$\mathbf{b} \cdot \mathbf{c} = \mathbf{b} \cdot \mathbf{c}(\overline{\mathbf{C}}, \overline{\mathbf{F}}^{-1} \cdot \overline{\text{GRAD}}(\overline{\mathbf{F}}), \overline{\text{GRAD}}(\overline{\mathbf{F}})^T \cdot \overline{\text{GRAD}}(\overline{\mathbf{F}}), \overline{\text{GRAD}}(\overline{\mathbf{I}})) \quad (7.136)$$

and

$$\mathbf{c} \cdot \mathbf{c} = \mathbf{c} \cdot \mathbf{c}(\overline{\mathbf{C}}, \overline{\mathbf{F}}^{-1} \cdot \overline{\text{GRAD}}(\overline{\mathbf{F}}), \overline{\text{GRAD}}(\overline{\mathbf{F}})^T \cdot \overline{\text{GRAD}}(\overline{\mathbf{F}}), \overline{\text{GRAD}}(\overline{\mathbf{I}})) \quad (7.137)$$

with $\overline{\text{GRAD}}(\bar{\mathbf{I}}) = \text{const.}$ It is shown in detail in Appendix D.5, that all coefficients (7.132) - (7.137) fulfill the requirement for material covariance and thereby, the mean curvature h is indeed a covariant function. This is exemplarily demonstrated here for the first coefficient $\mathbf{a} \cdot \mathbf{a}$:

$$\begin{aligned} \mathbf{a} \cdot \mathbf{a} &= \left[\left[\overline{\text{GRAD}}(\bar{\mathbf{F}}) \cdot \bar{\mathbf{F}}^{-1} \right] : \bar{\mathbf{F}}^{-1} \right] \cdot \left[\left[\overline{\text{GRAD}}(\bar{\mathbf{F}}) \cdot \bar{\mathbf{F}}^{-1} \right] : \bar{\mathbf{F}}^{-1} \right] \\ &= \bar{\mathbf{C}}^{-1} : \left(\overline{\text{GRAD}}^T(\bar{\mathbf{F}}) \cdot \overline{\text{GRAD}}(\bar{\mathbf{F}}) \right) : \bar{\mathbf{C}}^{-1}. \end{aligned} \quad (7.138)$$

Hence, it follows that it is possible to define a Helmholtz energy depending on the current curvature that fulfills the requirements of the material covariance principle. Accordingly, such a model automatically fulfills balance of angular momentum. Motivated by the incorporation of curvature effects leading to additional size effects it seems to be very promising to further investigate the proposed framework and for instance to define a particular energy combining $[[\mathbf{u}]]$, $\bar{\mathbf{F}}$ and $\overline{\text{GRAD}}(\bar{\mathbf{F}})$.

8 Conclusion and Outlook

8.1 Concluding remarks

8.1.1 Inconsistencies in classic cohesive zone models

The main focus of this thesis is the elaboration of a consistent interface framework that fulfills all fundamental physical requirements. In order to reveal the necessity for the extension of classic cohesive zone models, their possibilities and restrictions were reviewed in Chapter 3. As highlighted, only a few cohesive zone models are derived in a thermodynamically consistent way. Especially classic anisotropic cohesive models exhibit thermodynamical inconsistencies due to non-vanishing dissipation in the case of elasticity. Here, the term classic cohesive zone indicates that the stress power only considers a contribution related to the change of the displacement jump and not to the change of structural tensors such as the normal vector. Furthermore, it has been underlined that the traction vector has to point in the same direction as the displacement jump in order to fulfill balance of angular momentum. This is equivalent to isotropy which means that classic cohesive zone models can be interpreted as fiber models. To be more precise, a fiber between two fixed points (the same point in material coordinates) connects the upper and lower surface of the interface. The direction of the fiber is prescribed by the displacement jump and the traction has to point into this direction. It has also been shown that an extension of cohesive models to isotropic damage is straightforward while the incorporation of plasticity leads to further problems due to the principle of material frame indifference. In summary, Chapter 3 provides sufficient arguments for the derivation of a novel interface framework.

8.1.2 Generalised interface framework

Two different novel frameworks for non-coherent interfaces have been presented in Chapter 4 and 5.

Chapter 4 has provided a cohesive framework that abandons the classic fiber concept. To be more precise, the fiber connecting the upper and lower surface of the interface is

no longer defined by two points having the same material coordinates, but the fiber's corner points are allowed to slide along the surface when plasticity evolves. The direction of the fiber is thereby redefined. It has been shown that this redefinition is only active in the case of plasticity, and that for elastic interface opening the classic framework is unaffected. From a physical point of view the interface may be seen as a web of interconnecting fibers. When the interface opens inelastically some of the initial fibers break. This can be interpreted as a reorientation of an effective fiber.

Furthermore, the unloading behaviour of the fiber has been of special interest in Chapter 4. In the case of bulk elastoplasticity further unloading from the stress free configuration would classically lead to negative strains. In the case of interfaces this would lead to unphysical self penetration for which a novel unloading behaviour has been proposed. The key idea is to assign a vanishing bending stiffness to the fibers which buckle when compressive stresses arise. It has been pointed out that this unloading behaviour shows similarities to the wrinkling of membranes. Furthermore, the variational structure of the novel interface framework has been shown, i.e., the yield function and the wrinkling condition (the interface cannot capture compressive stresses) can be derived by minimising a potential. The global unloading behaviour presented within the numerical examples in Chapter 4 shows that a superposition of local wrinkling unloading and elastic unloading leads to a damage-like behaviour.

A different approach for an extended interface model was discussed in Chapter 5. In the literature this framework is denoted as general imperfect interface. It combines the theory of classic cohesive zones where the displacement shows a jump across the interface with surface elasticity theory where a traction jump across the interface is allowed. Both the cohesive zone model as well as the surface elasticity model can be understood as two limits of the novel interface framework. The Helmholtz free energy density of such general interface models contains the displacement jump and the surface deformation gradient or respectively structural tensors. In order to guarantee thermodynamical consistency of the model, a stress contribution has been introduced that is energetically conjugated to the change of the structural tensors – in contrast to classic cohesive zone models where only the traction vector is considered. Thereby, the novel framework contains membrane-like forces and out-of-plane shear forces acting within the interface, and the traction continuity across the interface is not required in order to fulfill balance of linear momentum. Only a few recent models actually consider these additional stresses, cf. [41, 50, 68, 77]. It has been highlighted that the presented framework indeed fulfills balance of angular momentum for an anisotropic interface.

8.1.3 Size effect due to material interfaces

In order to analyse the interface's influence on the macroscopic stress response of a body, an extended homogenisation scheme has been summarised in Chapter 6. It has been highlighted that the classic volume average theorems known from bulk continuum mechanics have to be extended in order to account for interface contributions due to

$[[\mathbf{u}]]$ and the interface stress tensor $\overline{\mathbf{P}}$. The associated numerical implementation was provided and the novel interface framework was incorporated into numerical simulations with a representative volume element. Based on this numerical framework a cubic RVE with a spherical inclusion was investigated. The presented homogenisation scheme allows the analysis of the influence of the novel interface model on the resulting macroscopic (effective) material response.

First, the possibility of accounting for material anisotropies was underlined. The novel framework can capture different fracture properties for normal and tangential, respectively mode I- and mode II/III-separation. This is an interesting feature of the model, since experiments indeed show that many materials provide different fracture energies in normal and tangential direction.

Furthermore, it has been shown in Chapter 6 that the interaction of bulk energies and interface energies leads, in a very natural manner, to a size effect due to the area-to-volume ratio. The size effect becomes more pronounced for smaller length scales. The influence of the area increases with decreasing volume of the RVE. It has been shown that for classic cohesive zones the resistance of the interface opening within a small RVE is much lower than for large RVEs. While on small scales the RVE acts as though it has a pore, the large scale simulations approach the behaviour of a homogeneous cube without interface. This corresponds to the observed „the smaller the softer“ effect in classic cohesive zones.

In contrast thereto, the surface elasticity theory exhibits a „the smaller the stiffer“ relation. While for large RVE dimensions the response once more approaches one of a homogeneous cube without interfaces, for small scales the cube deforms as though it has a rigid inclusion.

However, since the overall response is usually a superposition of both relations, the effective properties cannot generally be characterised by one of the aforementioned limiting relations. The novel interface framework can model a more complex non-monotonic size effect. Thereby, numerical simulations can be used in order design new materials with new properties.

8.1.4 Higher-order interfaces

In order to investigate the incorporation of higher gradients into the interface theory, two different approaches were presented in Chapter 7. On the one hand the gradient of the displacement jump $[[\mathbf{u}]]$ was considered. This consideration was motivated by means of homogenisation approaches. It was shown that, for a quadratic energy potential, the resulting novel model is equivalent to a classic cohesive zone model only depending on the length of the displacement jump, if this model is integrated over a finite spatial domain. Furthermore, it was shown that this equivalence no longer holds true if higher order terms of $[[\mathbf{u}]]$ are considered in the interface energy. Hence, the enhancement with the gradient of $[[\mathbf{u}]]$ enables the description of further physical modes.

The second part of Chapter 7 dealt with the incorporation of bending and curvature effects that influence the material behaviour especially at small length scales. It was shown that the mean curvature can be represented as a covariant function of $\overline{\mathbf{F}}$ and $\overline{\text{GRAD}}(\overline{\mathbf{F}})$. The incorporation of the mean curvature into the Helmholtz energy of the interface thereby automatically fulfills the principle of material frame indifference and thereby also fulfills balance of angular momentum.

8.2 Outlook

This thesis dealt with the elaboration and the investigation of novel material models describing non-coherent interfaces. As pointed out, the material models presented in Chapter 4 and 5 eliminate the most serious inconsistencies known from the classic cohesive zone theory. Nevertheless, they still leave space for further improvements. Some of which are discussed below.

The generalised interface framework presented in Chapter 5 does not yet contain plasticity. However, especially elastoplastic in-plane deformations or stretches within the interface seem to be physically relevant in many materials. This could be interesting for instance for the debonding process of fiber reinforced composites. Furthermore, only scalar-valued damage has until now been included in the anisotropic interface. One possible next step could be the inclusion of a damage tensor instead of scalars.

The higher order models presented in Chapter 7 have so far been restricted to hyperelasticity. Since interfaces should capture inelastic material behaviour like cracking as well, the framework has yet to be extended to dissipative material behaviour.

A Differential geometry for fiber sliding

A.1 Derivation of quantity j according to the relation between the upper and lower tractions (Eq. (4.13))

In this part of the appendix an explicit expression for quantity j in Eq. (4.13) is given. The derivation is taken from [75]. Starting from Nanson's formula it follows that

$$\mathbf{n}_+ ds_+ = J_+ \mathbf{F}_+^{-T} \cdot \mathbf{N}_+ dS_+, \quad (\text{A.1})$$

where \mathbf{n}_+ and \mathbf{N}_+ are the unit normal vectors in the current respectively in the reference configuration, $J_+ = \det \mathbf{F}_+$ and dS_+ is the infinitesimal area element in the reference configuration. Denoting the cofactor of \mathbf{F}_+ as $\text{cof} \mathbf{F}_+$, Eq. (A.1) can be rewritten as $\mathbf{n}_+ ds_+ = \text{cof} \mathbf{F}_+ \cdot \mathbf{N}_+ dS_+$ which leads to

$$ds_+ = \|\text{cof} \mathbf{F}_+ \cdot \mathbf{N}_+\| dS_+ \quad \text{and} \quad ds_- = \|\text{cof} \mathbf{F}_- \cdot \mathbf{N}_-\| dS_-. \quad (\text{A.2})$$

With \mathbf{E}_i being the fixed Cartesian base vectors it follows that $d\mathbf{X} = dX^i \mathbf{E}_i$. By combining this with its curvilinear counterpart, decomposition $dX_+^i = \partial h^i / \partial \theta_+^\alpha d\theta_+^\alpha$, i.e.,

$$d\mathbf{X}_+ = d\mathbf{X}_+^1 + d\mathbf{X}_+^2, \quad (\text{A.3})$$

results in

$$d\mathbf{X}_+^1 = \frac{\partial h^i}{\partial \theta_+^1} d\theta_+^1 \mathbf{E}_i \quad \text{and} \quad d\mathbf{X}_+^2 = \frac{\partial h^j}{\partial \theta_+^2} d\theta_+^2 \mathbf{E}_j. \quad (\text{A.4})$$

As a consequence, it follows that

$$dS_+ = \|d\mathbf{X}_+^1 \times d\mathbf{X}_+^2\| = a_+ d\theta_+^1 d\theta_+^2 \quad \text{with} \quad a_+ = \left\| \frac{\partial h^i}{\partial \theta_+^1} \frac{\partial h^j}{\partial \theta_+^2} \mathbf{E}_i \times \mathbf{E}_j \right\| \quad (\text{A.5})$$

and likewise

$$dS_- = \|d\mathbf{X}_-^1 \times d\mathbf{X}_-^2\| = a_- d\theta_-^1 d\theta_-^2 \quad \text{with} \quad a_- = \left\| \frac{\partial h^i}{\partial \theta_-^1} \frac{\partial h^j}{\partial \theta_-^2} \mathbf{E}_i \times \mathbf{E}_j \right\|. \quad (\text{A.6})$$

If positions θ_+^α and θ_-^α are known, a_+ and a_- are known.

Only coordinate θ_+^1 changes along the tangential vector $d\mathbf{X}_+^1$. According to [75], this yields

$$d\theta_+^1 = \frac{\left(1 + \frac{\partial c^1}{\partial \theta^1}\right) \left(1 + \frac{\partial c^2}{\partial \theta^2}\right) - \frac{\partial c^1}{\partial \theta^2} \frac{\partial c^2}{\partial \theta^1}}{1 + \frac{\partial c^2}{\partial \theta^2}} d\theta^1 \quad (\text{A.7})$$

and likewise

$$d\theta_+^2 = \frac{\left(1 + \frac{\partial c^1}{\partial \theta^1}\right) \left(1 + \frac{\partial c^2}{\partial \theta^2}\right) - \frac{\partial c^1}{\partial \theta^2} \frac{\partial c^2}{\partial \theta^1}}{1 + \frac{\partial c^1}{\partial \theta^1}} d\theta^2. \quad (\text{A.8})$$

Combination of Eq. (A.7) and Eq. (A.8) results in

$$d\theta_+^1 d\theta_+^2 = \frac{\left[\left(1 + \frac{\partial c^1}{\partial \theta^1}\right) \left(1 + \frac{\partial c^2}{\partial \theta^2}\right) - \frac{\partial c^1}{\partial \theta^2} \frac{\partial c^2}{\partial \theta^1}\right]^2}{\left(1 + \frac{\partial c^1}{\partial \theta^1}\right) \left(1 + \frac{\partial c^2}{\partial \theta^2}\right)} \quad (\text{A.9})$$

and analogously it follows that

$$d\theta_-^1 d\theta_-^2 = \frac{\left[\left(1 - \frac{\partial c^1}{\partial \theta^1}\right) \left(1 - \frac{\partial c^2}{\partial \theta^2}\right) - \frac{\partial c^1}{\partial \theta^2} \frac{\partial c^2}{\partial \theta^1}\right]^2}{\left(1 - \frac{\partial c^1}{\partial \theta^1}\right) \left(1 - \frac{\partial c^2}{\partial \theta^2}\right)}. \quad (\text{A.10})$$

Finally, applying all the derived relations leads to the quantity j as

$$j = \frac{\|\text{cof}\mathbf{F}_+ \cdot \mathbf{N}_+\| a_+ \left[\left(1 + \frac{\partial c^1}{\partial \theta^1}\right) \left(1 + \frac{\partial c^2}{\partial \theta^2}\right) - \frac{\partial c^1}{\partial \theta^2} \frac{\partial c^2}{\partial \theta^1}\right]^2 \left(1 - \frac{\partial c^1}{\partial \theta^1}\right) \left(1 - \frac{\partial c^2}{\partial \theta^2}\right)}{\|\text{cof}\mathbf{F}_- \cdot \mathbf{N}_-\| a_- \left[\left(1 - \frac{\partial c^1}{\partial \theta^1}\right) \left(1 - \frac{\partial c^2}{\partial \theta^2}\right) - \frac{\partial c^1}{\partial \theta^2} \frac{\partial c^2}{\partial \theta^1}\right]^2 \left(1 + \frac{\partial c^1}{\partial \theta^1}\right) \left(1 + \frac{\partial c^2}{\partial \theta^2}\right)}. \quad (\text{A.11})$$

B Implementation of generalised interfaces

B.1 Vector of internal forces and stiffness matrix of the prototype model according to Table 5.1

In this appendix, all derivatives necessary for the implementation of general interface models are presented. For instance, the derivatives of the prototype model summarised in Tab. 5.1 which is based on Helmholtz energy

$$\Psi = (1 - d_n^{(n)})(1 - d_n^{(t)}) \Psi_n^0(\llbracket \mathbf{u} \rrbracket, \mathbf{g}_\alpha) + (1 - d_t^{(n)})(1 - d_t^{(t)}) \Psi_t^0(\llbracket \mathbf{u} \rrbracket, \mathbf{g}_\alpha) \quad (\text{B.1})$$

read

$$\begin{aligned} \frac{\partial \Psi}{\partial \llbracket \mathbf{u} \rrbracket} &= (1 - d_n^{(n)})(1 - d_n^{(t)}) \frac{\partial \Psi_n^0}{\partial \llbracket \mathbf{u} \rrbracket} + (1 - d_t^{(n)})(1 - d_t^{(t)}) \frac{\partial \Psi_t^0}{\partial \llbracket \mathbf{u} \rrbracket}, \\ \frac{\partial \Psi}{\partial \mathbf{g}_\alpha} &= (1 - d_n^{(n)})(1 - d_n^{(t)}) \frac{\partial \Psi_n^0}{\partial \mathbf{g}_\alpha} + (1 - d_t^{(n)})(1 - d_t^{(t)}) \frac{\partial \Psi_t^0}{\partial \mathbf{g}_\alpha}. \end{aligned} \quad (\text{B.2})$$

In order to compute Eqs. (B.2), the involved partial derivatives are required. However, the most general case will be considered in this appendix. Accordingly, the Helmholtz energy may depend on the following invariants:

$$I_1 = \llbracket \mathbf{u} \rrbracket \cdot \llbracket \mathbf{u} \rrbracket, \quad I_2 = \llbracket \mathbf{u} \rrbracket \cdot (\mathbf{g}_1 \otimes \mathbf{g}^1) \cdot \llbracket \mathbf{u} \rrbracket, \quad I_3 = \llbracket \mathbf{u} \rrbracket \cdot (\mathbf{g}_2 \otimes \mathbf{g}^2) \cdot \llbracket \mathbf{u} \rrbracket \quad (\text{B.3})$$

and

$$\overline{\mathbf{C}} = \overline{\mathbf{F}}^T \cdot \overline{\mathbf{F}} = (\mathbf{g}_\alpha \cdot \mathbf{g}_\beta) \mathbf{G}^\alpha \otimes \mathbf{G}^\beta. \quad (\text{B.4})$$

B Implementation of generalised interfaces

Following Ottosen et al. [77], the partial derivatives of the co- and the contravariant base vectors can be written as

$$\frac{\partial \mathbf{g}_\alpha}{\partial \mathbf{g}_\beta} = \delta_\beta^\alpha \mathbf{I} \quad \text{and} \quad \frac{\partial \mathbf{g}^\alpha}{\partial \mathbf{g}_\beta} = -\mathbf{g}^\beta \otimes \mathbf{g}^\alpha + g^{\alpha\beta} \mathbf{g}^3 \otimes \mathbf{g}^3. \quad (\text{B.5})$$

Alternatively, by linearising the well known relation $\mathbf{g}^\beta = \overline{\mathbf{F}}^{-T} \cdot \mathbf{G}^\beta$, together with with

$$\frac{\partial \overline{\mathbf{F}}_{ij}^{-1}}{\partial \overline{\mathbf{F}}_{kl}} = -\overline{\mathbf{F}}_{ik}^{-1} \overline{\mathbf{F}}_{jl}^{-T} + \overline{\mathbf{F}}_{im}^{-1} \overline{\mathbf{F}}_{ml}^{-T} g_{3j} g_{3k}, \quad (\text{B.6})$$

(see Javili et al. [50]), one obtains

$$d\mathbf{g}_\alpha = \mathbf{G}^\alpha \cdot \frac{\partial \overline{\mathbf{F}}^{-1}}{\partial \overline{\mathbf{F}}} : (d\mathbf{g}_\beta \otimes \mathbf{G}^\beta). \quad (\text{B.7})$$

A straightforward computation shows that this is equivalent to Eq. (B.5).

Considering the most general Helmholtz energy $\Psi = \Psi(I_1, I_2, I_3, \overline{\mathbf{C}}, \boldsymbol{\alpha})$, partial derivatives $\partial_{[\mathbf{u}]}\Psi$ and $\partial_{\mathbf{g}_\alpha}\Psi$ can be expanded as

$$\begin{aligned} \frac{\partial \Psi}{\partial [\mathbf{u}]} &= \sum_{i=1}^3 \frac{\partial \Psi}{\partial I_i} \frac{\partial I_i}{\partial [\mathbf{u}]}, \\ \frac{\partial \Psi}{\partial \mathbf{g}_\alpha} &= \sum_{i=1}^3 \frac{\partial \Psi}{\partial I_i} \frac{\partial I_i}{\partial \mathbf{g}_\alpha} + \frac{\partial \Psi}{\partial \overline{\mathbf{C}}} : \frac{\partial \overline{\mathbf{C}}}{\partial \mathbf{g}_\alpha}. \end{aligned} \quad (\text{B.8})$$

The non-trivial (non-vanishing) derivatives involved in Eqs. (B.8), in turn, result with Eqs. (B.3) and (B.4) in

$$\begin{aligned} \frac{\partial I_1}{\partial [\mathbf{u}]} &= 2[\mathbf{u}], \\ \frac{\partial I_2}{\partial [\mathbf{u}]} &= ([\mathbf{u}] \cdot \mathbf{g}^1) \mathbf{g}_1 + ([\mathbf{u}] \cdot \mathbf{g}_1) \mathbf{g}^1, \\ \frac{\partial I_2}{\partial \mathbf{g}_1} &= ([\mathbf{u}] \cdot \mathbf{g}^1) [\mathbf{u}] + ([\mathbf{u}] \cdot \mathbf{g}_1) [-([\mathbf{u}] \cdot \mathbf{g}^1) \mathbf{g}^1 + g^{11} ([\mathbf{u}] \cdot \mathbf{g}^3) \mathbf{g}^3], \\ \frac{\partial I_2}{\partial \mathbf{g}_2} &= ([\mathbf{u}] \cdot \mathbf{g}_1) [-([\mathbf{u}] \cdot \mathbf{g}^2) \mathbf{g}^1 + g^{12} ([\mathbf{u}] \cdot \mathbf{g}^3) \mathbf{g}^3], \\ \frac{\partial I_3}{\partial [\mathbf{u}]} &= ([\mathbf{u}] \cdot \mathbf{g}^2) \mathbf{g}_2 + ([\mathbf{u}] \cdot \mathbf{g}_2) \mathbf{g}^2, \\ \frac{\partial I_3}{\partial \mathbf{g}_1} &= ([\mathbf{u}] \cdot \mathbf{g}_2) [-([\mathbf{u}] \cdot \mathbf{g}^1) \mathbf{g}^2 + g^{21} ([\mathbf{u}] \cdot \mathbf{g}^3) \mathbf{g}^3], \end{aligned}$$

B.1 Vector of internal forces and stiffness matrix of the prototype model according to Table 5.1

$$\begin{aligned}
\frac{\partial I_3}{\partial \mathbf{g}_2} &= ([\mathbf{u}] \cdot \mathbf{g}^2) [\mathbf{u}] + ([\mathbf{u}] \cdot \mathbf{g}_2) [- ([\mathbf{u}] \cdot \mathbf{g}^2) \mathbf{g}^2 + g^{22} ([\mathbf{u}] \cdot \mathbf{g}^3) \mathbf{g}^3], \\
\frac{\partial \overline{\mathcal{C}}}{\partial \mathbf{g}_1} &= [\mathbf{G}^1 \otimes \mathbf{G}^\alpha \otimes \mathbf{g}_\alpha] + [\mathbf{G}^\beta \otimes \mathbf{G}^1 \otimes \mathbf{g}_\beta], \\
\frac{\partial \overline{\mathcal{C}}}{\partial \mathbf{g}_2} &= [\mathbf{G}^\alpha \otimes \mathbf{G}^2 \otimes \mathbf{g}_\alpha] + [\mathbf{G}^2 \otimes \mathbf{G}^\beta \otimes \mathbf{g}_\beta],
\end{aligned} \tag{B.9}$$

where $g_{\alpha\beta} = \mathbf{g}_\alpha \cdot \mathbf{g}_\beta$ and $g^{\alpha\beta} = \mathbf{g}^\alpha \cdot \mathbf{g}^\beta$ are the components of the co- and contravariant metric tensor. Clearly, the derivatives of the Helmholtz energy with respect to the invariants depend on the choice of Ψ . For instance, in the case of the prototype model, the derivatives of Ψ_n^0 and Ψ_t^0 with respect to invariants I_1 , I_2 and I_3 take the format (for quadratic Helmholtz energies Ψ_n^0 and Ψ_t^0 according to Tab. 5.1)

$$\begin{aligned}
\frac{\partial \Psi_n^0}{\partial I_1} &= \frac{1}{2} c_n, \quad \frac{\partial \Psi_n^0}{\partial I_2} = -\frac{1}{2} c_n, \quad \frac{\partial \Psi_n^0}{\partial I_3} = -\frac{1}{2} c_n, \\
\frac{\partial \Psi_t^0}{\partial I_1} &= 0, \quad \frac{\partial \Psi_t^0}{\partial I_2} = \frac{1}{2} c_t, \quad \frac{\partial \Psi_t^0}{\partial I_3} = \frac{1}{2} c_t.
\end{aligned} \tag{B.10}$$

By inserting derivatives (B.9) and (B.10) into Eq. (B.8) and the resulting equation into Eq. (B.2), the vector of internal forces

$$\mathbf{R}_\pm^{(i)} = \int_{\mathcal{I}_0} \left[\pm N^{(i)} \frac{\partial \Psi}{\partial [\mathbf{u}]} + \underbrace{\frac{1}{2} \frac{\partial N^{(i)}}{\partial \xi^\beta} \frac{\partial \Psi}{\partial \mathbf{g}_\alpha}}_{\text{Summation over } \alpha} \right] dA \tag{B.11}$$

can be computed.

Next, the derivatives necessary for computing the stiffness matrix are derived. The general structure of the respective linearisation is given by

$$\Delta \mathbf{R}_\pm^{(i)} = \int_{\mathcal{I}_0} \left[\pm N^{(i)}(\boldsymbol{\xi}) \Delta \left(\frac{\partial \Psi}{\partial [\mathbf{u}]} \right) + \frac{1}{2} \frac{\partial N^{(i)}(\boldsymbol{\xi})}{\partial \xi^\beta} \Delta \left(\frac{\partial \Psi}{\partial \mathbf{g}_\beta} \right) \right] dA. \tag{B.12}$$

For the prototype model summarised in Tab. 5.1, this linearisation takes the format

$$\begin{aligned}
\Delta \mathbf{R}_\pm^{(i)} &= \int_{\mathcal{I}_0} (1 - d_n^{(n)})(1 - d_n^{(t)}) \left[\pm N^{(i)}(\boldsymbol{\xi}) \Delta \left(\frac{\partial \Psi_n^0}{\partial [\mathbf{u}]} \right) + \frac{1}{2} \frac{\partial N^{(i)}(\boldsymbol{\xi})}{\partial \xi^\beta} \Delta \left(\frac{\partial \Psi_n^0}{\partial \mathbf{g}_\beta} \right) \right] + \\
&\quad - \Delta d_n^{(n)}(1 - d_n^{(t)}) \left[\pm N^{(i)}(\boldsymbol{\xi}) \left(\frac{\partial \Psi_n^0}{\partial [\mathbf{u}]} \right) + \frac{1}{2} \frac{\partial N^{(i)}(\boldsymbol{\xi})}{\partial \xi^\beta} \left(\frac{\partial \Psi_n^0}{\partial \mathbf{g}_\beta} \right) \right] + \\
&\quad - \Delta d_n^{(t)}(1 - d_n^{(n)}) \left[\pm N^{(i)}(\boldsymbol{\xi}) \left(\frac{\partial \Psi_n^0}{\partial [\mathbf{u}]} \right) + \frac{1}{2} \frac{\partial N^{(i)}(\boldsymbol{\xi})}{\partial \xi^\beta} \left(\frac{\partial \Psi_n^0}{\partial \mathbf{g}_\beta} \right) \right] +
\end{aligned}$$

$$\begin{aligned}
 & (1 - d_t^{(n)})(1 - d_t^{(t)}) \left[\pm N^{(i)}(\boldsymbol{\xi}) \Delta \left(\frac{\partial \Psi_t^0}{\partial [\mathbf{u}]} \right) + \frac{1}{2} \frac{\partial N^{(i)}(\boldsymbol{\xi})}{\partial \xi^\beta} \Delta \left(\frac{\partial \Psi_t^0}{\partial \mathbf{g}_\beta} \right) \right] + \\
 & - \Delta d_t^{(n)}(1 - d_t^{(t)}) \left[\pm N^{(i)}(\boldsymbol{\xi}) \left(\frac{\partial \Psi_t^0}{\partial [\mathbf{u}]} \right) + \frac{1}{2} \frac{\partial N^{(i)}(\boldsymbol{\xi})}{\partial \xi^\beta} \left(\frac{\partial \Psi_t^0}{\partial \mathbf{g}_\beta} \right) \right] + \\
 & - \Delta d_t^{(t)}(1 - d_t^{(n)}) \left[\pm N^{(i)}(\boldsymbol{\xi}) \left(\frac{\partial \Psi_t^0}{\partial [\mathbf{u}]} \right) + \frac{1}{2} \frac{\partial N^{(i)}(\boldsymbol{\xi})}{\partial \xi^\beta} \left(\frac{\partial \Psi_t^0}{\partial \mathbf{g}_\beta} \right) \right] dA.
 \end{aligned} \tag{B.13}$$

Again, considering the most general case $\Psi = \Psi(I_1, I_2, I_3, \overline{\mathbf{C}}, \boldsymbol{\alpha})$, linearisations

$$\begin{aligned}
 \Delta \left(\frac{\partial \Psi}{\partial [\mathbf{u}]} \right) &= \frac{\partial^2 \Psi}{\partial [\mathbf{u}] \otimes \partial [\mathbf{u}]} \cdot \Delta [\mathbf{u}] + \frac{\partial^2 \Psi}{\partial [\mathbf{u}] \otimes \partial \mathbf{g}_\beta} \cdot \Delta \mathbf{g}_\beta + \frac{\partial^2 \Psi}{\partial [\mathbf{u}] \otimes \partial \boldsymbol{\alpha}} \cdot \Delta \boldsymbol{\alpha}, \\
 \Delta \left(\frac{\partial \Psi}{\partial \mathbf{g}_\beta} \right) &= \frac{\partial^2 \Psi}{\partial \mathbf{g}_\beta \otimes \partial \mathbf{g}_\alpha} \cdot \Delta \mathbf{g}_\alpha + \frac{\partial^2 \Psi}{\partial \mathbf{g}_\beta \otimes \partial [\mathbf{u}]} \cdot \Delta [\mathbf{u}] + \frac{\partial^2 \Psi}{\partial \mathbf{g}_\beta \otimes \partial \boldsymbol{\alpha}} \cdot \Delta \boldsymbol{\alpha}
 \end{aligned} \tag{B.14}$$

entering linearisation (B.12) can be computed. To be more explicit and by using the chain rule, the derivatives involved in Eqs. (B.14) are given by

$$\begin{aligned}
 \frac{\partial^2 \Psi}{\partial [\mathbf{u}] \otimes \partial [\mathbf{u}]} &= \sum_i^3 \left[\frac{\partial \Psi}{\partial I_i} \frac{\partial^2 I_i}{\partial [\mathbf{u}] \otimes \partial [\mathbf{u}]} + \sum_j^3 \frac{\partial^2 \Psi}{\partial I_i \partial I_j} \left(\frac{\partial I_i}{\partial [\mathbf{u}]} \otimes \frac{\partial I_j}{\partial [\mathbf{u}]} \right) \right], \\
 \frac{\partial^2 \Psi}{\partial [\mathbf{u}] \otimes \partial \mathbf{g}_\beta} &= \sum_i^3 \left[\frac{\partial \Psi}{\partial I_i} \frac{\partial^2 I_i}{\partial [\mathbf{u}] \otimes \partial \mathbf{g}_\beta} + \frac{\partial I_i}{\partial [\mathbf{u}]} \otimes \left[\frac{\partial^2 \Psi}{\partial I_i \partial \overline{\mathbf{C}}} : \frac{\partial \overline{\mathbf{C}}}{\partial \mathbf{g}_\beta} \right] \right. \\
 & \left. + \sum_j^3 \frac{\partial^2 \Psi}{\partial I_i \partial I_j} \left(\frac{\partial I_i}{\partial [\mathbf{u}]} \otimes \frac{\partial I_j}{\partial \mathbf{g}_\beta} \right) \right] = \left[\frac{\partial^2 \Psi}{\partial \mathbf{g}_\beta \otimes \partial [\mathbf{u}]} \right]^T, \\
 \frac{\partial^2 \Psi}{\partial \mathbf{g}_\alpha \otimes \partial \mathbf{g}_\beta} &= \sum_i^3 \left\{ \left[\sum_j^3 \frac{\partial^2 \Psi}{\partial I_i \partial I_j} \left(\frac{\partial I_i}{\partial \mathbf{g}_\alpha} \otimes \frac{\partial I_j}{\partial \mathbf{g}_\beta} \right) \right] + \frac{\partial \Psi}{\partial I_i} \frac{\partial^2 I_i}{\partial \mathbf{g}_\alpha \otimes \partial \mathbf{g}_\beta} \right. \\
 & \left. \left[\frac{\partial \overline{\mathbf{C}}}{\partial \mathbf{g}_\alpha} \right]^T : \frac{\partial^2 \Psi}{\partial \overline{\mathbf{C}} \partial I_i} \otimes \frac{\partial I_i}{\partial \mathbf{g}_\beta} + \left[\frac{\partial \overline{\mathbf{C}}}{\partial \mathbf{g}_\alpha} \right]^T : \frac{\partial^2 \Psi}{\partial \overline{\mathbf{C}} \otimes \partial \overline{\mathbf{C}}} : \frac{\partial \overline{\mathbf{C}}}{\partial \mathbf{g}_\beta} + \frac{\partial \Psi}{\partial \overline{\mathbf{C}}} : \frac{\partial^2 \overline{\mathbf{C}}}{\partial \mathbf{g}_\alpha \otimes \partial \mathbf{g}_\beta} \right\}
 \end{aligned} \tag{B.15}$$

in terms of the second derivatives of invariants I_1, I_2, I_3 and $\overline{\mathbf{C}}$. Based on Eqs. (B.9), the non-trivial (non-vanishing) second derivatives are

$$\frac{\partial^2 I_1}{\partial [\mathbf{u}] \otimes \partial [\mathbf{u}]} = 2 \mathbf{1},$$

B.1 Vector of internal forces and stiffness matrix of the prototype model according to Table 5.1

$$\begin{aligned}
\frac{\partial^2 I_2}{\partial \llbracket \mathbf{u} \rrbracket \otimes \partial \llbracket \mathbf{u} \rrbracket} &= \mathbf{g}^1 \otimes \mathbf{g}_1 + \mathbf{g}_1 \otimes \mathbf{g}^1, \\
\frac{\partial^2 I_2}{\partial \llbracket \mathbf{u} \rrbracket \otimes \partial \mathbf{g}_1} &= \llbracket \mathbf{u} \rrbracket \otimes \mathbf{g}^1 + (\llbracket \mathbf{u} \rrbracket \cdot \mathbf{g}^1) \mathbf{1} + [- (\llbracket \mathbf{u} \rrbracket \cdot \mathbf{g}^1) \mathbf{g}^1 + g^{11} (\llbracket \mathbf{u} \rrbracket \cdot \mathbf{g}^3) \mathbf{g}^3] \otimes \mathbf{g}_1 + \\
&\quad (\llbracket \mathbf{u} \rrbracket \cdot \mathbf{g}_1) (-\mathbf{g}^1 \otimes \mathbf{g}^1 + g^{11} \mathbf{g}^3 \otimes \mathbf{g}^3) = \left[\frac{\partial^2 I_2}{\partial \mathbf{g}_1 \otimes \partial \llbracket \mathbf{u} \rrbracket} \right]^T, \\
\frac{\partial^2 I_2}{\partial \llbracket \mathbf{u} \rrbracket \otimes \partial \mathbf{g}_2} &= [- (\llbracket \mathbf{u} \rrbracket \cdot \mathbf{g}^2) \mathbf{g}^1 + g^{12} (\llbracket \mathbf{u} \rrbracket \cdot \mathbf{g}^3) \mathbf{g}^3] \otimes \mathbf{g}_1 + \\
&\quad (\llbracket \mathbf{u} \rrbracket \cdot \mathbf{g}_1) [-\mathbf{g}^1 \otimes \mathbf{g}^2 + g^{12} \mathbf{g}^3 \otimes \mathbf{g}^3] = \left[\frac{\partial^2 I_2}{\partial \mathbf{g}_2 \otimes \partial \llbracket \mathbf{u} \rrbracket} \right]^T, \\
\frac{\partial^2 I_2}{\partial \mathbf{g}_1 \otimes \partial \mathbf{g}_1} &= \llbracket \mathbf{u} \rrbracket \otimes [- (\llbracket \mathbf{u} \rrbracket \cdot \mathbf{g}^1) \mathbf{g}^1 + g^{11} (\llbracket \mathbf{u} \rrbracket \cdot \mathbf{g}^3) \mathbf{g}^3] + [- (\llbracket \mathbf{u} \rrbracket \cdot \mathbf{g}^1) \mathbf{g}^1 + \\
&\quad g^{11} (\llbracket \mathbf{u} \rrbracket \cdot \mathbf{g}^3) \mathbf{g}^3] \otimes \llbracket \mathbf{u} \rrbracket + (\llbracket \mathbf{u} \rrbracket \cdot \mathbf{g}_1) \cdot \left[(\llbracket \mathbf{u} \rrbracket \cdot \mathbf{g}^1) \mathbf{g}^1 \otimes \mathbf{g}^1 - \right. \\
&\quad \left. g^{11} (\llbracket \mathbf{u} \rrbracket \cdot \mathbf{g}^3) \mathbf{g}^1 \otimes \mathbf{g}^3 + (\llbracket \mathbf{u} \rrbracket \cdot \mathbf{g}^1) (\mathbf{g}^1 \otimes \mathbf{g}^1 - g^{11} \mathbf{g}^3 \otimes \mathbf{g}^3) - \right. \\
&\quad \left. 2 [g^{11} (\llbracket \mathbf{u} \rrbracket \cdot \mathbf{g}^3) \mathbf{g}^3 \otimes \mathbf{g}^1] - g^{11} (\llbracket \mathbf{u} \rrbracket \cdot \mathbf{g}^1) \mathbf{g}^3 \otimes \mathbf{g}^3 - g^{11} (\llbracket \mathbf{u} \rrbracket \cdot \mathbf{g}^3) \mathbf{g}^1 \otimes \mathbf{g}^3 \right], \\
\frac{\partial^2 I_2}{\partial \mathbf{g}_2 \otimes \partial \mathbf{g}_2} &= (\llbracket \mathbf{u} \rrbracket \cdot \mathbf{g}_1) \left[\mathbf{g}^1 \otimes [(\llbracket \mathbf{u} \rrbracket \cdot \mathbf{g}^2) \mathbf{g}^2 - g^{22} (\llbracket \mathbf{u} \rrbracket \cdot \mathbf{g}^3) \mathbf{g}^3] - (\llbracket \mathbf{u} \rrbracket \cdot \mathbf{g}^2) \right. \\
&\quad \left. [-\mathbf{g}^2 \otimes \mathbf{g}^1 + g^{12} \mathbf{g}^3 \otimes \mathbf{g}^3] + (\llbracket \mathbf{u} \rrbracket \cdot \mathbf{g}^3) \mathbf{g}^3 \otimes [-(\mathbf{g}^2 \cdot \mathbf{g}^2) \mathbf{g}^1 - (\mathbf{g}^1 \cdot \mathbf{g}^2) \mathbf{g}^2] - \right. \\
&\quad \left. g^{12} (\llbracket \mathbf{u} \rrbracket \cdot \mathbf{g}^2) \mathbf{g}^3 \otimes \mathbf{g}^3 + g^{12} (\llbracket \mathbf{u} \rrbracket \cdot \mathbf{g}^3) [-\mathbf{g}^2 \otimes \mathbf{g}^3] \right] \\
\frac{\partial^2 I_2}{\partial \mathbf{g}_1 \otimes \partial \mathbf{g}_2} &= - (\llbracket \mathbf{u} \rrbracket \cdot \mathbf{g}^2) \llbracket \mathbf{u} \rrbracket \otimes \mathbf{g}^1 + g^{12} (\llbracket \mathbf{u} \rrbracket \cdot \mathbf{g}^3) \llbracket \mathbf{u} \rrbracket \otimes \mathbf{g}^3 + \\
&\quad (\llbracket \mathbf{u} \rrbracket \cdot \mathbf{g}_1) \left[(\llbracket \mathbf{u} \rrbracket \cdot \mathbf{g}^2) \mathbf{g}^1 \otimes \mathbf{g}^1 g^{12} (\llbracket \mathbf{u} \rrbracket \cdot \mathbf{g}^3) \mathbf{g}^1 \otimes \mathbf{g}^3 + (\llbracket \mathbf{u} \rrbracket \cdot \mathbf{g}^1) \mathbf{g}^2 \otimes \mathbf{g}^1 - \right. \\
&\quad \left. g^{12} (\llbracket \mathbf{u} \rrbracket \cdot \mathbf{g}^1) \mathbf{g}^3 \otimes \mathbf{g}^3 - g^{11} (\llbracket \mathbf{u} \rrbracket \cdot \mathbf{g}^2) \mathbf{g}^3 \otimes \mathbf{g}^3 - \right. \\
&\quad \left. g^{11} (\llbracket \mathbf{u} \rrbracket \cdot \mathbf{g}^3) \mathbf{g}^2 \otimes \mathbf{g}^3 + 2 (\llbracket \mathbf{u} \rrbracket \cdot \mathbf{g}^3) \mathbf{g}^3 \otimes [-g^{12} \mathbf{g}^1] \right] = \left[\frac{\partial^2 I_2}{\partial \mathbf{g}_2 \otimes \partial \mathbf{g}_1} \right]^T, \\
\frac{\partial^2 I_3}{\partial \llbracket \mathbf{u} \rrbracket \otimes \partial \llbracket \mathbf{u} \rrbracket} &= \mathbf{g}^2 \otimes \mathbf{g}_2 + \mathbf{g}_2 \otimes \mathbf{g}^2, \\
\frac{\partial^2 I_3}{\partial \llbracket \mathbf{u} \rrbracket \otimes \partial \mathbf{g}_1} &= [- (\llbracket \mathbf{u} \rrbracket \cdot \mathbf{g}^1) \mathbf{g}^2 + g^{21} (\llbracket \mathbf{u} \rrbracket \cdot \mathbf{g}^3) \mathbf{g}^3] \otimes \mathbf{g}_2 + \\
&\quad (\llbracket \mathbf{u} \rrbracket \cdot \mathbf{g}_2) (-\mathbf{g}^2 \otimes \mathbf{g}^1 + g^{21} \mathbf{g}^3 \otimes \mathbf{g}^3) = \left[\frac{\partial^2 I_3}{\partial \mathbf{g}_1 \otimes \partial \llbracket \mathbf{u} \rrbracket} \right]^T, \\
\frac{\partial^2 I_3}{\partial \llbracket \mathbf{u} \rrbracket \otimes \partial \mathbf{g}_2} &= \llbracket \mathbf{u} \rrbracket \otimes \mathbf{g}^2 + (\llbracket \mathbf{u} \rrbracket \cdot \mathbf{g}^2) \mathbf{1} + [- (\llbracket \mathbf{u} \rrbracket \cdot \mathbf{g}^2) \mathbf{g}^2 + g^{22} (\llbracket \mathbf{u} \rrbracket \cdot \mathbf{g}^3) \mathbf{g}^3] \otimes \mathbf{g}_2 +
\end{aligned}$$

$$\begin{aligned}
 & ([\mathbf{u}] \cdot \mathbf{g}_2) (-\mathbf{g}^2 \otimes \mathbf{g}^2 + g^{22} \mathbf{g}^3 \otimes \mathbf{g}^3) = \left[\frac{\partial^2 I_3}{\partial \mathbf{g}_2 \otimes \partial [\mathbf{u}]} \right]^T, \\
 \frac{\partial^2 I_3}{\partial \mathbf{g}_1 \otimes \partial \mathbf{g}_1} &= ([\mathbf{u}] \cdot \mathbf{g}_2) \left[\mathbf{g}^2 \otimes [([\mathbf{u}] \cdot \mathbf{g}^1) \mathbf{g}^1 - g^{11} ([\mathbf{u}] \cdot \mathbf{g}^3) \mathbf{g}^3] - ([\mathbf{u}] \cdot \mathbf{g}^1) \right. \\
 &\quad \left. [-\mathbf{g}^1 \otimes \mathbf{g}^2 + g^{21} \mathbf{g}^3 \otimes \mathbf{g}^3] + ([\mathbf{u}] \cdot \mathbf{g}^3) \mathbf{g}^3 \otimes [-(\mathbf{g}^1 \cdot \mathbf{g}^2) \mathbf{g}^1 - (\mathbf{g}^1 \cdot \mathbf{g}^1) \mathbf{g}^2] + \right. \\
 &\quad \left. g^{21} \mathbf{g}^3 \otimes [-(\mathbf{u}) \cdot \mathbf{g}^1] \mathbf{g}^3 + g^{21} ([\mathbf{u}] \cdot \mathbf{g}^3) [-\mathbf{g}^1 \otimes \mathbf{g}^3] \right], \\
 \frac{\partial^2 I_3}{\partial \mathbf{g}_2 \otimes \partial \mathbf{g}_2} &= [\mathbf{u}] \otimes [-([\mathbf{u}] \cdot \mathbf{g}^2) \mathbf{g}^2 + g^{22} ([\mathbf{u}] \cdot \mathbf{g}^3) \mathbf{g}^3] + \\
 &\quad [-([\mathbf{u}] \cdot \mathbf{g}^2) \mathbf{g}^2 + g^{22} ([\mathbf{u}] \cdot \mathbf{g}^3) \mathbf{g}^3] \otimes [\mathbf{u}] + \\
 &\quad ([\mathbf{u}] \cdot \mathbf{g}_2) \cdot \left[([\mathbf{u}] \cdot \mathbf{g}^2) \mathbf{g}^2 \otimes \mathbf{g}^2 - g^{22} ([\mathbf{u}] \cdot \mathbf{g}^3) \mathbf{g}^2 \otimes \mathbf{g}^3 + \right. \\
 &\quad \left. ([\mathbf{u}] \cdot \mathbf{g}^2) (\mathbf{g}^2 \otimes \mathbf{g}^2 - g^{22} \mathbf{g}^3 \otimes \mathbf{g}^3) - \right. \\
 &\quad \left. 2 [g^{22} ([\mathbf{u}] \cdot \mathbf{g}^3) \mathbf{g}^3 \otimes \mathbf{g}^2] - g^{22} ([\mathbf{u}] \cdot \mathbf{g}^2) \mathbf{g}^3 \otimes \mathbf{g}^3 - g^{22} ([\mathbf{u}] \cdot \mathbf{g}^3) \mathbf{g}^2 \otimes \mathbf{g}^3 \right], \\
 \frac{\partial^2 I_3}{\partial \mathbf{g}_1 \otimes \partial \mathbf{g}_2} &= -([\mathbf{u}] \cdot \mathbf{g}^1) \mathbf{g}^2 \otimes [\mathbf{u}] + g^{21} ([\mathbf{u}] \cdot \mathbf{g}^3) \mathbf{g}^3 \otimes [\mathbf{u}] + ([\mathbf{u}] \cdot \mathbf{g}_2) \\
 &\quad \left[([\mathbf{u}] \cdot \mathbf{g}^2) \mathbf{g}^2 \otimes \mathbf{g}^1 - g^{12} ([\mathbf{u}] \cdot \mathbf{g}^3) \mathbf{g}^2 \otimes \mathbf{g}^3 + ([\mathbf{u}] \cdot \mathbf{g}^1) \mathbf{g}^2 \otimes \mathbf{g}^2 - \right. \\
 &\quad \left. g^{22} ([\mathbf{u}] \cdot \mathbf{g}^1) \mathbf{g}^3 \otimes \mathbf{g}^3 - g^{21} ([\mathbf{u}] \cdot \mathbf{g}^2) \mathbf{g}^3 \otimes \mathbf{g}^3 - g^{21} ([\mathbf{u}] \cdot \mathbf{g}^3) \right. \\
 &\quad \left. \mathbf{g}^2 \otimes \mathbf{g}^3 - ([\mathbf{u}] \cdot \mathbf{g}^3) [g^{12} \mathbf{g}^3 \otimes \mathbf{g}^2 + g^{22} \mathbf{g}^3 \otimes \mathbf{g}^1] \right] = \left[\frac{\partial^2 I_3}{\partial \mathbf{g}_2 \otimes \partial \mathbf{g}_1} \right]^T, \\
 \frac{\partial^2 \overline{\mathcal{C}}}{\partial \mathbf{g}_1 \otimes \partial \mathbf{g}_1} &= 2 [\mathbf{G}^1 \otimes \mathbf{G}^1 \otimes \mathbf{g}_\beta \otimes \mathbf{g}^\beta], \\
 \frac{\partial^2 \overline{\mathcal{C}}}{\partial \mathbf{g}_1 \otimes \partial \mathbf{g}_2} &= [\mathbf{G}^1 \otimes \mathbf{G}^2 \otimes \mathbf{g}_\beta \otimes \mathbf{g}^\beta] + [\mathbf{G}^2 \otimes \mathbf{G}^1 \otimes \mathbf{g}_\beta \otimes \mathbf{g}^\beta] = \frac{\partial^2 \overline{\mathcal{C}}}{\partial \mathbf{g}_2 \otimes \partial \mathbf{g}_1}, \\
 \frac{\partial^2 \overline{\mathcal{C}}}{\partial \mathbf{g}_2 \otimes \partial \mathbf{g}_1} &= 2 [\mathbf{G}^2 \otimes \mathbf{G}^2 \otimes \mathbf{g}_\beta \otimes \mathbf{g}^\beta]. \tag{B.16}
 \end{aligned}$$

By inserting Eqs. (B.16) into Eqs. (B.15), Eqs. (B.14) can be computed. As a consequence, the only remaining unknown linearisations entering linearisation (B.13) are those related to internal variable $\boldsymbol{\alpha}$. Focusing, as an example, again on the prototype model according to Tab. 5.1, damage variables $d_i^{(j)}$ are connected to internal variables κ_j by $d_i^{(j)} = d_i^{(j)}(\kappa_j)$. Furthermore, $\kappa_j = \kappa_j(\Psi_j^0)$ in the case of loading. For this reason,

$$\begin{aligned}
 \Delta d_n^{(n)} &= \frac{\partial d_n^{(n)}}{\kappa_n} \Delta \Psi_n^0, \\
 \Delta d_t^{(n)} &= \frac{\partial d_t^{(n)}}{\kappa_n} \Delta \Psi_n^0,
 \end{aligned}$$

B.1 Vector of internal forces and stiffness matrix of the prototype model according to Table 5.1

$$\begin{aligned}\Delta d_n^{(t)} &= \frac{\partial d_n^{(n)}}{\kappa_t} \Delta \Psi_t^0, \\ \Delta d_n^{(n)} &= \frac{\partial d_t^{(t)}}{\kappa_t} \Delta \Psi_t^0.\end{aligned}\tag{B.17}$$

Clearly, the terms are zero in the case of unloading. The linearisations of $d_i^{(j)}$ are completed by linearisations

$$\begin{aligned}\Delta \Psi_n^0 &= \frac{\partial \Psi_n^0}{\partial [\mathbf{u}]} \cdot \Delta [\mathbf{u}] + \frac{\partial \Psi_n^0}{\partial \mathbf{g}_\alpha} \cdot \Delta \mathbf{g}_\alpha, \\ \Delta \Psi_t^0 &= \frac{\partial \Psi_t^0}{\partial [\mathbf{u}]} \cdot \Delta [\mathbf{u}] + \frac{\partial \Psi_t^0}{\partial \mathbf{g}_\alpha} \cdot \Delta \mathbf{g}_\alpha\end{aligned}\tag{B.18}$$

where α is a summation index. The partial derivatives involved in Eqs. (B.18) have already been given in Eqs. (B.8). As a result, all derivatives necessary for computing stiffness relation (B.13) are known.

C Derivation of contributions concerning the gradient of $\llbracket \mathbf{u} \rrbracket$

C.1 Representation of local energy including higher order displacement jump contributions

In the case of a quadratic local interface energy and a spatial distribution of the stiffness parameter, integration of the local model and the extended gradient model are equivalent, i.e.,

$$\int \Psi(\llbracket \mathbf{u} \rrbracket \cdot \llbracket \mathbf{u} \rrbracket) \, dA \Leftrightarrow \overline{\mathcal{I}}^{\text{eff}}(\llbracket \mathbf{u} \rrbracket_M, \overline{\text{GRAD}}_M \llbracket \mathbf{u} \rrbracket) A. \quad (\text{C.1})$$

However, already the extension of the left side to contributions of type $(\llbracket \mathbf{u} \rrbracket_{(i)} \cdot \llbracket \mathbf{u} \rrbracket_{(j)}) (\llbracket \mathbf{u} \rrbracket_{(k)} \cdot \llbracket \mathbf{u} \rrbracket_{(l)})$ requires further investigations, i.e.,

$$\int \Psi((\llbracket \mathbf{u} \rrbracket \cdot \llbracket \mathbf{u} \rrbracket)^2) \, dA \stackrel{?}{\Leftrightarrow} \overline{\mathcal{I}}^{\text{eff}}(\llbracket \mathbf{u} \rrbracket_M, \overline{\text{GRAD}}_M \llbracket \mathbf{u} \rrbracket) A. \quad (\text{C.2})$$

Due to 21 possible combinations of node scalar products $(\llbracket \mathbf{u} \rrbracket_{(i)} \cdot \llbracket \mathbf{u} \rrbracket_{(j)}) (\llbracket \mathbf{u} \rrbracket_{(k)} \cdot \llbracket \mathbf{u} \rrbracket_{(l)})$, the stiffness $\mathbf{a}_{II}^{\text{el}}$, cf. Eq. (7.31), is discretised with shape functions of order 5 in the natural coordinates ξ and η as

$$\mathbf{a}_{II}^{\text{el}}(\mathbf{X}) = \sum_{m=1}^{21} \hat{N}^{(m)} \hat{c}^{(m)}, \quad (\text{C.3})$$

where

$$\hat{N} = [1, \xi, \eta, \xi^2, \xi \eta, \eta^2, \xi^3, \xi^2 \eta, \xi \eta^2, \eta^3, \xi^4, \xi^3 \eta, \xi^2 \eta^2, \xi \eta^3, \eta^4, \xi^5, \xi^4 \eta, \xi^3 \eta^2, \xi^2 \eta^3, \xi \eta^4, \eta^5]. \quad (\text{C.4})$$

C Derivation of contributions concerning the gradient of $\llbracket \mathbf{u} \rrbracket$

Insertion of these shape functions, together with the affine functions representing the displacement jump, yields

$$\int_{\Delta} \Psi (\llbracket \mathbf{u} \rrbracket \cdot \llbracket \mathbf{u} \rrbracket)^2 \, dA \approx \frac{1}{2} A \llbracket \mathbf{u} \rrbracket_{(ijkl)} \cdot \mathbb{D} \cdot \hat{\mathbf{c}} \quad (\text{C.5})$$

with

$$\llbracket \mathbf{u} \rrbracket_{(ijkl)} = \begin{bmatrix} (\llbracket \mathbf{u} \rrbracket_{(1)} \cdot \llbracket \mathbf{u} \rrbracket_{(1)})^2 \\ (\llbracket \mathbf{u} \rrbracket_{(1)} \cdot \llbracket \mathbf{u} \rrbracket_{(1)}) (\llbracket \mathbf{u} \rrbracket_{(1)} \cdot \llbracket \mathbf{u} \rrbracket_{(2)}) \\ (\llbracket \mathbf{u} \rrbracket_{(1)} \cdot \llbracket \mathbf{u} \rrbracket_{(1)}) (\llbracket \mathbf{u} \rrbracket_{(1)} \cdot \llbracket \mathbf{u} \rrbracket_{(3)}) \\ (\llbracket \mathbf{u} \rrbracket_{(1)} \cdot \llbracket \mathbf{u} \rrbracket_{(1)}) (\llbracket \mathbf{u} \rrbracket_{(2)} \cdot \llbracket \mathbf{u} \rrbracket_{(2)}) \\ (\llbracket \mathbf{u} \rrbracket_{(1)} \cdot \llbracket \mathbf{u} \rrbracket_{(1)}) (\llbracket \mathbf{u} \rrbracket_{(2)} \cdot \llbracket \mathbf{u} \rrbracket_{(3)}) \\ (\llbracket \mathbf{u} \rrbracket_{(1)} \cdot \llbracket \mathbf{u} \rrbracket_{(1)}) (\llbracket \mathbf{u} \rrbracket_{(3)} \cdot \llbracket \mathbf{u} \rrbracket_{(3)}) \\ (\llbracket \mathbf{u} \rrbracket_{(1)} \cdot \llbracket \mathbf{u} \rrbracket_{(2)}) (\llbracket \mathbf{u} \rrbracket_{(1)} \cdot \llbracket \mathbf{u} \rrbracket_{(2)}) \\ (\llbracket \mathbf{u} \rrbracket_{(1)} \cdot \llbracket \mathbf{u} \rrbracket_{(2)}) (\llbracket \mathbf{u} \rrbracket_{(1)} \cdot \llbracket \mathbf{u} \rrbracket_{(3)}) \\ (\llbracket \mathbf{u} \rrbracket_{(1)} \cdot \llbracket \mathbf{u} \rrbracket_{(2)}) (\llbracket \mathbf{u} \rrbracket_{(2)} \cdot \llbracket \mathbf{u} \rrbracket_{(2)}) \\ (\llbracket \mathbf{u} \rrbracket_{(1)} \cdot \llbracket \mathbf{u} \rrbracket_{(2)}) (\llbracket \mathbf{u} \rrbracket_{(2)} \cdot \llbracket \mathbf{u} \rrbracket_{(3)}) \\ (\llbracket \mathbf{u} \rrbracket_{(1)} \cdot \llbracket \mathbf{u} \rrbracket_{(3)}) (\llbracket \mathbf{u} \rrbracket_{(3)} \cdot \llbracket \mathbf{u} \rrbracket_{(3)}) \\ (\llbracket \mathbf{u} \rrbracket_{(1)} \cdot \llbracket \mathbf{u} \rrbracket_{(3)}) (\llbracket \mathbf{u} \rrbracket_{(1)} \cdot \llbracket \mathbf{u} \rrbracket_{(3)}) \\ (\llbracket \mathbf{u} \rrbracket_{(1)} \cdot \llbracket \mathbf{u} \rrbracket_{(3)}) (\llbracket \mathbf{u} \rrbracket_{(2)} \cdot \llbracket \mathbf{u} \rrbracket_{(2)}) \\ (\llbracket \mathbf{u} \rrbracket_{(1)} \cdot \llbracket \mathbf{u} \rrbracket_{(3)}) (\llbracket \mathbf{u} \rrbracket_{(2)} \cdot \llbracket \mathbf{u} \rrbracket_{(3)}) \\ (\llbracket \mathbf{u} \rrbracket_{(1)} \cdot \llbracket \mathbf{u} \rrbracket_{(3)}) (\llbracket \mathbf{u} \rrbracket_{(3)} \cdot \llbracket \mathbf{u} \rrbracket_{(3)}) \\ (\llbracket \mathbf{u} \rrbracket_{(2)} \cdot \llbracket \mathbf{u} \rrbracket_{(2)})^2 \\ (\llbracket \mathbf{u} \rrbracket_{(2)} \cdot \llbracket \mathbf{u} \rrbracket_{(2)}) (\llbracket \mathbf{u} \rrbracket_{(2)} \cdot \llbracket \mathbf{u} \rrbracket_{(3)}) \\ (\llbracket \mathbf{u} \rrbracket_{(2)} \cdot \llbracket \mathbf{u} \rrbracket_{(2)}) (\llbracket \mathbf{u} \rrbracket_{(3)} \cdot \llbracket \mathbf{u} \rrbracket_{(3)}) \\ (\llbracket \mathbf{u} \rrbracket_{(2)} \cdot \llbracket \mathbf{u} \rrbracket_{(3)}) (\llbracket \mathbf{u} \rrbracket_{(2)} \cdot \llbracket \mathbf{u} \rrbracket_{(3)}) \\ (\llbracket \mathbf{u} \rrbracket_{(2)} \cdot \llbracket \mathbf{u} \rrbracket_{(3)}) (\llbracket \mathbf{u} \rrbracket_{(3)} \cdot \llbracket \mathbf{u} \rrbracket_{(3)}) \\ (\llbracket \mathbf{u} \rrbracket_{(3)} \cdot \llbracket \mathbf{u} \rrbracket_{(3)})^2 \end{bmatrix}, \quad \hat{\mathbf{c}} = \begin{bmatrix} \hat{c}^1 \\ \hat{c}^2 \\ \hat{c}^3 \\ \hat{c}^4 \\ \hat{c}^5 \\ \hat{c}^6 \\ \hat{c}^7 \\ \hat{c}^8 \\ \hat{c}^9 \\ \hat{c}^{10} \\ \hat{c}^{11} \\ \hat{c}^{12} \\ \hat{c}^{13} \\ \hat{c}^{14} \\ \hat{c}^{15} \\ \hat{c}^{16} \\ \hat{c}^{17} \\ \hat{c}^{18} \\ \hat{c}^{19} \\ \hat{c}^{20} \\ \hat{c}^{21} \end{bmatrix} \quad (\text{C.6})$$

and

$$\mathbb{D} = \begin{bmatrix} \int_{\Delta} \hat{N}^{(1)} \left[N^{(1)} \right]^4 \, dA & \int_{\Delta} \hat{N}^{(2)} \left[N^{(1)} \right]^4 \, dA & \cdots & \int_{\Delta} \hat{N}^{(21)} \left[N^{(1)} \right]^4 \, dA \\ \int_{\Delta} \hat{N}^{(1)} \left[N^{(1)} \right]^3 N^{(2)} \, dA & \int_{\Delta} \hat{N}^{(2)} \left[N^{(1)} \right]^3 N^{(2)} \, dA & \cdots & \int_{\Delta} \hat{N}^{(21)} \left[N^{(1)} \right]^3 N^{(2)} \, dA \\ \vdots & \vdots & \ddots & \vdots \\ \int_{\Delta} \hat{N}^{(1)} \left[N^{(3)} \right]^4 \, dA & \int_{\Delta} \hat{N}^{(2)} \left[N^{(3)} \right]^4 \, dA & \cdots & \int_{\Delta} \hat{N}^{(21)} \left[N^{(3)} \right]^4 \, dA \end{bmatrix}. \quad (\text{C.7})$$

C.1 Representation of local energy including higher order displacement jump contributions

A straightforward computation shows $\det \mathbb{D} = 0$ since

$$\int_{\Delta} \hat{N}^{(m)} \left[N^{(1)} N^{(2)} \right]^2 dA = \int_{\Delta} \hat{N}^{(m)} \left[N^{(1)} \right]^2 \left[N^{(2)} \right]^2 dA. \quad (\text{C.8})$$

D Derivation of curvature contributions

D.1 Symmetry properties of $\overline{\text{GRAD}}(\overline{\mathbf{F}})$

In this appendix it is shown that

$$\overline{\text{GRAD}}(\overline{\mathbf{F}}) : \overline{\mathbf{A}} = \overline{\text{GRAD}}(\overline{\mathbf{F}}) : \overline{\mathbf{A}}^T \quad \forall \overline{\mathbf{A}} \in \text{span}\{\mathbf{G}_1, \mathbf{G}_2\}. \quad (\text{D.1})$$

In the following, general representation

$$\begin{aligned} \overline{\mathbf{A}} &= A^{11} \mathbf{G}_1 \otimes \mathbf{G}_1 + A^{12} \mathbf{G}_1 \otimes \mathbf{G}_2 \\ &\quad + A^{21} \mathbf{G}_2 \otimes \mathbf{G}_1 + A^{22} \mathbf{G}_2 \otimes \mathbf{G}_2 \end{aligned} \quad (\text{D.2})$$

is considered. By applying representation

$$\overline{\text{GRAD}}(\overline{\mathbf{F}}) = \overline{\gamma}_{\alpha\beta}^k \mathbf{g}_k \otimes \mathbf{G}^\alpha \otimes \mathbf{G}^\beta - \overline{\Gamma}_{\beta\delta}^\alpha \mathbf{g}_\alpha \otimes \mathbf{G}^\delta \otimes \mathbf{G}^\beta, \quad (\text{D.3})$$

Eq. (D.3) can be rewritten as

$$\begin{aligned} &[\overline{\gamma}_{\alpha\beta}^k \mathbf{g}_k \otimes \mathbf{G}^\alpha \otimes \mathbf{G}^\beta - \overline{\Gamma}_{\beta\delta}^\alpha \mathbf{g}_\alpha \otimes \mathbf{G}^\delta \otimes \mathbf{G}^\beta] : \overline{\mathbf{A}} \\ &= [\overline{\gamma}_{\alpha\beta}^k \mathbf{g}_k \otimes \mathbf{G}^\alpha \otimes \mathbf{G}^\beta - \overline{\Gamma}_{\beta\delta}^\alpha \mathbf{g}_\alpha \otimes \mathbf{G}^\delta \otimes \mathbf{G}^\beta] : \overline{\mathbf{A}}^T. \end{aligned} \quad (\text{D.4})$$

Since $\mathbf{G}^\alpha \otimes \mathbf{G}^\alpha$ is a priori symmetric, Eq. (D.4) is equivalent to

$$[\overline{\gamma}_{\alpha\beta}^k \mathbf{g}_k \otimes \mathbf{G}^\alpha \otimes \mathbf{G}^\beta] : (\mathbf{G}_1 \otimes \mathbf{G}_2) \stackrel{!}{=} [\overline{\gamma}_{\alpha\beta}^k \mathbf{g}_k \otimes \mathbf{G}^\alpha \otimes \mathbf{G}^\beta] : (\mathbf{G}_2 \otimes \mathbf{G}_1) \quad \text{and} \quad (\text{D.5})$$

$$[\overline{\Gamma}_{\beta\delta}^\alpha \mathbf{g}_\alpha \otimes \mathbf{G}^\delta \otimes \mathbf{G}^\beta] : (\mathbf{G}_1 \otimes \mathbf{G}_2) \stackrel{!}{=} [\overline{\Gamma}_{\beta\delta}^\alpha \mathbf{g}_\alpha \otimes \mathbf{G}^\delta \otimes \mathbf{G}^\beta] : (\mathbf{G}_2 \otimes \mathbf{G}_1). \quad (\text{D.6})$$

A straightforward calculation yields

$$[\overline{\gamma}_{\alpha\beta}^k \mathbf{g}_k \otimes \mathbf{G}^\alpha \otimes \mathbf{G}^\beta] : (\mathbf{G}_1 \otimes \mathbf{G}_2) = \overline{\gamma}_{\alpha\beta}^k \mathbf{g}_k \delta_1^\alpha \delta_2^\beta = \overline{\gamma}_{12}^k \mathbf{g}_k \quad (\text{D.7})$$

and

$$[\bar{\gamma}_{\alpha\beta}^k \mathbf{g}_k \otimes \mathbf{G}^\alpha \otimes \mathbf{G}^\beta] : (\mathbf{G}_2 \otimes \mathbf{G}_1) = \bar{\gamma}_{\alpha\beta}^k \mathbf{g}_k \delta_2^\alpha \delta_1^\beta = \bar{\gamma}_{21}^k \mathbf{g}_k. \quad (\text{D.8})$$

Due to the symmetry of the Christoffel symbol $\bar{\gamma}_{12}^k = \bar{\gamma}_{21}^k$, it follows that Eq. (D.5) is indeed fulfilled. Likewise it follows

$$[\bar{\Gamma}_{\beta\delta}^\alpha \mathbf{g}_\alpha \otimes \mathbf{G}^\delta \otimes \mathbf{G}^\beta] : (\mathbf{G}_1 \otimes \mathbf{G}_2) = \bar{\Gamma}_{\beta\delta}^\alpha \mathbf{g}_\alpha \delta_1^\delta \delta_2^\beta = \bar{\Gamma}_{21}^\alpha \mathbf{g}_\alpha \quad (\text{D.9})$$

and

$$[\bar{\Gamma}_{\beta\delta}^\alpha \mathbf{g}_\alpha \otimes \mathbf{G}^\delta \otimes \mathbf{G}^\beta] : (\mathbf{G}_2 \otimes \mathbf{G}_1) = \bar{\Gamma}_{\beta\delta}^\alpha \mathbf{g}_\alpha \delta_2^\delta \delta_1^\beta = \bar{\Gamma}_{12}^\alpha \mathbf{g}_\alpha. \quad (\text{D.10})$$

Again, by using the symmetry property $\bar{\Gamma}_{21}^\alpha = \bar{\Gamma}_{12}^\alpha$ it is evident that Eq.(D.6) holds true.

D.2 Laplace-Beltrami operator

The relation of the Laplace-Beltrami operator and $\overline{\text{GRAD}}(\bar{\mathbf{F}})$ is given by

$$\begin{aligned} \overline{\text{div}}(\overline{\text{grad}}(\mathbf{x})) &= \overline{\text{div}}(\overline{\text{GRAD}}(\mathbf{x}) \cdot \bar{\mathbf{F}}^{-1}) \\ &= \overline{\text{div}}(\bar{\mathbf{F}} \cdot \bar{\mathbf{F}}^{-1}) \\ &= \overline{\text{grad}}(\bar{\mathbf{F}}) : \bar{\mathbf{F}}^{-1} + \bar{\mathbf{F}}^{-1} \cdot \overline{\text{div}}(\bar{\mathbf{F}}^{-1}) \\ &= [\overline{\text{GRAD}}(\bar{\mathbf{F}}) \cdot \bar{\mathbf{F}}^{-1}] : \bar{\mathbf{F}}^{-1} + \bar{\mathbf{F}} \cdot [\overline{\text{GRAD}}(\bar{\mathbf{F}}^{-1}) : \bar{\mathbf{F}}^{-T}], \end{aligned} \quad (\text{D.11})$$

cf. Eq. (7.118).

D.3 Re-derivation of the gradient of the inverse deformation gradient

Starting from

$$\overline{\text{GRAD}}(\bar{\mathbf{F}}^{-1} \cdot \bar{\mathbf{F}}) = \overline{\text{GRAD}}(\bar{\mathbf{I}}) \neq \mathbf{0}. \quad (\text{D.12})$$

and rewriting this equation in index notation

$$\begin{aligned} (\bar{F}_{ij}^{-1} \bar{F}_{jk})_{,l} &= (\overline{\text{GRAD}} \bar{\mathbf{I}})_{ikl} \\ &= \frac{\partial \bar{F}_{ij}^{-1}}{\partial \theta^\alpha} G_l^\alpha \bar{F}_{jk} + \bar{F}_{ij}^{-1} \frac{\partial \bar{F}_{jk}}{\partial \theta^\alpha} G_l^\alpha \end{aligned}$$

$$= (\overline{\text{GRAD}} \overline{\mathbf{F}}^{-1})_{ijl} \overline{\mathbf{F}}_{jk} + \overline{\mathbf{F}}_{ij}^{-1} (\overline{\text{GRAD}} \overline{\mathbf{F}})_{jkl}.$$

leads, after multiplication by $\overline{\mathbf{F}}^{-1}$

$$\begin{aligned} (\overline{\text{GRAD}} \overline{\mathbf{I}})_{ikl} \overline{\mathbf{F}}_{km}^{-1} &= (\overline{\text{GRAD}} \overline{\mathbf{F}}^{-1})_{ijl} \overline{\mathbf{F}}_{jk} \overline{\mathbf{F}}_{km}^{-1} + \overline{\mathbf{F}}_{ij}^{-1} (\overline{\text{GRAD}} \overline{\mathbf{F}})_{jkl} \overline{\mathbf{F}}_{km}^{-1} \\ \Leftrightarrow (\overline{\text{GRAD}} \overline{\mathbf{F}}^{-1})_{ijl} \overline{\mathbf{F}}_{jm}^{-1} &= (\overline{\text{GRAD}} \overline{\mathbf{I}})_{ikl} \overline{\mathbf{F}}_{km}^{-1} - \overline{\mathbf{F}}_{ij}^{-1} (\overline{\text{GRAD}} \overline{\mathbf{F}})_{jkl} \overline{\mathbf{F}}_{km}^{-1} \end{aligned} \quad (\text{D.13})$$

which is equivalent to

$$\overline{\text{GRAD}}(\overline{\mathbf{F}}^{-1}) : \overline{\mathbf{i}} = \overline{\text{GRAD}}(\overline{\mathbf{I}}) : \overline{\mathbf{F}}^{-1} - \overline{\mathbf{F}}^{-1} \cdot \overline{\text{GRAD}}(\overline{\mathbf{F}}) : \overline{\mathbf{F}}^{-1}, \quad (\text{D.14})$$

where

$$[\mathbf{A} \cdot \mathbf{B}]_{iml} = [\mathbf{A}]_{ijl} [\mathbf{B}]_{jm}.$$

D.4 Symmetry properties of $\overline{\text{GRAD}}(\overline{\mathbf{F}}^{-1})$

Equation (7.122) can be transformed since

$$[\overline{\text{GRAD}}(\overline{\mathbf{F}}^{-1}) : \overline{\mathbf{i}}] : \overline{\mathbf{F}}^{-T} = \overline{\text{GRAD}}(\overline{\mathbf{F}}^{-1}) : \overline{\mathbf{F}}^{-T}, \quad (\text{D.15})$$

which follows from

$$\begin{aligned} & [\overline{\text{GRAD}}(\overline{\mathbf{F}}^{-1}) : \overline{\mathbf{i}}] : \overline{\mathbf{F}}^{-T} \\ &= [(\mathbf{G}_{\alpha,\beta} \otimes \mathbf{g}^\alpha \otimes \mathbf{G}^\beta + \mathbf{G}_\alpha \otimes \mathbf{g}_{,\beta}^\alpha \otimes \mathbf{G}^\beta) \cdot (\mathbf{g}_\delta \otimes \mathbf{g}^\delta)] : (\mathbf{g}^\gamma \otimes \mathbf{G}_\gamma) \\ &= (\mathbf{G}_{\alpha,\beta} \otimes \mathbf{g}^\alpha \otimes \mathbf{G}^\beta + \mathbf{G}_\alpha \otimes \mathbf{g}_{,\beta}^\alpha \otimes \mathbf{G}^\beta) \cdot [(\mathbf{g}_\delta \otimes \mathbf{g}^\delta) \cdot (\mathbf{g}^\gamma \otimes \mathbf{G}_\gamma)] \\ &= (\mathbf{G}_{\alpha,\beta} \otimes \mathbf{g}^\alpha \otimes \mathbf{G}^\beta + \mathbf{G}_\alpha \otimes \mathbf{g}_{,\beta}^\alpha \otimes \mathbf{G}^\beta) : (\mathbf{g}_\gamma \mathbf{g}^{\gamma\delta} \otimes \mathbf{G}_\delta) \\ &= \mathbf{G}_{\alpha,\beta} \mathbf{g}^{\alpha\beta} + \mathbf{G}_\alpha (\mathbf{g}_{,\beta}^\alpha \cdot \mathbf{g}^\beta) \\ &= \overline{\text{GRAD}}(\overline{\mathbf{F}}^{-1}) : \overline{\mathbf{F}}^{-T}. \end{aligned} \quad (\text{D.16})$$

D.5 Coefficient comparison for the covariant representation of mean curvature h

Here, it is shown that mean curvature h can be represented as a covariant function depending on $\overline{\mathbf{F}}$, $\overline{\text{GRAD}}(\overline{\mathbf{F}})$, i.e.,

$$h = h(\overline{\mathbf{F}}, \overline{\text{GRAD}}(\overline{\mathbf{F}}), \overline{\text{GRAD}}(\overline{\mathbf{I}})) \quad \text{with} \quad \overline{\text{GRAD}}(\overline{\mathbf{I}}) = \text{const.} \quad (\text{D.17})$$

D Derivation of curvature contributions

In analogy to Eq. (7.128) the vectors \mathbf{a} , \mathbf{b} and \mathbf{c} are considered and the mean curvature is written as

$$h = \frac{1}{2} \|\mathbf{a} + \mathbf{b} - \mathbf{c}\| = \frac{1}{2} \sqrt{(\mathbf{a} \cdot \mathbf{a} + 2\mathbf{a} \cdot \mathbf{b} + \mathbf{b} \cdot \mathbf{b} - 2\mathbf{a} \cdot \mathbf{c} - 2\mathbf{b} \cdot \mathbf{c} + \mathbf{c} \cdot \mathbf{c})}. \quad (\text{D.18})$$

The involved scalar products can be written as

$$\begin{aligned} \mathbf{a} \cdot \mathbf{a} &= \left[\left[\overline{\text{GRAD}}(\overline{\mathbf{F}}) \cdot \overline{\mathbf{F}}^{-1} \right] : \overline{\mathbf{F}}^{-1} \right] \cdot \left[\left[\overline{\text{GRAD}}(\overline{\mathbf{F}}) \cdot \overline{\mathbf{F}}^{-1} \right] : \overline{\mathbf{F}}^{-1} \right] \\ &= \overline{\mathbf{C}}^{-1} : \left(\overline{\text{GRAD}}^T(\overline{\mathbf{F}}) \cdot \overline{\text{GRAD}}(\overline{\mathbf{F}}) \right) : \overline{\mathbf{C}}^{-1}, \end{aligned} \quad (\text{D.19})$$

$$\begin{aligned} \mathbf{a} \cdot \mathbf{b} &= \left[\left[\overline{\text{GRAD}}(\overline{\mathbf{F}}) \cdot \overline{\mathbf{F}}^{-1} \right] : \overline{\mathbf{F}}^{-1} \right] \cdot \left[\overline{\mathbf{F}} \cdot \left[\left(\overline{\text{GRAD}}(\overline{\mathbf{I}}) \cdot \overline{\mathbf{F}}^{-1} \right) : \overline{\mathbf{F}}^{-T} \right] \right] \\ &= \left[\left(\overline{\mathbf{F}}^T \cdot \overline{\text{GRAD}}(\overline{\mathbf{F}}) \right) : \overline{\mathbf{C}}^{-1} \right] \cdot \left[\overline{\text{GRAD}}(\overline{\mathbf{I}}) : \overline{\mathbf{C}}^{-1} \right] \end{aligned} \quad (\text{D.20})$$

depending on $\overline{\mathbf{F}}^T \cdot \overline{\text{GRAD}}(\overline{\mathbf{F}}) = \overline{\mathbf{C}} \cdot \left(\overline{\mathbf{F}}^{-1} \cdot \overline{\text{GRAD}}(\overline{\mathbf{F}}) \right)$ and $\overline{\text{GRAD}}(\overline{\mathbf{I}}) = \text{const.}$ The next coefficients take the form

$$\begin{aligned} \mathbf{a} \cdot \mathbf{c} &= \left[\left(\overline{\text{GRAD}}(\overline{\mathbf{F}}) \cdot \overline{\mathbf{F}}^{-1} \right) : \overline{\mathbf{F}}^{-1} \right] \cdot \left[\overline{\mathbf{F}} \cdot \left[\left(-\overline{\mathbf{F}}^{-1} \cdot \overline{\text{GRAD}}(\overline{\mathbf{F}}) \cdot \overline{\mathbf{F}}^{-1} \right) : \overline{\mathbf{F}}^{-T} \right] \right] \\ &= \left[\left(\overline{\mathbf{F}}^T \cdot \overline{\text{GRAD}}(\overline{\mathbf{F}}) \right) : \overline{\mathbf{C}}^{-1} \right] \cdot \left[\left(-\overline{\mathbf{F}}^{-1} \cdot \overline{\text{GRAD}}(\overline{\mathbf{F}}) \right) : \overline{\mathbf{C}}^{-1} \right], \end{aligned} \quad (\text{D.21})$$

$$\begin{aligned} \mathbf{b} \cdot \mathbf{b} &= \left[\overline{\mathbf{F}} \cdot \left[\left(\overline{\text{GRAD}}(\overline{\mathbf{I}}) \cdot \overline{\mathbf{F}}^{-1} \right) : \overline{\mathbf{F}}^{-T} \right] \right] \cdot \left[\overline{\mathbf{F}} \cdot \left[\left(\overline{\text{GRAD}}(\overline{\mathbf{I}}) \cdot \overline{\mathbf{F}}^{-1} \right) : \overline{\mathbf{F}}^{-T} \right] \right] \\ &= \overline{\mathbf{C}} : \left[\left(\overline{\text{GRAD}}(\overline{\mathbf{I}}) : \overline{\mathbf{C}}^{-1} \right) \otimes \left(\overline{\text{GRAD}}(\overline{\mathbf{I}}) : \overline{\mathbf{C}}^{-1} \right) \right], \end{aligned} \quad (\text{D.22})$$

$$\begin{aligned} \mathbf{b} \cdot \mathbf{c} &= \left[\overline{\mathbf{F}} \cdot \left[\left(\overline{\text{GRAD}}(\overline{\mathbf{I}}) \cdot \overline{\mathbf{F}}^{-1} \right) : \overline{\mathbf{F}}^{-T} \right] \right] \cdot \left[\overline{\mathbf{F}} \cdot \left[\left(-\overline{\mathbf{F}}^{-1} \cdot \overline{\text{GRAD}}(\overline{\mathbf{F}}) \cdot \overline{\mathbf{F}}^{-1} \right) : \overline{\mathbf{F}}^{-T} \right] \right] \\ &= - \left[\overline{\mathbf{C}} \cdot \left(\overline{\mathbf{F}}^{-1} \cdot \overline{\text{GRAD}}(\overline{\mathbf{F}}) \right) : \overline{\mathbf{C}}^{-1} \right] \cdot \left[\overline{\text{GRAD}}(\overline{\mathbf{I}}) : \overline{\mathbf{C}}^{-1} \right], \end{aligned} \quad (\text{D.23})$$

and

$$\begin{aligned}
 \mathbf{c} \cdot \mathbf{c} &= \\
 &\left[\overline{\mathbf{F}} \cdot \left[\left(-\overline{\mathbf{F}}^{-1} \cdot \overline{\text{GRAD}}(\overline{\mathbf{F}}) \cdot \overline{\mathbf{F}}^{-1} \right) : \overline{\mathbf{F}}^{-T} \right] \right] \cdot \left[\overline{\mathbf{F}} \cdot \left[\left(-\overline{\mathbf{F}}^{-1} \cdot \overline{\text{GRAD}}(\overline{\mathbf{F}}) \cdot \overline{\mathbf{F}}^{-1} \right) : \overline{\mathbf{F}}^{-T} \right] \right] \\
 &= \overline{\mathbf{C}} : \left[\left[\left(\overline{\mathbf{F}}^{-1} \cdot \overline{\text{GRAD}}(\overline{\mathbf{F}}) \right) : \overline{\mathbf{C}}^{-1} \right] \otimes \left[\left(\overline{\mathbf{F}}^{-1} \cdot \overline{\text{GRAD}}(\overline{\mathbf{F}}) \right) : \overline{\mathbf{C}}^{-1} \right] \right]. \quad (\text{D.24})
 \end{aligned}$$

Thus, all coefficients arising from Eq. (D.18) fulfill the principle of material covariance.

Bibliography

- [1] G. Alfano. On the influence of the shape of the interface law on the application of cohesive-zone models. *Composites Science and Technology*, 66(6):723 – 730, 2006. ISSN 0266-3538. doi:doi.org/10.1016/j.compscitech.2004.12.024. Advances in statics and dynamics of delamination.
- [2] F. Armero and K. Garikipati. An analysis of strong discontinuities in multiplicative finite strain plasticity and their relation with the numerical simulation of strain localization in solids. *International Journal of Solids and Structures*, 33:2863–2885, 1996. doi:10.1016/0020-7683(95)00257-X.
- [3] I. Babuška and J. M. Melenk. The partition of unity method. *International Journal for Numerical Methods in Engineering*, 40(4):727–758, 1997. ISSN 1097-0207. doi:10.1002/(SICI)1097-0207(19970228)40:4<727::AID-NME86>3.0.CO;2-N.
- [4] G. Barenblatt. The formation of equilibrium cracks during brittle fracture. general ideas and hypotheses. axially-symmetric cracks. *Journal of Applied Mathematics and Mechanics*, 23(3):622 – 636, 1959. ISSN 0021-8928. doi:doi.org/10.1016/0021-8928(59)90157-1.
- [5] G. Barenblatt. The mathematical theory of equilibrium cracks in brittle fracture. In H. Dryden, T. von Kármán, G. Kuerti, F. van den Dungen, and L. Howarth, editors, *Advances in Applied Mechanics*, volume 7, pages 55–129. Elsevier, 1962. doi:10.1016/S0065-2156(08)70121-2.
- [6] A. Bartels, T. Bartel, M. Canadija, and J. Mosler. On the thermomechanical coupling in dissipative materials: A variational approach for generalized standard materials. *Journal of the Mechanics and Physics of Solids*, 82:218 – 234, 2015. ISSN 0022-5096. doi:doi.org/10.1016/j.jmps.2015.04.011.
- [7] Y. Basar and D. Weichert. *Nonlinear Continuum Mechanics of Solids*. Springer, Berlin, Heidelberg, 2000. doi:10.1007/978-3-662-04299-1.
- [8] M. F. Beatty. On the foundation principles of general classical mechanics. *Archive for Rational Mechanics and Analysis*, 24(4):264–273, January 1967. ISSN 1432-0673. doi:10.1007/BF00283777.
- [9] T. Belytschko and T. Black. Elastic crack growth in finite elements with minimal remeshing. *International Journal for Numerical Methods in Engineering*, 45(5):601–620, 1999. ISSN 1097-0207. doi:10.1002/(SICI)1097-0207(19990620)45:5<601::AID-NME598>3.0.CO;2-S.

- [10] A. Bertram. *Elasticity and Plasticity of Large Deformations: an introduction*. Springer, 2005. ISBN 9783540240334.
- [11] A. Bertram. Compendium on gradient materials, 12 2017.
- [12] B. Bilby, L. Lardner, and A. Stroh. Continuous distributions of dislocations and the theory of plasticity. In *Actes du IXe congrès international de mécanique appliquée*, Bruxelles, 1956.
- [13] N. Bleier and J. Mosler. Efficient variational constitutive updates by means of a novel parameterization of the flow rule. *International Journal for Numerical Methods in Engineering*, 89:1120–1143, 03 2012. doi:10.1002/nme.3280.
- [14] C. Carstensen, K. Hackl, and A. Mielke. Non-convex potentials and microstructures in finite-strain plasticity. *Proceedings of the Royal Society of London. Series A: Mathematical, Physical and Engineering Sciences*, 458, 02 2002. doi:10.1098/rspa.2001.0864.
- [15] A. Cerrone, P. Wawrzynek, A. Nonn, G. H. Paulino, and A. Ingraffea. Implementation and verification of the park – paulino – roesler cohesive zone model in 3d. *Engineering Fracture Mechanics*, 120:26 – 42, 2014. ISSN 0013-7944. doi:10.1016/j.engfracmech.2014.03.010.
- [16] N. Chandra, H. Li, C. Shet, and H. Ghonem. Some issues in the application of cohesive zone models for metal – ceramic interfaces. *International Journal of Solids and Structures*, 39(10):2827 – 2855, 2002. ISSN 0020-7683. doi:10.1016/S0020-7683(02)00149-X.
- [17] P. Chhapadia, P. Mohammadi, and P. Sharma. Curvature-dependent surface energy and implications for nanostructures. *Journal of the Mechanics and Physics of Solids*, 59(10):2103 – 2115, 2011. ISSN 0022-5096. doi:10.1016/j.jmps.2011.06.007.
- [18] B. D. Coleman and M. E. Gurtin. Thermodynamics with internal state variables. *The Journal of Chemical Physics*, 47:597–613, 07 1967. doi:10.1063/1.1711937.
- [19] B. D. Coleman and W. Noll. The thermodynamics of elastic materials with heat conduction and viscosity. *Archive for Rational Mechanics and Analysis*, 13(1): 167–178, Dec 1963. ISSN 1432-0673. doi:10.1007/BF01262690.
- [20] F. Costanzo. A continuum theory of cohesive zone models: deformation and constitutive equations. *International Journal of Engineering Science*, 36(15):1763 – 1792, 1998. ISSN 0020-7225. doi:10.1016/S0020-7225(98)00025-1.
- [21] A. Curnier, Q.-C. He, and A. Klarbring. *Continuum Mechanics Modelling of Large Deformation Contact with Friction*, pages 145–158. Springer US, Boston, MA, 1995. ISBN 978-1-4615-1983-6. doi:10.1007/978-1-4615-1983-6_20.
- [22] R. de Borst. Numerical aspects of cohesive-zone models. *Engineering Fracture Mechanics*, 70(14):1743–1757, 2003. ISSN 0013-7944. doi:10.1016/S0013-7944(03)00122-X. Cohesive Models.

-
- [23] G. Del Piero. On the method of virtual power in continuum mechanics. *Journal of Mechanics of Materials and Structures*, 4:281–292, 04 2009. doi:10.2140/jomms.2009.4.281.
- [24] R. Dimitri, M. Trullo, L. D. Lorenzis, and G. Zavarise. Coupled cohesive zone models for mixed-mode fracture: A comparative study. *Engineering Fracture Mechanics*, 148:145 – 179, 2015. ISSN 0013-7944. doi:doi.org/10.1016/j.engfracmech.2015.09.029.
- [25] D. Dugdale. Yielding of steel sheets containing slits. *Journal of the Mechanics and Physics of Solids*, 8(2):100–104, 1960. ISSN 0022-5096. doi:10.1016/0022-5096(60)90013-2.
- [26] M. Epstein. On the wrinkling of anisotropic elastic membranes. *Journal of Elasticity*, 55(2):99–109, May 1999. ISSN 1573-2681. doi:10.1023/A:1007666106318.
- [27] M. Fagerström and R. Larsson. Theory and numerics for finite deformation fracture modelling using strong discontinuities. *International Journal for Numerical Methods in Engineering*, 66(6):911–948, 2006. doi:10.1002/nme.1573.
- [28] V. Fohrmeister, A. Bartels, and J. Mosler. Variational updates for thermomechanically coupled gradient-enhanced elastoplasticity – implementation based on hyper-dual numbers. *Computer Methods in Applied Mechanics and Engineering*, 339:239 – 261, 2018. ISSN 0045-7825. doi:10.1016/j.cma.2018.04.047.
- [29] X. Gao, Z. Huang, J. Qu, and D. Fang. A curvature-dependent interfacial energy-based interface stress theory and its applications to nano-structured materials: (i) general theory. *Journal of the Mechanics and Physics of Solids*, 66:59 – 77, 2014. ISSN 0022-5096. doi:10.1016/j.jmps.2014.01.010.
- [30] X. Gao, Z. Huang, and D. Fang. Curvature-dependent interfacial energy and its effects on the elastic properties of nanomaterials. *International Journal of Solids and Structures*, 113-114:100 – 107, 2017. ISSN 0020-7683. doi:10.1016/j.ijsolstr.2017.01.021.
- [31] K. Garikipati. *On strong discontinuities in inelastic solids and their numerical simulation*. PhD thesis, Stanford University, 1996.
- [32] T. C. Gasser and G. A. Holzapfel. Geometrically non-linear and consistently linearized embedded strong discontinuity models for 3d problems with an application to the dissection analysis of soft biological tissues. *Computer Methods in Applied Mechanics and Engineering*, 192(47):5059 – 5098, 2003. ISSN 0045-7825. doi:doi.org/10.1016/j.cma.2003.06.001.
- [33] A. E. Green and R. S. Rivlin. On cauchy’s equations of motion. *Zeitschrift für angewandte Mathematik und Physik ZAMP*, 15(3):290–292, Mar 1964. ISSN 1420-9039. doi:10.1007/BF01607019.
- [34] M. E. Gurtin. The nature of configurational forces. *Archives for Rational Mechanics and Analysis*, 131:67–100, 1995.

- [35] M. E. Gurtin. *Configurational Forces as Basic Concepts of Continuum Physics*. Springer-Verlag New York, 2000. doi:10.1007/b97847.
- [36] M. E. Gurtin and A. I. Murdoch. A continuum theory of elastic material surfaces. *Archive for Rational Mechanics and Analysis*, 57 (4):291–323, 1975.
- [37] E. H. Lee. Elastic-plastic deformation at finite strains. *Journal of Applied Mechanics*, 36:27, 06 1968. doi:10.1115/1.3564580.
- [38] K. Hackl. Generalized standard media and variational principles in classical and finite strain elastoplasticity. *Journal of the Mechanics and Physics of Solids*, 45 (5):667 – 688, 1997. ISSN 0022-5096. doi:10.1016/S0022-5096(96)00110-X.
- [39] B. Halphen and Q. Nguyen. Sur les matériaux standards généralisés. *J. Mécanique*, 14:39–63, 1975.
- [40] T. Heitbreder, N. S. Ottosen, M. Ristinmaa, and J. Mosler. Consistent elastoplastic cohesive zone model at finite deformations - variational formulation. *International Journal of Solids and Structures*, 106-107:284–293, 2017. ISSN 0020-7683. doi:10.1016/j.ijsolstr.2016.10.027.
- [41] T. Heitbreder, N. S. Ottosen, M. Ristinmaa, and J. Mosler. On damage modeling of material interfaces: Numerical implementation and computational homogenization. *Computer Methods in Applied Mechanics and Engineering*, 337:1–27, 2018. ISSN 0045-7825. doi:10.1016/j.cma.2018.03.023.
- [42] A. Hillerborg, M. Modéer, and P.-E. Petersson. Analysis of crack formation and crack growth in concrete by means of fracture mechanics and finite elements. *Cement and Concrete Research*, 6(6):773–781, 1976. ISSN 0008-8846. doi:10.1016/0008-8846(76)90007-7.
- [43] G. Holzapfel. *Nonlinear Solid Mechanics. A Continuum Approach for Engineering*. John Wiley & Sons, 2000.
- [44] A. Javili and P. Steinmann. A finite element framework for continua with boundary energies. part i: The two-dimensional case. *Computer Methods in Applied Mechanics and Engineering*, 198(27):2198–2208, 2009. ISSN 0045-7825. doi:10.1016/j.cma.2009.02.008.
- [45] A. Javili and P. Steinmann. A finite element framework for continua with boundary energies. part ii: The three-dimensional case. *Computer Methods in Applied Mechanics and Engineering*, 199(9):755–765, 2010. ISSN 0045-7825. doi:10.1016/j.cma.2009.11.003.
- [46] A. Javili, F. dell’Isola, and P. Steinmann. Geometrically nonlinear higher-gradient elasticity with energetic boundaries. *Journal of the Mechanics and Physics of Solids*, 61(12):2381 – 2401, 2013. ISSN 0022-5096. doi:doi.org/10.1016/j.jmps.2013.06.005.

-
- [47] A. Javili. Variational formulation of generalized interfaces for finite deformation elasticity. *Mathematics and Mechanics of Solids*, 23(9):1303–1322, 2018. doi:10.1177/1081286517719938.
- [48] A. Javili. A note on traction continuity across an interface in a geometrically nonlinear framework. *Mathematics and Mechanics of Solids*, 24(8):2478–2496, 2019. doi:10.1177/1081286518766980.
- [49] A. Javili, A. McBride, and P. Steinmann. Thermomechanics of solids with lower-dimensional energetics: On the importance of surface, interface, and curve structures at the nanoscale. a unifying review. *Applied Mechanics Reviews*, 65:010802, March 2013. doi:10.1115/1.4023012.
- [50] A. Javili, P. Steinmann, and J. Mosler. Micro-to-macro transition accounting for general imperfect interfaces. *Computer Methods in Applied Mechanics and Engineering*, 317:274 – 317, 2017. ISSN 0045-7825. doi:10.1016/j.cma.2016.12.025.
- [51] A. Javili, N. S. Ottosen, M. Ristinmaa, and J. Mosler. Aspects of interface elasticity theory. *Mathematics and Mechanics of Solids*, 23(7):1004–1024, 2018. doi:10.1177/1081286517699041.
- [52] S. Kaessmair, A. Javili, and P. Steinmann. Thermomechanics of solids with general imperfect coherent interfaces. *Archive of Applied Mechanics*, 84(9):1409–1426, October 2014. ISSN 1432-0681. doi:10.1007/s00419-014-0870-x.
- [53] W. Kühnel. *Differentialgeometrie - Kurven - Flächen - Mannigfaltigkeiten*. Springer-Verlag, Berlin Heidelberg New York, 6. aufl. edition, 2012. ISBN 978-3-658-00615-0.
- [54] T. A. Laursen. *Computational Contact and Impact Mechanics: Fundamentals of Modeling Interfacial Phenomena in Nonlinear Finite Element Analysis*. Springer, 2003.
- [55] J. Lubliner. *Plasticity Theory*. Dover Books on Engineering. Dover Publications, 2013. ISBN 9780486318202.
- [56] J. Mandel. *Plasticité classique et viscoplasticité: course held at the Department of Mechanics of Solids, September-October, 1971*. Courses and lectures - International Centre for Mechanical Sciences. Springer-Verlag, 1972. ISBN 9780387811970.
- [57] J. Marsden and T. Hughes. *Mathematical Foundations of Elasticity*. Dover Civil and Mechanical Engineering Series. Dover, 1994. ISBN 9780486678658.
- [58] J. P. McGarry, Éamonn Ó Máirtín, G. Parry, and G. E. Beltz. Potential-based and non-potential-based cohesive zone formulations under mixed-mode separation and over-closure. part i: Theoretical analysis. *Journal of the Mechanics and Physics of Solids*, 63:336 – 362, 2014. ISSN 0022-5096. doi:10.1016/j.jmps.2013.08.020.
- [59] J. Mergheim and P. Steinmann. A geometrically nonlinear fe approach for the simulation of strong and weak discontinuities. *Computer Methods in Ap-*

- plied Mechanics and Engineering*, 195(37):5037 – 5052, 2006. ISSN 0045-7825. doi:doi.org/10.1016/j.cma.2005.05.057. John H. Argyris Memorial Issue. Part I.
- [60] C. Miehe. Strain-driven homogenization of inelastic microstructures and composites based on an incremental variational formulation. *International Journal for Numerical Methods in Engineering*, 55:1285–1322, 2002.
- [61] R. Mindlin. Second gradient of strain and surface-tension in linear elasticity. *International Journal of Solids and Structures*, 1(4):417 – 438, 1965. ISSN 0020-7683. doi:10.1016/0020-7683(65)90006-5.
- [62] N. Moës, J. Dolbow, and T. Belytschko. A finite element method for crack growth without remeshing. *International Journal for Numerical Methods in Engineering*, 46(1):131–150, 1999. ISSN 1097-0207. doi:10.1002/(SICI)1097-0207(19990910)46:1<131::AID-NME726>3.0.CO;2-J.
- [63] J. Mosler. On advanced solution strategies to overcome locking effects in strong discontinuity approaches. *International Journal for Numerical Methods in Engineering*, 63(9):1313–1341, 2005. ISSN 1097-0207. doi:10.1002/nme.1329.
- [64] J. Mosler. *On the numerical modeling of localized material failure at finite strains by means of variational mesh adaption and cohesive elements*. Habilitation, Ruhr-Universität Bochum, 2007.
- [65] J. Mosler and O. Bruhns. Towards variational constitutive updates for non-associative plasticity models at finite strain: models based on a volumetric-deviatoric split. *International Journal of Solids and Structures*, 46(7-8):1676–1684, 2009.
- [66] J. Mosler and O. Bruhns. On the implementation of rate-independent standard dissipative solids at finite strain – Variational constitutive updates. *Computer Methods in Applied Mechanics and Engineering*, 199:417–429, 2010.
- [67] J. Mosler and F. Cirak. A variational formulation for finite deformation wrinkling analysis of inelastic membranes. *Computer Methods in Applied Mechanics and Engineering*, 198:2087–2098, 2009.
- [68] J. Mosler and I. Scheider. A thermodynamically and variationally consistent class of damage-type cohesive models. *Journal of the Mechanics and Physics of Solids*, 59(8):1647–1668, 2011. ISSN 0022-5096. doi:10.1016/j.jmps.2011.04.012.
- [69] A. Murdoch. A thermodynamical theory of elastic material interfaces. *Quarterly Journal of Mechanics and Applied Mathematics - QUART J MECH APPL MATH*, 29:245–275, 08 1976. doi:10.1093/qjmam/29.3.245.
- [70] A. Needleman. A continuum model for void nucleation by inclusion debonding. *Journal of applied mechanics*, 54(3):525–531, 1987. doi:10.1115/1.3173064.
- [71] W. Noll. *La Mécanique Classique, Basée sur un Axiome d’Objectivité*, pages 135–144. Springer Berlin Heidelberg, Berlin, Heidelberg, 1974. ISBN 978-3-642-65817-

4. doi:10.1007/978-3-642-65817-4_8.
- [72] M. Ortiz and A. Pandolfi. Finite-deformation irreversible cohesive elements for three-dimensional crack-propagation analysis. *International Journal for Numerical Methods in Engineering*, 44(9):1267–1282, 1999. ISSN 1097-0207. doi:10.1002/(SICI)1097-0207(19990330)44:9<1267::AID-NME486>3.0.CO;2-7.
- [73] M. Ortiz and E. Repetto. Nonconvex energy minimisation and dislocation in ductile single crystals. *Journal of the Mechanics and Physics of Solids*, 47:397–462, 1999. doi:10.1016/S0022-5096(97)00096-3.
- [74] M. Ortiz and L. Stainier. The variational formulation of viscoplastic constitutive updates. *Computer Methods in Applied Mechanics and Engineering*, 171(3):419 – 444, 1999. ISSN 0045-7825. doi:10.1016/S0045-7825(98)00219-9.
- [75] N. S. Ottosen, M. Ristinmaa, and J. Mosler. Fundamental physical principles and cohesive zone models at finite displacements - limitations and possibilities. *International Journal of Solids and Structures*, 53:70–79, 2015. doi:10.1016/j.ijsolstr.2014.10.020.
- [76] N. S. Ottosen and M. Ristinmaa. Thermodynamically based fictitious crack/interface model for general normal and shear loading. *International Journal of Solids and Structures*, 50(22):3555 – 3561, 2013. ISSN 0020-7683. doi:doi.org/10.1016/j.ijsolstr.2013.06.019.
- [77] N. S. Ottosen, M. Ristinmaa, and J. Mosler. Framework for non-coherent interface models at finite displacement jumps and finite strains. *Journal of the Mechanics and Physics of Solids*, 90(Supplement C):124–141, 2016. ISSN 0022-5096. doi:10.1016/j.jmps.2016.02.034.
- [78] K. Park and G. H. Paulino. Cohesive zone models: A critical review of traction-separation relationships across fracture surfaces. *Applied Mechanics Reviews*, 64: 1002–, 11 2011. doi:10.1115/1.4023110.
- [79] K. Park, G. H. Paulino, and J. R. Roesler. A unified potential-based cohesive model of mixed-mode fracture. *Journal of the Mechanics and Physics of Solids*, 57(6):891 – 908, 2009. ISSN 0022-5096. doi:doi.org/10.1016/j.jmps.2008.10.003.
- [80] G. Pietrzak and A. Curnier. Large deformation frictional contact mechanics: continuum formulation and augmented lagrangian treatment. *Computer Methods in Applied Mechanics and Engineering*, 177(3):351 – 381, 1999. ISSN 0045-7825. doi:10.1016/S0045-7825(98)00388-0.
- [81] A. C. Pipkin. The relaxed energy density for isotropic elastic membranes. *IMA Journal of Applied Mathematics*, 36(1):85–99, 1986. doi:10.1093/imamat/36.1.85.
- [82] A. C. Pipkin. Convexity conditions for strain-dependent energy functions for membranes. *Arch. Rational Mech. Anal.*, 121:361–376, 1993.

- [83] A. C. Pipkin. Relaxed energy densities for large deformations of membranes. *IMA Journal of Applied Mathematics*, 52:297–308, 1994.
- [84] R. Radulovic, O. T. Bruhns, and J. Mosler. Effective 3D failure simulations by combining the advantages of embedded strong discontinuity approaches and classical interface elements. *Engineering Fracture Mechanics*, 78(12):2470–2485, 2011. ISSN 0013-7944. doi:10.1016/j.engfracmech.2011.06.007.
- [85] S. Saeb, P. Steinmann, and A. Javili. Aspects of computational homogenization at finite deformations. a unifying review from reuss’ to voigt’s bound. *Applied Mechanics Reviews*, 68, 06 2016. doi:10.1115/1.4034024.
- [86] I. Scheider and W. Brocks. Simulation of cup – cone fracture using the cohesive model. *Engineering Fracture Mechanics*, 70(14):1943 – 1961, 2003. ISSN 0013-7944. doi:10.1016/S0013-7944(03)00133-4. Cohesive Models.
- [87] J. Schellekens and R. de Borst. A non-linear finite element approach for the analysis of mode-i free edge delamination in composites. *International Journal of Solids and Structures*, 30(9):1239–1253, 1993. ISSN 0020-7683. doi:10.1016/0020-7683(93)90014-X.
- [88] J. Schröder. *Homogenisierungsmethoden der nichtlinearen Kontinuumsmechanik unter Beachtung von Stabilitätsproblemen*. Habilitation, Univ., Inst. für Mechanik, Stuttgart, January 2000.
- [89] J. C. Simo and J. W. Ju. On continuum damage-elastoplasticity at finite strains. *Computational Mechanics*, 5(5):375–400, September 1989. ISSN 1432-0924. doi:10.1007/BF01047053.
- [90] J. Simo and T. Hughes. *Computational Inelasticity*. Springer-Verlag New York, 1998. doi:10.1007/b98904.
- [91] D. W. Spring, O. Giraldo-Londoño, and G. H. Paulino. A study on the thermodynamic consistency of the park–paulino–roesler (ppr) cohesive fracture model. *Mechanics Research Communications*, 78:100 – 109, 2016. ISSN 0093-6413. doi:doi.org/10.1016/j.mechrescom.2016.05.006. Recent Advances in Multiscale, Multifunctional and Functionally Graded Materials.
- [92] D. J. Steigmann and R. W. Ogden. Plane deformations of elastic solids with intrinsic boundary elasticity. *Proceedings of the Royal Society of London. Series A: Mathematical, Physical and Engineering Sciences*, 453(1959):853–877, 1997. doi:10.1098/rspa.1997.0047.
- [93] D. J. Steigmann and R. W. Ogden. Elastic surface–substrate interactions. *Proceedings of the Royal Society of London. Series A: Mathematical, Physical and Engineering Sciences*, 455(1982):437–474, 1999. doi:10.1098/rspa.1999.0320.
- [94] P. Steinmann. On boundary potential energies in deformational and configurational mechanics. *Journal of the Mechanics and Physics of Solids*, 56(3):772–800, 2008. ISSN 0022-5096. doi:10.1016/j.jmps.2007.07.001.

-
- [95] P. Steinmann. *Geometrical Foundations of Continuum Mechanics*, volume 2. 01 2015. doi:10.1007/978-3-662-46460-1.
- [96] E. Svenning. A weak penalty formulation remedying traction oscillations in interface elements. *Computer Methods in Applied Mechanics and Engineering*, 310 (Supplement C):460–474, 2016. ISSN 0045-7825. doi:10.1016/j.cma.2016.07.031.
- [97] C. Truesdell and R. Toupin. The classical field theories. *Handbuch der Physik*, 2: 226–858, 1960. doi:10.1007/978-3-642-45943-6_2.
- [98] C. Truesdell and W. Noll. *The Non-Linear Field Theories of Mechanics*. Springer-Verlag Berlin Heidelberg, 3 edition, 2004. doi:10.1007/978-3-662-10388-3.
- [99] V. Tvergaard and J. W. Hutchinson. The influence of plasticity on mixed mode interface toughness. *Journal of the Mechanics and Physics of Solids*, 41(6):1119 – 1135, 1993. ISSN 0022-5096. doi:doi.org/10.1016/0022-5096(93)90057-M.
- [100] M. van den Bosch, P. Schreurs, and M. Geers. An improved description of the exponential xu and needleman cohesive zone law for mixed-mode decohesion. *Engineering Fracture Mechanics*, 73(9):1220 – 1234, 2006. ISSN 0013-7944. doi:doi.org/10.1016/j.engfracmech.2005.12.006.
- [101] M. van den Bosch, P. Schreurs, and M. Geers. A cohesive zone model with a large displacement formulation accounting for interfacial fibrillation. *European Journal of Mechanics - A/Solids*, 26(1):1 – 19, 2007. ISSN 0997-7538. doi:doi.org/10.1016/j.euromechsol.2006.09.003.
- [102] M. van den Bosch, P. Schreurs, and M. Geers. Identification and characterization of delamination in polymer coated metal sheet. *Journal of the Mechanics and Physics of Solids*, 56(11):3259 – 3276, 2008. ISSN 0022-5096. doi:doi.org/10.1016/j.jmps.2008.07.006.
- [103] B. Vossen, P. Schreurs, O. van der Sluis, and M. Geers. On the lack of rotational equilibrium in cohesive zone elements. *Computer Methods in Applied Mechanics and Engineering*, 254(Supplement C):146–153, 2013. ISSN 0045-7825. doi:10.1016/j.cma.2012.10.004.
- [104] P. Wriggers. *Computational Contact Mechanics*. Springer, 2006.
- [105] X.-P. Xu and A. Needleman. Void nucleation by inclusion debonding in a crystal matrix. *Modelling and Simulation in Materials Science and Engineering*, 1:111–132, January 1993. doi:10.1088/0965-0393/1/2/001.
- [106] Q. Yang, L. Stainier, and M. Ortiz. A variational formulation of the coupled thermo-mechanical boundary-value problem for general dissipative solids. *Journal of the Mechanics and Physics of Solids*, 54(2):401 – 424, 2006. ISSN 0022-5096. doi:10.1016/j.jmps.2005.08.010.
- [107] Éamonn Ó Máirtín, G. Parry, G. E. Beltz, and J. P. McGarry. Potential-based and non-potential-based cohesive zone formulations under mixed-mode

Bibliography

separation and over-closure—part ii: Finite element applications. *Journal of the Mechanics and Physics of Solids*, 63:363 – 385, 2014. ISSN 0022-5096. doi:doi.org/10.1016/j.jmps.2013.08.019.

Curriculum Vitae

Personal Data

Name	Tim Steffen Heitbreder
Date of Birth	October 13, 1987
Place of Birth	Gladbeck, Germany
Nationality	German

Professional Occupation

03/2014 – onwards	Scientific Assistant, Institute of Mechanics, TU Dortmund University
05/2010 – 10/2013	Student Assistant, Chair of Continuum Mechanics, Ruhr University Bochum

University Education

10/2013	Academic Degree: Master of Science
06/2012 – 10/2013	Studies of Mechanical Engineering, Ruhr University Bochum
06/2012	Academic Degree: Bachelor of Science
10/2008 – 06/2012	Studies of Mechanical Engineering, Ruhr University Bochum

School Education

06/2007	University-entrance Diploma, Max-Planck Secondary School, Gelsenkirchen
---------	--

Publication series of the Institute of Mechanics

published to date:

- 2010/01 Palnau, V.: Implementierung eines netzfreien Diskretisierungsverfahrens und seine Anwendung auf die Scherbandanalyse. ISBN 978-3-921823-51-4
- 2010/02 Klusemann, B.: Application of homogenization methods and crystal plasticity to the modeling of heterogeneous materials of technological interest. ISBN 978-3-921823-53-8
- 2011/01 Hortig, C.: Local and non-local thermomechanical modeling and finite-element simulation of high-speed cutting. ISBN 978-3-921823-54-5
- 2011/02 Parvizian, F.: Modeling of microstructure evolution in aluminum alloys during hot extrusion. ISBN 978-3-921823-56-9
- 2011/03 Noman, M.: Characterization and model identification for the simulation of the forming behavior of ferritic steels. ISBN: 978-3-921823-55-2
- 2011/04 Kayser, T.: Characterization of microstructure in aluminum alloys based on electron backscatter diffraction. ISBN: 978-3-921823-57-6
- 2011/05 Bargmann, S.: Computational modeling of material behavior on different scales based on continuum mechanics. ISBN: 978-3-921823-58-3
- 2013/01 Waffenschmidt, T.: Modelling and simulation of adaptation and degradation in anisotropic biological tissues. ISBN: 978-3-921823-61-3
- 2015/01 Ostwald, R.: Modelling and simulation of phase-transformations in elastoplastic polycrystals. ISBN: 978-3-921823-66-8
- 2016/01 Subramanian, M.: Phenomenological modelling and simulation of ferroelectric ceramics. ISBN: 978-3-921823-74-3
- 2016/02 Clausmeyer, T.: Evolution of plastic anisotropy in metals. ISBN: 978-3-921823-76-7
- 2017/01 Holtermann, R.: Computational multiscale modelling of grinding processes. ISBN: 978-3-921823-86-6
- 2017/02 Bartels, A.: Modelling of evolving microstructures at different scales. ISBN: 978-3-921823-93-4

- 2017/03 Dusthakar Kumar Rao, D. K.: Computational modelling of single and polycrystalline ferroelectric materials. ISBN 978-3-921823-94-1
- 2019/01 Buckmann, K.: Microstructure evolution in functional magnetic materials. ISBN 978-3-947323-09-8
- 2019/02 Kaiser, T.: Computational modelling of non-simple and anisotropic materials. ISBN 978-3-947323-14-2
- 2019/03 Heitbreder, T.: Modelling of material interfaces at different length scales. ISBN 978-3-947323-18-0